

Novel Non-Aqueous Symmetric  
Redox Materials for Redox Flow  
Battery Energy Storage



**Craig G. Armstrong**

**This dissertation is submitted for the degree of Doctor  
of Philosophy**

**January 2020**

**Department of Chemistry**

*The search for 'electrochemically promiscuous' redox materials...*

*- Craig Armstrong, 2017*

# Declaration

This thesis has not been submitted in support of an application for another degree at this or any other university. It is the result of my own work and includes nothing that is the outcome of work done in collaboration except where specifically indicated. Many of the ideas in this thesis were the product of discussion with my supervisor Dr Kathryn E. Toghill. Dr Ross W. Hogue assisted in the acquisition of experimental results in chapters 4, 6 and 7. He is also credited for co-writing [3], of which Chapter 6 is based, and is a second author on [4]. Excerpts of this thesis have been published in the following academic publications [1–4].

[1] C.G. Armstrong, K.E. Toghill, Cobalt(II) complexes with azole-pyridine type ligands for non-aqueous redox-flow batteries: Tunable electrochemistry via structural modification, *J. Power Sources*. 349 (2017) 121–129.

doi:10.1016/j.jpowsour.2017.03.034.

[2] C.G. Armstrong, K.E. Toghill, Stability of molecular radicals in organic non-aqueous redox flow batteries: A mini review, *Electrochem. Commun.* 91 (2018) 19–24.

doi:10.1016/j.elecom.2018.04.017.

[3] R. Hogue, C. Armstrong, K. Toghill, Dithiolene Complexes of First Row Transition Metals for Symmetric Non-Aqueous Redox Flow Batteries, *ChemSusChem*. (2019) 1–11. doi:10.1002/cssc.201901702.

[4] C.G. Armstrong, R.W. Hogue, K.E. Toghill, Application of the dianion croconate violet for symmetric organic non-aqueous redox flow battery electrolytes, *J. Power Sources*. 440 (2019) 227037.

doi:10.1016/j.jpowsour.2019.227037.

The research presented within this thesis was in part financially supported by the Engineering and Physical Sciences Research Council (EPSRC), however the author declares no conflicts of interest.

Craig Gregory Armstrong. MSci

Lancaster University, UK

## Acknowledgements

*First and foremost, I would like to thank my supervisor Dr Kathryn Toghill. I am very grateful for her offering me this PhD position in the first instance and mentoring me since then. Despite my initial lack of electrochemistry knowledge, I can now call myself an electrochemist and battery chemist, because of Kathryn's tutoring. She has been an exceptional academic to work for as she deeply cares for her group members. In reflection, being Kathryn's first PhD student has been a challenge as it was mostly on me to build our experiments from scratch, however, her continuing support has led to a very fruitful PhD with four publications. In addition, I have developed a resourcefulness and progressive attitude from Kathryn because of our limited resources, which I think is lost on some PhD students. I therefore consider Kathryn to be my role model both in academic and personal life. Thank you for all the opportunities I have had, such as the international conferences and working in Switzerland for three months. I would also like to thank other Toghill group members past and present for their assistance. Most noteworthy Dr Ross Hogue, of whom I learnt many synthetic chemistry tricks, and Dr Declan Bryans for sharing his battery knowledge.*

*Many thanks should be directed to my family for financially supporting me through my university endeavours and their positivity towards my studies. I apologise for all those long car journeys to ferry me back and forth with all my junk to university, however I know they never minded too much. The last eight years has certainly been worth it all. Most importantly, I would like to thank my life partner Sapphire McNeil for keeping me alive while writing this heinous document. She continues to support all my big decisions in life, and I treasure her company. Sorry for every late night in the office or laboratory in completing my PhD.*

*Finally, I would like to thank the members of my department and fellow PhD students for making my studies so enjoyable. Despite the endless building works, false alarms, power cuts and biblical flooding, I am very grateful to have worked in such an inclusive and nurturing department. I would also like to thank the university for funding my PhD as well as the RSC and EPSRC for additional funding.*

*Thank you!*

*-Craig*

## Abstract

Redox flow batteries are promising energy storage devices for grid-scale applications due to their decoupled power and capacity. The utilisation of non-aqueous electrolytes, as opposed to conventional water-based electrolytes, is a promising pathway for achieving techno-economic targets via advancements in energy density. Herein a selection of novel redox materials were explored for application as symmetric redox flow battery electrolytes whereby the same compound is used in both the battery cathode and anode reactions. Metal coordination compounds such as Co(II) complexes with tridentate azole-pyridine ligands demonstrated good long-term stability and cell potentials in excess of 1.5 V, however low solubility due to their large size is problematic. Smaller metal complexes with bidentate dithiolene ligands gave promising redox properties however instability of charged oxidation states causes rapid decomposition of the inorganic electrolyte. Similar instability was observed for a new symmetric redox material, croconate violet, which arises from high reactivity of radical states. The instability of the charged oxidation states of novel redox materials remains a challenge for the research field, as capacity loss has been reported in practically every novel non-aqueous redox material. Indeed, by developing the ferrocene-ferrocenium ion redox couple for non-aqueous cell characterisation, a noteworthy capacity loss over extended battery cycling experiments was observed. The present work therefore highlights the challenges with identifying suitable non-aqueous redox materials for application.

# Contents

<b>Chapter 1</b>	<b>Introduction to Redox Flow Batteries</b>	<b>1</b>
1.1	Energy storage technologies	1
1.2	Development of the commercial redox flow battery	4
1.3	Redox flow battery architecture	7
1.3.1	Electrodes and current collectors	8
1.3.2	Membranes	9
1.4	Electrolytes for redox flow batteries	11
1.4.1	Aqueous electrolytes	11
1.4.2	Non-aqueous electrolytes	14
1.5	Progress in non-aqueous redox flow batteries	17
1.6	Thesis objectives and overview	21
<b>Chapter 2</b>	<b>Fundamental Electrochemistry Theory</b>	<b>23</b>
2.1	Equilibrium electrochemistry and thermodynamics	23
2.1.1	Electrochemical equilibrium	24
2.1.2	Electrode potentials	27
2.1.3	Thermodynamics of electrochemical reactions	29
2.1.4	Practical reference electrodes	30
2.2	Dynamic electrochemistry	32
2.2.1	Mass transport	33
2.2.2	Structure of the electric double layer	35
2.2.3	Electrode kinetics	37
2.2.4	Marcus theory	43
2.2.5	The Cottrell equation and the Nernst diffusion layer	44
2.3	Electrochemical techniques	46
2.3.1	Principals of voltammetry	47
2.3.2	Hydrodynamic methods: the rotating disc electrode	52
2.3.3	Impedance	54
2.3.4	Electrolysis	56
2.4	The electrochemistry of redox flow batteries	57
2.4.1	Theoretical cell potential	57
2.4.2	Polarisation	58
2.4.3	Battery metrics	59
2.4.4	Cell configurations	62
<b>Chapter 3</b>	<b>Electrochemical Cell Designs</b>	<b>65</b>
3.1	Introduction	65
3.2	Glass H-type and bulk electrolysis cells	67
3.3	Non-aqueous flow-cells	70
3.3.1	Flow-cell I	71
3.3.2	Flow-cell II	73
3.4	Electrode materials	76
3.5	Membranes	80
3.6	Peristaltic pump calibrations	83
3.7	Conclusions	83

<b>Chapter 4</b>	<b>Ferrocene as a Model Chemistry for Cell Characterisation ...</b>	<b>85</b>
4.1	Introduction .....	85
4.2	Experimental .....	88
4.2.1	Chemicals and materials .....	88
4.2.2	Ferrocenium tetrafluoroborate synthesis .....	88
4.2.3	UV-vis and solubility measurements .....	88
4.2.4	Electrolyte preparation .....	89
4.2.5	Voltammetry techniques .....	89
4.2.6	Battery methods .....	90
4.3	Results and Discussion .....	91
4.3.1	Characterisation of the Fc/FcBF <sub>4</sub> redox couple .....	91
4.3.2	Cell characterisation by use of the Fc/FcBF <sub>4</sub> chemistry .....	95
4.3.3	Charge-discharge studies of the Fc/FcBF <sub>4</sub> redox couple .....	100
4.3.4	Capacity loss investigations .....	104
4.4	Conclusions .....	113
<b>Chapter 5</b>	<b>Co(II) Complexes with Azole-Pyridine Ligands.....</b>	<b>115</b>
5.1	Introduction .....	115
5.2	Experimental .....	116
5.2.1	Chemicals and reagents .....	116
5.2.2	Synthesis of azole-pyridine ligands .....	116
5.2.3	Synthesis of Co(II) complexes .....	118
5.2.4	Voltammetry studies .....	119
5.2.5	Battery methods .....	120
5.2.6	Solubility measurements .....	121
5.3	Results and discussion .....	121
5.3.1	Synthesis and characterisation .....	121
5.3.2	Solubilities in MeCN .....	122
5.3.3	Voltammetry behaviour of Co(II) complexes .....	123
5.3.4	Electrochemical kinetics .....	130
5.3.5	Charge-discharge performance in H-type glass cell .....	137
5.3.6	Flow-cell battery studies .....	142
5.4	Conclusions .....	147
<b>Chapter 6</b>	<b>Dithiolene Complexes of First-Row Transition Metals.....</b>	<b>151</b>
6.1	Introduction .....	151
6.2	Experimental .....	152
6.2.1	Synthesis of sodium maleonitriledithiolate .....	152
6.2.2	Synthesis of metal maleonitriledithiolate complexes .....	153
6.2.3	UV-vis spectroscopic methods .....	156
6.2.4	Solubility measurements .....	156
6.2.5	Voltammetry studies .....	157
6.2.6	Battery methods .....	157
6.3	Results and discussion .....	158
6.3.1	Synthesis and characterisation .....	158
6.3.2	Voltammetry behaviour of metal complexes .....	160
6.3.3	V <sub>mnt</sub> battery studies .....	168
6.3.4	Co <sub>mnt</sub> battery studies .....	174
6.3.5	Ni <sub>mnt</sub> battery studies .....	176
6.3.6	Cu <sub>mnt</sub> battery studies .....	180

6.3.7 Fe <sub>mnt</sub> battery studies.....	184
6.3.8 M <sub>mnt</sub> battery comparison.....	185
6.4 Conclusions.....	186
<b>Chapter 7 Symmetric Organic Electrolyte: Croconate Violet .....</b>	<b>189</b>
7.1 Introduction.....	189
7.2 Experimental.....	192
7.2.1 Chemicals and reagents.....	192
7.2.2 Synthesis of Croconate Violet.....	193
7.2.3 Solubility measurement .....	194
7.2.4 Voltammetry investigations.....	194
7.2.5 Battery methods .....	195
7.3 Results and discussion .....	195
7.3.1 Synthesis of TBA <sub>2</sub> Croc and solubility.....	196
7.3.2 Voltammetry investigations.....	198
7.3.3 Battery application .....	205
7.4 Conclusions.....	215
<b>Chapter 8 Conclusions.....</b>	<b>217</b>
8.1 Summary.....	217
8.2 Retrospectives .....	218
8.3 Future work.....	220
<b>References.....</b>	<b>223</b>
<b>Appendix A: Physical properties of solvents.....</b>	<b>247</b>
<b>Appendix B: EDX analysis.....</b>	<b>249</b>
<b>Appendix C: UV-vis Solubility Calibrations.....</b>	<b>250</b>

## List of Tables

Table 1: Comparison of the energy density and cell potentials of common battery technologies [7].	7
Table 2. Comparison of representative aqueous and non-aqueous RFB properties [5,12,52,68,69]. (a) The aqueous RFB data corresponds to the VRFB with an electrolyte composition of 3-4 M H <sub>2</sub> SO <sub>4</sub> with 1.5-2 M vanadium [5]. (b) The non-aqueous RFB data corresponds to the V(acac) <sub>3</sub> RFB with a typical electrolyte composition of 0.5 M TEA BF <sub>4</sub> with 0.1 M V(acac) <sub>3</sub> [69].	12
Table 3. Commonly used reference electrodes and their potential vs SHE at 25 °C. (a) supporting electrolyte. (b) Value omitted. The Ag/Ag <sup>+</sup> potential is very dependent on the electrolyte composition. Values reproduced from [67].	32
Table 4. Properties and applications of the glass electrochemical cells as shown in Figure 22. (a) The electrolyte volume is dependent on the electrodes used due to solution displacement, however a minimum volume is required to fill the cell bridge and connect the two half-cells. (b) The inter-electrode separation is dependent on the electrodes used and their positioning in the cell.	69
Table 5. Properties of the flow-cell designs and their application in NA experiments. (a) 1 mM electrolyte with 0.5 M supporting salt. (b) 10 mM electrolyte with 0.1 M supporting electrolyte. (c) the C-Flow flow-cell was never used for NA experiments.	71
Table 6. Properties and application of commercial membranes. Acronyms: (CEM) = cation-exchange membrane, (AEM) = anion-exchange membrane, (PS) = porous separator, (A) = aqueous, (NA) = non-aqueous. (a) the FKE-30 CEM did not return to the original condition after soaking in MeCN electrolyte. Swelling estimated. (b) The FAA-3 AEM swelling was non-measurable due to degradation however the swelling was estimated at 400 %.	82
Table 7. Redox potentials, as measured from cyclic voltammograms at 50 mV s <sup>-1</sup> , of cobalt(II) complexes in 0.1 M TBA PF <sub>6</sub> MeCN solution, reported relative to Fc. Peak separations are given in parentheses and redox potentials are rounded to three significant figures.	127

Table 8. Standard electrochemical rate constants for complexes 1-4 on Au and GC electrode as measured by the Koutecký-Levich method. Meaningful RDE LSVs of the Co(III/II) redox couple for complex 3 could not be achieved due to (a) excessive overpotential and (b) irreproducible results due to high sensitivity of the kinetics on the electrode surface. (c) The quality of the data and analysis was poor, giving an unreliable rate constant and an unlikely transfer coefficient. ....	131
Table 9. Redox potentials vs Fc, as measured by CV at 100 mV s <sup>-1</sup> on GC electrode on 1 mM solutions of complex in 0.1 M TBA PF <sub>6</sub> MeCN electrolyte. The theoretical cell potential, $V_{cell} = E_{1/2} (M_{mnt}^{2-/1-}) - E_{1/2} (M_{mnt}^{3-/2-})$ , for a symmetric battery of the corresponding electrolyte is given. (a) The larger cell potential for a battery employing the more negative $M_{mnt}^{4-/3-}$ redox couple of $V_{mnt}$ . ....	162
Table 10. Solubilities in MeCN, theoretical maximum RFB energy densities, diffusion coefficients, and standard electrochemical rate constants for the $M_{mnt}$ complexes. (a) the theoretical energy density assuming that the $V_{mnt}^{3-/4-}$ redox couple was used as the battery negolyte vs the $V_{mnt}^{2-/1-}$ redox couple as the posolyte. (b) the diffusion coefficient and rate constant for $Fe_{mnt}$ were not calculated because the data does not obey the Randles-Sevcik and Koutecký-Levich equations respectively. ....	163
Table 11. Physical properties of solvents for electrochemical devices (standard conditions). Values reproduced from [19,67,68,98,100,101]. ....	247

## List of Schemes

Scheme 1. Chemical structures of MCC ligands for NA RFBs [96,105,131–140,119,141–148,120,122,123,126,128–130]. Ligand chemical names (in order left to right): Bidentate – Acetylacetonate derivatives, Maleonitriledithiolene, 2,2'-Bipyridine derivatives, 1,10-Phenanthroline. Tridentate - bis(2,6-diimine-pyridines), 2,2':6',2''-Terpyridine, bipyridylimino isoindolines. Tetradentate - 1,4,8,11-Tetrathiacyclotetradecane, 1,4,8,11-Tetraazacyclotetradecane, Linked Picolinamides. Other – Metallocenes, Trimetaphosphate anions.....	19
Scheme 2. Chemical structures of ROMs for NA RFBs [99,107,156–165,118,166–175,149,176–185,150,186–191,151–155]. In most cases different derivatives exist for each structure. ....	20
Scheme 3. Chemical structures and redox transitions of left) AcNH-TEMPO [159] and right) Fc1N112 <sup>+</sup> [97] model redox couples. ....	87
Scheme 4. The decomposition mechanism of ferrocenium cations in the presence of oxygen [219–221].....	109
Scheme 5. Synthesis of ligands L1-L5 and cobalt(II) complexes 1-5.....	122
Scheme 6. The chemical structures of metal dithiolene complexes studied for symmetric NA RFBs in this work. ....	152
Scheme 7. Synthetic pathways to the Na <sub>2</sub> mnt ligand: a) from NaCN and CS <sub>2</sub> in DMF [239–241] and b) from chloroacetonitrile, NaOH and sulfur in DMF [235]. .	159
Scheme 8. Chemical structures and molecular weights of symmetric ROMs for NA RFBs.....	190
Scheme 9. Radialene-type oxocarbon dianion structures. ....	191
Scheme 10. Preparation of croconate pseudooxocarbons via Knoevenagel condensation reactions with malononitrile [262,264]. ....	192
Scheme 11. Synthetic scheme for the preparation of croconate violet .....	196
Scheme 12. The preparation of rhodizonate via the reaction of an alkali metal with carbon monoxide [253].....	198

## List of Figures

- Figure 1. A Ragone plot of energy storage technologies. The combustion engine and lines of equal energy storage time are given for comparison. Regions approximated based on the literature [7,12–17]..... 2
- Figure 2. Schematic illustration of a generic redox flow battery..... 4
- Figure 3. Schematic diagram of a conventional RFB cell construction. .... 8
- Figure 4. The pH dependence of the hydrogen and oxygen evolution reactions in aqueous electrolyte [22]. The thermodynamic potentials are shown by solid lines whereas dashed lines show the onset potentials given overpotentials at carbon-based electrodes. An overpotential of 400 mV and 600 mV has been assumed for the OER and HER respectively..... 13
- Figure 5. Physical properties of selected solvents for RFBs. a) Electrochemical stability regions. The full range is given in parentheses in units V. b) Relative permittivity. c) liquid-phase temperature regions. The full range is given in parentheses in units °C. d) Viscosity. Data acquired from [19,67,68,98,100,101]. See Table 11 (Appendix A) for solvent abbreviations. .... 15
- Figure 6. The energy of electrons in the metal and solution before and after equilibrium is reached. Figure drawn with inspiration from [194]. .... 25
- Figure 7. The standard hydrogen electrode used to measure the potential of an arbitrary redox couple. Figure drawn with inspiration from [194]. .... 28
- Figure 8. Schematic illustration for the Grahame model of the electric double layer [194]. .... 36
- Figure 9. A reaction profile for the  $A^z/B^{z-1}$  redox reaction. The effect of varying the metal and solution electrical potentials is shown [194]. .... 38
- Figure 10. Graphical representations of the Butler-Volmer equation. a) Flux as function of the electrode potential  $E$  where  $\alpha = \beta = 0.5$ . The anodic and cathodic contributions are shown as  $j_a$  and  $j_c$ , respectively. b) The logarithm of current as a function of  $E$  for different values of the exchange coefficients. The Tafel law is given for both the cathodic and anodic current, however here they are only applicable for potentials less than  $-0.05$  V and greater than  $0.05$  V

respectively. Parameters), $[A^z] = [B^{z-1}] = 1 \text{ M}$ and $k^0 = 1 \text{ m s}^{-1}$ , $E_f = 0 \text{ V}$ , $A = 1 \text{ m}^2$ . .....	41
Figure 11. Schematic illustration of Tafel analysis. Parameters), $\alpha = \beta = 0.5$ , $[A^z] = [B^{z-1}] = 1 \text{ M}$ , $k^0 = 1 \text{ m s}^{-1}$ , $A = 1 \text{ m}^2$ . The extrapolated linear regressions are shown in grey. ....	42
Figure 12. Potential energy curve for an arbitrary reaction. The ground states (GS) of reactant (R) and product (P) as well as the transition state ( $\ddagger$ ) are shown [194]. ....	43
Figure 13. a) Concentration profiles at varying times as a function of electrode distance after a potential step for a diffusion coefficient of $5 \times 10^{-5} \text{ cm}^2 \text{ s}^{-1}$ . b) The current transients resulting from a potential step as a function of diffusion coefficient. Parameters: $A = 1 \text{ cm}^2$ , $c^* = 1 \text{ mol cm}^{-3}$ , $n = 1$ . ....	46
Figure 14. Simulated CV by use of EC_Simulator [199]. Parameters: $k^0 = 1 \text{ cm s}^{-1}$ , $D = 10^{-5} \text{ cm}^2 \text{ s}^{-1}$ , $\nu = 100 \text{ mV s}^{-1}$ , $E_f^0 = 0 \text{ V}$ , $n = 1$ , $r = 1.5 \text{ mm}$ , $T = 298 \text{ K}$ , $[\text{Red}] = 1 \text{ mM}$ . Characteristic voltammogram features are highlighted. ....	47
Figure 15. Simulated CVs by use of EC_Simulator [199]. a) CVs with $k^0 = 1, 10^{-4}$ and $10^{-5} \text{ cm s}^{-1}$ for the reversible, quasi-reversible and irreversible electron transfers respectively. b) CVs as a function of scan rate for a reversible voltammogram with $k^0 = 1 \text{ cm s}^{-1}$ . The black arrows show the starting points of voltammetry. Parameters: $D = 10^{-5} \text{ cm}^2 \text{ s}^{-1}$ , $\nu = 100 \text{ mV s}^{-1}$ , $E_f^0 = 0 \text{ V}$ , $n = 1$ , $r = 1.5 \text{ mm}$ , $T = 298 \text{ K}$ , $[\text{Red}] = 1 \text{ mM}$ . ....	49
Figure 16. The Levich equation applied to theoretical data with parameters: $D = 1 \times 10^{-5} \text{ cm}^2 \text{ s}^{-1}$ , $k^0 = 1 \times 10^{-2} \text{ cm s}^{-1}$ , $\beta = 0.5$ , $[\text{C}]_{\text{bulk}} = 1 \text{ mM}$ , $\nu = 8.92 \times 10^{-7} \text{ m}^2 \text{ s}^{-1}$ , $T = 298 \text{ K}$ , $A = 1.5 \text{ mm}$ , $n = 1$ . a) RDE LSVs for a redox couple with $E_f^0 = 0$ . The sampled limiting currents are shown. b) A plot of the limiting current against the square root of rotation rate. The relationship between the gradient and $D$ is shown. ....	53
Figure 17. The Koutecký-Levich method applied to theoretical data with parameters: $D = 1 \times 10^{-5} \text{ cm}^2 \text{ s}^{-1}$ , $k^0 = 1 \times 10^{-2} \text{ cm s}^{-1}$ , $\beta = 0.5$ , $[\text{C}]_{\text{bulk}} = 1 \text{ mM}$ , $\nu = 8.92 \times 10^{-7} \text{ m}^2 \text{ s}^{-1}$ , $T = 298 \text{ K}$ , $A = 1.5 \text{ mm}$ , $n = 1$ . a) RDE LSVs for a redox couple with $E_f^0 = 0$ . The sampled overpotentials are shown. b) Koutecký-Levich plot for select overpotentials. The intercepts corresponding to $1/i_K$ are highlighted.	

c) A plot of the logarithm of the kinetically limited current against overpotential. The relationships between the intercept/gradient and  $k^0/\beta$  are shown..... 54

Figure 18. a) Randles circuit with parameters shown. b) Simulated EIS Nyquist plot using the parameters in a). Example frequencies are shown as black circles. 56

Figure 19. A plot of the cell potential  $E_{\text{cell}}$  as a function of SOC..... 58

Figure 20. Generalised polarization curve for a RFB indicating the dominant source of overpotential in each region [203,204]. ..... 59

Figure 21. Cell configurations for battery experiments..... 63

Figure 22. Glass electrochemical cell designs and accessory. a) Membrane H-cell (GC-I). b) Linear cells (GC-II), i membrane and ii glass frit variants. c) Glass frit H-cell (GC-III), i bulk electrolysis and ii battery variants. d) Membrane bulk electrolysis cell (GC-IV). Front and side views shown. e) Flange slider-clamps. .... 68

Figure 23. FC-I flow-cell design in deconstructed and assembled view inside a  $N_2$  glovebox. Top left) FC-I flow-cell components: a) 3D-printed flow-cell bodies, b) brass current collectors and electrical contact, c) graphite current collectors, d) viton rubber internal seal, e) graphite felt electrodes, f) viton rubber gasket, g) membrane. Top right) Dimensions. Bottom) complete cell with peristaltic pump, glass-bottle reservoirs Tygon tubing and electrolyte.. 72

Figure 24. FC-II flow-cell design in deconstructed and assembled view inside a  $N_2$  glovebox. Top left) FC-II flow-cell components: a) PP electrolyte diffusers, b) ppg-86 graphite flow-field current collectors and gold pin contacts, c) EPDM and PTFE gaskets, d) EPDM O-rings, e) membrane, f) carbon paper electrodes, g) PP compression fittings, h) PFA assembly pins, i) M6 nuts and bolts. Top right) flow-field current collectors: FTFF = flow through flow-field, PFF = parallel flow-field, IDFF = interdigitated flow-field, SFF = serpentine flow-field. Bottom left) assembled FC-II flow-cell and PFA electrolyte reservoir. Bottom right) complete cell with peristaltic pump, PFA/Norprene tubing lines and electrolytes in  $N_2$  glovebox. .... 74

Figure 25. Schematic illustrations for the FC-II flow-field current collectors with flow-channels highlighted. FTFF = flow through flow-field, PFF = parallel flow-

field, IDFF = interdigitated flow-field, SFF = serpentine flow-field. Each flow-channel is 0.5 mm deep and 1 mm wide [40]. .....	75
Figure 26. Electrodes for use in glass cell battery/electrolysis experiments. a) graphite rod, b) graphite felt and graphite composite contact (SGL Sigracell® PV15), c) high-porosity RVC electrode and Cu wire contact.....	77
Figure 27. SEM images of the graphite felt electrode material (SGL Sigracell® GFD 4,6 EA). a) optical photograph of a typical electrode piece (20×40×4 mm dimensions), b) macroscopic structure of the graphite felt (100 μm scale), c) microscopic structure of the fibres (10 μm scale), d) microscopic structure of an individual fibre with ~6.5 μm diameter and surface impurities.....	79
Figure 28. SEM images of the carbon paper electrode material (20301A, Technical Fibre Products Ltd.). a) optical photograph of a typical electrode piece (13×16×1 mm dimensions), b) macroscopic structure of the carbon paper (100 μm scale), c) microscopic structure of the fibres and binder (10 μm scale), d) microscopic structure of an individual fibre with ~7 μm diameter and metal impurity.....	80
Figure 29. Pump calibrations for the flow-rate as a function of rpm for the a) digital and b) analogue Masterflex® peristaltic pumps used. L/S 14 Norprene tubing with pure MeCN. Each datapoint represented the mean flow-rate, averaged over three measurements.....	83
Figure 30. Cyclic voltammetry of 10 mM Fc in 0.1 M TEA BF <sub>4</sub> , MeCN. Blank voltammetry of the supporting electrolyte is given in grey and vertical dashed lines represent the upper and lower battery potential thresholds at ±1 V. a) Fc redox potential in comparison to the supporting electrolyte. (50 mV s <sup>-1</sup> ). b) CV of Fc in a wider potential range. 10 scans shown (100 mV s <sup>-1</sup> ). c) CVs as a function of scan number up to 100 scans.....	93
Figure 31. a) CVs as a function of scan-rate in the range of 10 to 100 mV s <sup>-1</sup> of 10 mM Fc. First scans shown. b) Peak potentials and separations for the Fc/FcBF <sub>4</sub> redox couple. c) Peak currents and current ratios (I <sub>c</sub> /I <sub>a</sub> ). d) Randles-Sevcik analysis for the forward Fc oxidation. The peak analysis for the back FcBF <sub>4</sub> is also given.....	94

Figure 32. Koutecký-Levich analysis of 1 mM Fc in 0.1 M TEA BF <sub>4</sub> , MeCN electrolyte. a) RDE LSVs as a function of rotation rate. b) Koutecký-Levich plots as a function of overpotential. c) plot of the logarithm of the kinetically limited current against overpotential. ....	95
Figure 33. Electrochemical impedance of the FC-II flow-cell. a) EIS as a function of flow-rate. b) analysis of the EIS spectrum of the flow-cell at 12 mL min <sup>-1</sup> . The ohmic resistance (R <sub>Ω</sub> ), charge-transfer resistance (R <sub>CT</sub> ) and mass transport resistance (R <sub>MT</sub> ) are shown. ....	96
Figure 34. a) Polarization curves as a function of flow-rate for the FC-II flow-cell. B) Maximum power density (at 1 V cell potential) as a function of flow-rate.....	98
Figure 35. a) EIS of the GC-II cell as a function of electrode separation (no membrane). b) The variation of ohmic resistance with electrode separation. c) EIS of the GC-II cell with different separator configurations. The electrodes are separated by 10 mm of electrolyte. d) Zoomed perspective of graph c as shown.....	100
Figure 36. a) Typical charge-discharge curve of the Fc/FcBF <sub>4</sub> single redox couple cell. Photographs are shown of the electrolyte reservoirs at 0, 50 and 100 % SOC. b) Selected charge-discharge curves during battery cycling. The vertical dashed line indicates the 2.68 mA h cell capacity. c) Capacity and coulombic efficiency as a function of cycle number (cell cycled from an initial SOC of 50 %). 5 mM Fc/FcBF <sub>4</sub> , 0.1 M TEA BF <sub>4</sub> , MeCN electrolyte at 10 mL min <sup>-1</sup> , 2.40 mA cm <sup>-2</sup> (1.87 C). ....	101
Figure 37. a) Selected charge-discharge curves during battery cycling of PC-based electrolyte at 2.40 mA cm <sup>-2</sup> (1.87 C). b) Capacity and coulombic efficiency as a function of cycle number (cell cycled from an initial SOC of 100 % after ~12 hour equilibration). 5 mM Fc/FcBF <sub>4</sub> , 0.1 M TEA BF <sub>4</sub> , PC electrolyte at 10 mL min <sup>-1</sup> .....	102
Figure 38. Cycling of the Fc/FcBF <sub>4</sub> single redox couple cell as a function of current density. a) Capacity and b) coulombic efficiency against cycle number. c) An overlay of charge-discharge curves at different current densities. Cycles 2, 22, 42, 62 and 82 are shown. The vertical dashed line shows the theoretical 2.68 mA h capacity. (5 mM Fc/FcBF <sub>4</sub> in 0.1 M TEA BF <sub>4</sub> , MeCN electrolyte).....	103

Figure 39. a) Typical Fc/FcBF <sub>4</sub> charge-discharge curves for the GC-III glass H-cell, using RVC and graphite rod electrodes. b) Representative cell capacities for the GC-III glass H-cell (RVC electrodes at 1 mA). (5 mM Fc/FcBF <sub>4</sub> in 0.1 M TEA BF <sub>4</sub> , MeCN electrolyte).....	104
Figure 40. characteristic capacity loss mechanisms in RFBs. ....	105
Figure 41. Capacity loss study of the Fc/FcBF <sub>4</sub> system in the FC-II flow-cell. a) capacity vs cycle number. The battery electrolytes were recombined and rebalanced at the 50 <sup>th</sup> cycle whereas the cell cycling was paused for 5 h at the 80 <sup>th</sup> . b) capacity vs time during the cycling pause (cycle time defined by the start of each charge/discharge step). c) OCP measurement of the flow-cell during the 5 h cycling pause. Inset graph – the cell potential as a function of Fc or FcBF <sub>4</sub> concentration as predicted by the Nernst equation. 5 mM Fc/FcBF <sub>4</sub> , 0.1 M TEA BF <sub>4</sub> , MeCN electrolyte at 10 mL min <sup>-1</sup> , 4.81 mA cm <sup>-2</sup> (3.73 C).....	107
Figure 42. The evolution with time of the UV-vis spectrum of a) 1 mM FcBF <sub>4</sub> in MeCN and b) 1 mM FcBF <sub>4</sub> in 0.1 M TEA BF <sub>4</sub> , MeCN.....	108
Figure 43. a) The evolution with time of the UV-vis spectrum of 0.9 mM FcBF <sub>4</sub> in MeCN with 2.78 M H <sub>2</sub> O (1 mL H <sub>2</sub> O in 20 mL volume). b) The variation in peak absorbance at $\lambda_{\text{max}} = 252$ nm with time for different quantities of added water. ....	110
Figure 44. The scan-rate dependence of 10 mM Fc and FcBF <sub>4</sub> in 0.1 M TEA BF <sub>4</sub> , MeCN electrolyte. First scans shown.....	111
Figure 45. RDE LSVs of 1 mM FcBF <sub>4</sub> in 0.1 M TEA BF <sub>4</sub> , MeCN electrolyte at 50 mV s <sup>-1</sup> on GC electrode. The effect of increasing the rotation rate is shown. ....	112
Figure 46. Cycling of the Fc/FcBF <sub>4</sub> single redox couple cell at 4.81 mA cm <sup>-2</sup> . (5 mM Fc/FcBF <sub>4</sub> in 0.1 M TEA BF <sub>4</sub> , MeCN electrolyte). The capacity retention of the freshly prepared electrolyte (blue) is compared to the three month old electrolyte (red). The total experiment time for the completion of 200 cycles is given for reference. ....	112
Figure 47. Cyclic voltammetry of Fc/FcBF <sub>4</sub> battery electrolytes (5 mM Fc and 5 mM FcBF <sub>4</sub> in 0.1 M TEA BF <sub>4</sub> , MeCN) at 50 mV s <sup>-1</sup> . The current response of a freshly prepared electrolyte is compared to a three month old electrolyte, as well as electrolytes recovered from battery studies.....	113

Figure 48. First cyclic voltammograms of 1 mM cobalt(II) complexes 1-4 on a) GC and b) Au electrode in 0.1 M TBA PF <sub>6</sub> MeCN solution at 50 mV s <sup>-1</sup> . Arrows indicate the start point of cyclic voltammetry. ....	124
Figure 49. Overlay of the first scan CVs of the Co(III/II) redox couple, of complexes 1-3, representing the stepwise substitution of terminal 2,2':6',2''-terpyridine pyridyl groups with 3,5-dimethylpyrazole donor groups. 1 mM complex in 0.1 M TBA PF <sub>6</sub> MeCN solution at 50 mV s <sup>-1</sup> on Au electrode.....	125
Figure 50. Randles-Sevcik plot for complexes 1 – 4 at 1 mM concentration in 0.1 M TBA PF <sub>6</sub> , MeCN electrolyte at room temperature. Peak currents were measured via baseline extrapolation of the Co(II/I) cathodic peakon on first scan. ....	127
Figure 51. Second scan CVs of 1 mM complex in 0.1 M TBA PF <sub>6</sub> MeCN solution as a function of scan rate. Left) Co(II/I) redox couple. Right) Co(III/II) redox couple.....	129
Figure 52. Koutecký-Levich analysis of 1 mM complex 1 in 0.1 M TBA PF <sub>6</sub> at Au (graphs a, c and e) and GC (graphs b, d and f) electrode. a/b) RDE LSVs as a function of rotation rate. c/d) Koutecký-Levich graphs for overpotentials 0 to 300 mV. e/f) logarithm of the kinetically limited current as a function of overpotential.....	132
Figure 53. Koutecký-Levich analysis of 1 mM complex 2 in 0.1 M TBA PF <sub>6</sub> at Au (graphs a, c and e) and GC (graphs b, d and f) electrode. a/b) RDE LSVs as a function of rotation rate. c/d) Koutecký-Levich graphs for overpotentials 0 to 300 mV. e/f) logarithm of the kinetically limited current as a function of overpotential.....	133
Figure 54. Koutecký-Levich analysis of 1 mM complex 3 in 0.1 M TBA PF <sub>6</sub> at Au (graphs a, c and e) and GC (graphs b, d and f) electrode. a/b) RDE LSVs as a function of rotation rate. c/d) Koutecký-Levich graphs for overpotentials 0 to 300 mV. e/f) logarithm of the kinetically limited current as a function of overpotential.....	134
Figure 55. Koutecký-Levich analysis of 1 mM complex 4 in 0.1 M TBA PF <sub>6</sub> at Au (graphs a, c and e) and GC (graphs b, d and f) electrode. a/b) RDE LSVs as a function of rotation rate. c/d) Koutecký-Levich graphs for overpotentials 0 to	

300 mV. e/f) logarithm of the kinetically limited current as a function of overpotential. The linear fits of the Co(III/II) on GC in d) are based on rotation rates of 300 to 1500 rpm. ....	135
Figure 56. Conceptual diagram for the spin crossover of the $[\text{Co}(\text{III/II})(\text{Ln})_2]^{2+/3+}$ redox couple.....	136
Figure 57. a) Charge-discharge cycles of 1 mM complex 1 in 0.5 TBA PF <sub>6</sub> MeCN solution at $\pm 4.4 \mu\text{A cm}^{-2}$ between 1.6 and 0.4 V upper and lower potential thresholds in GC-I. b) evolution of charge-discharge curves as a function of capacity. c) Charge-discharge capacities as a function of cycle number. d) Cycling efficiencies as a function of cycle number. ....	138
Figure 58. a) Charge-discharge cycles of 1 mM complex 2 in 0.5 TBA PF <sub>6</sub> MeCN solution at $\pm 4.4 \mu\text{A cm}^{-2}$ between 2.0 and 0.8 V upper and lower potential thresholds in GC-I. b) evolution of charge-discharge curves as a function of capacity. c) Charge-discharge capacities as a function of cycle number. d) Cycling efficiencies as a function of cycle number. ....	139
Figure 59. a) Charge-discharge cycles of 1 mM complex 3 in 0.5 TBA PF <sub>6</sub> MeCN solution at $\pm 4.4 \mu\text{A cm}^{-2}$ between 2.3 and 1.1 V upper and lower potential thresholds in GC-I. b) evolution of charge-discharge curves as a function of capacity. c) Charge-discharge capacities as a function of cycle number. d) Cycling efficiencies as a function of cycle number. ....	140
Figure 60. a) Charge-discharge cycles of 1 mM complex 4 in 0.5 TBA PF <sub>6</sub> MeCN solution at $\pm 4.4 \mu\text{A cm}^{-2}$ between 2.1 and 0.9 V upper and lower potential thresholds in GC-I. b) evolution of charge-discharge curves as a function of capacity. c) Charge-discharge capacities as a function of cycle number. d) Cycling efficiencies as a function of cycle number. ....	141
Figure 61. a) Charge-discharge cycles of 1 mM 2 in 0.5 TBA PF <sub>6</sub> MeCN solution at $\pm 0.125 \text{ mA cm}^{-2}$ between 2.0 and 0.8 V upper and lower potential thresholds in prototype flow-cell. b) evolution of charge-discharge curves as a function of capacity. c) Charge-discharge capacities as a function of cycle number. d) Cycling efficiencies as a function of cycle number. ....	143
Figure 62. a) Charge-discharge cycles of 1 mM 2 in 0.5 TBA PF <sub>6</sub> MeCN solution at $\pm 1.25 \text{ mA cm}^{-2}$ between 2.0 and 0.8 V upper and lower potential thresholds in	

prototype flow-cell. b) evolution of charge-discharge curves as a function of capacity. c) Charge-discharge capacities as a function of cycle number. d) Cycling efficiencies as a function of cycle number.....144

Figure 63. Cyclic voltammograms of 10 mM complex 2 in 0.1 M TBA PF<sub>6</sub>, MeCN at GC electrode, 50 mV s<sup>-1</sup>. a) fresh and unused Co(II) electrolyte. b) an electrolyte of complex 2 recovered from a battery experiment by combining the posolyte and negolyte. ....145

Figure 64. a) Charge-discharge cycles of 50 mM 3 in 0.5 TEA BF<sub>4</sub> MeCN solution at ± 9.62 mA cm<sup>-2</sup> between 2.4 and 1.0 V upper and lower potential thresholds in FC-II flow-cell (first 20 of 100 cycles shown). b) evolution of charge-discharge curves as a function of capacity. c) Charge-discharge capacities as a function of cycle number. d) Cycling efficiencies as a function of cycle number.....147

Figure 65. Cyclic voltammograms of 1 mM M<sub>mnt</sub> complexes in 0.1 M TBA PF<sub>6</sub>, MeCN electrolyte on GC electrode at 100 mV s<sup>-1</sup>. Black arrows indicate the starting point and direction for voltammetry. Second scans shown.....161

Figure 66. Voltammetry analysis of 1 mM Fe<sub>mnt</sub> in 0.1 M TBA PF<sub>6</sub> MeCN electrolyte on GC electrode. a) Second scan cyclic voltammograms at 100 mV s<sup>-1</sup>. The full region and restricted region scans are represented by the dashed and solid lines respectively. b) Scan-rate behaviour. First scans shown. c) RDE LSVs as a function of rotation rate at 50 mV s<sup>-1</sup>.....163

Figure 67. Voltammetry analysis of 1 mM V<sub>mnt</sub> in 0.1 M TBA PF<sub>6</sub> MeCN electrolyte on GC electrode. a) Second scan cyclic voltammograms at 100 mV s<sup>-1</sup>. The full region and restricted region scans are represented by the dashed and solid lines respectively. b) Scan-rate behaviour. First scans shown. c) Peak current as a function of the square-root of scan rate. d) RDE LSVs as a function of rotation rate at 50 mV s<sup>-1</sup>. e) Koutecký-Levich plot as a function of overpotential. f) The logarithm of the kinetically limited current vs overpotential.....164

Figure 68. Voltammetry analysis of 1 mM Co<sub>mnt</sub> in 0.1 M TBA PF<sub>6</sub> MeCN electrolyte on GC electrode. a) Second scan cyclic voltammograms at 100 mV s<sup>-1</sup>. The full region and restricted region scans are represented by the dashed and solid lines respectively. b) Scan-rate behaviour. First scans shown. c) Peak current

as a function of the square-root of scan rate. d) RDE LSVs as a function of rotation rate at 50 mV s<sup>-1</sup>. e) Koutecký-Levich plot as a function of overpotential. f) The logarithm of the kinetically limited current vs overpotential. .... 165

Figure 69. Voltammetry analysis of 1 mM Ni<sub>mnt</sub> in 0.1 M TBA PF<sub>6</sub> MeCN electrolyte on GC electrode. a) Second scan cyclic voltammograms at 100 mV s<sup>-1</sup>. The full region and restricted region scans are represented by the dashed and solid lines respectively. b) Scan-rate behaviour. First scans shown. c) Peak current as a function of the square-root of scan rate. d) RDE LSVs as a function of rotation rate at 50 mV s<sup>-1</sup>. e) Koutecký-Levich plot as a function of overpotential. f) The logarithm of the kinetically limited current vs overpotential. .... 166

Figure 70. Voltammetry analysis of 1 mM Cu<sub>mnt</sub> in 0.1 M TBA PF<sub>6</sub> MeCN electrolyte on GC electrode. a) Second scan cyclic voltammograms at 100 mV s<sup>-1</sup>. The full region and restricted region scans are represented by the dashed and solid lines respectively. b) Scan-rate behaviour. First scans shown. c) Peak current as a function of the square-root of scan rate. d) RDE LSVs as a function of rotation rate at 50 mV s<sup>-1</sup>. e) Koutecký-Levich plot as a function of overpotential. f) The logarithm of the kinetically limited current vs overpotential. .... 167

Figure 71. a) Cell potential vs capacity and b) capacities and efficiencies for selected charge-discharge cycles at ±0.48 mA cm<sup>-2</sup> current density for 1 mM (TEA)<sub>2</sub>V<sub>mnt</sub> in 0.1 M TBA PF<sub>6</sub> MeCN solution with Celgard separator. Dashed grey lines in a) indicate the theoretical cell potential and capacity. .... 169

Figure 72. a) Cell potential vs capacity and b) capacities and efficiencies for selected charge-discharge cycles at ±0.48 mA cm<sup>-2</sup> current density for 1 mM (TEA)<sub>2</sub>V<sub>mnt</sub> in 0.1 M TBA PF<sub>6</sub> MeCN solution with Fumapem F-930 CEM. Dashed grey lines in a) indicate the theoretical cell potential and capacity. .. 170

Figure 73. a) Cell potential vs capacity and b) capacities and efficiencies for selected charge-discharge cycles at ±0.24 mA cm<sup>-2</sup> current density for 1 mM (TEA)<sub>2</sub>V<sub>mnt</sub> in 0.1 M TBA PF<sub>6</sub> PC solution with Celgard separator. Dashed grey lines in a) indicate the theoretical cell potential and capacity. .... 170

Figure 74. Cell potential vs capacity for the first three charge-discharge cycles for the 2.26 V potential battery of 1 mM (TEA)<sub>2</sub>V<sub>mnt</sub> in 0.1 M TBA PF<sub>6</sub> electrolyte. a) MeCN solvent with fumapem F-930 CEM at ±0.48 mA cm<sup>-2</sup>. b) PC solvent with Celgard separator at ±0.24 mA cm<sup>-2</sup>. Also shown are 'cycle 0', the initial charge cycle to 1.5 V before the posolyte was replaced with fresh (TEA)<sub>2</sub>V<sub>mnt</sub> solution.....171

Figure 75. Time evolution of the UV-vis spectra of the a) V<sub>mnt</sub><sup>3-</sup> negolyte and b) V<sub>mnt</sub><sup>1-</sup> posolyte solutions diluted to 50 μM concentration in 5 mM TBA PF<sub>6</sub> MeCN solution, of the 1.09 V battery of (TEA)<sub>2</sub>V<sub>mnt</sub> after an initial charge to 1.5 V. Also shown is the uncharged starting solution (grey); 50 μM (TEA)<sub>2</sub>V<sub>mnt</sub> MeCN solution.....172

Figure 76. Cell potential vs capacity for the independent redox couple battery cycling of a) V<sub>mnt</sub><sup>3-/2-</sup> and b) V<sub>mnt</sub><sup>2-/1-</sup>. Dashed grey lines indicate the theoretical potential and capacity. c) Charge-discharge capacities for selected cycles of independent redox couple battery cycling of V<sub>mnt</sub><sup>3-/2-</sup> and V<sub>mnt</sub><sup>2-/1-</sup>. Conditions: 1mM (TEA)<sub>2</sub>V<sub>mnt</sub> in 0.1 M TBA PF<sub>6</sub> MeCN solution, ±0.96 mA cm<sup>-2</sup> constant current density, ±0.4 V charge-discharge voltage thresholds, Celgard separator.....173

Figure 77. a) Cell potential vs capacity for selected charge-discharge cycles for (TEA)<sub>2</sub>Co<sub>mnt</sub>. Dashed lines indicate the theoretical cell potential and capacity. b) Capacities and efficiencies for selected charge-discharge cycles for (TEA)<sub>2</sub>Co<sub>mnt</sub>. Conditions: 1 mM (TEA)<sub>2</sub>Co<sub>mnt</sub> in 0.1 M TBA PF<sub>6</sub> MeCN solution, Celgard separator, ±0.48 mA cm<sup>-2</sup> constant current density, 2.2/1.0 V potential thresholds.....175

Figure 78. Time evolution of the UV-vis spectra of the a) Co<sub>mnt</sub><sup>3-</sup> negolyte and b) Co<sub>mnt</sub><sup>1-</sup> posolyte solutions diluted to 50 μM concentration in 5 mM TBA PF<sub>6</sub> MeCN solution, after initial charge of (TEA)<sub>2</sub>Co<sub>mnt</sub> to 2.2 V. Also shown is the uncharged starting solution (grey); 50 μM (TEA)<sub>2</sub>Co<sub>mnt</sub> in 5 mM TBA PF<sub>6</sub> MeCN solution.....175

Figure 79. Cell potential vs capacity for the independent redox couple battery cycling of a) Co<sub>mnt</sub><sup>3-/2-</sup> and b) Co<sub>mnt</sub><sup>2-/1-</sup>. Dashed grey lines indicate the theoretical potential and capacity. c) Charge-discharge capacities for selected

cycles of independent redox couple battery cycling of  $\text{Co}_{\text{mnt}}^{3-/2-}$  and  $\text{Co}_{\text{mnt}}^{2-/1-}$ . Conditions: 1mM  $(\text{TEA})_2\text{Co}_{\text{mnt}}$  in 0.1 M TBA  $\text{PF}_6$  MeCN solution,  $\pm 0.48 \text{ mA cm}^{-2}$  constant current density,  $\pm 1 \text{ V}$  charge-discharge voltage thresholds, Celgard separator. .... 176

Figure 80. Cell potential vs capacity for the first two charge-discharge cycles at  $\pm 0.24 \text{ mA cm}^{-2}$  for 1 mM  $(\text{TEA})_2\text{Ni}_{\text{mnt}}$  in 0.1 M TBA  $\text{PF}_6$  MeCN solution with Celgard separator. Dashed grey lines indicate the theoretical cell potential and capacity. .... 177

Figure 81. a) Cell potential vs capacity for selected charge-discharge cycles for  $(\text{TEA})_2\text{Ni}_{\text{mnt}}$ . Dashed lines indicate the theoretical cell potential and capacity. b) Capacities and efficiencies for selected charge-discharge cycles for  $(\text{TEA})_2\text{Ni}_{\text{mnt}}$ . Conditions: 1 mM  $(\text{TEA})_2\text{Ni}_{\text{mnt}}$  in 0.1 M TBA  $\text{PF}_6$  PC solution, Celgard separator,  $\pm 0.48 \text{ mA cm}^{-2}$  constant current density, 2.4/0.8 V potential thresholds. .... 178

Figure 82. Cell potential vs capacity for the independent redox couple battery cycling of a)  $\text{Ni}_{\text{mnt}}^{3-/2-}$  and b)  $\text{Ni}_{\text{mnt}}^{2-/1-}$ . Dashed grey lines indicate the theoretical potential and capacity. c) Charge-discharge capacities for selected cycles of independent redox couple battery cycling of  $\text{Ni}_{\text{mnt}}^{3-/2-}$  and  $\text{Ni}_{\text{mnt}}^{2-/1-}$ . Conditions: 1mM  $(\text{TEA})_2\text{Ni}_{\text{mnt}}$  in 0.1 M TBA  $\text{PF}_6$  MeCN solution,  $\pm 0.48 \text{ mA cm}^{-2}$  constant current density, Celgard separator. .... 179

Figure 83. Time evolution of the UV-vis spectra of the a)  $\text{Ni}_{\text{mnt}}^{3-}$  negolyte and b)  $\text{Ni}_{\text{mnt}}^{1-}$  posolyte solutions diluted to 50  $\mu\text{M}$  concentration in 5 mM TBA  $\text{PF}_6$  MeCN solution, after initial charge of  $(\text{TEA})_2\text{Ni}_{\text{mnt}}$  to 2.4 V. Also shown is the uncharged starting solution (grey); 50  $\mu\text{M}$   $(\text{TEA})_2\text{Ni}_{\text{mnt}}$  in 5 mM TBA  $\text{PF}_6$  MeCN solution. .... 180

Figure 84. a) Cell potential vs capacity for selected charge-discharge cycles for  $(\text{TEA})_2\text{Cu}_{\text{mnt}}$ . Dashed lines indicate the theoretical cell potential and capacity. b) Capacities and efficiencies for selected charge-discharge cycles for  $(\text{TEA})_2\text{Cu}_{\text{mnt}}$ . Conditions: 1 mM  $(\text{TEA})_2\text{Cu}_{\text{mnt}}$  in 0.1 M TBA  $\text{PF}_6$  MeCN solution, Celgard separator,  $\pm 0.48 \text{ mA cm}^{-2}$  constant current density, 1.6/0.6 V potential thresholds. .... 181

- Figure 85. a) Cell potential vs capacity for selected charge-discharge cycles for  $(\text{TEA})_2\text{Cu}_{\text{mnt}}$ . Dashed lines indicate the theoretical cell potential and capacity. b) Capacities and efficiencies for selected charge-discharge cycles for  $(\text{TEA})_2\text{Cu}_{\text{mnt}}$ . Conditions: 1 mM  $(\text{TEA})_2\text{Cu}_{\text{mnt}}$  in 0.1 M TBA  $\text{PF}_6$  MeCN solution, fumapem F-930 CEM,  $\pm 0.48 \text{ mA cm}^{-2}$  constant current density, 1.6/0.6 V potential thresholds. ....182
- Figure 86. Time evolution of the UV-vis spectra of the a)  $\text{Cu}_{\text{mnt}}^{3-}$  negolyte and b)  $\text{Cu}_{\text{mnt}}^{1-}$  posolyte solutions diluted to 50  $\mu\text{M}$  concentration in 5 mM TBA  $\text{PF}_6$  MeCN solution, after initial charge of  $(\text{TEA})_2\text{Cu}_{\text{mnt}}$  to 1.6 V. Also shown is the uncharged starting solution (grey); 50  $\mu\text{M}$   $(\text{TEA})_2\text{Cu}_{\text{mnt}}$  in 5 mM TBA  $\text{PF}_6$  MeCN solution.....182
- Figure 87. Cell potential vs capacity for the independent redox couple battery cycling of a)  $\text{Ni}_{\text{mnt}}^{3-/2-}$  and b)  $\text{Ni}_{\text{mnt}}^{2-/1-}$ . Dashed grey lines indicate the theoretical potential and capacity. c) Charge-discharge capacities for selected cycles of independent redox couple battery cycling of  $\text{Ni}_{\text{mnt}}^{3-/2-}$  and  $\text{Ni}_{\text{mnt}}^{2-/1-}$ . Conditions: 1mM  $(\text{TEA})_2\text{Ni}_{\text{mnt}}$  in 0.1 M TBA  $\text{PF}_6$  MeCN solution,  $\pm 0.48 \text{ mA cm}^{-2}$  constant current density, Celgard separator. ....183
- Figure 88. Cell potential vs capacity for the first two charge-discharge cycles at  $\pm 0.24 \text{ mA cm}^{-2}$  for 1 mM  $(\text{TEA})_2\text{Fe}_{\text{mnt}}$  in 0.1 M TBA  $\text{PF}_6$  MeCN solution with Celgard separator. Dashed grey lines indicate the theoretical cell potential and capacity.....184
- Figure 89. a) the Croc redox series. b) Cyclic voltammetry of 1 mM  $\text{TBA}_2\text{Croc}$  in 0.1 M TBA  $\text{PF}_6$ , MeCN electrolyte at a GC electrode, 50  $\text{mV s}^{-1}$ . Full and partial electrochemical region scans are shown. First cycle shown. ....199
- Figure 90. a) Cyclic voltammograms of the  $\text{Croc}^{2-}/\text{Croc}^{\bullet-}$  redox couple as a function of scan rate (1 mM  $\text{TBA}_2\text{Croc}$  in 0.1 M TBA  $\text{PF}_6$ , MeCN). b) The variation of peak potentials and peak separation as a function of scan rate for the  $\text{Croc}^{2-}/\text{Croc}^{\bullet-}$  redox couple. c) The variation of peak currents and peak current ratio as a function of scan rate for the  $\text{Croc}^{2-}/\text{Croc}^{\bullet-}$  redox couple. d) Randles-Sevcik analysis of the  $\text{Croc}^{2-}/\text{Croc}^{\bullet-}$  redox couple (the  $\text{Croc}^{2-}$  diffusion coefficient is given based upon the forward anodic reaction data on first scan).....200

- Figure 91. a) Cyclic voltammograms of the  $\text{Croc}^{\bullet-}/\text{Croc}$  redox couple as a function of scan rate (1 mM  $\text{TBA}_2\text{Croc}$  in 0.1 M TBA  $\text{PF}_6$ , MeCN). b) The variation of peak potentials and peak separation as a function of scan rate for the  $\text{Croc}^{\bullet-}/\text{Croc}$  redox couple. c) The variation of peak currents and peak current ratio as a function of scan rate for the  $\text{Croc}^{\bullet-}/\text{Croc}$  redox couple. d) The linear dependence of peak current on the square-root of scan rate for the  $\text{Croc}^{\bullet-}/\text{Croc}$  redox couple. .... 201
- Figure 92. a) Cyclic voltammograms of the  $\text{Croc}^{\bullet 3-}/\text{Croc}^{2-}$  redox couple as a function of scan rate (1 mM  $\text{TBA}_2\text{Croc}$  in 0.1 M TBA  $\text{PF}_6$ , MeCN). b) The variation of peak potentials and peak separation as a function of scan rate for the  $\text{Croc}^{\bullet 3-}/\text{Croc}^{2-}$  redox couple. c) The variation of peak currents and peak current ratio as a function of scan rate for the  $\text{Croc}^{\bullet 3-}/\text{Croc}^{2-}$  redox couple. d) Randles-Sevcik analysis of the  $\text{Croc}^{\bullet 3-}/\text{Croc}^{2-}$  redox couple (the  $\text{Croc}^{2-}$  diffusion coefficient is given based upon the forward cathodic reaction data on first scan). .... 202
- Figure 93. Cyclic voltammograms of 1 mM  $\text{TBA}_2\text{Croc}$  in 0.1 M TBA  $\text{PF}_6$  in solvent; a) MeCN. b) PC. c) DMF. Blue = 1.6 mm diameter Pt WE. Red = 1.6 mm diameter Au WE. Green = 3.0 mm diameter GC WE.  $50 \text{ mV s}^{-1}$ , second cycles shown. . 203
- Figure 94. Cyclic voltammetry of 1 mM  $\text{TBA}_2\text{Croc}$ , 0.1 M Li TFSI, MeCN at GC WE,  $50 \text{ mV s}^{-1}$ . First and second cycles are shown. Inset graph) Voltammetry in the anodic region after previously cycling the electrode in the cathodic region. 204
- Figure 95. a) Linear sweep voltammograms of 1 mM  $\text{Croc}^{2-}$  oxidation and reduction as a function of electrode rotation rate, at  $50 \text{ mV s}^{-1}$  on GC electrode. b) Koutecký-Levich plots for the first one-electron oxidation and reduction of  $\text{Croc}^{2-}$ ; inverse current ( $i$ ) as a function of the inverse square root of the rotation rate ( $\omega$ ) at overpotentials ( $\eta$ ) 0 to 200 mV. c) Analysis of the kinetically-limited current ( $i_k$ ) dependency on  $\eta$  gives the exchange current at  $\eta = 0$ . .... 205
- Figure 96. Bulk electrolysis of  $\text{Croc}^{2-}$  to a)  $\text{Croc}^{\bullet-}$ , c)  $\text{Croc}^{\bullet 3-}$ , e)  $\text{Croc}$  oxidation states at 1 mA current (1 mM  $\text{TBA}_2\text{Croc}$  in 0.1 M TBA  $\text{PF}_6$ , MeCN) and Cyclic voltammetry of b)  $\text{Croc}^{\bullet-}$ , d)  $\text{Croc}^{\bullet 3-}$ , f)  $\text{Croc}$  oxidation states as a function of time after formation via electrolysis. The approximate time of each

voltammogram is indicated in the figure legend. (second scan shown, 100 mV s<sup>-1</sup> at GC electrode). .....207

Figure 97. Bulk electrolysis cycling of the Croc<sup>•-</sup>/Croc redox couple (1 mM TBA<sub>2</sub>Croc in 0.1 M TBA PF<sub>6</sub>, MeCN) at 1 mA. ....208

Figure 98. a) Symmetric battery charge-discharge curves of 10 mM TBA<sub>2</sub>Croc in 0.5 M TEA BF<sub>4</sub>, MeCN electrolyte at ±2.4 mA cm<sup>-2</sup>. The upper and lower threshold potentials are 2.0 and 1.5 V respectively. First 10 cycles are shown. Fumapem<sup>®</sup> F-930 CEM. b) Battery cycling capacities and coulombic efficiency of the 1.82 V symmetric RFB. c) Post-battery cycling voltammetry of used Croc<sup>•3-</sup> and Croc<sup>•-</sup> electrolytes. 50 mV s<sup>-1</sup> at a GC electrode. ....209

Figure 99. Independent battery cycling experiments of single croconate violet redox couples. a) first five cycles of the Croc<sup>2-</sup>/Croc<sup>•-</sup> cell, 1 mM TBA<sub>2</sub>Croc, 0.1 M TBA PF<sub>6</sub>, MeCN at ±0.96 mA cm<sup>-2</sup>. Celgard separator. b) Normalised capacity retention and coulombic efficiencies for the independent battery cycling of the Croc<sup>2-</sup>/Croc<sup>•-</sup> and Croc<sup>2-</sup>/Croc<sup>•3-</sup> cells.....210

Figure 100. Battery cycling of the 1.88 V asymmetric BzNSN/Croc<sup>2-</sup> RFB; 10 mM TBA<sub>2</sub>Croc posolyte vs 10 mM BzNSN negolyte in 0.5 M TEA BF<sub>4</sub>, MeCN electrolyte at ± 2.4 mA cm<sup>-2</sup>. a) cyclic voltammetry of 1 mM BzNSN and TBA<sub>2</sub>Croc in 0.1 M TBA PF<sub>6</sub> MeCN electrolyte at GC electrode, 50 mV s<sup>-1</sup> b) First ten charge-discharge curves. The upper and lower threshold potentials are 2.2 and 1.5 V respectively. c) Battery cycling capacities and coulombic efficiency. Fumapem<sup>®</sup> F-930 CEM. ....211

Figure 101. a) Cyclic voltammetry of 1 mM TCNQ and TBA<sub>2</sub>Croc in 0.1 M TBA PF<sub>6</sub>, MeCN, GC WE at 50 mV s<sup>-1</sup>. Asymmetric battery charge-discharge curves of 1 mM TBA<sub>2</sub>Croc vs 1 mM TCNQ mixed electrolytes in 0.1 M TBA PF<sub>6</sub>, MeCN electrolyte at ±0.48 mA cm<sup>-2</sup> (Celgard porous separator) to b) the one-electron battery and d) two-electron battery. The upper and lower threshold potentials were 0.4 and 0 V respectively for the one-electron battery and 1.7 and 0 V respectively for the two-electron battery. The capacities and coulombic efficiencies for the one-electron and two-electron batteries are given in c) and e) respectively.....213

Figure 102. EDX analysis of the carbon paper electrode material (20301A, Technical Fibre Products Ltd.) in Figure 28. a) EDX analysis region containing fibres and binder, b) false-colour map of carbon, c) false-colour map of oxygen. 250 $\mu\text{m}$ scale.....	249
Figure 103. UV-vis calibrations and Beer-Lambert plots for a) Fc and b) FcBF <sub>4</sub> ...	250
Figure 104. UV-vis spectra as a function of M <sub>mnt</sub> concentration and Beer-Lambert calibrations. a) V <sub>mnt</sub> , b) Fe <sub>mnt</sub> , c) Co <sub>mnt</sub> , d) Ni <sub>mnt</sub> , e) Cu <sub>mnt</sub> .....	251
Figure 105. a) UV-vis absorption spectra as a function TBA <sub>2</sub> Croc concentration and b) Beer-Lambert calibration plot. The unknown concentration sample is shown on the spectra in grey and in the calibration in pink.....	252

# List of Abbreviations and Acronyms

Abbreviation/ Acronym	Meaning		
A	Aqueous	NA	Non-aqueous
Acac	Acetylacetonate	NA RFB	Non-aqueous redox flow battery
AEM	Anion-exchange membrane	NMR	Nuclear magnetic resonance spectroscopy
ASR	Area-specific resistance	OER	Oxygen evolution reaction
BF <sub>4</sub> <sup>-</sup>	Tetrafluoroborate anion	OHP	Outer Helmholtz plane
bpy	2,2'-bipyridine	P	Product
BzNSN	2,1,3-Benzothiadiazole	PC	Propylene carbonate
CE	Counter electrode	PD	Potential difference
CEM	Cation-exchange membrane	PF <sub>6</sub> <sup>-</sup>	Hexafluorophosphate anion
ClO <sub>4</sub> <sup>-</sup>	Perchlorate anion	PFA	Perfluoroalkoxy alkane
CNC	Computer numerical control (milling)	PFF	Parallel flow field
Croc	Croconate violet	phen	Phenanthroline
CV	Cyclic voltammetry	PP	Polypropylene
DCM	Dichloromethane	PS	Pore-size
DME	1,2-Dimethoxyethane	PTFE	Polytetrafluoroethylene
DMF	Dimethylformamide	PVA	Polyvinyl alcohol
EDX	Energy-dispersive X-ray (spectroscopy)	R	Reactant
EIS	Electrochemical impedance spectroscopy	RDE	Rotating disc electrode
EPDM	Ethylene-propylene diene monomer	RE	Reference electrode
ESS	Energy storage system	RFB	Redox flow battery
Fc	Ferrocene	ROM	Redox-active organic molecule
FcBF <sub>4</sub>	Ferrocenium tetrafluoroborate	RVC	Reticulated vitreous carbon (foam)
FC-n	Flow-cell (number n)	SCE	Saturated calomel electrode
FTEF	Flow-through flow field	SEM	Scanning electron microscopy
GC-n	Glass H-cell (number n)	SHE	Standard hydrogen electrode
GS	Ground state	SOC	State-of-charge
HER	Hydrogen evolution reaction	SOMO	Singly occupied molecular orbital
HOMO	Highest occupied molecular orbital	SPEEK	sulfonated polyether ether ketone
HPLC	High performance liquid chromatography	SPP	Serpentine flow field
HRMS ESI	High-resolution mass spectrometry (electrospray ionisation)	TBA <sup>+</sup>	Tetrabutylammonium cation
IDFF	Interdigitated flow field	TCNQ	Tetracyanoquinodimethane
IHP	Inner Helmholtz plane	TEA <sup>+</sup>	Tetraethylammonium cation
LSV	Linear sweep voltammetry	TEMPO	2,2,6,6-tetramethylpiperidin-1-oxyl
LUMO	Lowest unoccupied molecular orbital	TFSI <sup>-</sup>	Bis(trifluoromethanesulfonyl)imide anion
MCC	Metal-coordination compound	tpy	2,2':6',2''-Terpyridine
MeCN	Acetonitrile	VRFB	Vanadium redox flow battery
mnt	Maleonitriledithiolate	WE	Working electrode
MPS	Microporous separator		

# Chapter 1

# Introduction to Redox Flow Batteries

## 1.1 Energy storage technologies

At present, energy infrastructures across the world operate by supplying power to match the demand from industrial, domestic and transport users. This supply is mostly generated as needed from predominantly non-renewable energy resources such as coal, natural gas and nuclear fuels. The overdependence on these fuels in past decades however has detrimentally polluted the atmosphere with carbon dioxide which is causing climate change, acidification of the oceans and elevated global temperatures [5,6]. More recently the implementation of renewable generators such as wind, tidal, geothermal, hydroelectric and solar energy has increased to lower carbon emissions and mitigate the effects of climate change. The application of renewables is inherently challenging however as solar and wind are intermittent resources which depend on light intensity and wind-speed respectively. It is therefore not currently feasible to switch to an entirely renewable energy infrastructure because the fluctuating power generation does not match the demand which predominantly depends on human behaviour. Therefore, there is a critical need for large-scale energy storage systems (ESSs) which can better modulate supply and demand by storing excess renewable energy generation. For example, excess solar energy during the day can be stored for usage in the night when no solar energy is produced. In addition, ESSs also benefit the grid in terms of power management, reliability and energy security [7]. For example, 'load levelling' is the storage of energy during periods of light loading on the system so that the energy can be delivered back during periods of high demand. 'Peak shaving' is the usage of energy storage to reduce abnormal peaks in power demand from grid users. Finally, 'frequency response' is the charging or

discharging of ESSs in response to an increase or decrease of grid frequency [5,8–11].

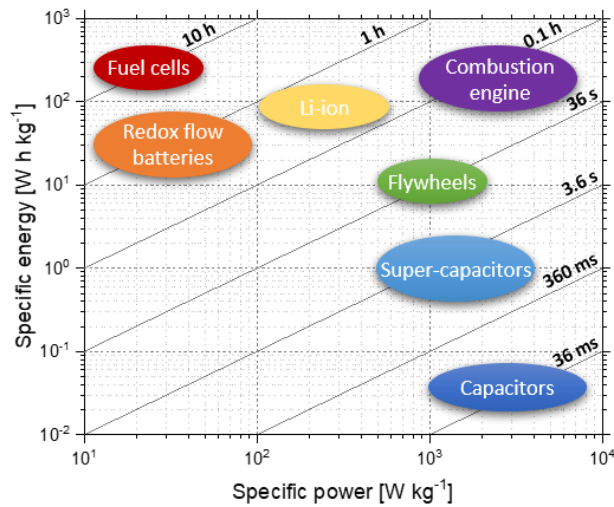


**Figure 1. A Ragone plot of energy storage technologies. The combustion engine and lines of equal energy storage time are given for comparison. Regions approximated based on the literature [7,12–17].**

ESSs can be classified into several different categories; thermal, kinetic, magnetic, potential, electrical, thermochemical, chemical and electrochemical [7]. Pumped hydro and compressed air are perhaps the simplest technologies as they store energy by converting electrical energy into potential energy. By pumping water to a higher elevation reservoir or by compressing air to higher pressures, the potential energy can be recovered by converting back to electricity via a turbine. These technologies are capable of very large power outputs of above 100 MW [7] however they are geographically restricted such that mountainous regions or underground caverns are needed, respectively. In addition, potential ESSs have slow response times (minutes) which makes them unsuitable for high frequency response (seconds max). In contrast, flywheels (kinetic) and capacitors (electrical) have a very fast response times (seconds) but have very limited capacity, giving just minutes of storage. Electrochemical ESSs are arguably the most suitable energy storage technologies because they are location non-specific, highly efficient, scalable and suitable for several hours of storage. Among electrochemical ESSs are supercapacitors, electrolyzers/fuel cells and batteries. These technologies are

compared in the Ragone plot in Figure 1 whereby the energy density (specific energy) is plotted against the power output per gram (specific power). As shown, batteries occupy the region of relatively high energy density ( $10 - 10^3 \text{ Wh kg}^{-1}$ ), thus allowing for multiple hours of storage, however their power output is typically much lower than capacitors and flywheels. In comparison, the internal combustion engine resides in the region of highest energy and power densities because hydrocarbons have a high intrinsic energy density due to their enthalpy of combustion. Among battery technologies are lead-acid [7], sodium-sulfur [18], lithium-ion [19], metal-air [20] and the redox flow battery [8,12,13,21,22]. The Lead-acid battery is the most established commercialised battery technology as it is primarily used in vehicles for engine-ignition and onboard electronics whereas Li-ion technology is now widely implemented in electric vehicles, consumer electronics and portable devices. Despite this, neither technology is suitable for large-scale energy storage because the technologies are not directly scalable. For most batteries the electrochemical reactions involve the plating or intercalation of ions onto/into the electrode materials, therefore the overall battery power and capacity are dependent on, and limited by, the electrode surface area. As a result, the capacity of these batteries can only be scaled up by increasing the number of individual cells. This becomes problematic at large scales because each cell requires battery management and the health of each cell can deteriorate at different rates, causing safety issues.

Redox flow batteries (RFBs) are electrochemical energy storage devices that operate akin to fuel cells/electrolysers, however RFBs are reversible systems that do not necessarily require electrocatalysts to operate [22]. As shown in Figure 2, RFBs store energy in entirely solution-phase redox materials which are housed in electrolyte reservoirs external to the electrochemical reactor. Here two distinct electrolytes are used, the 'posolyte' and 'negolyte', which contain the redox materials for the anodic and cathodic reactions respectively (defined on charging). These electrolytes are cyclically pumped through their respective half-cell compartment in the flow-cell to charge or discharge the battery. Each flow-cell is typically comprises current collectors, electrodes and a membrane which

separates the two half-cells. Many of these flow-cells are then stacked in series or parallel to produce the desired power output. Given that the electrochemical reactions do not involve a change of phase, only the battery power is dependent on the electrode surface area. Therefore, the power and capacity of RFBs are decoupled [8,22,23] and can be scaled independently by increasing the electrode surface area or electrolyte volume respectively. It is this property which makes RFBs the most suitable battery technology for large-scale storage because the battery can be built for any desired capacity/power output. In addition, RFBs have several other attractive features for commercial application; modular design, few moving parts, room-temperature operation, low maintenance, long lifetimes, simple engineering, high safety and a low environmental impact. Hence, in comparison to other storage systems, RFBs are versatile devices that can be easily scaled to any desired size and can be constructed without location limitations making them applicable for various applications.

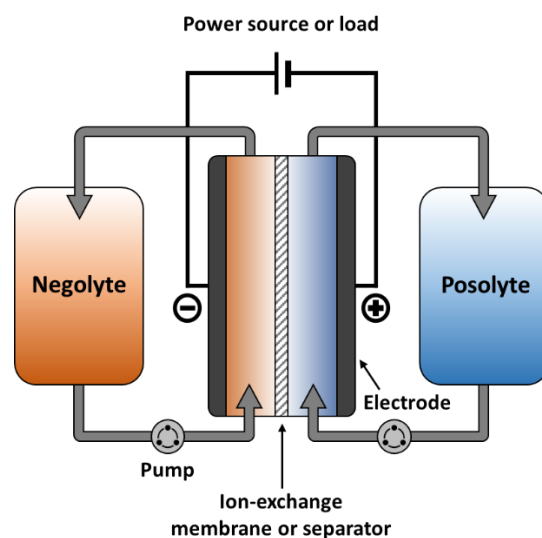
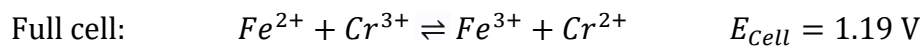


Figure 2. Schematic illustration of a generic redox flow battery.

## 1.2 Development of the commercial redox flow battery

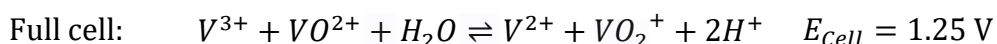
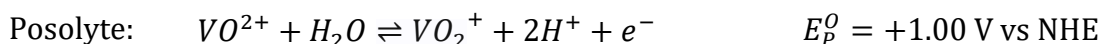
This history of RFBs dates back over 40 years to the early work of Kangro and Pieper who proposed a titanium/iron accumulator in 1962, as an alternative to lead and nickel based batteries at the time [24]. A similar electrolyte-flowing battery was also proposed by Ashimura and Miyake in 1971 [25], however modern

RFBs did not emerge until 1973, when NASA were tasked with the development of an energy storage system following the 1967 oil embargo. As a result, Hagedorn and Thaller [9] proposed and developed the iron/chromium RFB which was based upon hydrochloric acid solutions of Fe(III/II) and Cr(III/II) [26]. Although many redox-couples were investigated, iron and chromium were chosen due to the large cell potential they provided (1.19 V) and their low cost, such that the battery design could be economically viable [26]. Between 1974 and 1983 many issues of the RFB design were addressed; namely a competing hydrogen evolution reaction in the chromium half-cell and cross-contamination of the electrolytes through the membrane. As such, many electrode materials/catalysts were studied by Giner and Cahill [27] until a gold/lead carbon felt catalyst was developed which suppressed hydrogen evolution [27]. Unfortunately, although various membranes were evaluated, the membrane crossover issue was never solved [28]. After a decade of research, the technology was deemed non-viable due to the issues associated with hydrogen evolution, electrolyte cross-contamination, membrane-fouling and slow chromium kinetics. More recently the Fe-Cr RFB has been commercialised by resolving some of the previous issues with a complex cascade process [29,30]. At present the Fe-Cr RFB gives only a modest energy density of  $15 \text{ W h L}^{-1}$  [31] due to the relatively small cell potential and limiting solubility.



After conclusion of the NASA project, little RFB research occurred until 1986, when the all-vanadium RFB (VRFB) was announced by Skyllas-Kazacos et al. [25,27]. The use of vanadium redox couples had previously been considered by Kangro, Pieper and the NASA group, due to the available oxidation states, but it was ruled out due to cost and poor kinetics of the vanadium redox couples [25]. However, in 1985, Sum et al. [32,33] showed that the vanadium kinetics were highly dependent on the electrode material. The all-vanadium system was heralded as a major breakthrough because the battery not only gave a higher cell

potential but also avoided cross-contamination issues because vanadium inhabits both compartments of the battery. Thus, the VRFB was the first example of a ‘symmetric’ battery, such that any migration of the vanadium species through the membrane only results in self-discharge rather than cross-contamination. In addition, the VRFB was capable of higher depths of discharge and allowed the use of a cationic exchange membrane which decreased the cell resistance [10,31]. These properties made the VRFB design commercially attractive, despite the higher cost of vanadium, and many years of optimisation later it has become the most commercialised system to date due to its *relatively* high (with respect to RFBs) 19-38 W h L<sup>-1</sup> energy density [31]. In addition, the VRFB electrolytes are easily produced via electrolysis of the VOSO<sub>4</sub> starting material and the VRFB is conveniently rebalanced by periodically remixing the electrolytes and recharging. As such, the VRFB is capable of long lifetimes >10 years, without replacement of the electrolytes [31]. Most notably, installations of 4 and 3 MW size have been built in Hokkaido and Osaka-Japan respectively [21], demonstrating that RFBs can be built at grid-scale.



Despite the success of the VRFB, the design has limitations and its development has halted. Firstly, the V(V) H<sub>2</sub>SO<sub>4</sub> electrolyte is very corrosive and oxidising and the V(V) species tends to precipitate in concentrated solutions at low pH or at high temperatures [34]. Secondly, hydrogen evolution is a parasitic reaction when the battery is operated at high states-of-charge (SOC), thus limiting the maximum operating capacity [35]. Lastly, the practical solubility (typically 2 M) is limited due to water transport through the membrane under operation which causes dilution of one compartment and precipitation of the other [36]. Beyond the VRFB, the zinc-bromide hybrid RFB [37] and the bromine-polysulfide RFB [13] have also been commercialised however additional issues exist for these technologies. Ultimately,

the main limitations of the VRFB technology is the relatively low energy density as compared to other battery technologies, as shown in Table 1, which results in undesirably high energy storage costs. In addition, the cost of vanadium fluctuates and is generally increasing, whereas the sulfonated tetrafluoroethylene based fluoropolymer-copolymer (Nafion®) membrane of the VRFB accounts for 10-15 % of the total VRFB battery cost [38].

**Table 1: Comparison of the energy density and cell potentials of common battery technologies [7].**

Battery type	Cell voltage [V]	Energy density [W h Kg <sup>-1</sup> ]
Lead acid	2.10	30-50
Na-S	~2.00	150-240
Li-ion	~3.70	75-200
RFB (all V)	1.26	10-30

### 1.3 Redox flow battery architecture

The architecture of a RFB is considerably different to conventional batteries because convection of the electrolyte through the electrochemical reactor is required to charge-discharge the battery. The conventional RFB reactor design comprises current collectors, electrode material, gaskets and a membrane which are assembled in a stack [39], as shown in Figure 3. In general, the flow-cell stack is sealed via compression ( $\approx 25\%$  [39]) to simultaneously maximise the electrical contact at the current collector-electrode interface and minimise the inter-electrode separation. Commonly known as a ‘zero-gap configuration’ the design minimises the cell resistance such that the battery power density can be optimised. Here, a brief overview of the conventional flow-cell design is given to provide context.

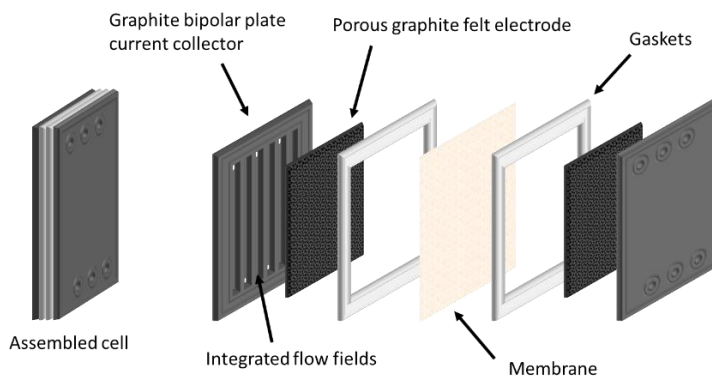


**Figure 3. Schematic diagram of a conventional RFB cell construction.**

### 1.3.1 Electrodes and current collectors

The electrode assembly comprises current collectors and porous electrodes. The current collector is responsible for conducting the battery current into the electrode material and ensuring good electrical conductivity to all surfaces of the electrode [22]. Typically, graphite or graphite-composites are used for the current collector material because graphite is a rigid non-porous material with acceptable conductivity which is low-cost [39]. The usage of metals is typically avoided because the direct contact of electrified metal surfaces, such as copper, with the electrolyte causes corrosion. Beyond simply connecting the electrode to the battery terminals, the current collectors in modern RFBs are also responsible for maximising the mass transport of the electrolyte into the porous electrode. As shown in Figure 3, ‘flow-field’ patterns [6,39] are commonly integrated into the current collector design and work by directing the electrolyte flow through channels under the electrode material [39,40]. Several different patterns exist such as serpentine and interdigitated flow-fields which have been adapted from conventional fuel cell technologies [39].

The electrodes in a RFB are the electrochemical interface where the battery reactions take place. As such, they must provide fast heterogeneous kinetics of the solution redox couples, but they must also be inert so that the electrode material is not modified or consumed during operation. Furthermore, it is desirable for the electrode to have a high surface area porous structure to achieve high current densities. The material must also be highly conductive, mechanically robust and

low cost. Therefore, carbon-based materials are often the electrode of choice, such as graphite felts or carbon papers, as they provide very large surface areas (electrochemically-active surface areas of  $\sim 0.1 \text{ m}^2 \text{ g}^{-1}$  [41]), are chemically inert and very inexpensive [22]. Various surface modifications have been studied to improve the kinetics of graphitic electrodes, such as the commonly used thermal treatment [42,43], or to increase the hydrogen overpotential [44], however electrode research for RFBs is often concerned with optimising commercial systems rather than that of new chemistries, as the properties of graphite usually suffice for new designs.

### 1.3.2 Membranes

The membrane is perhaps the most critically important component in the RFB architecture because it must prevent the crossover of redox materials but allow the transport of supporting electrolyte ions between the electrolytes to complete the circuit [45]. In addition, the membrane must be chemically resistant and inert in the applied battery electrolyte, durable (long lifetime) and preferably low cost. Unfortunately, highly selectivity and conductivity are often mutually exclusive properties, such that highly selective separators are often accompanied by an undesirable cell resistance. As such, the choice of membrane material directly impacts battery performance and it is often preferable to sacrifice specificity for higher conductivity, especially in the case of symmetric RFBs where cross-contamination issues are mitigated [44,46–50]. In addition, it should be noted that the choice of membrane material is specific to the chemical nature of the applied electrolyte.

In general, membranes for RFBs are either ionic-exchange membranes or porous separators (PS). PS filter electrolytes purely based on the size of the species in solution [51] and as such, their performance is dependent on their pore-size and the ionic radii of the redox-active species. The pore size of these materials depends on the material composition and preparation method and can therefore cover a broad range of sizes from microporous (0.2-2 nm) to macroporous (20-1000 nm). Despite this, conventional separators such as Celgard® (made of polyethylene and

polypropylene) and DARAMIC® (a composite made of polyethylene and amorphous silica) have pore sizes more typically in the mesoporous range (2-50 nm) [51]. Due to the relative large size of the separator pores compared to ions in solution, separators typically cause large losses of coulombic efficiency in RFBs due to high crossover rates of redox materials. Therefore, separator materials tend more to be used in academic research rather than in industry [48,49,52,53]. In contrast, ionic exchange membranes give far better selectivity than porous separators, however their conductivity is reduced [48]. Generally, such membranes are formed by introducing acidic or basic polar groups into the polymer structure. Once the membrane is wetted, these groups dissociate and pair with supporting electrolyte counter-ions, thus allowing ion-exchange through the membrane via the shuttling of ions through the porous structure. In contrast, the membrane polar groups electrostatically repel ions of the same type to prevent their crossover. It is therefore important that the battery redox materials are all of the same ionic type, such that the membrane does not preferentially transport one or more of the species in order to avoid cross-contamination. Ionic-exchange membranes are designed to be either cationic (CEM) or anionic (AEM), such that electrolyte anions or cations are prevented from diffusing through, respectively [22].

CEMs are highly conductive in acidic media due to the high diffusivity of hydronium ions [54,55], however they decrease aqueous RFB efficiency as most inorganic salts are also cationic species. CEMs are typically formed from either a perfluorosulfonic acid or sulfonated polyether ether ketone base (SPEEK) polymer, to which groups such as sulfonic acid or polyimides are bound respectively [48]. Fluorinated CEMs, such as Nafion®, boast high chemical stability towards acidic solutions and aggressive oxidants/reductants, such as the highly reactive V(V) electrolyte [22,46,56] whereas nonfluorinated CEMs tend to be less resistant [57,58].

AEMs generally consist of a base polymer such as poly(vinylbenzylstyrene), to which basic groups such as trimethylamine groups are inserted [22]. Due to their limited conductivity and lower stability in VRFBs, AEMs have been mainly

neglected for use in aqueous RFBs [59,60]. Despite this, due to the emergence of non-aqueous RFB designs, AEMs are of interest in the present work [61–65] because anionic species such as  $\text{BF}_4^-$  or  $\text{PF}_6^-$  diffuse more quickly than the bulkier  $\text{TBA}^+$  anions [52,66].

## 1.4 Electrolytes for redox flow batteries

The electrolytes in a RFB are the most important battery components because they are the principal energy storage material and their properties mostly determine the overall battery performance. Fundamentally, the electrolyte is composed of three parts; solvent, supporting electrolyte and redox materials. It is the solvent that dictates the electrolyte properties because different solutes (supporting salt and redox materials) will be compatible with different solvents. Furthermore, the physical properties of the solvent, such as viscosity and relative permittivity (often called the dielectric constant) contribute significantly to the overall electrolyte conductivity, which therefore affects the ohmic resistance and voltaic efficiency of the RFB. For these reasons, a distinction is commonly made between water-based RFBs (aqueous) and alternative RFBs which apply non-aqueous (NA RFBs) solvents. In principal, any solvent could be conceivably used in a RFB, however in accordance with the basic requirements for electrolytes, the solvent must meet the following minimum criteria: the solvent should

1. solvate the solutes to sufficient concentrations to achieve high capacity and conductivity
2. be fluid to allow facile ion transport (low viscosity)
3. be chemically and electrochemically inert
4. remain liquid at a range of operating temperatures
5. be low-hazard/toxicity and economical

### 1.4.1 Aqueous electrolytes

Water is at present the most appealing solvent for commercial RFBs because aqueous RFBs are low cost, relatively safe, non-volatile, non-flammable and easily processed. Furthermore, as shown in Table 1, the conductivity of aqueous RFBs is

typically much higher than comparable NA RFBs, due to a combination of a high relative permittivity (78.39) and low viscosity (0.89 mPa s) [67]. It is these physical properties of water that allow it to dissolve conventional acids, bases and salts, as either charge carriers or redox-active materials, to high concentrations in excess of 10 M. Therefore, ionic redox materials with high charge densities, such as simple metal salts or inorganic ions, are most suitable for energy storage in aqueous RFBs to achieve high energy densities. For these reasons, the VRFB has been so successful because the VRFB electrolyte is composed of typically 1.5-2 M vanadium with 3-4 M H<sub>2</sub>SO<sub>4</sub> [5], giving an electrolyte conductivity of 500-700 mS cm<sup>-1</sup> [68] and an energy density of ~33 W h L<sup>-1</sup> [5].

**Table 2. Comparison of representative aqueous and non-aqueous RFB properties** [5,12,52,68,69]. **(a) The aqueous RFB data corresponds to the VRFB with an electrolyte composition of 3-4 M H<sub>2</sub>SO<sub>4</sub> with 1.5-2 M vanadium [5]. (b) The non-aqueous RFB data corresponds to the V(acac)<sub>3</sub> RFB with a typical electrolyte composition of 0.5 M TEA BF<sub>4</sub> with 0.1 M V(acac)<sub>3</sub> [69].**

Property	Aqueous RFB <sup>(a)</sup>	Non-aqueous RFB <sup>(b)</sup>
Redox species	Metal ions	Metal coordination compounds or redox-active organic molecules
Supporting electrolyte	H <sub>2</sub> SO <sub>4</sub> in H <sub>2</sub> O	TEA BF <sub>4</sub> in MeCN
Electrolyte conductivity [mS cm <sup>-1</sup> ]	500-700	40-55
Membrane (charge carrier)	Nafion® (H <sup>+</sup> )	AEM (BF <sub>4</sub> <sup>-</sup> )
Membrane conductivity [mS cm <sup>-1</sup> ]	50-200	0.1-20
Power density [mW cm <sup>-1</sup> ]	10-600	1-10

Despite the success of the VRFB and other aqueous RFBs, the widespread implementation of the technology has been limited by technical and economic challenges. In part, this is due to the low energy density of the technology which results from the limitations of using water as the battery solvent. As shown in Figure 4, water decomposes via the hydrogen evolution reaction (HER) at 0 V vs SHE and via the oxygen evolution reaction (OER) at 1.23 V vs SHE (standard conditions). These potentials are pH-dependent; however, the potential difference is thermodynamically 1.23 V at every electrolyte pH. Therefore, the cell potential of an aqueous RFB is fundamentally limited to 1.23 V if solvent decomposition is to be avoided. In reality, aqueous cell potentials of up to 2.2 V are possible given overpotentials at carbon-based electrodes, however exceeding the 1.23 V limit is

generally ill-advised because  $H_2/O_2$  evolution become parasitic reactions in the battery. Therefore, given that the energy density is proportional to the cell potential, material solubility and electrochemical stoichiometry, advances in aqueous RFB energy density can only be made in terms of increasing redox material solubility or the number of electrons stored per molecule.

Present research in aqueous RFBs is mostly concerned with decreasing the system cost of the technology, whilst matching or exceeding the energy density of the VRFB. This has mainly been approached by applying water soluble redox-active organic molecules (ROMs) which are capable of higher solubilities than vanadium or store two electrons per molecule. Ground-breaking work has been demonstrated by the groups of M. Aziz, U. Schubert, W. Wang and others into the application of quinones [70,71,80–86,72–79], viologens [86–92] and 2,2,6,6-tetramethylpiperidin-1-oxyl (TEMPO) derivatives [87,90,91,93] for example. Despite this, it is the opinion of the author that there is limited scope for dramatically increasing the energy density of aqueous RFBs, because the narrow electrochemical stability region of water severely restricts the number and variety of possible redox materials.

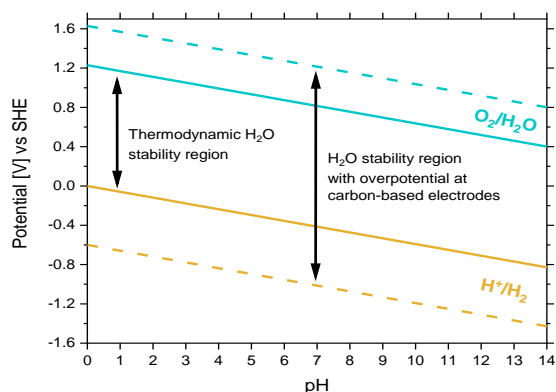


**Figure 4.** The pH dependence of the hydrogen and oxygen evolution reactions in aqueous electrolyte [22]. The thermodynamic potentials are shown by solid lines whereas dashed lines show the onset potentials given overpotentials at carbon-based electrodes. An overpotential of 400 mV and 600 mV has been assumed for the OER and HER respectively.

### 1.4.2 Non-aqueous electrolytes

Despite the advantages of water-based electrolytes, the physical properties of water as a solvent are not so special when compared to the extensive list of alternative solvents, such as ethers, nitriles, amides and carbonates. Figure 5 compares the physical properties of commonly used solvents to water in terms of their electrochemical stability region, temperature range, relative permittivity and viscosity. Considering first the electrochemical stability regions in Figure 5a, water provides one of the smallest stability regions of all solvents. It should be noted here that the stability regions of organic solvents are empirically derived typically. As such, a degree of kinetic overpotential is expected in the regions given in Figure 5a and dependence on the electrode material is likely. In addition, the electrochemical stability of organic electrolytes is often dependent on the electrolyte composition because supporting electrolytes are also typically redox-active in the same potential range. Regardless, in general most solvents are reasonably stable over a range of at least 4 V, as compared to the maximum 2.2 V stability region of water. Most noteworthy, the aprotic polar solvents acetonitrile (MeCN) and propylene carbonate (PC) are stable across  $\approx 6$  V and are popular choices for NA RFBs [94–97] and NA electrochemistry in general. In addition, the oxidative/reductive decomposition of organic solvents tends to occur at higher/lower potentials respectively than water which means that redox materials which reside just outside the water stability region are applicable in NA solvents.

Another important property of solvents for RFB applications is the temperature range at which they are liquid (Figure 5c). Water is liquid between 0 and 100 °C which is satisfactory for temperate climates, however energy storage in aqueous electrolytes is unsuitable for geographical locations where the ambient temperature falls below 0 °C [68,98]. In contrast, solvents are typically liquid for much larger temperature ranges; -54.5 to 241.7 °C for PC and -60.4 to 153.0 °C for N,N-Dimethylformamide (DMF), and remain liquid to much lower temperatures than water;  $T_F = -125$  °C for 4-methyl-1,3-dioxolane (Appendix A). It has therefore been suggested that NA RFBs are suitable for low-temperature energy storage; for

example a NA RFB has been demonstrated at  $-40\text{ }^{\circ}\text{C}$  by use of dichloromethane (DCM) solvent [99].

The main difference between water and organic solvents is the conductivity of their electrolytes; a property which depends on the viscosity and the relative permittivity. The viscosity plays an important role for electrolyte solutions as ions are less diffuse in more viscous solvents. Specifically, the limiting molar conductivity ( $\Lambda_m$ ) of an ion is inversely proportional to the solution viscosity ( $\mu$ ) and ionic radius (Stokes' law [98]), making lower viscosity solvents and smaller ions more preferable. Given that supporting salts for NA electrolytes are typically organic salts; cations are usually tetraethylammonium ( $\text{TEA}^+$ ) or tetrabutylammonium ( $\text{TBA}^+$ ) and anions are typically tetrafluoroborate ( $\text{BF}_4^-$ ), perchlorate ( $\text{ClO}_4^-$ ) or hexafluorophosphate ( $\text{PF}_6^-$ ) [66], the limiting molar conductivity of NA electrolyte ions are often low due to large ionic radii.

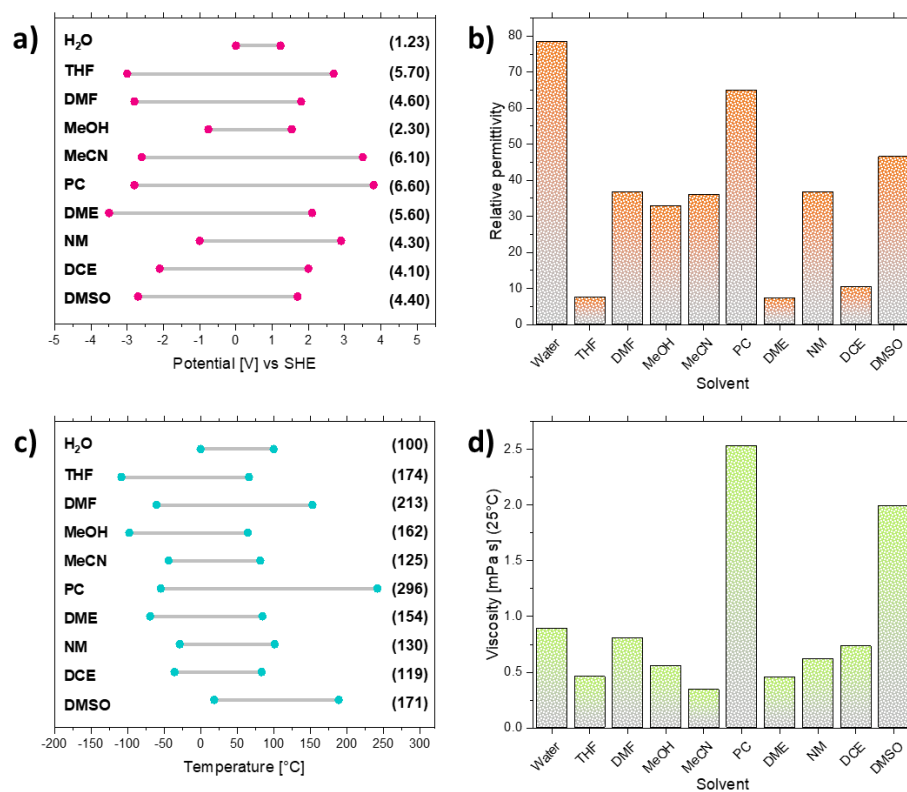


**Figure 5. Physical properties of selected solvents for RFBs. a) Electrochemical stability regions. The full range is given in parentheses in units V. b) Relative permittivity. c) liquid-phase temperature regions. The full range is given in parentheses in units °C. d) Viscosity.**

**Data acquired from [19,67,68,98,100,101]. See Table 11 (Appendix A) for solvent abbreviations.**

For example, the  $\Lambda_m$  for  $H^+$  in water is  $349.81 \text{ S cm}^2 \text{ mol}^{-1}$  whereas that of  $TBA^+$  in MeCN is merely  $61.63 \text{ S cm}^2 \text{ mol}^{-1}$  [98]. It is important to stress here that the  $\Lambda_m$  for  $H^+$  in water is abnormally large because  $H^+$  ions can shuttle between adjacent water molecules by the Grotthuss mechanism. Therefore, the  $\Lambda_m$  for  $Na^+$  in water ( $50.10 \text{ S cm}^2 \text{ mol}^{-1}$ ) is a more fair comparison to that of NA RFB electrolytes. Regardless, it is clear that highly viscous solvents should be avoided in NA RFBs because of low conductivity. In addition, high electrolyte viscosity is also problematic for the RFB technology because of increased pumping costs.

The effect of the solvent relative permittivity on the electrolyte conductivity must also be considered. Firstly, there exists a general trend that the solubility of supporting electrolyte increases with the relative permittivity of the solvent [98]. Therefore, the maximum solubility of salts in MeCN ( $\epsilon_r = 35.9$ ) is significantly higher than in 1,2-dimethoxyethane (DME) ( $\epsilon_r = 7.2$ ), however both are much less than in water ( $\epsilon_r = 78.39$ ), thus limiting the maximum conductivity of NA electrolytes. Secondly, the relative permittivity affects the dissociation constant of solutes [98], such that solvents with larger values cause more dissociation of molecules into ions. Bearing this in mind, water has the rather unique combination of a high relative permittivity and low viscosity which affords unparalleled conductivity. Although there are other solvents which possess lower viscosity than water (Figure 5d) or a higher relative permittivity, for example 191.3 for N-Methylacetamide, few solvents possess the combination of a high relative permittivity/low viscosity. For these reasons, the choice of NA solvent is relatively limited, with MeCN, PC and DME being the most commonly used solvents for NA RFBs [68,98]. Besides traditional solvents, room-temperature ionic liquids and deep eutectic solvents have also been considered for use in RFBs as solvents or supporting electrolytes [102–107]. Such liquids have high thermal and electrochemical stability, low vapour pressures and wide potential windows [102,106], however high cost and viscosity limits application.

## 1.5 Progress in non-aqueous redox flow batteries

The NA RFB concept was first proposed by Singh [108] and then later demonstrated by Matsuda et al. [96] in 1988. Since then, interest in the field has increased because the multiple solvent options affords more opportunities for developing redox materials [109,110]. In addition, by operating in a more electrochemically stable battery solvent, NA RFBs with very large cell potentials of  $\leq 6$  V are theoretically possible, which corresponds to theoretical RFB energy densities significantly higher than the VRFB [66]. Therefore, the application of NA electrolytes is a plausible pathway towards increasing the energy density of the RFB technology and it has been predicted that NA RFBs can in theory be economically viable given that reactor area-specific resistance (ASR), cell potential and redox material cost targets can be realised [110]. In addition, alternative compounds which are not compatible with water in terms of their solubility or stability, or those which reside outside the water stability region are applicable for use in NA electrolytes by carefully choosing an appropriate solvent [99]. The base electrolyte properties can also be optimised by preparing solvent mixtures to maximise the electrolyte conductivity and redox material solubility [111–113].

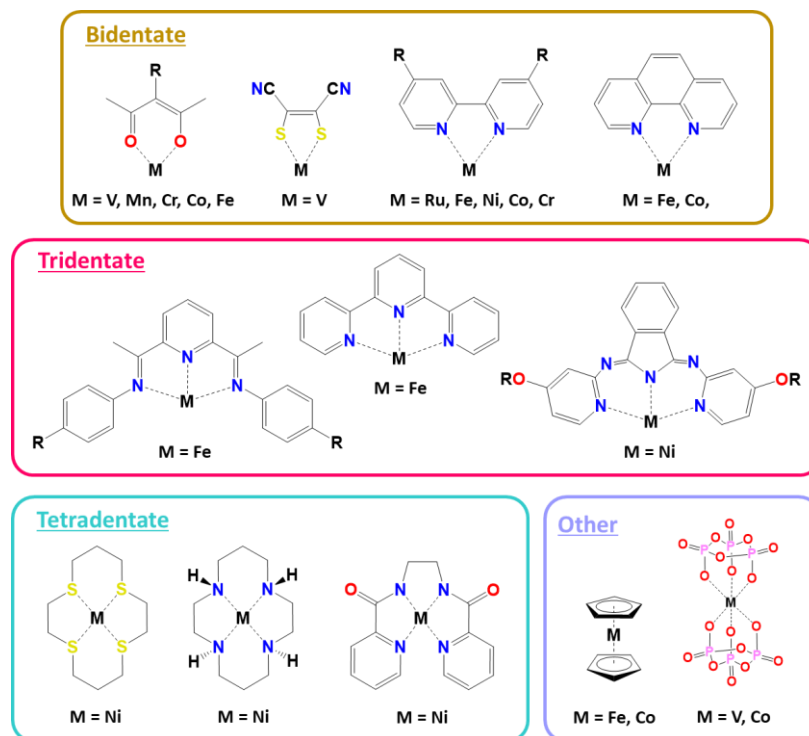
In recent years many different redox materials have been applied in NA RFB research including metal coordination compounds (MCCs) [114], redox-active organic molecules (ROMs) [2], polymers [51,115–118] and polyoxometalates [119].

### 1.5.1.1 Metal coordination compounds

Whereas simple metal salts such as vanadyl sulfate are highly ionic and therefore sufficiently polar to be soluble in aqueous electrolyte, MCCs with organic ligands are typically water-insoluble because their larger size results in a low charge density. Furthermore, the structure of the organic ligands is usually incompatible with water as conventional ligand scaffolds such as 2,2'-bipyridine (bpy) are incapable of hydrogen bonding with water. In contrast, when dissolved in a low- or medium-polarity organic solvent, relatively high MCC solubilities ( $\sim 1$  M for vanadium(III) acetylacetonate ( $V(\text{acac})_3$ ) in MeCN [120]) are possible

because of stronger solvent-solute interactions such as dipole moments and Van der Waals forces. It is therefore unsurprising that simplistic MCCs were targeted for application in NA RFBs during the early stages of the research field. Specifically, MCCs with bpy [96,105,121–125], acac [126–130] and phenanthroline (phen) [122,131,132] ligands with Ru, Co, Fe, Ni, V, Cr and Mn metal centres were extensively explored as shown in Scheme 1.

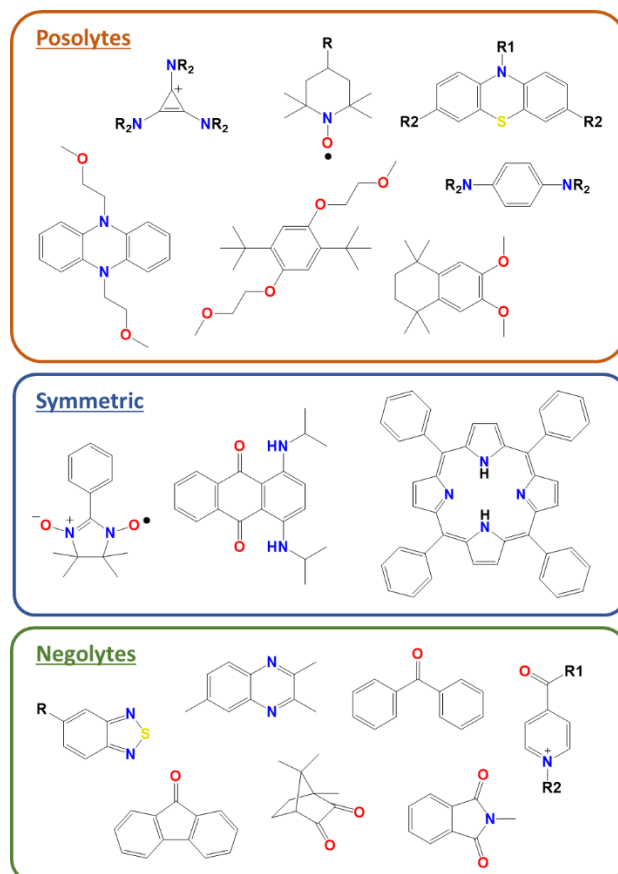
Due to the transition metal centre utilised, MCCs typically exist in multiple stable oxidation states. Several symmetric NA RFBs employing MCCs have therefore been demonstrated giving cell potentials in the range of 1.5 to 2.5 V. Although reasonably successful, these studies did not exploit the inherent advantage of MCCs: the properties of the MCC can be improved by rational design and molecular engineering of the ligand scaffold. Due to the nature of the bonding between the metal centre and the ligand, the MCC electrochemistry can be considerably altered by modifications of the ligand structure. In addition, the MCC solubility can be dramatically improved by the addition of solubilising groups to the external ligand structure. This was first demonstrated by Suttill et al. who synthesised several  $\text{Cr}(\text{acac})_3$  complexes with various functional groups giving a variation in MeCN solubility from  $\sim 60 \mu\text{M}$  to 1.92 M and also a derivative which is a viscous liquid at room temperature [133]. A similar study was performed by Cabrera et al. regarding 4,4'-Ester-Substituted Bipyridine complexes of chromium whereby the variation in MeCN solubility was from  $\sim 1 \mu\text{M}$  to 0.71 M, however the MCC electrochemistry and stability was also adversely affected [134,135].



**Scheme 1. Chemical structures of MCC ligands for NA RFBs [96,105,131–140,119,141–148,120,122,123,126,128–130]. Ligand chemical names (in order left to right): Bidentate – Acetylacetonate derivatives, Maleonitriledithiolene, 2,2'-Bipyridine derivatives, 1,10-Phenanthroline. Tridentate - bis(2,6-diimine-pyridines), 2,2':6',2''-Terpyridine, bipirydilimino isoindolines. Tetradentate - 1,4,8,11-Tetrathiacyclotetradecane, 1,4,8,11-Tetraazacyclotetradecane, Linked Picolinamides. Other – Metallocenes, Trimetaphosphate anions.**

### 1.5.1.2 Redox-active organic molecules

The application of ROMs for NA RFB energy storage has received increasing attention in recent years because organic molecules have a much higher intrinsic capacity compared to MCCs due to their lower molecular weight [149]. In addition, ROM electrolytes are capable of high energy density because ROMs can be highly soluble (5.7 M in MeCN for 2,1,3-benzothiadiazole [150]) or miscible liquids at room temperature [151], and undergo redox transitions at high/low potentials [99,152]. Thus, ROMs are attractive energy storage materials because they are also, in principal, sustainable and low cost as transition metal centres are avoided. Hence, the application of ROMs is a promising pathway towards achieving economic targets given that high energy densities are realised [149].



**Scheme 2. Chemical structures of ROMs for NA RFBs [99,107,156–165,118,166–175,149,176–185,150,186–191,151–155]. In most cases different derivatives exist for each structure.**

The practical application of ROMs is at present challenging because ROMs are significantly less stable than MCCs [2]. Specifically, the oxidation or reduction of organic molecules in an aprotic electrolyte typically produce molecular radicals (a chemical species with an unpaired valence electron) which decompose via free-radical mechanisms. This is further complicated in the cases where the radical species are also ionic because these species are often also reactive via nucleophilic or electrophilic mechanisms [149,151]. For these reasons decomposition can rapidly occur via a variety of pathways, often involving the battery solvent or salt [151], and it is difficult to ascertain the exact mechanism. The chemical conditions of the battery must be carefully considered as the radical shelf-life may be highly dependent on the electrolyte composition, trace oxygen/water, material concentration or temperature.

Scheme 2 shows the variety of ROMs which have been applied in NA RFBs thus far. As shown, these ROMs are typically small unsaturated cyclic molecules with heteroatomic functional groups, such as amines, carbonyls or nitroxyls. These molecules yield 'persistent' radical oxidation states due to several stabilising effects. Firstly, the addition of electron-withdrawing or donating groups near to the radical locus can reduce the charge density of anionic or cationic radicals respectively, making electrophilic/nucleophilic reactions less likely [192]. Secondly, conjugation in unsaturated molecules causes significant delocalisation of the unpaired electron across the whole molecule, thus decreasing the spin density at the radical locus. Finally, the addition of bulky substituent groups near the radical centre can provide steric protection by physically blocking bond formation with other molecules [20].

## 1.6 Thesis objectives and overview

The objective of the present work was to study and develop new MCC or ROM redox materials for applications in NA RFBs. Specifically, redox materials possessing multiple stable oxidation states were targeted for use as symmetric RFB electrolytes to mitigate the membrane limitations associated with the NA RFB concept. Ultimately these novel redox materials must fulfil several criteria in terms of energy density, performance and long-term stability. Therefore, the objective of this project was to examine all aspects of the new materials and test them in realistic battery experiments to assess viability. Towards this goal, a set of electrochemical cell designs were developed for conducting battery studies and are presented in Chapter 3. In Chapter 4 a model chemistry is described to benchmark the electrochemical cells and provide comparison for the novel redox materials presented in Chapters 5 to 7. Initially MCCs were targeted due to their simplicity however in Chapter 7 a promising ROM was identified and fully characterised.



# Chapter 2

# Fundamental Electrochemistry Theory

Electrochemistry is a branch of physical chemistry and is defined as the study of chemical processes which occur at electrified interfaces. Hence, electrochemistry is the study of charge at the molecular level and how charge moves through physical, chemical and biological systems. This field therefore encompasses a vast range of chemical and physical phenomena which are fundamentally governed by the laws of thermodynamics and kinetics. Furthermore, given that the electrochemical response of a system can be directly measured and quantified, electrochemistry is rigorously defined by mathematical formulae that relate measurable properties to the chemical compositions of electrochemical processes. This makes electrochemistry a uniquely powerful tool for experimentalists to quantify chemical processes, however beyond this academic interest, electrochemistry has countless real-world applications including sensors, manufacturing and energy storage/conversion.

Herein the fundamentals of electrochemistry are discussed to provide foundation knowledge that is required to understand the electrochemical methods used in this thesis.

The electrochemical theory presented here has been mostly influenced by the works of Bard and Faulkner [193], Compton and Banks [194] and Girault [195].

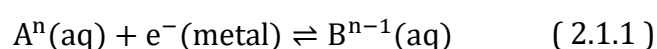
## **2.1 Equilibrium electrochemistry and thermodynamics**

Before progressing to discuss electrochemical techniques, it is important to first appreciate how charge interacts at an electrode-electrolyte interface. That is to say, what is the driving force for electron transfer at the interface? This question is

answered by the existence of electrochemical equilibria which in turn is the manifestation of thermodynamics. Here an overview of how electrochemical equilibrium relates to thermodynamics is given.

### 2.1.1 Electrochemical equilibrium

Consider first the simple act of placing a metal wire into a solution containing dissolved species A and B. Assuming that A and B differ only in their relative electronic structure, it then follows that the ions may be interconverted by adding an electron to A (reduction) or removing an electron from B (oxidation);



Thus, if a source or sink of electrons is present in the solution (the metal wire) then both the interconversion processes will start to occur. Inevitably, an equilibrium will be established at the electrode surface when the rates of the oxidation and reduction reactions are equal such that the electrolyte composition remains indefinitely constant. This equilibrium can be rationalised in terms of the electron energy as shown in Figure 6. According to solid-state theory, the energy levels in a solid are degenerate, such that a filled valence and empty conduction band exist. In a conductor these bands overlap, allowing conductivity of electrons, however the occupation and corresponding electron energy is given by the 'Fermi level'. In contrast, the energy levels of the A and B species are discrete and only two electrons can exist in each molecular orbital, as defined by the Pauli exclusion principal. If it is assumed that A and B have similar geometry and electronic structures, then the lowest unoccupied molecular orbital (LUMO) of A is almost exactly equal to the highest occupied molecular orbital (HOMO) of B (different solvation of A and B will make these levels unequal). Therefore, as A is reduced, the metal Fermi level decreases in energy whereas the A(LUMO) and B(HOMO) increase in energy locally to the electrode surface because of the accumulation of negative charge. At the point when the Fermi level of the metal is equal to the A(LUMO) and B(HOMO) energy, then the rate of the oxidation and reduction reactions become equal and equilibrium is established.

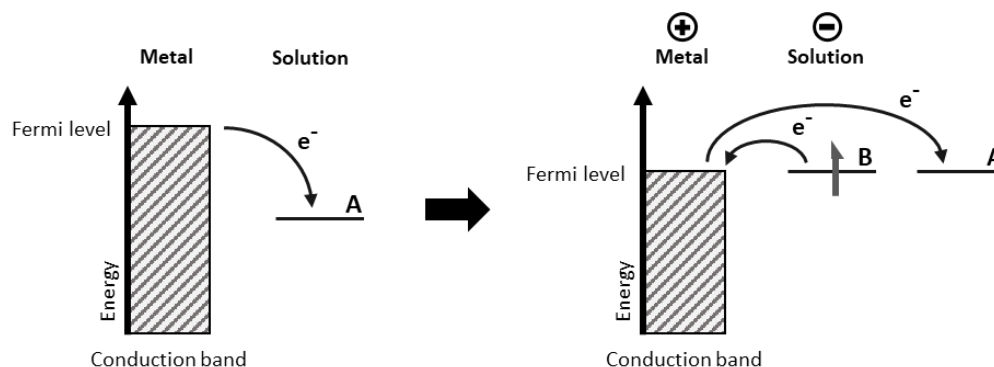


**Figure 6. The energy of electrons in the metal and solution before and after equilibrium is reached. Figure drawn with inspiration from [194].**

Upon reaching equilibrium, the interconversion processes will result in a net charge forming on the metal surface whereas an equal and opposite charge will be established in the solution as shown in Figure 6. The polarity of these charges will depend on where the equilibrium lies because if the equilibria favours the reduced state B, then a net conversion of A to B will occur giving the electrode a positive charge. This charge separation results in a double layer capacitance and therefore a potential difference exists between the metal and solution. In other words, an 'electrode potential' has been established on the metal wire relative to the solution, which arises due to the 'potential determining equilibria' in equation ( 2.1.1 ). It is important to note here that when the equilibrium is established, the quantity of charge transferred between electrode and solution is infinitesimal, therefore the concentrations of A and B are unmeasurably changed upon inserting the electrode.

By use of this simple system, the electrode potential can be related to the equilibrium. Firstly, the principal of an 'electrochemical potential',  $\bar{\mu}_A$  of each species is introduced where

$$\bar{\mu}_A = \mu_A + z_A F \Phi \quad (2.1.2)$$

Here, the electrochemical potential has two terms; the former is the chemical potential of A, whereas the second describes the electrical energy of A, expressed as the product of its charge ( $z_A$ ) and its potential ( $\Phi$ ) (phase specific) [194]. The Faraday constant F is introduced here as the charge of a mole of electrons where F

=  $eN_A$ . Applying this to the equilibrium in ( 2.1.1 ), gives the condition that the sum of electrochemical potentials of reactants is equal to that of the products, therefore

$$\bar{\mu}_A + \bar{\mu}_{e^-} = \bar{\mu}_B \quad (2.1.3)$$

Substituting ( 2.1.2 ) into ( 2.1.3 ) gives

$$(\mu_A + nF\Phi_S) + (\mu_{e^-} - F\Phi_M) = (\mu_B + (n - 1)F\Phi_S) \quad (2.1.4)$$

Expanding and rearranging for the chemical potentials gives

$$F(\Phi_M - \Phi_S) = \mu_B + \mu_{e^-} - \mu_A \quad (2.1.5)$$

Taking ( 2.1.5 ) and assuming ideal solutions, each chemical potential can be related to a standard chemical potential  $\mu_A^\circ$  and the concentration of each species by use of

$$\mu_A = \mu_A^\circ + RT\ln[A] \quad \text{and} \quad \mu_B = \mu_B^\circ + RT\ln[B] \quad (2.1.6)$$

where  $\mu_A^\circ$  is defined as chemical potential of A at unit concentration  $[A] = 1 \text{ mol dm}^{-3}$ . Thus

$$\Phi_M - \Phi_S = \Delta\Phi^\circ - \frac{RT}{F} \ln \left\{ \frac{[B]}{[A]} \right\} \quad (2.1.7)$$

where

$$\Delta\Phi^\circ = \frac{1}{F} (\mu_A^\circ + \mu_{e^-} - \mu_B^\circ) \quad (2.1.8)$$

is a constant. Equation ( 2.1.7 ) is the Nernst equation for a single electrode-solution interface where  $\Phi_M - \Phi_S$  denotes the electrode potential of the metal and solution interface. Equation ( 2.1.12 ) clearly shows that the electrode potential is dependent on the temperature of the electrolyte and more importantly the concentrations of A and B. Therefore, if more A is added to the solution then the equilibrium will shift towards the product B, thus increasing the quantity of charge separation and the electrode potential. Here ideal solutions have been assumed however this is unlikely to be true for electrolyte solutions. Therefore, it is necessary to substitute the concentration of each species for its 'activity'; a measure of the effective concentration of a species under non-ideal conditions. Briefly, solutions approach ideality at dilute concentrations ( $< 10^{-2} \text{ M}$ ). The activity

of a solutions can be calculated from the concentration of a species by use of the activity coefficient  $\gamma$

$$a_A = \gamma_A[A] \quad (2.1.9)$$

When  $\gamma$  is unity the solution is ideal, however  $\gamma$  is typically not unity because it has dependency on both ion-ion and ion-solvent interactions and on the solution ionic strength. The activity coefficient is best modelled by the Robinson and stokes equation [193]

$$\log_{10} \gamma_{\pm} = - \left( \frac{A(z_+z_-)\sqrt{I}}{1 + aB\sqrt{I}} \right) + cI \quad (2.1.10)$$

where the first term on the right is the extended Debye-Hückel law which relates the activity coefficient to the ionic strength, the charge on the anions/cations and the radius of the ion [193]. The remaining terms in ( 2.1.10 ) are solvent and temperature dependent parameters. Here  $\gamma_{\pm}$  is the mean activity coefficient of salt  $M_aX_b$  as given by

$$\gamma_{\pm} = (\gamma_+^a \gamma_-^b)^{\frac{1}{(a+b)}} \quad (2.1.11)$$

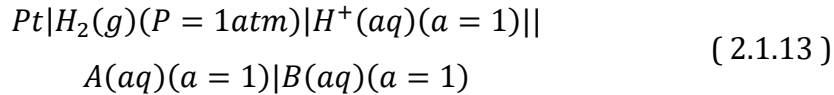
### 2.1.2 Electrode potentials

Thus far, an equation has been derived to theoretically predict the concentration dependence of the drop in electrode potential at an interface, however this is an unmeasurable quantity because the measurement of a single electrode potential is impossible. A minimum of two electrodes are required because only potential differences (PD) can be measured. To achieve this, a circuit is built where two metal electrodes are inserted into the solution and a high resistance voltmeter is used to probe the PD across them by passing a tiny current (electrolyte composition is unchanged). Thus, the PD is

$$\Delta\Phi = (\Phi_{M1} - \Phi_S) - (\Phi_{M2} - \Phi_S) = \Phi_{M1} - \Phi_{M2} \quad (2.1.12)$$

however, both  $\Phi_{M1}$  and  $\Phi_{M2}$  are unknown and will have concentration dependence as in ( 2.1.7 ). Suppose now though that one of the electrode potentials was made constant; a 'reference electrode' and this was measured, then the PD in ( 2.1.12 ) can be calculated by subtracting the known reference electrode potential.

To fix  $\Phi_{\text{reference}} - \Phi_S$ , the electrode must be designed in such a way that the composition of the electrode/solution remains constant. The electrode by which all measured redox potentials should be measured against is the ‘standard hydrogen electrode’ as shown in Figure 7. This electrode consists of hydrogen gas at one atmosphere bubbling over a platinised platinum electrode in a solution of 1.18 M HCl (corresponds to unity  $H^+$  activity) at 298.15 K. The cell notation for this cell is



The Nernst equation for this two-electrode cell can be written as

$$\Delta\Phi = \Delta\Phi_{B/A}^\ominus - \Delta\Phi_{H_2/H^+}^\ominus + \frac{RT}{F} \ln \left\{ \frac{[A]P_{H_2}^{1/2}}{[B]a_{H^+}} \right\} \quad (2.1.14)$$

or

$$E = E^\ominus + \frac{RT}{F} \ln \left\{ \frac{[A]P_{H_2}^{1/2}}{[B]a_{H^+}} \right\} \quad (2.1.15)$$

where  $E^\ominus$  is the ‘standard electrode potential’. Thus, when the activities of A and B are equal to unity, the second term in ( 2.1.15 ) collapses to 0 and the measured cell PD  $E$  is then equal to  $E^\ominus$ . Therefore, it is by convention that  $\Delta\Phi_{H_2/H^+}^\ominus$  is defined as exactly 0 V such that  $E^\ominus$  is now the standard electrode potential of the A/B redox couple.

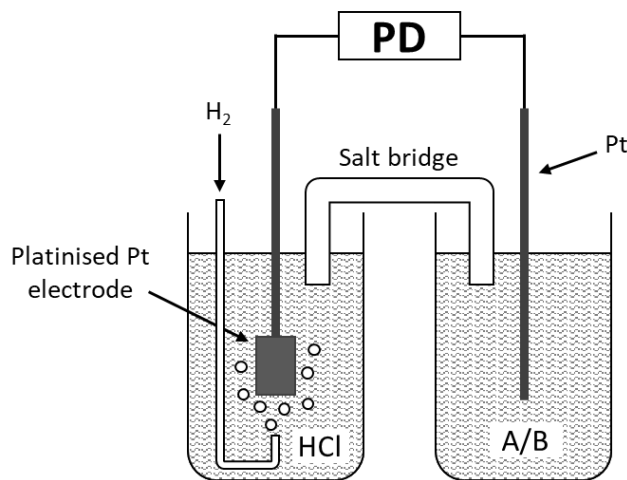


**Figure 7. The standard hydrogen electrode used to measure the potential of an arbitrary redox couple. Figure drawn with inspiration from [194].**

Finally, the general Nernst equation can be expressed as

$$E = E^0 - \frac{RT}{nF} \ln \frac{[Red]}{[Ox]} \quad (2.1.16)$$

This famous equation can be applied to any electrochemical cell by substituting the reaction quotient  $Q_c$  into the logarithmic term. The standard electrode potentials of various redox couples are well known and are expressed as standard reduction potentials.

### 2.1.3 Thermodynamics of electrochemical reactions

The link between the measured electrode potentials and equilibria is apparent in the previous section, therefore electrochemistry is fundamentally governed by thermodynamics. Specifically, thermodynamics provides the driving force for passing current through a circuit. If an arbitrary cell is considered and the potential difference measured, then during this measurement a tiny current will flow. Associated with this, a change in Gibbs energy  $dG$  will occur which can be equated to the work done  $dW$  in the process. Here the work done corresponds to the flow of  $dn$  of electrons through the external circuit across a PD of  $E_{cell}$ .

Therefore

$$dG = dW = (-Fdn)E_{cell} \quad (2.1.17)$$

and the total Gibbs energy change is given by

$$\Delta G = -nFE_{cell} \quad (2.1.18)$$

If all the cell components are at unit activity, then the standard free energy change is found. Considering now how the change in free energy relates to entropy

$$dG = VdP - SdT \quad (2.1.19)$$

Given that the pressure change is zero, then the entropy change is

$$F \left( \frac{\partial E^0}{\partial T} \right)_P = \Delta S^0 \quad (2.1.20)$$

Combining ( 2.1.20 ) and the definition of enthalpy in ( 2.1.21 )

$$\Delta H^0 = \Delta G^0 + T\Delta S^0 \quad (2.1.21)$$

gives

$$\Delta H^\ominus = -FE^\ominus + TF \left( \frac{\partial E^\ominus}{\partial T} \right)_P \quad (2.1.22)$$

which indicates that the enthalpy and entropy change of a cell reaction is related to the cell potential and its variation with temperature. The cell potential can therefore indicate the direction of chemical reactions. Considering first that the free energy can be related to both the cell potential and the equilibrium constant then

$$E^\ominus = \left( \frac{RT}{F} \right) \ln K \quad (2.1.23)$$

Equation (2.1.23) shows that when the  $E^\ominus$  is greater than zero,  $K$  will be greater than 1. Conversely, when  $E^\ominus$  is less than zero,  $K$  will be less than 1. Therefore, if two standard potentials are known, it can be immediately deduced which direction the combined reaction will occur.

#### 2.1.4 Practical reference electrodes

Reference electrodes (RE) are used in practically every electrochemical investigation because it is necessary to measure the cell potential relative to some well-defined electrochemical reaction, however the practicalities of different REs is worthy of discussion.

REs must be reliable and suitable for a range of different experiments and that their electrode potential is stable. Clearly, no one RE will be suitable for every experiment or electrolyte, so several different REs exist. In principle any redox couple could be used as a RE, however the electrode composition must be highly controlled, and it is desirable that the potential determining equilibria is established quickly (fast kinetics). Unsurprisingly, redox couples that involve a change of phase are most suitable because the composition of the non-solution phase state (e.g.  $H_2$  gas) is highly stable, hence, the number of chemical species to control is less.

Although the standard hydrogen electrode (SHE) is the definition 0 V RE, it is used very infrequently in practice because the use of flammable  $H_2$  gas is hazardous and inconvenient. In contrast, the silver-silver chloride RE is the most

commonly used RE because it is easily prepared, its potential is very stable, and it is suitable for aqueous electrolytes with pH from 0 to 14. The AgCl RE is prepared by depositing solid AgCl onto a Ag wire and then submerging the wire into NaCl solution. This solution is typically stored in a glass tube that is capped with a glass frit which is permeable to  $\text{Na}^+$  ions to allow conductivity. Based on the potential determining equilibrium, the AgCl RE is sensitive to  $[\text{Cl}^-]$  concentration, however this is well controlled by preventing the RE electrolyte and the electrolyte of study from mixing. Other REs include the saturated calomel electrode (SCE), mercury oxide and mercury sulfate. A comparison of REs is given in Table 3.

This thesis is exclusively concerned with electrochemistry in non-aqueous electrolytes, however typical aqueous REs (such as the SHE and AgCl REs) are unsuitable for use in NA experiments because unpredictable liquid-junction potentials would exist between the organic and aqueous electrolytes. Therefore, the NA RE must contain the same solvent as the electrolyte under study. Thus, there is no perfect NA RE because different NA electrolytes can vary significantly, and conventional aqueous REs are generally unsuitable because of low solubility of  $\text{Cl}^-$  ions in aprotic solvents for example. The Ag/Ag<sup>+</sup> quasi-RE is the most popular choice because it is tailorable to different electrolytes [67]. It is constructed by submerging a Ag wire into a solution of AgNO<sub>3</sub> in the supporting electrolyte under study. Here the Ag/AgNO<sub>3</sub> RE is dependent on the  $[\text{Ag}^+]$  concentration, however in practice Ag ions can diffuse through the glass frit with time, thus shifting the potential. In addition, the presence of Ag<sup>+</sup> ions in the test solution inevitably causes deposition and stripping of Ag at the working electrode. To avoid the use of AgNO<sub>3</sub>, a layer of solid AgBF<sub>4</sub>, AgPF<sub>6</sub> or AgClO<sub>4</sub> can be deposited on the Ag wire to stabilise the RE potential. This wire can then be submerged into supporting electrolyte of corresponding counter ions such that the RE potential is dependent on the  $[\text{X}^-]$  concentration. The Ag/Ag<sup>+</sup> RE is therefore a 'quasi-reference' because its potential is very sensitive to the electrolyte under study.

Although the Ag/Ag<sup>+</sup> quasi-RE is sufficiently stable for conducting experiments, it is not suitable for reporting potentials because its potential is not so easily reproduced between different studies. Thus, it is more appropriate to report

potentials against an internal standard which is reproducible. The use of the ferrocene/ferrocenium ion redox couple was proposed as an internal referencing standard by IUPAC [196,197] for reporting potentials at quasi-reference electrodes because ferrocene is soluble in various organic solvents and its potential shows little variation [67,196] with respect to electrolyte composition. It is therefore widely adopted as a method for referencing non-aqueous electrochemical systems [140,161,174,178,198].

**Table 3. Commonly used reference electrodes and their potential vs SHE at 25 °C. (a) supporting electrolyte. (b) Value omitted. The Ag/Ag<sup>+</sup> potential is very dependent on the electrolyte composition. Values reproduced from [67].**

Reference electrode	Half-cell	Condition	E [V] vs SHE
Standard hydrogen electrode	H <sup>+</sup>  H <sub>2</sub> (1 atm) Pt	a(H <sup>+</sup> )=1, p(H <sub>2</sub> )=10 <sup>5</sup> Pa	0.0000
Silver-silver chloride electrode	Cl <sup>-</sup>  AgCl Ag	1 M KCl	+0.2368
Saturated calomel electrode	Cl <sup>-</sup>  Hg <sub>2</sub> Cl <sub>2</sub>  Hg	Saturated KCl	+0.2415
Mercury sulfate electrode	SO <sub>4</sub> <sup>2-</sup>  Hg <sub>2</sub> SO <sub>4</sub>  Hg	Saturated K <sub>2</sub> SO <sub>4</sub>	+0.650
Mercury oxide electrode	OH <sup>-</sup>  HgO Hg	0.1 M NaOH	+0.165
Silver-silver ion electrode	Ag <sup>+</sup>  Ag	0.1 M AgNO <sub>3</sub> , 0.1 M SE <sup>(a)</sup>	(b)

## 2.2 Dynamic electrochemistry

Thus far the potential difference (open-circuit voltage) across any electrochemical cell has been related to thermodynamics and equilibria. However, as will be discussed in the following sections, thermodynamics merely predicts which direction the electrochemical reactions will spontaneously occur. This perspective does not consider the kinetics of the reaction or whether it will occur in any appreciable timeframe. Furthermore, by applying a potential across an electrochemical system, non-spontaneous reaction can be forced to occur. To describe such experiments, the theory of electrode dynamics is required: the study of how electron transfer reactions occur between electrodes and reactant molecules. Specifically, this subject is concerned with the mechanisms by which these reactions occur and their rates. Therefore, dynamic electrochemistry is often the interplay between the kinetics of a reaction and the ‘mass transport’ which delivers the reactant to the electrode surface. Before discussing the heterogeneous

kinetics of electrochemical reactions, it is important to first appreciate the mass transport of solution species and secondly the structure of the electrode-electrolyte interface.

It is important at this point to note the distinction between *faradaic* and *non-faradaic* processes. The former describes the transfer of charge across the electrode-electrolyte interface, hence causing oxidation/reduction of the electrolyte. A faradaic process is therefore governed by Faraday's law (Section 2.3.4) such that the amount of chemical reaction is proportional to the amount of electricity passed. In contrast, non-faradaic processes involve the change of the interface structure with changing potential or solution composition, i.e. via adsorption of ions. Both faradaic and non-faradaic processes take place during electrochemical reactions [193].

## 2.2.1 Mass transport

Mass transport is the collective term used to describe the preferential movement of dissolved species in solution. It comprises the effects of diffusion – movement in response to a concentration gradient, migration – movement of ions due to an electric field, and convection – movement of bulk electrolyte due to mixing.

### 2.2.1.1 Diffusion

Diffusion is the evolution of a system to maximise entropy by homogenising uneven concentration distributions in an electrolyte. The rate of diffusion is both spatially dependent on the local concentration gradient at any point, and temporally dependent such that the concentration distribution evolves with time. Diffusion is described by Fick's laws of diffusion, the first of which says that the diffusional flux vector  $\mathbf{J}$  of species A is related to the gradient of concentration

$$\mathbf{J} = -D_A \nabla[A] = -D_A \left( \frac{\partial[A]}{\partial x} \hat{i} + \frac{\partial[A]}{\partial y} \hat{j} + \frac{\partial[A]}{\partial z} \hat{k} \right) \quad (2.2.1)$$

where the constant  $D_A$  is the diffusion coefficient of species A. Considering now how  $[A]$  changes with time, Fick's second law of diffusion is attained:

$$\frac{\partial[A]}{\partial t} = D_A \nabla^2[A] = D_A \left( \frac{\partial^2[A]}{\partial x^2} + \frac{\partial^2[A]}{\partial y^2} + \frac{\partial^2[A]}{\partial z^2} \right) \quad (2.2.2)$$

In both ( 2.2.1 ) and ( 2.2.2 ), the diffusion coefficient is a temperature-sensitive parameter that is essentially a measure of the diffusional velocity of a species in solution. Therefore, the root mean square displacement in time  $t$  provides a measure of how far a molecule diffuses in a certain time:

$$\sqrt{\langle x^2 \rangle} = \sqrt{2Dt} \quad (2.2.3)$$

The magnitude of  $D$  is typically in the range of  $10^{-6}$  to  $10^{-5}$   $\text{cm}^2 \text{s}^{-1}$  for species in conventional solvents at room temperature, hence, mass transport by diffusion is very slow. Equation ( 2.2.3 ) predicts that the time required for a species to diffuse 1 cm is of the order of one day, assuming no convection or migration effects.

### 2.2.1.2 Migration

Migration is the movement of charge due to an external electric field. The most common source of an electric field is due to the drop in electrical potential at an electrode-electrolyte interface. The migrational flux of  $A$  through field  $\partial\Phi/\partial x$  is proportional to its concentration and the ionic mobility  $u$  as given in

$$J_m = u[A] \frac{\partial\Phi}{\partial x} \quad (2.2.4)$$

The electric field at an electrode-electrolyte interface is generated during electrolysis. Ions then move in response to the field by either being attracted towards or repelled from the interface. In turn, this ion rearrangement causes the electric field to evolve, thus migrational effects are difficult to predict or interpret from experimental data. Therefore, it is often desirable to minimise the migration of ions in solution by the addition of a chemically and electrochemically inert background electrolyte. In solutions with a high ionic strength, the manifestation of significant electric fields does not occur because the background electrolyte ions quickly migrate to maintain electrical neutrality across the interface region. Thus, the effects of migration are negligible and can be neglected in solutions where the supporting electrolyte concentration is high.

### 2.2.1.3 Convection

Lastly, convection is due to mechanical forces acting on the bulk electrolyte. Convection can be either due to natural forces within the electrolyte or due to external forces. In the first case, natural convection can be due to thermal gradients or density differences in the solution. Indeed, electrolysis reactions at the interface are either exo- or endo-thermic and the products of a reaction can have a substantially different density to those of the reactants in the bulk solution. These effects are however negligible at small surface area electrodes and at small current densities. Convection due to external forces such as due to the bubbling of gasses or vibrations are very unpredictable, however these effects can be prevented. In certain cases, the convection can be mathematically described as in the cases of hydrodynamic electrodes. Here the convection is beneficial because the electrochemical response from the system can be directly related to the convection such as electrode rotation rate or electrolyte flow-rate.

### 2.2.2 Structure of the electric double layer

As introduced in section 2.1.1, the establishment of an electrode potential causes a separation of charge at the electrode-electrolyte interface, and by electroneutrality, the total charges in the metal and solution phases must be equal in magnitude but opposed in polarity. Therefore, it is expected that an electrical double layer will exist at the interface and that this double layer will have a corresponding capacitance. The structure of the interface is best modelled with simplicity by the Grahame model as shown in Figure 8, however it should be noted that the exact structure will be dependent on the electrode material and the composition of the electrolyte. In addition, the double layer is non-static as ions are mobile at all times and the magnitude of the capacitance will inevitably evolve with time during electrochemical experiments. First, if it is assumed that no faradaic processes are occurring at the electrode surface then it can be said that the interface is behaving like a conventional electrical capacitor. Counterions in solution are therefore electrostatically attracted to the charged electrode surface to balance the charge, however their closest approach will be limited by their solvation. This minimum distance is called the Outer Helmholtz Plane (OHP) and is

physically the radius of the solvated ion. It is therefore expected that a layer of solvated counterions will be established on the electrode surface, however in reality this layer is not static. The double layer is more accurately described by a diffuse layer because the electrostatic attraction/repulsion forces on ions in the interface region are counteracted by Brownian motion which tends to disperse the excess ions. In this model, the potential drop extends into the electrolyte – a region called the ‘diffuse layer’, whereby both the potential and charge density decrease with distance from the electrode (time averages). Thus, the potential decays from the metal potential (at the electrode surface) to the solution potential at the diffuse layer thickness as shown in Figure 8. In reality, the double layer is more a combination of the OHP and the diffuse layer model, however in addition it is possible for ions to adsorb to the electrode surface. This is possible if unsolvated ions exist in solution or when ions lose their solvation shell as they approach the electrode surface. These ions are said to be ‘specifically adsorbed’ because the adsorption is chemical in nature meaning that ions of like-charge to the electrode can adsorb. The closest approach of these ions is therefore their ionic radii, and this is given by the Inner Helmholtz Plane (IHP) as shown in Figure 8.

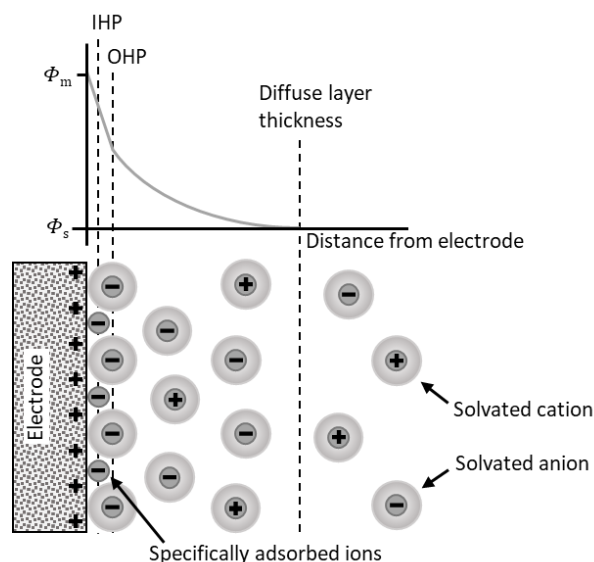


**Figure 8. Schematic illustration for the Grahame model of the electric double layer [194].**

In consideration of the electric double layer, the thickness of the diffuse layer is dependent on the ionic strength of the electrolyte. Therefore, the diffuse layer

thickness decreases as the supporting electrolyte increases, and at high concentrations the potential drop will occur over a distance of a few Angstroms. If one now considers that electron tunnelling during faradaic processes is efficient only up to a few Angstroms, then the full potential drop is available to drive the electrode reaction for concentrated solutions. In addition, as the diffuse layer thickness is small, reactant species are able to move into this electron tunnelling range purely by diffusion because the electric field is essentially zero beyond this range. These effects highlight why high ionic strength electrolytes preferentially aid electrolytic processes.

### 2.2.3 Electrode kinetics

Electrochemical reactions are by their nature heterogeneous reactions; therefore, reactant molecules must reside within the electrode-electrolyte interface in order to react. If one considers that electron transfer occurs by quantum mechanical tunnelling, the efficiency of which decreases to zero beyond distances of ca 10-20 Å, then reactant molecules must first diffuse from bulk electrolyte into this region to react. Hence, it can be deduced that the electrical current must depend on the flux  $j$  of reactant to the electrode surface:

$$I = nFAj \quad (2.2.5)$$

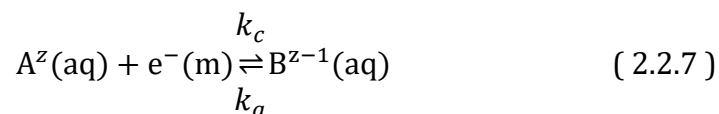
where  $n$  is the number of electrons transferred. Once the reactant species reaches the electrode surface, this flux must relate to a rate constant and the local concentration of the reactant. where

$$j = k(x)[reactant]_0^x \quad (2.2.6)$$

Here the familiar Faraday constant  $F$  and the electrode area  $A$  are constants, whereas  $k(x)$  is an  $x^{\text{th}}$  order rate constant and the concentration term is the local concentration within the critical electron tunnelling distance. A little reflection shows that this concentration will not equal the bulk concentration and it is expected that the conversion of reactant to product will inevitably cause depletion of reactant locally to the electrode. Therefore, fresh reactant must diffuse through this 'depletion layer' adjacent to the electrode to sustain the reaction. The concentrations of reactant and products near the electrode will therefore vary

significantly to the bulk solution and these concentrations are expected to evolve with time. Thus, the nature of the electrochemical kinetics are complex however it is further complicated by the dependency of the rate constant on the environment (temperature and pressure) and critically the electrical potential across the interface.

To begin, consider first a generic redox reaction of A being reduced to B. Both the forward reduction (cathodic) and reverse oxidation (anodic) reactions will proceed with independent rate constants given by  $k_c$  and  $k_a$ :



The net rate law for this process is

$$j = k_c[A^z] - k_a[B^{z-1}] \quad (2.2.8)$$

By altering the electrode potential  $\Phi_M - \Phi_S$  the equilibrium in (2.2.7) will inevitably shift. For example, if  $\Phi_M$  is made more negative while  $\Phi_S$  remained constant then the reactant  $A^z$  and  $e^-(\text{m})$  energies would increase with the product  $B^{z-1}$  remaining unchanged. Conversely, by keeping  $\Phi_M$  constant and making  $\Phi_S$  more negative, both the  $A^z$  and  $B^{z-1}$  energies would increase, but by different amounts on account of their difference in charge. Therefore, the reaction profile is dependent on  $\Phi_M - \Phi_S$ . This is shown pictorially in the reaction profile in Figure 9.

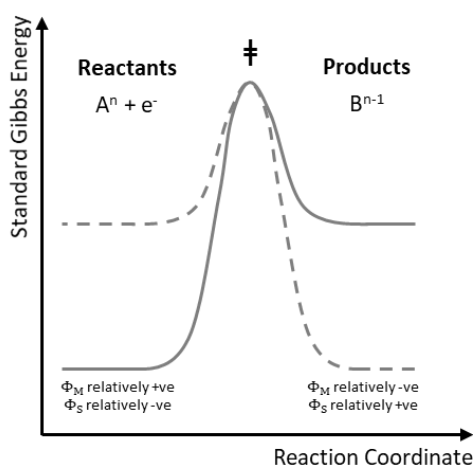


**Figure 9. A reaction profile for the  $A^z/B^{z-1}$  redox reaction. The effect of varying the metal and solution electrical potentials is shown [194].**

If Figure 9 is now considered comparable to homogeneous kinetics, the Arrhenius equation can be expressed for each rate constant to relate them to the free energy difference between the transition state † and the reactants/products and typical pre-exponential factors:

$$k_c = A_c \exp \frac{-\Delta G_c^0(\ddagger)}{RT} \text{ and } k_a = A_a \exp \frac{-\Delta G_a^0(\ddagger)}{RT} \quad (2.2.9)$$

where

$$\Delta G_c^0(\ddagger) = G^0(\ddagger) - G^0(R) \text{ and } \Delta G_a^0(\ddagger) = G^0(\ddagger) - G^0(P) \quad (2.2.10)$$

and  $G^0(\ddagger)$  is the transition state energy (a constant). Employing ( 2.1.18 ), then the reactant and product free energies are

$$G^0(R) = C_1 - zF\Phi_S - F\Phi_M \text{ and } G^0(P) = C_2 - (z - 1)F\Phi_S \quad (2.2.11)$$

where  $C_1$  and  $C_2$  are constants. Inspection of ( 2.2.11 ) shows that the free energy of reactants/products differ by the term  $-F(\Phi_M - \Phi_S)$ . Thus, if it is assumed that the transition state lies between that of reactants and products, then  $G^0(R)$  and  $G^0(P)$  can be related by inventing a coefficient  $\beta$  where  $0 < \beta < 1$ . Now, the equations in ( 2.2.10 ) can be generalised to

$$\Delta G_{a/c}^0(\ddagger) = G^0(\ddagger) - C_{1/2} - (z - 1)F\Phi_S - \beta F(\Phi_M - \Phi_S) \quad (2.2.12)$$

Thus giving  $\Delta G_c^0(\ddagger)$  for  $\beta = 1$ , or  $\Delta G_a^0(\ddagger)$  for  $\beta = 0$ . If  $\beta$  is close to zero then the transition state is product-like whereas if  $\beta$  is close to unity, the transition state is reactant-like. Substituting equation ( 2.2.12 ) into the corresponding equations in ( 2.2.9 ) allows the rate constant to be evaluated with the following proportionalities

$$k_c \propto \exp \left[ \frac{-\alpha F(\Phi_M - \Phi_S)}{RT} \right] \text{ and } k_a \propto \exp \left[ \frac{\beta F(\Phi_M - \Phi_S)}{RT} \right] \quad (2.2.13)$$

where  $\alpha + \beta = 1$ . Consideration of ( 2.2.13 ) now shows that if the electrode is made more positive ( $\Phi_M$  increases) then the anodic rate constant increases whereas that of the cathodic rate constant decreases. Conversely, if the electrode is made more negative ( $\Phi_M$  decreases) then the opposite will occur. Furthermore, if the term  $(\Phi_M - \Phi_S)$  is changed by 1 V then the rate constants change by a factor of ca.  $10^9$ , highlighting the excessive sensitivity of the heterogeneous rate constants to small changes in the electrode potential. The values  $\alpha$  and  $\beta$  are known as the 'transfer coefficients' and are in essence an indicator of where the transition state

of an electrochemical reaction lies relative to the reactants and products.

Frequently  $\alpha \sim \beta \sim \frac{1}{2}$  because the transition state lies intermediate in its electrical behaviour between reactants and products.

As discussed previously the electrode potential of a single electrode cannot be measured, only potential differences can. Therefore, the equations in ( 2.2.13 ) can be adapted to consider the potential difference between the ‘working electrode’ (the electrode of study) and a reference electrode by use of

$$E - E_f^0 = (\Phi_M - \Phi_S)_{working} - (\Phi_M - \Phi_S)_{reference} \quad ( 2.2.14 )$$

where the reference electrode potential is constant. Thus, combining ( 2.2.13 ) and ( 2.2.14 ) into ( 2.2.8 ) the flux is now related to the heterogeneous rate constants:

$$j = k_c^0 \exp \left[ \frac{-\alpha F (E - E_f^0)}{RT} \right] [A^z] - k_a^0 \exp \left[ \frac{\beta F (E - E_f^0)}{RT} \right] [B^{z-1}] \quad ( 2.2.15 )$$

This equation is the famous Butler-Volmer equation, which quantifies the total electrode flux as a function of the electrode potential. If one now considers the special case of dynamic equilibrium, then  $j = 0$  and equation ( 2.2.15 ) can be solved for the quantity  $E$

$$E = E_f^0 + \frac{RT}{F} \ln \left( \frac{[B^{z-1}]}{[A^z]} \right) + \frac{RT}{F} \ln \left( \frac{k_a^0}{k_c^0} \right) \quad ( 2.2.16 )$$

Evidently in ( 2.2.16 ) the rates of the forward and reverse reactions must be equal at equilibrium, thus giving  $k_c^0 = k_a^0 = k^0$  where the new parameter  $k^0$  is the ‘standard electrochemical rate constant’. In addition, substituting  $k_a^0/k_c^0 = 1$  into ( 2.2.16 ) collapses the equation to the familiar Nernst equation derived in section 2.1.2. Finally, the heterogeneous rate constants can be related to the standard electrochemical rate constant by:

$$k_c = k^0 \exp \left[ \frac{-\alpha F (E - E_f^0)}{RT} \right] \text{ and } k_a = k^0 \exp \left[ \frac{\beta F (E - E_f^0)}{RT} \right] \quad ( 2.2.17 )$$

where  $k^0$  is the rate constant when the potential of the electrode is equal to the formal potential  $E_f^0$  of the redox couple.

The interpretation of equation ( 2.2.15 ) is perhaps best approached graphically as shown in Figure 10a. First, considering that the total flux  $j$  is the sum of the cathodic  $j_c$  and anodic  $j_a$  flux contributions, then it is evident that ( 2.2.15 ) becomes dominated by the cathodic/anodic flux contribution as the electrode potential shifts to more negative/positive potentials relative to the formal potential. This is because the individual components to the flux exponentially increase at 'overpotentials' whereas they asymptotically approach zero at 'underpotentials'. Here the term overpotential is defined as  $\eta = E - E_f^0$ , thus, an overpotential is  $\eta > 0$  and underpotential is  $\eta < 0$  for the anodic reaction, whereas for the cathodic reaction the opposite is true. Second, when the electrode potential is equal to the formal potential, then the net flux is zero ( $j$  passes through the origin, given  $E^0 = 0$  V), despite  $j_a = j_c \neq 0$ , indicating that both the forward and reverse reactions are at dynamic equilibrium as expected.

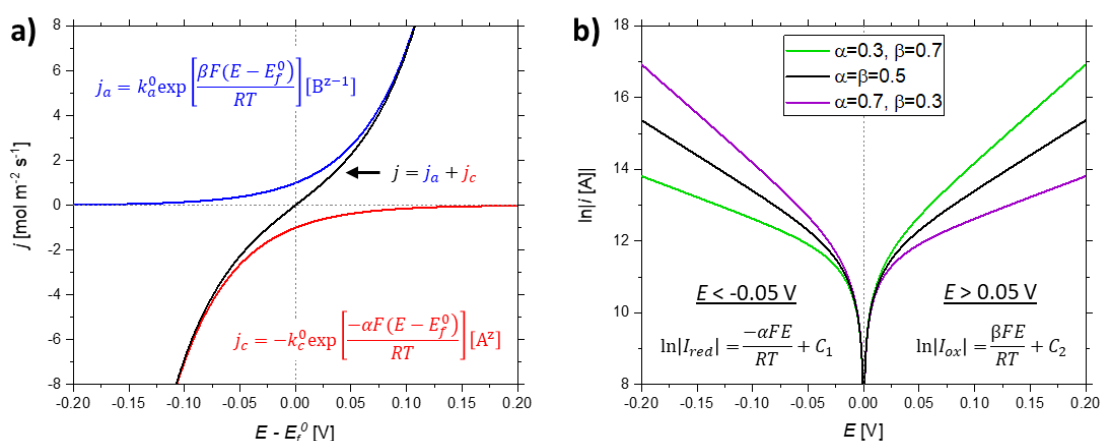


**Figure 10. Graphical representations of the Butler-Volmer equation. a) Flux as function of the electrode potential  $E$  where  $\alpha = \beta = 0.5$ . The anodic and cathodic contributions are shown as  $j_a$  and  $j_c$ , respectively. b) The logarithm of current as a function of  $E$  for different values of the exchange coefficients. The Tafel law is given for both the cathodic and anodic current, however here they are only applicable for potentials less than  $-0.05$  V and greater than  $0.05$  V respectively. Parameters),  $[A^z] = [B^{z-1}] = 1$  M and  $k^0 = 1$  m s $^{-1}$ ,  $E_f = 0$  V,  $A = 1$  m $^2$ .**

If equation ( 2.1.13 ) is now considered at extreme potentials relative to the formal potential, then the electrochemical reaction essentially proceeds in only one direction. Therefore, the cathodic contribution can be neglected for  $E \gg E_f^0$ , whereas the anodic contribution can be neglected for  $E \ll E_f^0$ . If it is then further

assumed that concentrations of  $A^z$  and  $B^{z-1}$  are not substantially changed from their constant bulk values, then the current can be expressed as

$$\ln|I_{red}| = \frac{-\alpha FE}{RT} + C_1 \text{ and } \ln|I_{ox}| = \frac{\beta FE}{RT} + C_2 \quad (2.2.18)$$

where  $C_1$  and  $C_2$  are constants. Accordingly, so called Tafel plots of  $\ln|I_{red}|$  or  $\ln|I_{ox}|$  vs  $E$  can provide information about the transfer coefficients  $\alpha$  and  $\beta$  and direct measurement of the standard electrochemical rate constant. Figure 10b shows the logarithm of current (as predicted by the Butler-Volmer equation) plotted as a function of potential for a generic redox couple. As the current is proportional to the exponential of overpotential, Figure 10b gives linear relationships with a gradient of  $-\alpha F/RT$  or  $\beta F/RT$  for cathodic and anodic currents respectively. Thus, the Tafel law is valid for the regions of linear character. As shown however, the dependency is significantly non-linear at low overpotentials because both the cathodic and anodic currents contribute significantly to the current. Care must therefore be taken to linearly extrapolate the data at large overpotentials in Tafel plots to avoid errors in the calculated transfer coefficients and standard electrochemical rate constants. An example Tafel analysis is given in Figure 11, whereby the transfer coefficients can be deduced from the gradient, whereas the standard electrochemical rate constant can be calculated from the intercept (at zero overpotential).

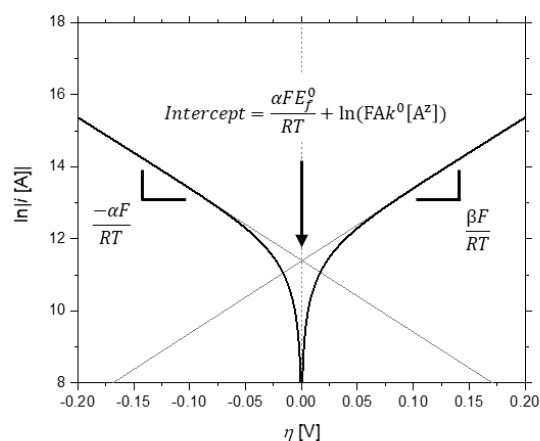


**Figure 11. Schematic illustration of Tafel analysis. Parameters),  $\alpha = \beta = 0.5$ ,  $[A^z] = [B^{z-1}] = 1 \text{ M}$ ,  $k^0 = 1 \text{ m s}^{-1}$ ,  $A = 1 \text{ m}^2$ . The extrapolated linear regressions are shown in grey.**

### 2.2.4 Marcus theory

In consideration of the standard electrochemical rate constant  $k^0$  in the previous section, it is evident that the magnitude of this parameter reflects the lowest possible heterogeneous rate constant for the  $A^z/B^{z-1}$  redox couple. Therefore,  $k^0$  is a suitable parameter for comparing the kinetics of different electrochemical reactions. Indeed,  $k^0$  is known to vary over eight orders of magnitude. The explanation for this staggering variation in electrochemical kinetics originates from changes in the chemical structure of a compound during conversion from one oxidation state to another – Marcus theory.

According to the Frank-Condon principal, the transfer of electrons occurs on a much shorter timescale in comparison to that of nuclear vibrations. Therefore, the spatial positions of all atoms in a molecule and that of its solvation shell are essentially constant during electron transfer. If one then considers the geometry of the reactant molecule, it is evident that the reactant molecule must first be excited into the transition state geometry before the molecule can accept/donate an electron. Once the molecule has been reduced/oxidised, it can then relax into the product's ground state geometry. This is shown pictorially in Figure 12 whereby the potential energy curves are given for a particular 'reaction coordinate'.

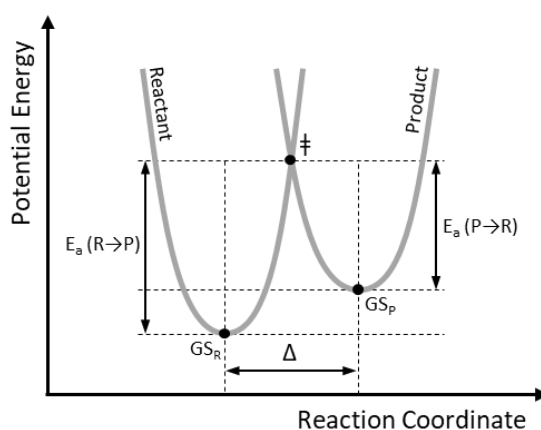


**Figure 12. Potential energy curve for an arbitrary reaction. The ground states (GS) of reactant (R) and product (P) as well as the transition state (‡) are shown [194].**

It is important to note here that the excitation of the ground state geometry to the transition state occurs via thermal activation. The physical interpretation of

this is where molecular vibrations induce energetically unfavourable geometries of the molecule such as changes in bond lengths, bond angles or torsion angles. The transition state therefore reflects the common excited geometry that lies midway between the reactant and product and is also the energetic barrier for the reaction. The difference between the ground state and transition state is therefore the activation energy ( $E_a$ ), which depends on the difference in reaction coordinate ( $\Delta$ ) and the ground state energies of the reactant and product. Mathematically, the electrochemical rate constant is related to the activation energy by an Arrhenius-like equation

$$k = KZe^{\frac{-\Delta G(\ddagger)}{RT}} \quad (2.2.19)$$

where  $\Delta G(\ddagger)$  is the Gibbs energy of activation and  $Z$  is a pre-exponential term. Here  $K$  is the transition probability which takes a value of  $K \sim 1$  for adiabatic reactions and  $K \ll 1$  for non-adiabatic reactions.

By use of Marcus theory, the magnitude of electrochemical rate constants can be rationalised in terms of the change in molecular geometry or solvation between different oxidation states. For example, the one-electron reduction of anthracene to the anthracene radical anion in DMF presents with a very high  $k^0$  of  $4 \text{ cm s}^{-1}$  because the molecular geometries are identical. Due to the high symmetry of the planar molecule and the extensive delocalisation of the radical, the barrier to electron transfer is correspondingly low with only changes in solvation occurring [194]. In contrast, the one-electron reduction of cyclooctatetraene to the radical anionic state in DMF has a much lower  $k^0$  of  $\sim 10^{-3} \text{ cm s}^{-1}$  because the geometry significantly changes from a tub-conformation to near-planarity. Further reduction of the radical anion to the cyclooctatetraene dianion is much faster ( $k^0$  of  $\sim 10^{-1} \text{ cm s}^{-1}$ ) however because the dianion has a similar near-planar geometry [194].

### 2.2.5 The Cottrell equation and the Nernst diffusion layer

In section 2.2.1.1 the general laws of diffusion were introduced, however here the second law is applied to describe how the current response at an electrode is dependent on the diffusion of reactant. Considering the case where a large potential is applied to a solution of electroactive species with a bulk concentration

$c^*$ . At time zero, the solution close to the electrode ( $x = 0$ ) is immediately electrolysed giving a surface concentration of zero ( $c/c^*$ ). As time passes, more material diffuses to the electrode surface from further distances, giving a zone of depletion of the reactant which is called the 'diffusion layer'. The diffusion layer is described mathematically by

$$c = c^* \frac{2}{\sqrt{\pi}} \int_0^\Gamma \exp(-\Gamma^2) d\Gamma \text{ where } \Gamma = \frac{x}{2\sqrt{Dt}} \quad (2.2.20)$$

and is shown in Figure 13a. The diffusion layer thickness therefore grows with time as the reaction continues at the electrode surface. The corresponding current as a function of time is shown in Figure 13b as predicted by the Cottrell equation

$$I = \frac{nFA\sqrt{D}c^*}{\sqrt{\pi t}} \quad (2.2.21)$$

which shows that the current from potentiostatic experiments decays to zero with proportionality to the inverse square root of time. In reality, the Cottrell equation is inaccurate at very long times because experimentally the current response approaches a constant value, rather than zero. This behaviour is modelled by the 'Nernst diffusion layer' which states that the diffusion layer reaches a critical value ( $\delta \sim$  hundreds of  $\mu\text{m}$ ) beyond which the concentration of the electroactive species is maintained at the bulk value. Physically, this is due to natural convection which mixes the electrolyte and overrides the negligible effect of the concentration gradient. Therefore, the limiting current is related to the 'mass transport coefficient' ( $m_T$ ) as given by

$$I_{ss} = nFAm_T c^* \text{ where } m_T = \frac{D}{\delta} \quad (2.2.22)$$

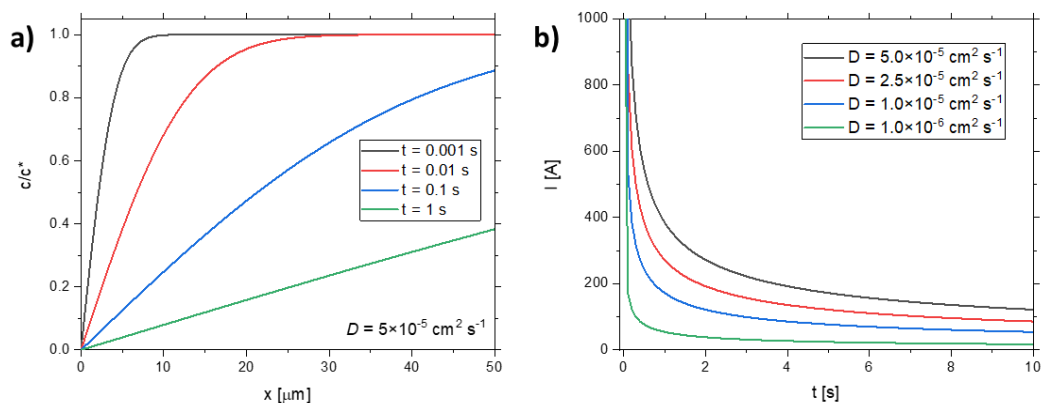


**Figure 13. a) Concentration profiles at varying times as a function of electrode distance after a potential step for a diffusion coefficient of  $5 \times 10^{-5} \text{ cm}^2 \text{ s}^{-1}$ . b) The current transients resulting from a potential step as a function of diffusion coefficient. Parameters:  $A = 1 \text{ cm}^2$ ,  $c^* = 1 \text{ mol cm}^{-3}$ ,  $n = 1$ .**

## 2.3 Electrochemical techniques

Now that the principals of electrochemical equilibrium and electrode dynamics have been introduced, the applied electrochemical techniques in this thesis can be discussed. It is important to note first that the study of dynamic electrode processes typically requires three electrodes. In conventional equilibrium electrochemical experiments only two electrodes are required because the current through the cell is negligible. In contrast, dynamic electrochemical experiments usually involve ‘potentiostating’ the cell at non-equilibria potentials such that significant currents are produced. This is problematic for referencing the ‘working electrode’ (WE) (the interface under study) because electrolysis will occur at the reference electrode, thus changing its composition and its electrode potential. In addition, the measured potential would become convoluted by the solution resistance due to the resistivity of the electrolyte:

$$E = (\Phi_M - \Phi_S)_{\text{Working}} + IR - (\Phi_M - \Phi_S)_{\text{Reference}} \quad (2.3.1)$$

Accordingly, a third electrode called the ‘counter electrode’ (CE) is introduced to pass the faradaic current such that the potential-determining equilibria of the reference electrode is maintained. A large surface area robust electrode such as a Pt wire or mesh is conventionally employed as the CE because the potential at the

counter electrode is not controlled. To achieve the desired potential at the WE, the potential of the CE is driven to a sufficiently high voltage by the potentiostat to allow the current to flow. Therefore, it is necessary to use a non-oxidizable CE material to avoid metal dissolution into the electrolyte

### 2.3.1 Principals of voltammetry

Voltammetry is the principal method for characterising redox materials used in this thesis. By varying the WE potential and measuring the current response, it is possible to study the interplay between the kinetics of redox reactions and the mass transport of reactants to the electrode surface. In addition, voltammetry enables the identification and potential measurement of unknown redox processes relative to a known RE potential. Therefore, voltammetry has numerous applications from quantifying properties to studying reaction mechanisms. Here, an introduction to voltammetry at macroelectrodes is given, where the electrode diameter is typically between 1 to 5 mm. It is important to note here that voltammetry is usually performed under quiescent and high ionic strength conditions, so only the effects of diffusion need to be considered.

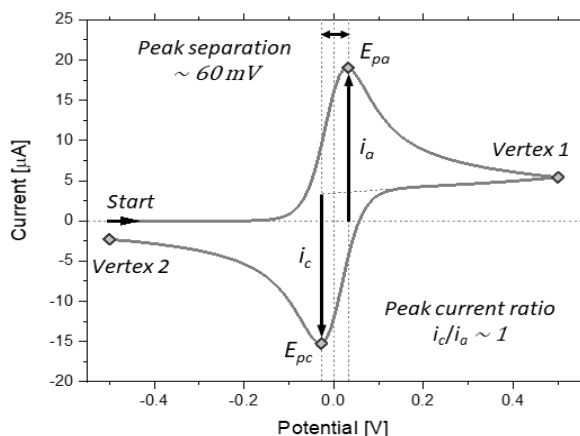
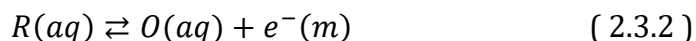


**Figure 14. Simulated CV by use of EC\_Simulator [199]. Parameters:  $k^0 = 1 \text{ cm s}^{-1}$ ,  $D = 10^{-5} \text{ cm}^2 \text{ s}^{-1}$ ,  $v = 100 \text{ mV s}^{-1}$ ,  $E_r^0 = 0 \text{ V}$ ,  $n = 1$ ,  $r = 1.5 \text{ mm}$ ,  $T = 298 \text{ K}$ ,  $[\text{Red}] = 1 \text{ mM}$ . Characteristic voltammogram features are highlighted.**

Linear sweep voltammetry (LSV) involves ‘sweeping’ the electrode potential at a constant rate from one vertex potential to a second vertex potential. Cyclic

voltammetry (CV) is a comparable technique where after the first vertex is reached, the sweep direction is immediately reversed and returned to the starting vertex. Figure 14 shows the typical waveform from a diffusion limited one-electron solution-phase redox couple in which both oxidation states are indefinitely stable.



Here the electrolyte contains only the reduced form and the cyclic voltammogram begins at a potential less than the formal potential. Initially, zero current is observed because the electrode potential is too low to oxidise R, however as the potential is swept towards and past the formal potential, the anodic current increases exponentially. Eventually the current reaches a maximum (the peak anodic current  $E_{pa}$ ) and then decays until the upper vertex potential is reached, with approximately  $1/\sqrt{t}$  as described by the Cottrell equation (section 2.2.5). The potential is then swept back towards and beyond the formal potential, whereby the current reverses such that a cathodic current is observed. Correspondingly, the reverse reduction reaction begins to occur with a current that grows exponentially until a peak cathodic current ( $E_{pc}$ ) is observed. The existence of the peak anodic and cathodic currents can be rationalised as the depletion of electroactive materials near the electrode surface corresponding to a diffusion layer. On the forward scan the concentration of R is depleted by the formation of O, whereas on the reverse scan the solution of O within the diffusion layer is back-converted to R.

### 2.3.1.1 Electrochemical reversibility

Figure 15a shows the effect of the electrochemical ‘reversibility’ on the cyclic voltammetry waveform. Considering first the peak currents, it is evident that the reversible voltammogram is the most symmetrical with the smallest peak separation and the largest peak currents. In contrast, the irreversible voltammogram is very unsymmetrical and exhibits a very large peak separation, whereas the ‘quasi-reversible’ voltammogram appears as a middle ground between the two extreme cases. Irrespective of the reversibility, the formal potential is given by  $(E_{pa} + E_{pc})/2$  if it is assumed that the diffusion coefficients of the O and R species are equal.

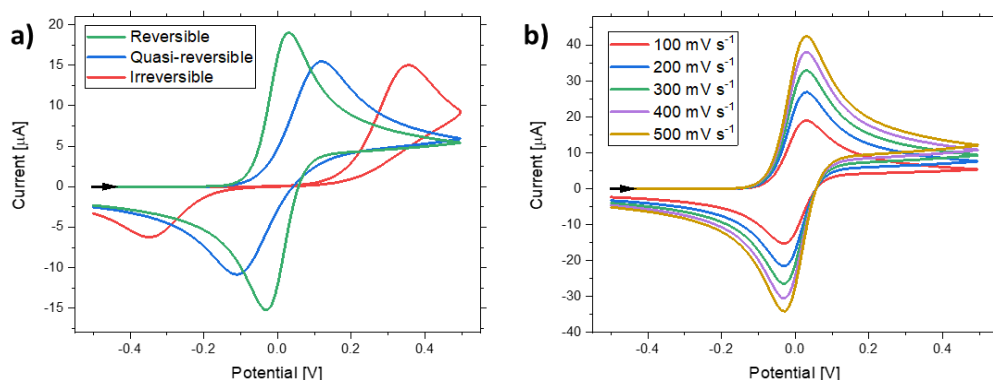


**Figure 15. Simulated CVs by use of EC\_Simulator [199]. a) CVs with  $k^0 = 1, 10^{-4}$  and  $10^{-5} \text{ cm s}^{-1}$  for the reversible, quasi-reversible and irreversible electron transfers respectively. b) CVs as a function of scan rate for a reversible voltammogram with  $k^0 = 1 \text{ cm s}^{-1}$ . The black arrows show the starting points of voltammetry. Parameters:  $D = 10^{-5} \text{ cm}^2 \text{ s}^{-1}$ ,  $v = 100 \text{ mV s}^{-1}$ ,  $E_i^0 = 0 \text{ V}$ ,  $n = 1$ ,  $r = 1.5 \text{ mm}$ ,  $T = 298 \text{ K}$ ,  $[\text{Red}] = 1 \text{ mM}$ .**

The difference in the reversibility can be rationalised in terms of the magnitude of the standard electrochemical rate constant  $k^0$  relative to the mass transfer coefficient  $m_T$  such that:

$k^0 \gg m_T$	Reversible
$k^0 \sim m_T$	Quasi-reversible
$k^0 \ll m_T$	Irreversible

Considering first the reversible case, the kinetics of the reaction are significantly faster than the mass transport (by diffusion) of the electroactive species, hence the voltammogram is said to be ‘mass transport limited’. In addition, due to the fast kinetics, a Nernstian equilibrium is established at the electrode surface at all potentials. The features of the reversible voltammogram are therefore related to the Nernst equation such that at the formal potential  $[O]_0/[R]_0 = 1$ .

In addition, the peak separation of a fully-reversible redox couple is  $\sim 57 \text{ mV}/n$  and independent of scan rate within the reversible limit. The peak currents of a fully reversible redox couple are also equal in magnitude, such that the ratio  $I_{pc}/I_{pa}$  is equal to unity. Considering now the opposite extreme case of the fully-irreversible voltammogram, a significant overpotential is required to drive both the forward and reverse reactions, such that zero current flows near the formal

potential. Hence the voltammogram is said to be 'kinetically controlled' because the current is sensitive to the electrode potential. In addition, the peak separation of an irreversible redox couple is dependent on the scan rate whereas the peak current ratio is typically far from unity.

### 2.3.1.2 Scan rate dependence

Measurement of the peak current as a function of scan rate ( $\nu$ ) shows that the current increases with  $\sqrt{\nu}$  for both the cases of reversible and irreversible behaviour. The proportionality of  $I_p \propto \sqrt{\nu}$  is rationalised by the thickness of the diffusion layer such that at faster scan rates,  $\delta$  is smaller. Correspondingly, the mass transfer coefficient ( 2.2.22 ) grows with scan rate and causes greater flux of material to the electrode surface. The constants of proportionality are given by:

$$I_p = 0.446FAC_{bulk} \sqrt{\frac{FD\nu}{RT}} \quad \text{Reversible} \quad ( 2.3.3 )$$

$$I_p = 0.496\sqrt{\alpha}FAC_{bulk} \sqrt{\frac{FD\nu}{RT}} \quad \text{Irreversible} \quad ( 2.3.4 )$$

Equation ( 2.3.3 ) is the Randles-Sevcik equation [194] for a one-electron redox process which is commonly applied for measuring the diffusion coefficient of a species that is fully reversible. Strictly speaking, ( 2.3.3 ) can only be applied to the peak current that is measured from bulk concentration conditions; i.e. it is not valid for CVs at steady state or for the backwards reaction because the diffusion layer is in a state of depletion.

Considering the effect of the scan rate on the electrochemical reversibility, it is frequently observed that the reversibility of a redox couple transitions towards irreversibility as the scan rate is increased. Quantitatively, this transition is dependent on the magnitudes of  $k^0$ ,  $m_T$  and  $\nu$  however the parameter  $\Lambda$  simplifies this dependency such that

$$\Lambda = \frac{k^0}{\left(\frac{FD\nu}{RT}\right)^{1/2}} \quad ( 2.3.5 )$$

where a value of  $\Lambda \geq 15$  is considered as reversible behaviour,  $15 > \Lambda > 10^{-3}$  is quasi-reversible and  $\Lambda \leq 10^{-3}$  is characteristic of irreversible behaviour.

### 2.3.1.3 Multiple electron transfers and coupled homogeneous kinetics

Cyclic voltammetry is especially useful for examining electrochemical mechanisms because certain reaction mechanisms give characteristic current responses. In general, these mechanisms are described as a chronological order of heterogeneous electron transfer steps (E) and coupled homogeneous chemical reactions (C). In each case the steps can be reversible or irreversible processes.

The EE mechanism is where successive electron transfers can occur due to the electroactive material existing in multiple oxidation states;  $A \rightleftharpoons B^+ \rightleftharpoons C^{2+}$ . If it is assumed that the formal potential of A/B is lower than B/C, then the two-electron oxidation from A to C will occur sequentially. In contrast, if B/C is lower than A/B, then the two-electron oxidation will occur at the A/B formal potential because the electrode potential is sufficiently anodic to oxidise B as soon as it is formed. It is important to note that each electron transfer can occur with significantly different reversibility because each electron transfer will occur with a different  $k^0$  and D.

The EC mechanism is very common in electrochemistry because molecules can be oxidised or reduced into unstable oxidation states which are reactive towards the electrolyte. Following the reaction, the products are typically electrochemically inert. Indeed, oxidation of many compounds tends to cause decomposition because an electron is typically removed from a bonding molecular orbital. The rate of this chemical reaction however will depend on the homogeneous kinetics of the C step and is therefore independent of the heterogeneous E step. If the voltammetry is studied as a function of scan rate the current response of the back reaction will typically increase with  $v$  because there is less time for the chemical reaction to occur.

The ECE mechanism is an extension of the EC mechanism whereby the products of the chemical reaction are electrochemically active in the potential range under study. The shape of an ECE waveform can vary greatly because of the number of different variables to consider, however in general a new oxidative or reductive

peak is observed due to the second E step. In studying an ECE mechanism, it is possible to probe the nature of each step as a function of scan rate and potential region. Most illuminating is the case of a fast and irreversible C step which causes the A/B waveform to transition to the C/D formal potential, over several cycles, because the diffusion layer becomes depleted of A and B.

### 2.3.2 Hydrodynamic methods: the rotating disc electrode

Hydrodynamic electrodes introduce mechanical convection to an electrochemical reaction such that the current response can be related to the mass transport via convection and diffusion. In the case of the rotating disc electrode (RDE) a vortex is formed in the electrolyte which draws electroactive material to the electrode surface and then pushes it out horizontally. The convection therefore enhances the mass transport by ensuring that the diffusion layer is maintained at a constant thickness with time. Furthermore, as the electrode rotation rate is increased, the size of the diffusion layer is compressed, hence increasing the flux of electroactive material [194]. Inevitably, the current response at an RDE reaches a limiting value at large overpotentials as shown in Figure 16a. This is due to the heterogeneous rate constant being sufficiently large to electrolyse all material flux incident at the electrode surface. This limiting current as a function of rotation rate is given by the Levich equation:

$$I_{lim} = 0.620nFAD^{2/3}\nu^{-1/6}[C]_{bulk}\omega^{1/2} \quad (2.3.6)$$

where  $\nu$  is the kinematic viscosity (viscosity/density) and  $\omega$  is the rotation rate in radians per second. A plot of  $I_{lim}$  vs  $\omega^{1/2}$  therefore yields a linear relationship with an origin intercept and a gradient that is dependent on the diffusion coefficient (Figure 16b). The Levich equation [200] is therefore a reliable method for measuring diffusion coefficients if the kinematic viscosity of the electrolyte is accurately known.

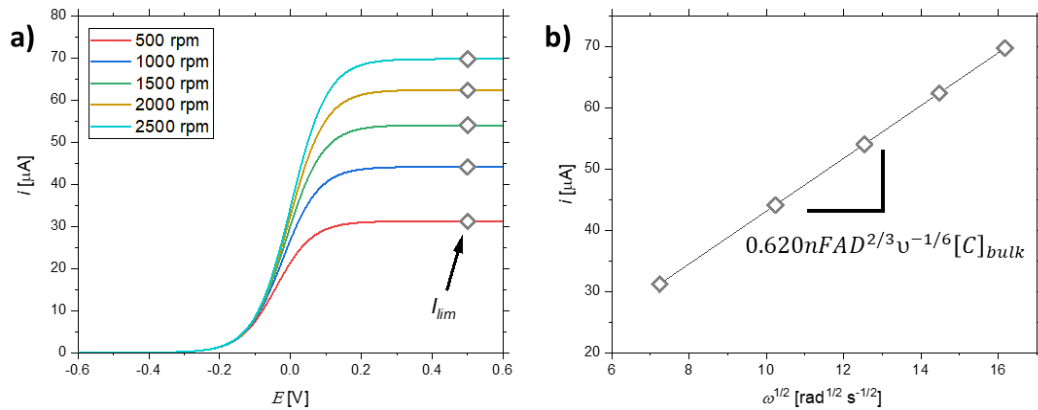


**Figure 16.** The Levich equation applied to theoretical data with parameters:  $D = 1 \times 10^{-5} \text{ cm}^2 \text{ s}^{-1}$ ,  $k^0 = 1 \times 10^{-2} \text{ cm s}^{-1}$ ,  $\beta = 0.5$ ,  $[C]_{\text{bulk}} = 1 \text{ mM}$ ,  $\nu = 8.92 \times 10^{-7} \text{ m}^2 \text{ s}^{-1}$ ,  $T = 298 \text{ K}$ ,  $A = 1.5 \text{ mm}$ ,  $n = 1$ .  
**a)** RDE LSVs for a redox couple with  $E_r^0 = 0$ . The sampled limiting currents are shown. **b)** A plot of the limiting current against the square root of rotation rate. The relationship between the gradient and  $D$  is shown.

Upon inspecting the sigmoidal shapes of the RDE I-V response it is evident that before the limiting current is established, the current has contributions from both the kinetics of the reaction and the mass transport. This region can therefore be analysed to measure the standard electrochemical rate constant and the transfer coefficient by use of the Koutecký-Levich equation [193]:

$$\frac{1}{i} = \frac{1}{i_K} + \frac{1}{i_{MT}} \quad (2.3.7)$$

where  $i_K$  and  $i_{MT}$  are the kinetically limited and mass transport limited currents respectively.  $i_{MT}$  is given by the Levich equation in (2.3.6), whereas  $i_K$  relates to the heterogeneous rate constant as a function of overpotential ( $\eta$ ), by use of equation (2.2.17):

$$i_K = nFAk_h[C]_{\text{bulk}} = nFA[C]_{\text{bulk}}k^0 \exp\left[\frac{\beta F \eta}{RT}\right] \quad (2.3.8)$$

Figure 17 shows the Koutecký-Levich method applied to simulated RDE LSV data. In Figure 17a five different overpotentials were selected in the kinetic controlled region and then used to construct the Koutecký-Levich plot ( $i^{-1}$  vs  $\omega^{-1/2}$ ) in Figure 17b [201]. From which, the kinetically limited currents are measured from the intercepts by extrapolating the data to infinite rotation [200]. A graph of

$\ln|i_K|$  vs overpotential can then be plotted which gives the transfer coefficient  $\beta$  from the gradient and  $k^0$  from the intercept (at the formal potential) [201].

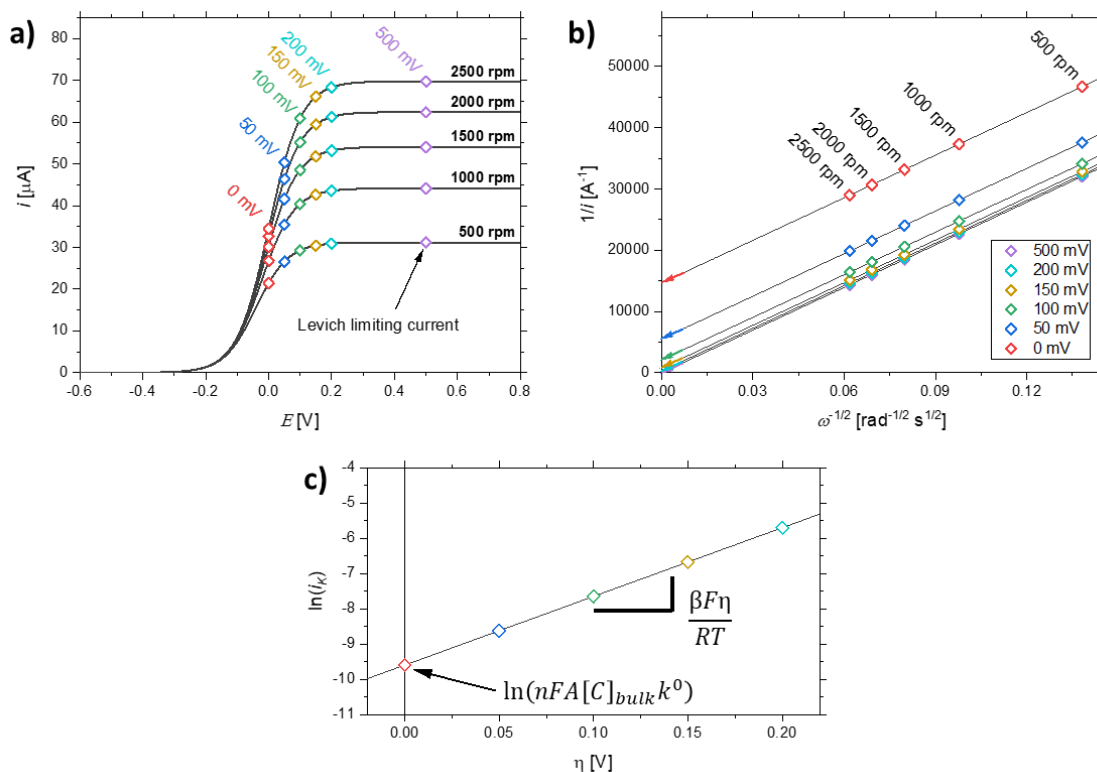


**Figure 17.** The Koutecký-Levich method applied to theoretical data with parameters:  $D = 1 \times 10^{-5} \text{ cm}^2 \text{ s}^{-1}$ ,  $k^0 = 1 \times 10^{-2} \text{ cm s}^{-1}$ ,  $\beta = 0.5$ ,  $[C]_{\text{bulk}} = 1 \text{ mM}$ ,  $\nu = 8.92 \times 10^{-7} \text{ m}^2 \text{ s}^{-1}$ ,  $T = 298 \text{ K}$ ,  $A = 1.5 \text{ mm}$ ,  $n = 1$ . a) RDE LSVs for a redox couple with  $E_f^0 = 0$ . The sampled overpotentials are shown. b) Koutecký-Levich plot for select overpotentials. The intercepts corresponding to  $1/i_K$  are highlighted. c) A plot of the logarithm of the kinetically limited current against overpotential. The relationships between the intercept/gradient and  $k^0/\beta$  are shown.

### 2.3.3 Impedance

Electrochemical impedance spectroscopy (EIS) is an experimental technique for deconvoluting the component resistances in a circuit. In electrochemistry, this generally means measuring the resistances corresponding to the bulk solution (Ohmic), charge transfer at the electrode surface and the mass transport of electroactive material to the interface. Ohm's law defines resistance as an impeding force to the flow of current. Mathematically this is

$$R \equiv \frac{E}{I} \quad (2.3.9)$$

Although this law defines resistance, it can only be applied to only one circuit element – an ideal resistor. This is because a resistor has several simplifying properties: Constant resistance at all currents and voltages, the resistance is independent of frequency, and alternating current/voltage through the resistor are in phase. Clearly, these properties are not true for all components, therefore the concept of an ‘impedance’ ( $Z$ ) is required to quantify complex elements and circuits [193]. Measurement of  $Z$  is achieved by applying a small amplitude sinusoidal potential perturbation ( $\sim 10$  mV) and then measuring the sinusoidal current response and associated phase shift, as a function of frequency. Thus, assuming pseudo-linear current response, the impedance;

$$Z = \frac{E}{I} = Z_0 e^{i\theta} = Z_0 (\cos \theta + i \sin \theta) \quad (2.3.10)$$

is expressed as a function of the magnitude ( $Z_0$ ) and phase shift ( $\theta$ ). The impedance is therefore a complex number which is best represented by a ‘Nyquist’ plot;  $Z'$  (real component) vs  $Z''$  (imaginary component) as shown in Figure 18b. The impedance vector to any coordinate ( $Z', Z''$ ) on a Nyquist plot therefore gives  $|Z|$  at that point whereas the angle to the x-axis gives the ‘phase angle’.

Analysis of the impedance spectrum from an electrochemical cell is typically approached by modelling the data to a comparable electrical circuit [195]. Typically, this circuit comprises simple components such as resistors, inductors and capacitors in series or parallel. Thus, by building a theoretical circuit the data can be fit to the model to yield parameters for each individual circuit element.

The Randles circuit shown in Figure 18a is a noteworthy example as it models the electrochemical interface in the simplest possible way. Here  $R_s$  models the solution resistance, whereas  $R_{CT}$  models the charge-transfer resistance associated with the heterogeneous kinetics. In series with  $R_{CT}$  is a ‘Warburg element’ ( $W$ ) which models the diffusion of the electroactive material to the electrode surface. A capacitor  $C_d$  is placed in parallel to  $R_{CT} + W$  to model the capacitive current associated with the electric double layer. As shown in Figure 18b the

corresponding EIS spectrum consists of a high frequency x-axis intercept, a semi-circle at intermediate frequencies and a linear region at low frequencies. The semi-circle is due to the charge transfer (diameter =  $R_{CT}$ ) whereas the intercept corresponds to the solution resistance  $R_s$ . In contrast, the low frequency linear region corresponds to diffusion and is dependent on  $W$ . The interpretation of the EIS frequencies therefore gives an indication of the timescale of certain processes in the electrochemical cell.

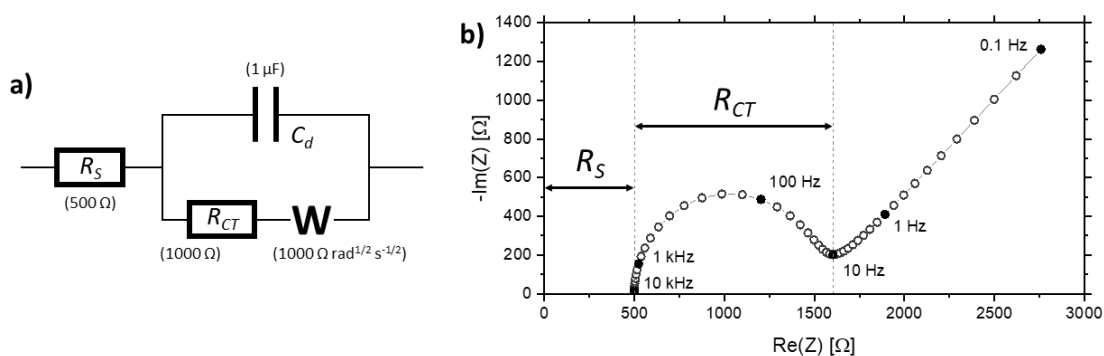


**Figure 18. a) Randles circuit with parameters shown. b) Simulated EIS Nyquist plot using the parameters in a). Example frequencies are shown as black circles.**

### 2.3.4 Electrolysis

Electrolysis is the principal method for conducting charge-discharge experiments of batteries. By imposing a certain potential or current on an electrochemical cell, the electrochemical reactions can be driven to occur at appreciable rates, irrespective of whether they are spontaneous or not. Therefore, the electrolyte can be ‘electrolysed’ such that considerable changes in reactant concentration occur. Typically, the experiment is continued until all of the electroactive material has been converted as defined by an end point. For chronopotentiometry a constant current is applied until a defined potential threshold has been reached, whereas for chronoamperometry a constant potential is applied until a certain charge has been passed or when the current decreases below a certain value. Irrespective of the technique, the bulk electrolysis cell has to be carefully designed to maximise the electrode area and in general, significant mechanical convection is required to enhance the mass transport of reactant

molecules. By conservation of charge, the time required to complete an electrolysis is given by Faraday's laws of electrolysis:

$$t = \frac{nFz}{I} \quad (2.3.11)$$

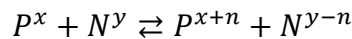
where  $n$  is the number of moles of reactant and  $z$  is the number of electrons transferred per reactant molecule.

## 2.4 The electrochemistry of redox flow batteries

Given that a RFB is an entirely solution-phase technology, their current-voltage characteristics are related to the solution concentrations of the electroactive species and their kinetics at the electrodes.

### 2.4.1 Theoretical cell potential

The standard cell potential  $E_{cell}^0$  of a RFB is defined as the difference between the formal potential of the posolyte and negolyte redox couples. The cell potential  $E_{cell}$  is therefore a function of the electrolyte composition and is given by the Nernst equation. For a general RFB involving posolyte and negolyte species P and N respectively



The Nernst equation is therefore:

$$E_{cell} = E_{cell}^0 - \frac{RT}{nF} \ln \left( \frac{[P^{x+n}][N^{y-n}]}{[P^x][N^y]} \right) \quad (2.4.1)$$

Given that the total quantity of posolyte material is equal to that of the negolyte, then  $[P^x] + [P^{x+n}] = C_{Total} = [N^y] + [N^{y-n}]$ . If it is now assumed that the cell is balanced such that  $[P^x] = [N^y]$  and  $[P^{x+n}] = [N^{y-n}]$ , then equation (2.4.1) becomes [202]:

$$E_{cell} = E_{cell}^0 - \frac{2RT}{nF} \ln \left( \frac{[P^{x+n}]}{[P^x]} \right) \quad (2.4.2)$$

Now defining  $[P^x]/C_{Total} = 1 - SOC$  and  $[P^{x+n}]/C_{Total} = SOC$ , then

$$E_{cell} = E_{cell}^0 - \frac{2RT}{nF} \ln \left( \frac{SOC}{1 - SOC} \right) \quad (2.4.3)$$

which describes the cell potential as a function of the state of charge. Thus, the cell potential is equal to  $E_{cell}^0$  when the cell is at 50 % SOC, as shown in Figure 19.

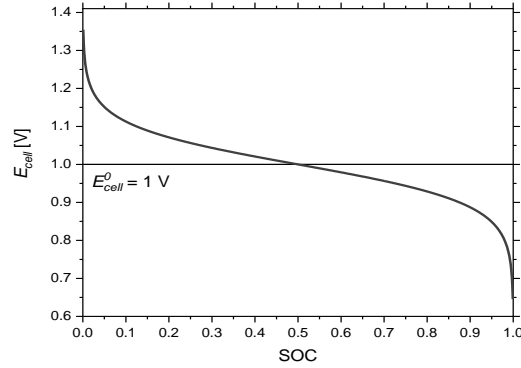


**Figure 19. A plot of the cell potential  $E_{cell}$  as a function of SOC.**

## 2.4.2 Polarisation

In reality, equation ( 2.4.3 ) is only valid when measuring the open-circuit voltage at any given SOC. This is because irreversible losses occur during battery operation, causing the actual cell potential  $V_{cell}$  to be less than the theoretical  $E_{cell}^0$  [203]. This departure of the cell potential from the equilibrium value upon the passage of a faradaic current is termed ‘polarization’. The losses in RFBs are attributed to three sources; activation, concentration and ohmic overpotentials. Thus, the overall cell potential is described by:

$$V_{cell} = E_{cell} - \eta_A - \eta_C - iR_{cell} \quad ( 2.4.4 )$$

$\eta_A$  is the activation overpotential for both anode and cathode reactions and is the extra potential required to overcome the activation energy barrier.  $\eta_A$  is therefore related to the kinetics of the reactions and will depend on the cell temperature. The  $\eta_C$  term is the overpotential that arises from the mass transport of reactants to the electrode surface and therefore depends on the electrolyte flow rate and the concentration of reactant. The concentration overpotential therefore significantly increases as the cell approaches high/low SOC on charge/discharge respectively. In contrast, the ohmic overpotential ( $iR_{cell}$ ) is a term which scales linearly with the applied current. The constant  $R_{cell}$  is the total cell resistance

which is the sum of the resistance contributions from the solution resistance, membrane and electrodes/current collectors.

If the I-V characteristics of a RFB is measured at constant electrolyte composition by a series of potentiostatic measurements, a polarization curve can be constructed as in Figure 20. Polarization curves therefore show the overall cell performance at a fixed SOC and quantify the limiting current at a given overpotential. In general, battery losses can be minimised by careful engineering of the flow reactor. For example, by employing high surface area electrodes or more catalytic electrode materials, the activation overpotential can be significantly reduced [203]. Furthermore, by decreasing the overall cell resistance, the ohmic overpotential can be minimised. In contrast, overpotentials due to mass transport are inevitable because of finite convection.

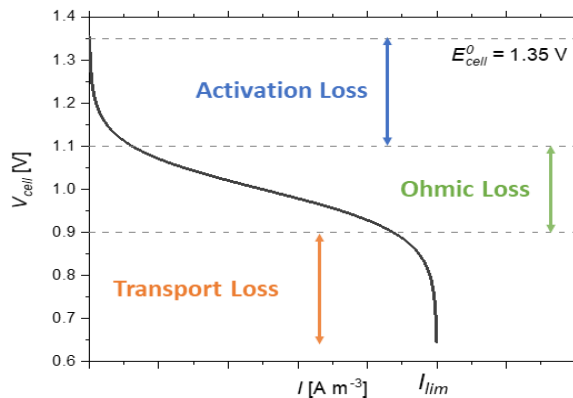


**Figure 20. Generalised polarization curve for a RFB indicating the dominant source of overpotential in each region [203,204].**

### 2.4.3 Battery metrics

The performance of batteries is quantified by way of battery metrics; a set of parameters that are adopted across the wider research field beyond just RFBs.

The battery capacity is defined by the total amount of electric charge which is stored in the battery during charge or discharge. Although equivalent to the SI unit for charge, the Coulomb (C), it is often more advantageous to express the battery capacity in units of ampere hours (A h), where 1 A h = 3600 C. By use of this unit, it

is therefore convenient to calculate the time required to charge/discharge a battery at a specific current (or the current for a specific charge time) by simply dividing the theoretical capacity by the current (or time). The capacity of a cell can also be normalised by expressing the actual measured capacity (sometimes referred to as the ‘accessible capacity’) as a percentage, decimal or fraction of the theoretical capacity. The normalised capacity therefore indicates the degree of utilisation of the electrolyte, such that a capacity of <100 % indicates cell leakage, imbalance or redox material instability, whereas a normalised capacity of >100 % suggests self-discharge. The normalised capacity is also equivalent to the SOC (or the inverse of the depth-of-discharge), however the SOC of a battery is often measured indirectly to assess the physical condition of the battery, such as by spectroscopy [179].

$$\textit{Theoretical capacity} = \frac{Q}{3600} = \frac{zC_{\text{active}}vF}{3600} \quad (2.4.5)$$

The volumetric capacity of a novel RFB is quantified in terms of its energy density; a measure of the theoretical maximum amount of energy which can be stored per litre of electrolyte. The energy density is calculated as the product of the cell potential  $V_{\text{cell}}$  and active species concentration  $C_{\text{active}}$ :

$$\hat{E} = 0.5V_{\text{cell}}C_{\text{active}}nF \quad (2.4.6)$$

where  $n$  is the number of electrons transferred in the cell reaction. Here the units of the Faraday constant are  $\text{A h mol}^{-1}$  and the coefficient of 0.5 arises from two volumes of electrolyte being used in the RFB technology.

The current at which a RFB is charged or discharged is more commonly expressed as a current density in units of  $\text{A cm}^{-2}$  by dividing the applied current by the two-dimensional geometric electrode surface area. The use of current density allows the performance of different cell designs to be directly compared, regardless of their electrode area. Despite this, the current density does not consider the total capacity of the battery, therefore it is often more useful to consider the battery ‘C-rate’ which is defined as the current required to discharge a battery in one hour. Therefore, batteries can be compared in terms of the C-rate

such that better performing batteries will achieve higher C-rates. The C-rate is calculated by;

$$C \text{ rate} = \frac{1}{\text{electrolysis time [h]}} = \frac{\text{Current}}{\text{Theoretical capacity}} \quad (2.4.7)$$

Battery performance is typically evaluated in terms of the coulombic, voltaic and energy efficiencies [203]. The coulombic efficiency ( $\eta_c$ ) is defined as the percentage of the total battery charge/capacity (or time if equal charge/discharge currents were used) on charging, that is achieved on discharging the battery. The coulombic efficiency is therefore a measure of the stability of the battery because a  $\eta_c$  less than 100 % indicates self-discharge or capacity loss each cycle. Losses in the coulombic efficiency can result from a range of physical and chemical processes that occur in the battery; electrolyte leakage, self-discharge due to membrane diffusion, cross-contamination of electrolytes, loss or degradation of the redox species, side reactions that occur in solution or at the electrode surface or parasitic decomposition of the electrolyte. In contrast, the voltaic efficiency is a measure of the electrochemical performance of the battery. It is dependent on the effects of cell voltage losses which arise due to ohmic resistance and overpotentials (activation and concentration). Given that these losses scale with the applied current density, the voltaic efficiency of a battery therefore decreases with increasing current densities. The voltaic efficiency ( $\eta_v$ ) is calculated by integrating the cell potential with respect to time for charge and discharge and expressing the discharge cell voltage as a percentage. Strictly speaking the voltaic efficiency should be invariant of the coulombic efficiency so therefore it is necessary to normalise the charge/discharge times in cases where the coulombic efficiency is low. Alternatively, the voltaic efficiency can be approximated to good accuracy for batteries with symmetrical potential thresholds, by averaging the cell potentials on charge and discharge. Finally, the energy efficiency or 'round-trip efficiency' ( $\eta_E$ ) is a measure of the total energy released from the battery on discharge in comparison to the energy required to charge it. Therefore,  $\eta_E$  is an indicator of the overall battery performance and its parabolic dependency on applied current density will give the optimum battery current density [203]. The  $\eta_E$  is calculated by taking the product of the coulombic and voltaic efficiencies [16].

$$\eta_{Coulombic} = \frac{\oint I_{Discharge} dt}{\oint I_{Charge} dt} \times 100 = \frac{Q_{Discharge}}{Q_{Charge}} \times 100 \quad (2.4.8)$$

$$\eta_{Voltaic} = \frac{\oint V_{Discharge} dt}{\oint V_{Charge} dt} \times 100 \quad (2.4.9)$$

$$\eta_{Energy} = \frac{\oint I_{Discharge} V_{Discharge} dt}{\oint I_{Charge} V_{Charge} dt} \times 100 = \frac{\eta_{Coulombic} \times \eta_{Voltaic}}{100} \quad (2.4.10)$$

#### 2.4.4 Cell configurations

To study different battery phenomena, the experiments conducted in this thesis make use of the flow-cell in different configurations, as shown in Figure 21. In each case the cell is assembled with a membrane or separator however the electrolyte configuration differs. The full cell is the most conventional cell configuration as it mimics a full RFB and functions as an energy storage device (non-zero cell potential). Here the full cell configuration enables true battery testing of novel chemistries under practical conditions via battery cycling or polarization to study capacity decay and performance respectively. In addition, the cell can be assembled in a symmetric [179] or asymmetric [150] configuration such that either the same redox material is used in both the posolyte and negolyte (symmetric) or the posolyte/negolyte contain distinct redox materials (asymmetric).

Although the full cell is the most realistic configuration, the data analysis is typically convoluted by multiple battery phenomena such as membrane crossover, kinetics, overpotentials and capacity loss. In contrast, the ‘independent redox couple cell’ considerably simplifies the battery experiments as only one redox couple is used in the cell, thus giving a cell potential difference of exactly 0 V (at 50 % SOC). Here, the cell can be ‘charged’ and ‘discharged’ (arbitrarily defined for passing positive/negative current) by electrolysing the two electrolytes, however no energy is stored. The benefit to this experiment type is that the capacity retention and performance of a single redox couple can be studied without the effects of membrane crossover causing irreversible capacity loss which occurs in

asymmetric full cell experiments. To avoid confusion with the symmetric full cell, the term ‘symmetric cell’ [156,159] which is used in the literature to describe the independent redox couple cell configuration, has been avoided in this thesis. Finally, the single electrolyte cell is where the flow-cell is connected to a single electrolyte reservoir that contains both the oxidised and reduced form of a single redox couple at equal concentration; i.e. at 50 % SOC. Here the flow-cell remains at steady state, despite the applied current or potential, because the charged electrolytes from the flow-cell recombine in the reservoir. This cell configuration therefore enables cell diagnosis at steady state under different electrolyte/mass transport conditions, via impedance or polarization, to measure and deconvolute cell resistances.

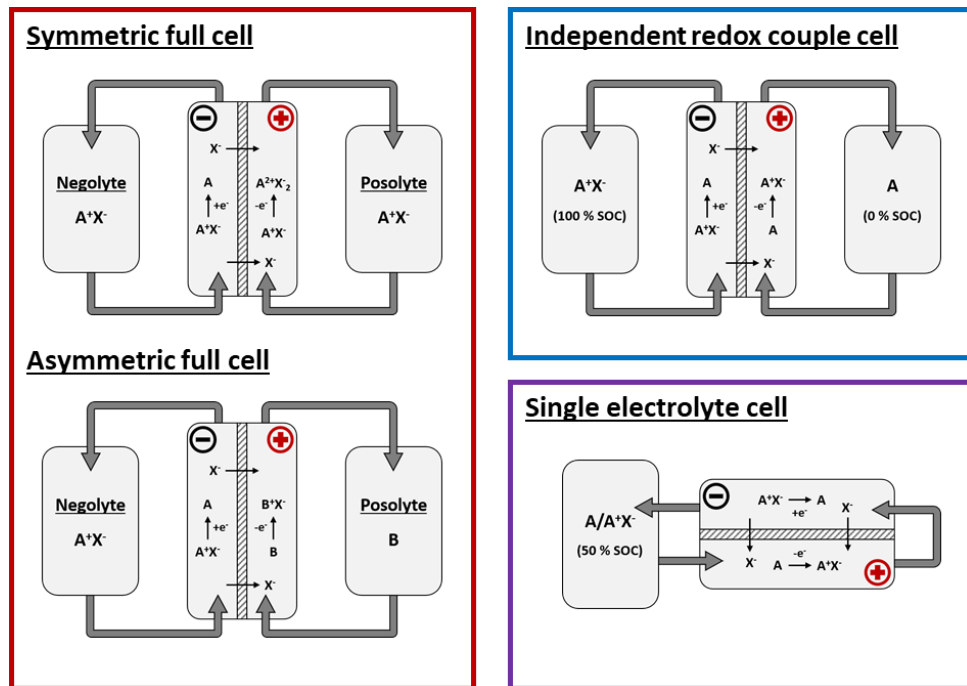


Figure 21. Cell configurations for battery experiments.



# Chapter 3

# Electrochemical Cell Designs

## 3.1 Introduction

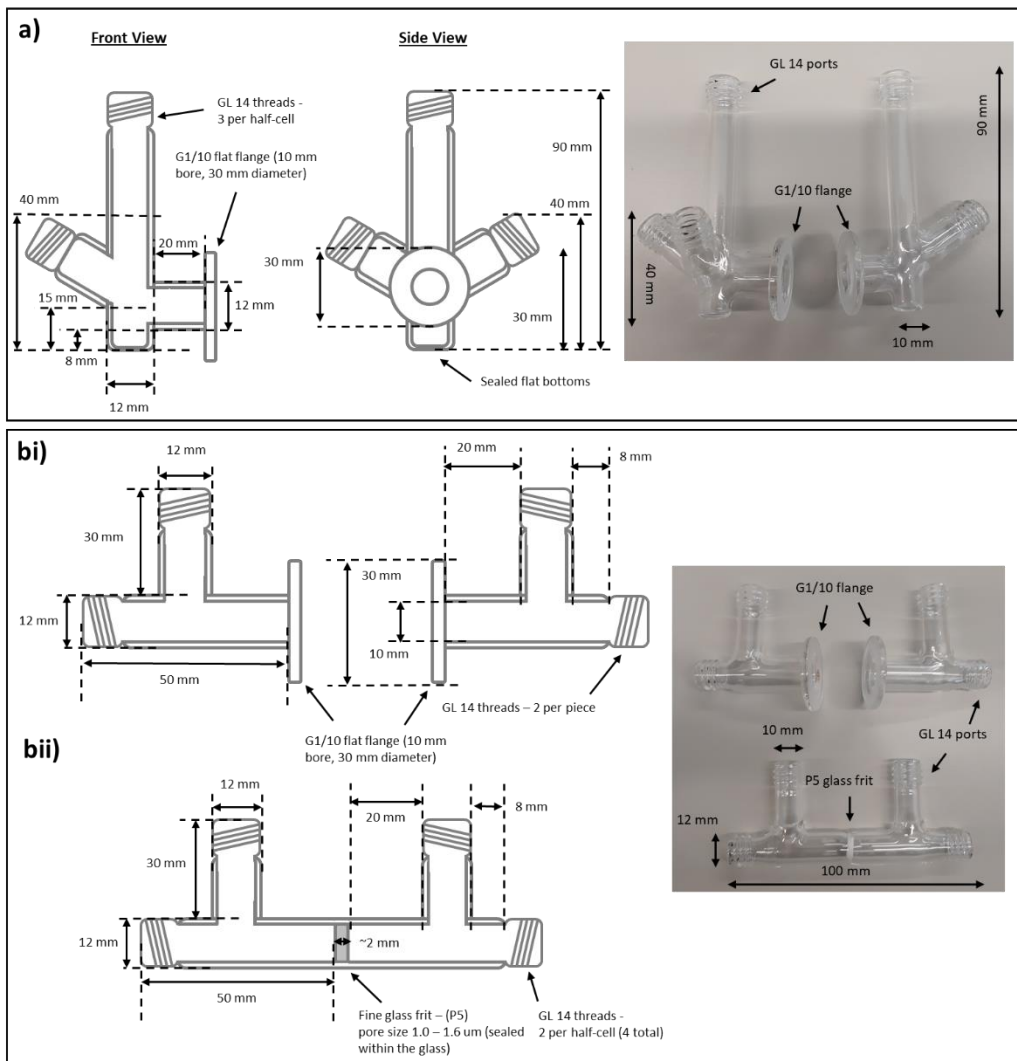
As introduced in Chapter 1, RFBs are entirely solution-phase energy storage devices whereby the electrolyte is cyclically pumped through an electrochemical flow-cell to charge-discharge the battery. From an electrochemistry perspective, RFBs are relatively simplistic because the battery processes can be arbitrarily studied in any conventional voltammetry or bulk electrolysis apparatus. However, from a chemical engineering perspective the design of RFBs is non-trivial because the performance of the battery is entirely dependent on the flow-cell design. Specifically, the power density of the technology is limited by the redox kinetics, mass transport and ohmic resistance. In principal the battery performance can be improved by optimising the cell design for the applied chemistry. As mass transport is dependent on the material diffusion coefficient and electrolyte convection, the battery power density can be improved by higher electrolyte flow rates and better flow distributions. Meanwhile, the ohmic resistance can be minimised by increasing the conductivity of the electrolyte and membrane, by reducing the inter-electrode separation or by achieving homogeneous conductivity across the whole electrode material. Furthermore, although the redox kinetics are governed by the fundamental electrochemistry of the redox materials, enhancements can still be made by employing more catalytic electrode materials or surface treatments. Therefore, the optimisation of the flow-cell design is very important for achieving high C-rates and minimising losses in voltaic efficiency due to overpotentials.

Beyond the performance of the battery, the design of the flow-cell must also be suitable for the desired application in terms of the scale of the battery and compatibility with the electrolyte. In this thesis, the focus is the application of novel redox materials in NA solvents, such as MeCN. Therefore, the battery architecture, electrodes and membrane must be inert in the applied solvent and must not degrade with time. This is often challenging as organic solvents are typically aggressive towards polymeric materials and can cause swelling, dissolution or the leech of plasticisers, hence the battery materials must be carefully chosen to ensure that degradation does not occur and that the electrolytes are not affected. Here small volume batteries are desirable in order to minimise the amount of redox material used per experiment because it is often challenging or impractical to synthesise large quantities of novel redox material or operate at saturation conditions. In addition, it is desirable to minimise the quantity of supporting NA electrolyte used due to cost. Beyond this, the experimental timescales are also decreased by decreasing the battery volume, hence allowing more battery cycles to be conducted in the same time period compared to a larger volume cell. Therefore, the cell designs typically used in academic research are significantly different and much smaller than life-size RFBs and are more bespoke per application.

From the onset of this work our research group did not possess suitable electrochemical cells to study the novel redox materials in Chapters 4 to 7. It was therefore crucial to design and develop functional electrochemical cells which could be used to battery cycle the novel redox materials and achieve high performance. Furthermore, it was also important to build cells which were flexible and adaptable towards different experimental techniques or materials. This objective was achieved by developing both glass cells, which are suitable for various electrochemical experiments, and flow-cells, which are more optimised towards battery experiments. Herein, the designs, applications and limitations of each cell developed in this thesis are described in detail. In the following chapter, a model chemistry will be applied to characterise the cells here and validate the battery performance of the novel chemistries explored in later chapters.

### 3.2 Glass H-type and bulk electrolysis cells

Glass electrochemical cells are the simplest and most adaptable cell designs for various experiments. Whereas commercial cells were used for voltammetry experiments (20 and 100 mL beakers with PTFE lids, ALS Co., Ltd or BASi), glass cells for battery and electrolysis methods are typically bespoke. These specialised pieces are not commercially available and therefore must be purpose-designed per application. Here, four different designs were developed for the purpose of battery and electrolysis experiments on low-concentration electrolytes as shown in Figure 22.



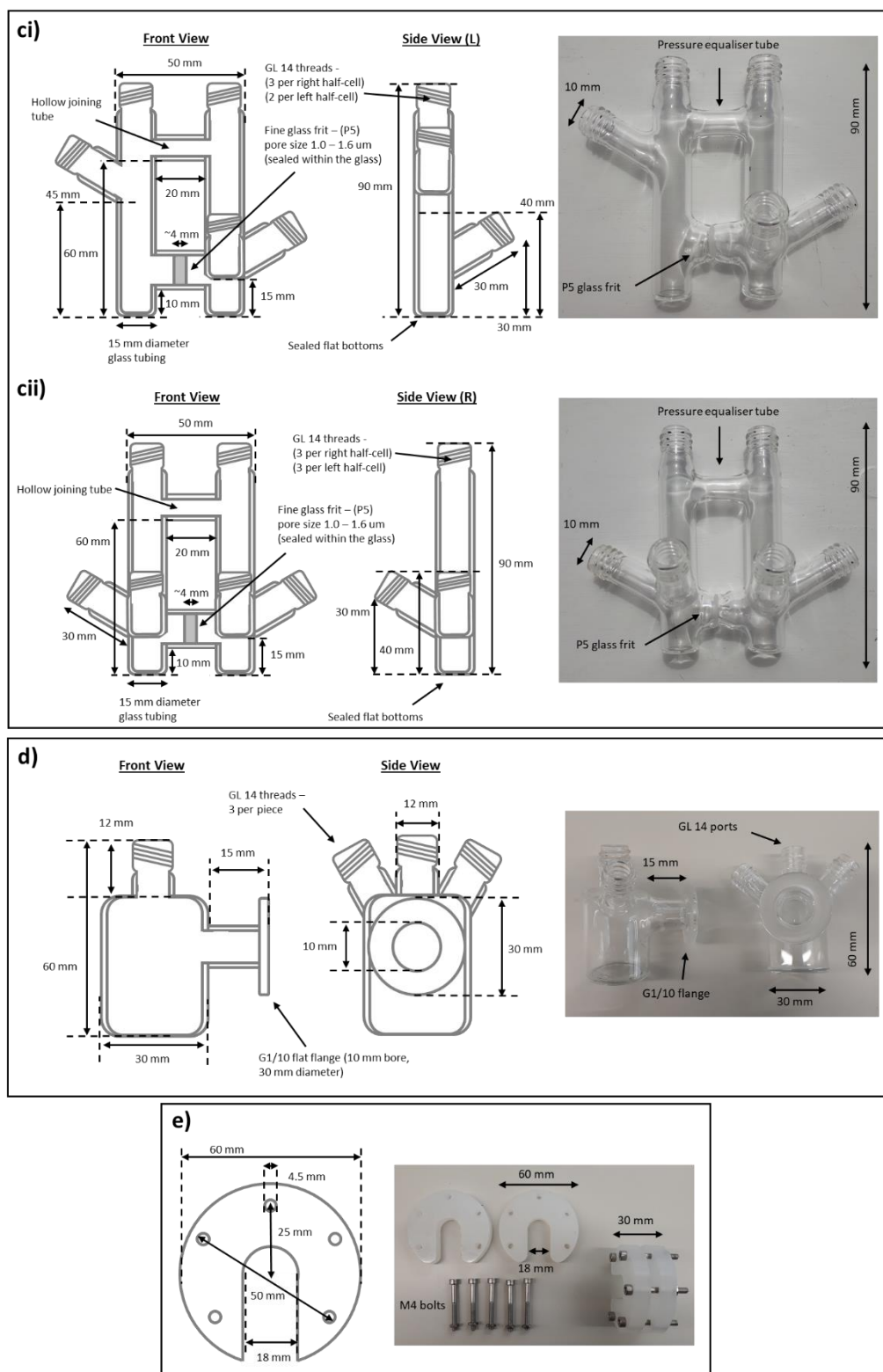


**Figure 22. Glass electrochemical cell designs and accessory. a) Membrane H-cell (GC-I). b) Linear cells (GC-II), i membrane and ii glass frit variants. c) Glass frit H-cell (GC-III), i bulk electrolysis and ii battery variants. d) Membrane bulk electrolysis cell (GC-IV). Front and side views shown. e) Flange slider-clamps.**

The designs generally feature multiple ports for electrode access into the electrolyte, flat bottoms for magnetic stirrer bars and membrane flanges/glass frits to separate the half-cells. The GC-I and GC-III cells were optimised for battery experiments whereas the GC-IV cell was designed for larger-scale bulk electrolysis. The GC-II cell was designed for multiple purposes including small-volume battery/electrolysis methods and membrane studies such as membrane crossover, resistance and selectivity. Furthermore, for the cells with membrane flanges, the cells were designed to be interchangeable such that the glassware could be adapted as needed. A purpose-built clamp was also designed for the membrane cells (Figure 22e) to apply even pressure to the flanges and gaskets to seal the cells against leakage. Typically, graphitic electrodes were used in the glass-cells such as graphite rods, felts or reticulated vitreous carbon (RVC) foams and the electrolytes were stirred during use. It is important to note that H-type cells have been applied in various electrochemistry studies and the cell designs here were adapted from literature studies in the field of NA RFBs [78,150,152,160,172].

**Table 4. Properties and applications of the glass electrochemical cells as shown in Figure 22.**

**(a) The electrolyte volume is dependent on the electrodes used due to solution displacement, however a minimum volume is required to fill the cell bridge and connect the two half-cells. (b) The inter-electrode separation is dependent on the electrodes used and their positioning in the cell.**

Glass cell design	Approximate volume per half-cell [mL](a)	Approximate inter-electrode separation [mm]	Intended applications
GC-I. Membrane H-cell	4 - 9	40	Battery charge-discharge, bulk electrolysis
GC-II. Linear cells (membrane and glass frit variants)	2 - 5	0 - 50(b)	Small-volume battery charge-discharge, bulk electrolysis, membrane studies, diffusion
GC-III. Glass frit H-cell (bulk electrolysis and battery variants)	5 - 8	25	Battery charge-discharge, bulk electrolysis
GC-IV. Membrane bulk electrolysis cell	20	50	Bulk electrolysis

The application of glass cells for battery studies gives specific advantages and disadvantages as compared to flow-cells. Glass cells typically allow smaller

volumes of electrolyte to be used which reduces the amount of novel redox materials used per experiment. In addition, experiments can be conducted using reference electrodes placed close to the working electrode to independently measure the working and counter electrode potentials and study each electrolyte independently. By use of a reference electrode, battery studies can also be conducted via bulk electrolysis whereby the electrolyte of study is charged-discharged against a sacrificial electrolyte or against the irreversible decomposition of the supporting electrolyte. The extra ports on the glass cells also enable easy sampling of the electrolytes for ex-situ methods or for conducting in-situ methods such as cyclic voltammetry or spectroscopy. Despite their high functionality, glass cells generally suffer from poorer performance as compared to flow-cells due to a combination of high ohmic resistance, limited electrode surface area and inferior convection. This typically limits the C-rates which can be achieved and often, higher overpotentials are observed than in a comparable flow-cell experiment at the same C-rate. Given that the high ohmic resistance results from the large inter-electrode separation (flow-cells are usually zero-gap) and from the membrane/glass frit separator, the GC-IV cell gave the worst battery performance because the inter-electrode separation was high (50 mm, Table 4), the electrode area was very limited and the cell volume was high (20 mL), thus only very low C-rates of  $< 0.4$  were possible.

### 3.3 Non-aqueous flow-cells

Two different NA flow-cells were developed in this project for battery studies of novel redox materials. The FC-I flow-cell (Figure 23) was designed based upon similar designs from the literature [150,179,205], whereas the FC-II flow-cell (Figure 24) was reproduced from literature specifications [40]. In addition, a commercial flow-cell (C-flow 5×5, C-Tech Innovation) was purchased for this project, however the scale was inappropriate for the study of novel redox materials; 25 cm<sup>2</sup> electrode area, 100 mL per half-cell minimum volume. As shown in Table 5, the FC-II flow-cell is the most suitable for the experiments conducted in this thesis as the electrolyte volume is only 10 mL and high C-rates were achieved.

**Table 5. Properties of the flow-cell designs and their application in NA experiments. (a) 1 mM electrolyte with 0.5 M supporting salt. (b) 10 mM electrolyte with 0.1 M supporting electrolyte. (c) the C-Flow flow-cell was never used for NA experiments.**

Flow-cell design	Electrolyte volume per half-cell [mL]	Maximum flow-rate [mL min <sup>-1</sup> ]	Electrode material and thickness [mm]	Electrode area [cm <sup>2</sup> ]	Typical current density (C-rate) [mA cm <sup>-2</sup> ]
FC-I	50	≈ 60	Graphite felt (4)	8 (2×4)	0.125 – 1.25 <sup>(a)</sup> (0.75 – 7.48 C)
FC-II	10	≈ 20	Carbon paper (0.25 – 1)	2.08 (1.3×1.6)	2.40 – 12.02 <sup>(b)</sup> (1.87 – 9.33 C)
C-Flow 5x5	100	≈ 200	Graphite felt (4)	25 (5×5)	N/A <sup>(c)</sup>

### 3.3.1 Flow-cell I

Drawing inspiration from the commercial C-Flow cell, the FC-I flow-cell was designed as a small-volume conventional flow-through zero-gap flow-cell. The cell was stack assembled and sealed via electrode compression (estimated at approx. 50 %) such that the electrodes made good contact with the current collectors and membrane to minimise cell resistances. The FC-I cell was manufactured by 3D-printing the flow-cell bodies out of ‘VeroWhite®’ resin (Stratasys®, a solvent-resistant polymer) with a 14 µm layer resolution and machining/cutting the remaining components. Conventional graphite felt was used for electrode material, whereas a graphite composite (ppg-86, Eisenhuth, 14 % polypropylene) was used for the current collectors. An electrical contact was made by using thin brass current collectors which resided behind the graphite current collector. To seal the cell, Viton gaskets were used between the half-cells and then also between the graphite current collector and electrodes. Although reasonable performance was achieved using this cell in Chapter 5, the cell design was rather crude and suffered several practical limitations. First, the cell components showed poor long-term stability in the MeCN electrolyte. The 3D-printed cell bodies degraded with time due to excessive swelling and absorption of the electrolyte whereas the Tygon tubing and Viton gaskets were essentially single-use components. Second, the cell was prone to leakage from the back recesses (the electric contacts) and therefore the electrolyte frequently contacted the brass current collectors, which caused

corrosion with time and the release of metal ions into the electrolyte. Thirdly, the cell was inconvenient to assemble, disassemble and clean such that the cell was prone to warping upon compressing and the current collectors could not be easily removed from the cell bodies due to swelling of the flow-cell bodies. Due to these issues, the design was unsuitable for long-term experiments (> 24 h) or to be reused repeatedly without degradation. Furthermore, the cell volume (50 mL) was undesirably large and high overpotentials were observed at modest C-rates, thus a better flow-cell was needed for future experiments.

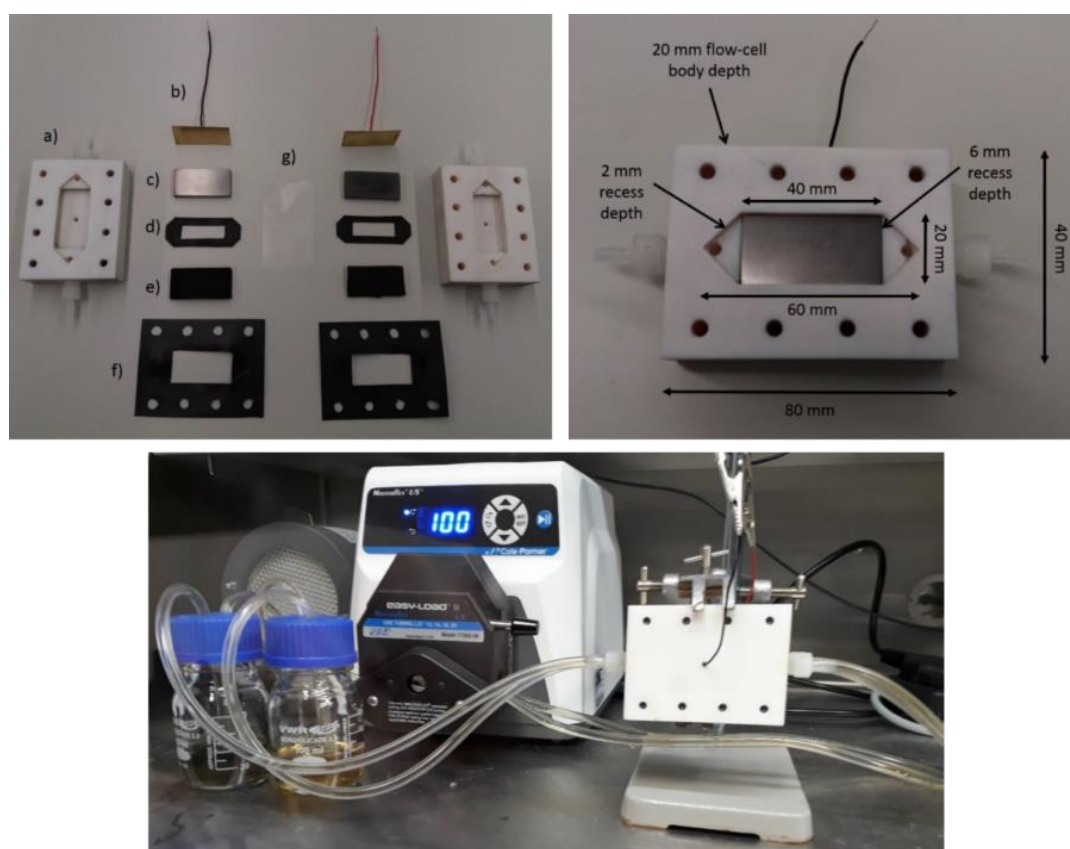


**Figure 23. FC-I flow-cell design in deconstructed and assembled view inside a N<sub>2</sub> glovebox.**

**Top left) FC-I flow-cell components: a) 3D-printed flow-cell bodies, b) brass current collectors and electrical contact, c) graphite current collectors, d) viton rubber internal seal, e) graphite felt electrodes, f) viton rubber gasket, g) membrane. Top right) Dimensions.**

**Bottom) complete cell with peristaltic pump, glass-bottle reservoirs Tygon tubing and electrolyte.**

### 3.3.2 Flow-cell II

In contrast to the FC-I flow-cell, the FC-II flow-cell displays excellent stability towards several organic solvents and has been used for up to 10-day experiments without significant loss of electrolyte. The design is also a zero-gap cell; however, as the graphite current collectors are part of the stack, the cell is more easily assembled. Furthermore, as the metal electrical contacts reside outside of the cell the flow-cell is metal-free avoiding current collector issues. The design is also more modular, thus allowing different flow-field and electrode configurations to be used, giving flexibility for using different electrode materials and thicknesses. The flow-cell bodies were computer numerical control (CNC) milled out of polypropylene (PP), whereas the flow-field current collectors were CNC milled out of ppg-86 graphite-PP composite. Gaskets were cut from highly-chemically resistant Polytetrafluoroethylene (PTFE) plastic by hand whereas ethylene-propylene diene monomer (EPDM) rubber gaskets were laser-cut for accuracy. EPDM rubber was chosen for the gaskets and O-rings due to its good chemical resistance and its lower cost as compared to Kalrez<sup>®</sup>, however before use the EPDM rubber components were soaked in an aggressive solvent cocktail to remove plasticisers (MeCN, MeOH, EtOH and acetone). Here, two different gasket materials were used in the same cell assembly unlike in the literature whereby a single layer of expanded PTFE foam was used [40]. This was due to the difficulty in reliably cutting the single-use expanded PTFE material by hand. The 0.5 mm EPDM gaskets were used to seal the cell against leakage whereas the 0.25 mm (uncompressible) PTFE gaskets were used to ensure electrical insulation between the half-cells. When using a more aggressive solvent such as DME, the compressed EPDM gaskets would become relatively conductive due to the soaking of electrolyte, thus short-circuiting the flow-cell. An optimised electrode configuration was achieved by using a single 1 mm thick piece of carbon paper (13x16 mm) (A20301 Technical Fibre Products Ltd. Polyvinyl alcohol binder), such that an electrode compression of 30-40 % was achieved. The electrolyte was pumped between the flow-cell and reservoirs via tubing lines constructed of highly chemically resistant perfluoroalkoxy alkane (PFA) and Norprene peristaltic pump tubing (Cole Parmer), both with a 1.6 mm internal diameter, which were joined via stainless

steel twin-ferrule unions (Swagelok). For the storage of the battery electrolyte, 10 mL PFA vials with ferrule connectors (Saville) were used as shown in Figure 24.

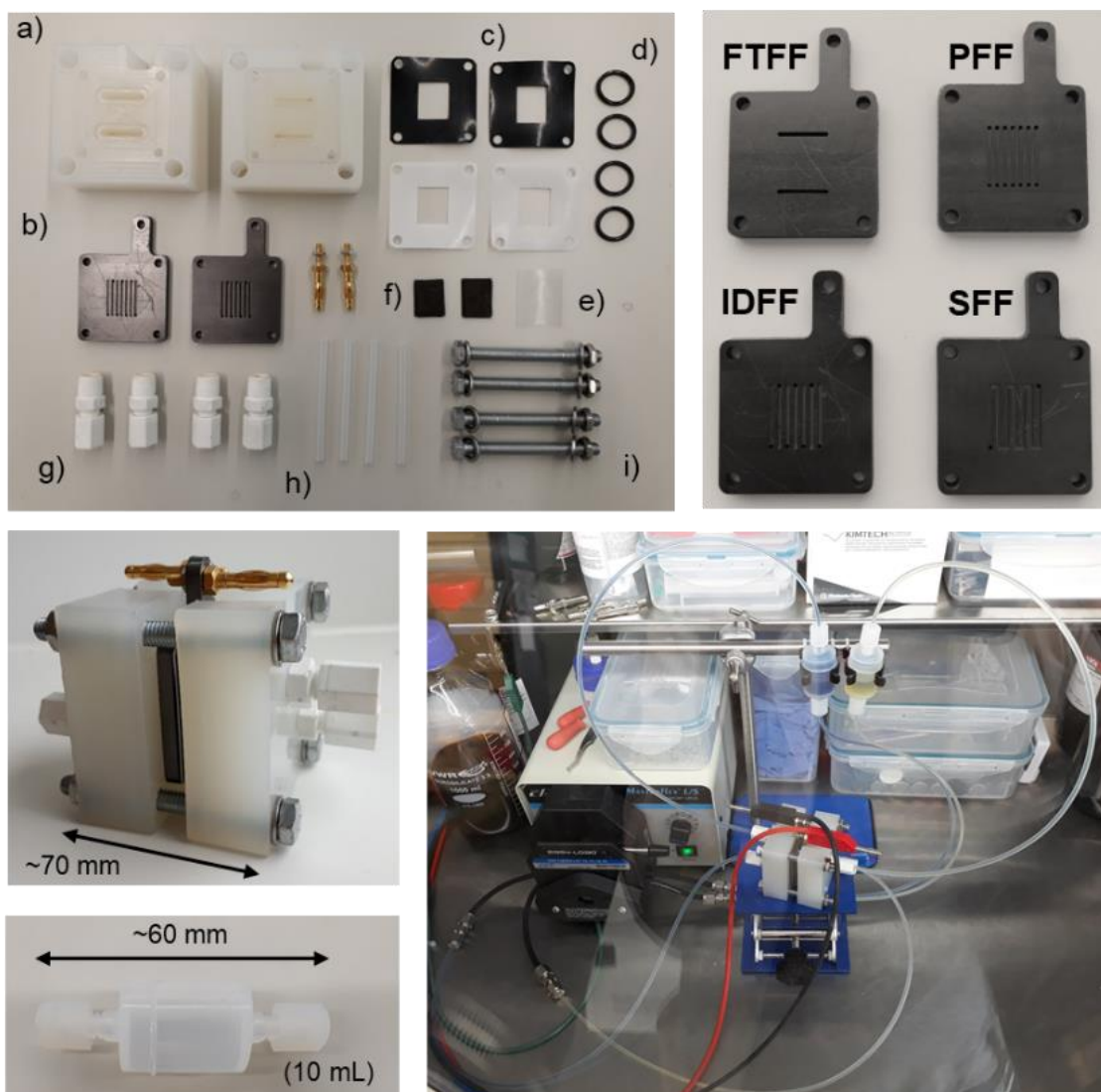


**Figure 24. FC-II flow-cell design in deconstructed and assembled view inside a N<sub>2</sub> glovebox. Top left) FC-II flow-cell components: a) PP electrolyte diffusers, b) ppg-86 graphite flow-field current collectors and gold pin contacts, c) EPDM and PTFE gaskets, d) EPDM O-rings, e) membrane, f) carbon paper electrodes, g) PP compression fittings, h) PFA assembly pins, i) M6 nuts and bolts. Top right) flow-field current collectors: FTFF = flow through flow-field, PFF = parallel flow-field, IDFF = interdigitated flow-field, SFF = serpentine flow-field. Bottom left) assembled FC-II flow-cell and PFA electrolyte reservoir. Bottom right) complete cell with peristaltic pump, PFA/Norprene tubing lines and electrolytes in N<sub>2</sub> glovebox.**

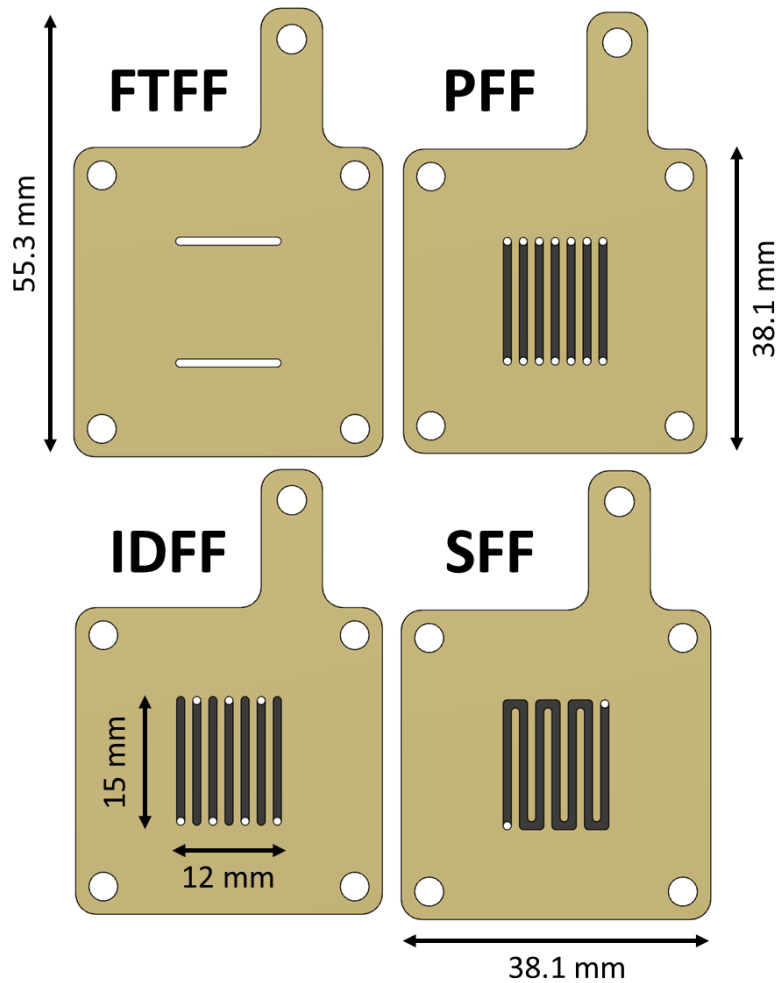


**Figure 25. Schematic illustrations for the FC-II flow-field current collectors with flow-channels highlighted. FTFF = flow through flow-field, PFF = parallel flow-field, IDFF = interdigitated flow-field, SFF = serpentine flow-field. Each flow-channel is 0.5 mm deep and 1 mm wide [40].**

The FC-II flow-cell enables different flow-field patterns (Figure 25) to be used to vary and enhance the electrolyte flow through the 3D porous electrodes. This in principal improves the mass transport through the electrode and decreases the cell resistance by homogenising the current density on the electrode surface [40]. Four different patterns were manufactured and used interchangeably; flow-through (FTFF), parallel (PFF), interdigitated (IDFF) and serpentine (SFF). The flow-through design is the simplest as it forces all of the electrolyte to pass through the porous electrode, whereas the other three provide channels under the electrode to more evenly distribute the electrolyte through the electrode. The parallel flow-

field causes the electrolyte flow to be most linear, however the added turbulence caused by the analogous interdigitated and serpentine flow-fields causes more permeation of the electrolyte into the electrodes, thus giving better overall mass transport according to the literature [206]. In the present work the objective was to study the stability of novel redox materials, thus the optimisation of flow-cell performance was less of a concern given that the flow-cell can cycle the compounds with minimal overpotential at reasonable C-rates. Commonly the FTFF was the flow-field of choice in this research for practical reasons: the FTFF was the easiest to manufacture, it is the least fragile and it is the easiest to clean. In addition, the FTFF is reversible due to its symmetric design, thus giving two faces per component to use in case of damage.

### **3.4 Electrode materials**

The design of the electrodes in any battery technology is critical for achieving high performance, therefore, several design criteria exist for selecting appropriate materials. The electrode material must be stable in the battery electrolyte, inert at all potentials applied, conductive and catalytic towards the redox processes occurring at the electrode surface. In addition, it is often desirable that the electrodes have a very large surface area to maximise current densities, however cost and sustainability are also criteria to consider. In RFBs, graphitic or carbon-based electrodes are most commonly used because graphite is low cost and materials such as felts and papers can be easily manufactured with high surface area. Here carbon-based electrodes were applied in both glass cell and flow-cell experiments.

For battery experiments in glass cells it is crucial to maximise the electrode surface area, however this is challenging because the physical dimensions of the electrode are restricted by the geometry of the cell. Three different electrodes were used for glass cell experiments in this research; high-purity graphite rods (Goodfellow Cambridge Limited, 99.997 %, 5.0 mm diameter), graphite felt (SGL Group, ~6 mm width and 4.0 mm thickness) and high-porosity RVC foam (Duocel, 100 PPI (average pore diameter of  $\approx 0.25$  mm), ~6 mm width and thickness), as

shown in Figure 26. The application of porous electrodes proved challenging due to the difficulties in ensuring a good electrical contact with the electrode piece without allowing the electrolyte to contact the current collector. Specifically, it was found to be unsuitable to use copper wire with the graphite felt electrodes because the NA electrolyte would be absorbed into and drawn up the electrode piece causing the electrolyte to contact the Cu wire during use, thus an alternative metal-free electrode was developed by use of a thin (0.5 mm) graphite composite and shrink-wrap tubing (Figure 26b). In contrast, as RVC foam does not tend to draw up electrolyte, a Cu wire wrapped around the electrode piece is acceptable, however it is challenging to achieve a good electrical connection because the RVC foam is very brittle (Figure 26c).



**Figure 26. Electrodes for use in glass cell battery/electrolysis experiments. a) graphite rod, b) graphite felt and graphite composite contact (SGL Sigracell® PV15), c) high-porosity RVC electrode and Cu wire contact.**

Electrode materials for flow-cells tend to be porous graphite felts, carbon papers or cloths [41,207]. Typically, each material is composed of graphitic fibres with diameters in the range of 5-10  $\mu\text{m}$ , however the materials differ in their macrostructure. Whereas paper-like electrodes such as Toray paper tend to have randomised fibre orientations (non-woven), cloths and felts have more ordered woven structures [41]. In this project, graphite felt (SGL Sigracell® GFD4,6 EA) and carbon paper (A20301 'carbon mat', Technical fibre products) materials were used as electrodes for the FC-I and FC-II cells respectively. Before use the electrode

materials were studied by scanning electron microscopy (SEM) and energy-dispersive X-ray spectroscopy (EDX), to examine their micro- and macrostructure.

The graphite felt electrode was found to consist of a tangled web of long flexible graphitic fibres that have near-random orientations in three dimensions as shown in Figure 27. On large length-scales rope-like domains of parallel running fibres were observed with approximate diameters of  $\sim 300 \mu\text{m}$ . The domains appeared to orientate in all three dimensions, however they are most obvious in Figure 27b in the z-plane, whereby the domains have been cleaved giving a frayed-rope appearance. Each fibre was measured to have a  $\sim 6.5 \mu\text{m}$  diameter and upon close inspection the fibre surfaces are patterned with sub-micron scale longitudinal striations which presumably originate from extrusion of the fibres. In addition, pitting of the surface and crystal-like surface structures were infrequently observed (Figure 27c and d), which based upon the relative conductivity (image brightness) was attributed to metal impurities. Very large voids between individual fibres and domains were observed of approximate size 30-60 and 400-700  $\mu\text{m}$  respectively which indicates the low density of the material and that all the material surface area is accessible to the electrolyte during use. The material was also examined by EDX which showed that the material is 99 % carbon with 1 % oxygen which was attributed to surface oxide groups from prior thermal treatments in air.

In contrast to graphite felt, the carbon paper material was found to be composed of a more random distribution of long inflexible fibres and in addition, a binder substance was observed which coheres the macrostructure, as shown in Figure 28. The fibres were observed to have preferential in-plane orientation (xy plane in Figure 28b) which indicates that the material is manufactured via a layering approach, however within the plane no ordered orientation was observed. The diameter of each fibre was measured to be  $\sim 7 \mu\text{m}$  and upon close inspection, the surface of each fibre had similar longitudinal striations to graphite felt, which again originate from extrusion. Micron-scale metallic particles were also infrequently observed on the fibre surfaces, which were attributed to similar impurities during manufacturing. Smaller pores (void regions) than in graphite felt

were observed between the carbon paper fibres in the range of  $\sim 50\text{-}300\ \mu\text{m}$ , therefore it is evident that the carbon paper is significantly denser than graphite felt.

The binder was observed to be a polymeric material which randomly connected separate fibres with web-like structures (Figure 28c). According to the manufacturer, this binder is composed of polyvinyl alcohol (PVA) plastic, thus the electrode was studied by EDX to confirm the existence of oxygen functional groups in the polymer. As expected, EDX showed that the fibres were composed of exclusively carbon, however inspection of the binder material showed a high abundance of oxygen consistent with PVA (Appendix B).

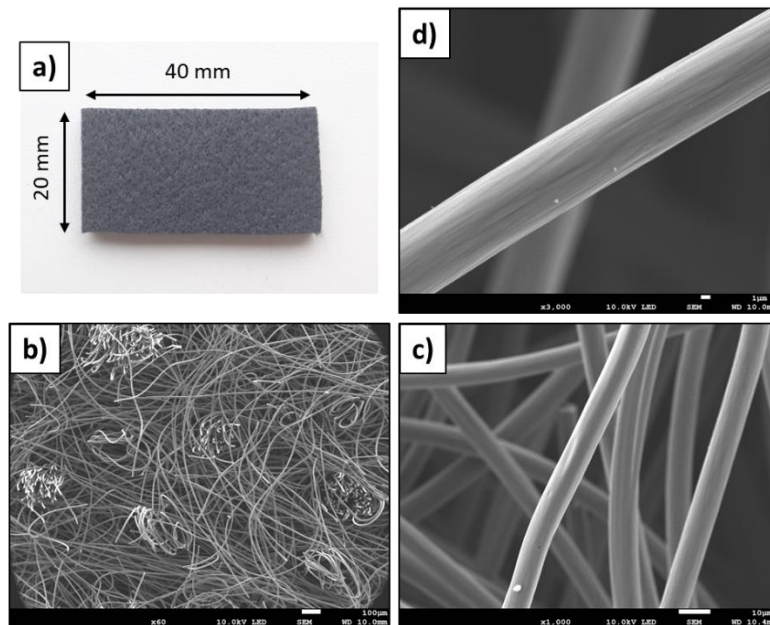


**Figure 27. SEM images of the graphite felt electrode material (SGL Sigracell® GFD 4,6 EA). a) optical photograph of a typical electrode piece (20×40×4 mm dimensions), b) macroscopic structure of the graphite felt (100  $\mu\text{m}$  scale), c) microscopic structure of the fibres (10  $\mu\text{m}$  scale), d) microscopic structure of an individual fibre with  $\sim 6.5\ \mu\text{m}$  diameter and surface impurities.**

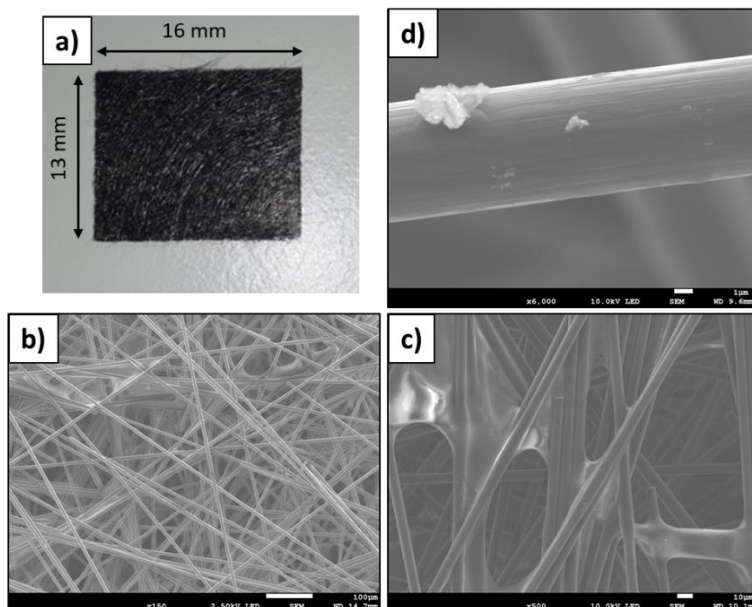


**Figure 28. SEM images of the carbon paper electrode material (20301A, Technical Fibre Products Ltd.). a) optical photograph of a typical electrode piece (13×16×1 mm dimensions), b) macroscopic structure of the carbon paper (100 μm scale), c) microscopic structure of the fibres and binder (10 μm scale), d) microscopic structure of an individual fibre with ~7 μm diameter and metal impurity.**

The electrode materials were also characterised in terms of their hydrophobicity via water-droplet tests. The untreated graphite felt is completely hydrophobic as it does not readily absorb water droplets, however the carbon paper was found to be hydrophilic such that water is immediately absorbed. This difference was attributed to the much higher oxygen content in the carbon paper electrodes resulting from the PVA binder. Droplet tests with MeCN solvent showed immediate absorption into both materials, which suggested that the hydrophobicity of graphite felt does not inhibit lower-polarity solvents such as MeCN. Based on this result, routine thermal treatments of the electrodes, commonly used in aqueous RFB research, were not deemed necessary in this project.

### 3.5 Membranes

The membrane is perhaps the most important component in the RFB design as it must separate the battery electrolytes but also allow the diffusion of ions to

complete the circuit. Thus, highly selective and conductive membrane materials are desirable for application, however at present membranes are only developed for aqueous RFBs. A literature review was conducted to evaluate which membranes are used in NA RFB research, however it was concluded that the issue has been mostly neglected. Infrequently, bespoke membranes have been developed for certain NA chemistries [99], however more commonly the research field has opted to apply commercial aqueous ionic-exchange membranes. Most notably, Nafion® [138,183,208,209] or ionic exchange membranes from Membrane International Inc., USA [136,146,154] or FuMA-Tech [137,155,169] have been applied, however in many studies researchers have opted for non-selective porous separators [51,115,116,175,198,210] such as Celgard [135,157,211] or Daramic [150,156,159,165,179]. In practice, the choice of membrane is less significant than first anticipated because NA RFBs are commonly operated at low concentrations (1-10 mM) where the crossover rates are low. In addition, the research field has actively pursued symmetric electrolytes to mitigate membrane constraints [99,133,138,152,179,209] or developed redox oligomers/polymers which require simple and inexpensive size-exclusion separators [51,115,116,198,210]. Furthermore, in cases where asymmetric batteries have been studied, alternative methods have been used to render the membrane inconsequential, such as using a lithium anode [107,166,187] or using a single mixed electrolyte, which contains both the negolyte and posolyte molecules in both half-cells [150,151] (assuming the posolyte molecule is electrochemically inert at the negolyte potentials and vice-versa), or by independent redox couple cycling [156,160] (0 V cell potential).

At the onset of this project, a small collection of commercial membranes was acquired and characterised for their use in battery studies in 0.1 M TEA BF<sub>4</sub> MeCN electrolyte. In all cases the membranes are not designed for NA electrolyte, except for Celgard which is applied as a physical separator in Li-ion batteries, thus the suitability of each membrane is generally inappropriate (Table 6). However, Nafion, F-930 and FAP-450 showed minimal swelling in the electrolyte (after 30 mins soaking) and once dried they returned to their initial condition without

**Table 6. Properties and application of commercial membranes. Acronyms: (CEM) = cation-exchange membrane, (AEM) = anion-exchange membrane, (PS) = porous separator, (A) = aqueous, (NA) = non-aqueous. (a) the FKE-30 CEM did not return to the original condition after soaking in MeCN electrolyte. Swelling estimated. (b) The FAA-3 AEM swelling was non-measurable due to degradation however the swelling was estimated at 400 %.**

Membrane	Composition	Thickness [ $\mu\text{m}$ ]	Stability in 0.1 M TEA $\text{BF}_4$ MeCN electrolyte (swelling [%])	Intended application
Nafion® 117 (CEM)	Sulfonated tetrafluoroethylene based fluoropolymer-copolymer	117	Excellent. (<10 %)	VRFB and other batteries/fuel cells (A)
fumapem® F-930 (CEM)	Perfluorinated polymer (reinforced)	30	Good. (140 %)	H <sub>2</sub> -PEMFC (A)
fumasep® FKE-30 (CEM)	Unknown (non-reinforced)	30	Poor. Membranes properties are physically degraded. ( $\approx$ 200 %) <sup>(a)</sup>	Electrodialysis /demineralisation /desalination (A)
Fumasep® FAA-3 (AEM)	Unknown (non-reinforced)	50	Very poor. Membrane disintegrates. ( $\approx$ 400 %) <sup>(b)</sup>	Electrodialysis /demineralisation /desalination (A)
fumasep® FAP-450 (AEM)	Fluorinated polymer (non-reinforced)	50	Good. (138 %)	Acidic RFBs (A)
Celgard® 2500 (PS)	Polypropylene	25	Superb. (<1 %)	Li-ion battery separator (NA)

visible degradation. The stability of these materials was attributed to their fluorinated or reinforced scaffold which is resistant to non-polar solvents. In contrast, the non-battery membranes FKE-30 and FAA-3 degraded after a short time and are unusable in organic electrolyte, which was attributed to the lack of a robust reinforcing polymer scaffold. It is challenging to explore the chemistry of the commercial membranes because their composition is not provided by the manufacturer, however based on their stability, the F-930 and FAP-450 ionic exchange membranes were adopted for battery experiments. In addition, for symmetric RFB experiments at low concentrations, the non-selective Celgard separator was found to be adequate because membrane crossover only results in a loss of coulombic efficiency and typically crossover rates are slow. The use of Nafion was generally avoided because of high cost.

### 3.6 Peristaltic pump calibrations

Conventional peristaltic pumps were used for pumping the electrolyte through the FC-I and II flow-cells. For accuracy in the flow-rates used, the peristaltic pumps were calibrated by measuring the time taken to dispense 25 mL of pure MeCN as a function of rpm. As shown in Figure 29, strongly correlating linear relationships ( $R^2 > 0.998$ ) were achieved and used thereafter to set specific flow-rates with the FC-II flow-cell. The flow-rate of  $60 \text{ mL min}^{-1}$  used in the FC-I flow-cell in Chapter 5 was calibrated by iterative measurements until the correct rpm was found. Given that the flow-rate is dependent on the solution physical properties such as viscosity and temperature, pure MeCN was used for calibrations under the assumption that the viscosity of MeCN-based battery electrolytes can be approximated by pure MeCN. For the compact analogue pump, the numbers on the dial were used for calibrating, however the flow-rate was found to linearly scale with the dial settings, allowing flow-rates to be set with reasonable accuracy.

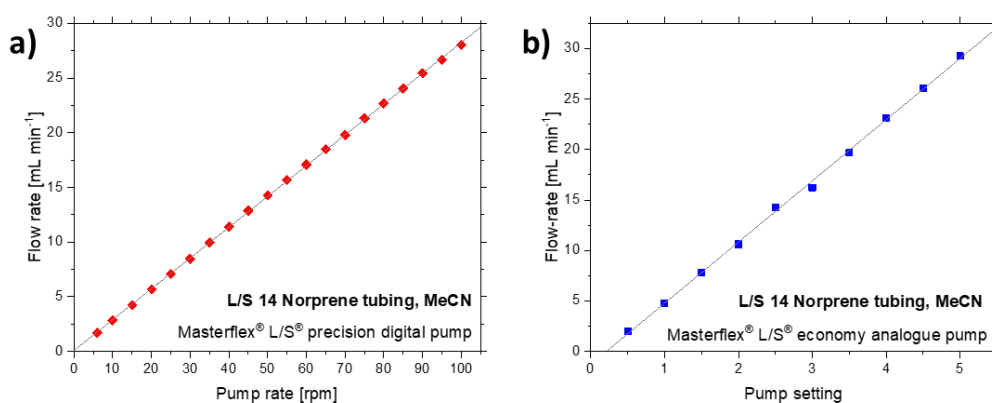


**Figure 29. Pump calibrations for the flow-rate as a function of rpm for the a) digital and b) analogue Masterflex® peristaltic pumps used. L/S 14 Norprene tubing with pure MeCN. Each datapoint represented the mean flow-rate, averaged over three measurements.**

### 3.7 Conclusions

To summarise, a series of small-volume electrochemical cells were developed for conducting battery and bulk electrolysis experiments of novel redox materials. The glass H-type cells are suitable for low-concentration experiments and

fundamental studies which require additional electrodes or electrolyte sampling. Their performance is limited by high ohmic resistances and inferior mass transport which results in high battery overpotentials and limited current densities (low C-rates). In contrast, the FC-II flow-cell gives exceptional battery performance because the cell is engineered towards optimising the power density by decreasing the cell resistance. Therefore, high rates of electrolyte conversion are possible which minimises experimental timescales and allows experiments to be conducted at much higher concentrations [97,159]. To quantify the performance of the cell designs, the Fc/FcBF<sub>4</sub> redox couple was adopted as a model chemistry. The results of this study are reported in Chapter 4.

# Chapter 4

## Ferrocene as a Model Chemistry for Cell Characterisation

### 4.1 Introduction

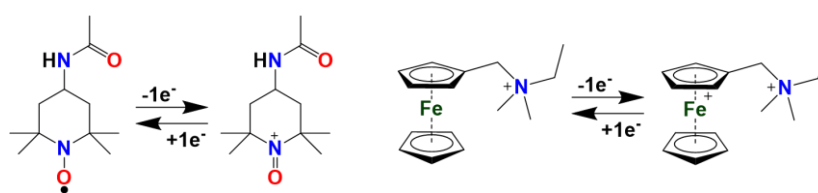
Flow-cell designs for aqueous RFBs have been extensively studied, yet comparable advancements have not been achieved for NA RFBs, despite the plethora of studied novel redox materials. Although model chemistries have been fully characterised for aqueous RFBs, such as the  $V^{2+}/V^{3+}$  and  $VO^{2+}/VO_2^+$  redox couples, notably few NA RFB chemistries have been fully characterised or proposed as standard redox couples for flow-cell characterisation studies. Therefore, there is growing need for robust NA redox couples to be characterised and widely adopted for comparing and validating NA flow-cell designs. Perhaps due to these reasons, capacity loss mechanisms of novel systems are infrequently presented in the literature because it is difficult to discern poor performance of the chemistry from the inherent performance of the flow-cell design. Furthermore, it is often difficult to deconvolute full-cell cycling data into the contributions from physical or chemical processes such as membrane crossover or parasitic reactions, respectively. This is highlighted by the vanadium tris-acetylacetonate ( $V(acac)_3$ ) system, first proposed by Liu et al. in 2009 [129] which is perhaps the most studied NA RFB system to date due to its 2.2 V cell potential and relatively high  $\approx 1$  M solubility in MeCN [69,104,111–113,120,129,212]. Although this compound has featured in at least 11 publications [69,104,213,111–113,120,129,133,211,212] in various electrolyte conditions, the battery performance of the material has shown significant variation between studies and frequently poor charge-discharge

performance was reported; unsymmetrical charge-discharge curves with extreme potential thresholds ( $0 \text{ V} \geq V_{\text{cell}} \geq 4.5 \text{ V}$  [129]) [104,112,120,129], rapid capacity loss and at best 90 % coulombic efficiency [69]. In addition  $\text{V}(\text{acac})_3$  is not a good model chemistry as degradation has been identified via reactivity towards oxygen and water to produce vanadyl acetylacetonate and free acetylacetone [120]; products which are also redox active and cause multiple charge/discharge plateaus during cycling [120,129]. Furthermore, commercial  $\text{V}(\text{acac})_3$  from some suppliers must be purified before use as  $\text{VO}(\text{acac})_2$  is a significant impurity. It is therefore evident that more robust alternative redox couples are needed.

An ideal model chemistry would fulfil several criteria; synthetically accessible and stable oxidation states, reasonably high solubility, significant potential separation of the redox couples from the onset of solvent decomposition, fast redox kinetics, high diffusion coefficients and ease of use (low toxicity, desirable physical and chemical properties). To date only two redox couples have been proposed as model chemistries for NA RFB research; 4-acetamido-2,2,6,6-tetramethylpiperidine-1-oxyl (AcNH-TEMPO) and N-(ferrocenylmethyl)-N,N-dimethyl-N-ethylammonium bis(trifluoromethane)sulfonimide ([Fc1N112](TFSI)). Proposed by Milshtein et al. in 2016 [159] and 2017 [97] respectively (Scheme 3). In the case of AcNH-TEMPO the redox couple was used for charge-discharge studies in independent redox couple experiments (0 V cell potential) over relatively short timescales (25 cycles) and in cell characterisation studies via single electrolyte experiments (PC solvent) [159]. In contrast, the Fc1N112<sup>+</sup> model redox couple was only used for cell characterisation in single electrolyte experiments to study the origins of cell resistances as a function of electrolyte conductivity (MeCN vs PC) and electrode/membrane configurations [97]. It was postulated by the authors that ferrocene (Fc) was a suitable redox couple to apply as a model chemistry for flow-cell validation, however the low solubility was undesirable [159]. Thus, a more soluble derivative Fc1N112<sup>+</sup> was developed and used at concentrations up to 1 M. Despite this, the authors did not assess the stability of Fc1N112<sup>+</sup> via charge-discharge experiments or fully characterise the material in terms of redox kinetics, diffusion coefficients or the solubility of each oxidation

state. Some battery cycling of  $\text{Fc1N112}^+$  was conducted in Li coin cells by other workers [145], however the results of this study were very limited.

Surprisingly, the Fc redox couple has not yet been fully characterised despite being applied in a NA RFB [205] as well as its derivatives [97,138,145,214]. Herein the simple and highly studied ferrocene/ferrocenium ion redox couple ( $\text{Fc}/\text{FcBF}_4$ ) was examined as a model chemistry for NA RFB research and its properties were characterised in terms of battery performance and stability for flow-cell validation purposes.



**Scheme 3. Chemical structures and redox transitions of left) AcNH-TEMPO [159] and right)  $\text{Fc1N112}^+$  [97] model redox couples.**

Fc is an organometallic compound, consisting of an Fe(II) core coordinated to two cyclopentadienyl ligands, which undergoes reversible oxidation to the stable  $\text{Fc}^+$  ion. The oxidation  $\text{Fc}$  to  $\text{FcBF}_4$  is a classical and well understood reversible one-electron redox process which involves the removal of an electron from the incredibly stable  $18e\ d^6$  Fe(II) electron configuration to the  $17e\ d^5$  Fe(III) species [215]. The kinetics of this process are known to be fast because the Fc and  $\text{Fc}^+$  geometries are almost identical (an Fe-C bond lengthening of  $0.1\ \text{\AA}$  occurs upon oxidation [215]), thus making Fc a promising redox couple for energy storage devices. In addition, as Fc is soluble in various organic solvents and its electrochemistry is mostly unaffected by variations in solvation [196]. As such, Fc displays several characteristics desirable for a model chemistry; usability in different solvents, high stability, low molecular weight, low toxicity and desirably low cost. Furthermore,  $\text{FcBF}_4$  is a commercially available product, however here a simple and inexpensive one-step synthetic method for its preparation is used.

## 4.2 Experimental

### 4.2.1 Chemicals and materials

TEA BF<sub>4</sub>, (Alfa Aesar 99 %), para-benzoquinone (*p*-BQ, Acros Organics 99 %), tetrafluoroboric acid solution (HBF<sub>4</sub>, Alfa Aesar ca 50 % w/w aq. Soln.), diethyl ether (Et<sub>2</sub>O, Fisher reagent grade) and MeCN (Acros Organics 99.9 % Extra Dry over molecular sieves, Acroseal®) were purchased and used as received. Fc (98 %, Sigma Aldrich) was purified by vacuum sublimation to remove the major impurity cyclopentadiene prior to usage. All other compounds were used without purification.

### 4.2.2 Ferrocenium tetrafluoroborate synthesis

FcBF<sub>4</sub> used in this work was synthesised as per literature procedures [216]. In a typical procedure, pre-purified Fc (1.01 g, 5.43 mmol) was dissolved in 30 ml Et<sub>2</sub>O and added dropwise to a 60 ml Et<sub>2</sub>O solution of *p*-BQ (1.17 g, 10.86 mmol) and HBF<sub>4</sub> 50 % acid solution (3.82 g, 21.72 mmol). The resulting dark blue precipitate was filtered by Buchner filtration under vacuum and washed with 100 ml of Et<sub>2</sub>O. The dark blue FcBF<sub>4</sub> powder was then dried under high vacuum at 60 °C and flushed with argon for storage, (1.36 g, 4.99 mmol, 91.8 %). <sup>1</sup>H NMR (CH<sub>3</sub>CN, 400 MHz): δ = 33.80 ppm. Anal calcd. for FeC<sub>10</sub>H<sub>10</sub>: C 43.97, H 3.69 %; found: C 42.98, H 3.58 %.

### 4.2.3 UV-vis and solubility measurements

The spectra of Fc and FcBF<sub>4</sub> solutions in MeCN solvent were recorded at an Agilent Cary 60 spectrophotometer using either a 1 or 10 mm path length anaerobic cuvettes (Starna scientific). The solubilities of sublimed Fc and synthesised FcBF<sub>4</sub> were measured by a UV-vis method by first acquiring calibration spectra of Fc and FcBF<sub>4</sub> at 0.2, 0.4, 0.6, 0.8 and 1.0 mM concentrations in MeCN that were prepared by series dilutions of 1 mM solutions in 50 mL volumetric flasks. Beer-Lambert calibration plots were then produced based upon the absorbance of Fc ( $\lambda_{\max}$  = 325 and 440 nm) and FcBF<sub>4</sub> ( $\lambda_{\max}$  = 616 nm) at UV-vis peaks. A saturated solution of each oxidation state was then prepared by making a

suspension of 1 g of solid in a small quantity of MeCN (5 mL for Fc and 2 mL for FcBF<sub>4</sub>) and stirring/sonicating. The solutions were then allowed to settle for at least 30 mins and then precisely 0.5 mL of each solution was collected, and series diluted into the calibration range. UV-vis decomposition studies were conducted by preparing 1 or 0.9 mM solutions of Fc and FcBF<sub>4</sub> in MeCN and then taking spectra every 24 h for up to 11 days. The cuvettes were stored in a N<sub>2</sub> glovebox between spectra to ensure anaerobic conditions. All manipulations of the FcBF<sub>4</sub> solutions were performed in a N<sub>2</sub> glovebox and spectra were recorded within 1 hour of preparing solutions.

#### 4.2.4 Electrolyte preparation

All experiments were conducted on non-aqueous electrolytes composed of Fc and/or FcBF<sub>4</sub> redox material and TEA BF<sub>4</sub> as supporting electrolyte salt. Electrolytes used for voltammetry contained either 10 mM of Fc or FcBF<sub>4</sub> whereas battery cycling experiments utilised a single electrolyte in both half-cells containing 5 mM of both Fc and FcBF<sub>4</sub>. Supporting electrolyte concentration was kept at a constant 0.1 M for all experiments. To generate dry electrolyte, solutions were prepared within a nitrogen glovebox (O<sub>2</sub> and H<sub>2</sub>O ≤ 1 ppm) using anhydrous solvents and vacuum dried compounds. Sublimation-purified Fc was used for all experiments and flushed with nitrogen before use. The hygroscopic TEA BF<sub>4</sub> salt was dried in a vacuum oven at 100 °C for at least 1 day before use. All manipulations of the air-sensitive FcBF<sub>4</sub> species in solution were conducted under anaerobic conditions.

#### 4.2.5 Voltammetry techniques

Cyclic voltammograms were recorded at a glassy carbon (GC) WE (3 mm diameter, BASinc) using a standard 20 ml three-electrode voltammetry cell (BASinc). Rotating disk electrode linear sweep voltammograms were conducted using an RRDE-3A apparatus (ALS Co.), 60 ml voltammetry cell and a 3 mm GC WE (ALS Co.). A platinum wire (BASinc) served as a counter electrode whereas a silver wire in a CoralPor-fritted glass tube (BASinc) containing supporting electrolyte (0.1 M TEA BF<sub>4</sub>) served as a quasi-reference. All experiments on Fc electrolytes

were conducted under a blanket of sparging argon gas and data was recorded using either an EmStat<sup>3+</sup> (Palmsens) or PGSTAT204 (Metrohm). Electrode potentials are reported versus the Fc/FcBF<sub>4</sub> redox couple. Voltammetry of FcBF<sub>4</sub> containing electrolytes was performed inside a N<sub>2</sub> glovebox, including RDE studies.

#### 4.2.6 Battery methods

The FC-II flow-cell (Chapter 3, Figure 24) with FTFFs was employed for flow-cell experiments [40]. A single 1 mm thick piece of carbon paper (Technical fibre products Ltd. 20301A, PVA binder) served as the electrode material whereas a single piece of separator (Celgard<sup>®</sup> 2500; 25  $\mu$ m porous monolayer, 55 % porosity) served as the membrane. The electrolyte was composed of 5 mM Fc and 5 mM FcBF<sub>4</sub> in 0.1 M TEA BF<sub>4</sub>, MeCN/PC. Polarization curves and EIS data were recorded with the flow-cell assembled in a single electrolyte configuration with 10 mL of electrolyte at 50 % state-of-charge at different flow rates. EIS was conducted at the 0 V cell potential with a 10 mV amplitude from 200 kHz to 5 mHz. Charge-discharge studies were performed with the cell in an independent redox couple configuration which was pumped at a flow rate of 10 ml min<sup>-1</sup>.

Experiments in glass cells was performed using GC-II for EIS studies and GC-III for charge-discharge studies, (Chapter 3, Figure 1b and cii respectively). In both cases the electrolytes were composed of 5 mM Fc and 5 mM FcBF<sub>4</sub> in 0.1 M TEA BF<sub>4</sub>, MeCN. EIS was performed as a function of electrode separation and membrane configuration using 4 mL electrolyte per half-cell without stirring. A GC macroelectrode (3 mm diameter) was inserted into each half-cell laterally such that the electrode surfaces opposed each other directly. EIS was then conducted at the 0 V cell potential with a 10 mV amplitude from 2 MHz to 1 Hz. Charge-discharge studies were performed using 5 mL of electrolyte per half-cell with stirring. A high-porosity glass frit served as the separator whereas either graphite rods or RVC foam served as the electrodes (Figure 26a and c respectively).

Galvanostatic and potentiostatic experiments were recorded using either a PGSTAT204 (Metrohm) or Compactstat (IVIUM) with a maximum temporal resolution of 2 s. For polarization studies, a chronoamperometry method was used

with 300 s potential holds in 50/100 mV increments from 0 to 1 V. The current and potential responses were then averaged across each 300 s step to give single I-V datapoints as a function of flow-rate.

## 4.3 Results and Discussion

### 4.3.1 Characterisation of the Fc/FcBF<sub>4</sub> redox couple

The synthesis of FcBF<sub>4</sub> from Fc and p-BQ in the presence of HBF<sub>4</sub> was found to give a highly pure product with a high yield of 91.8 %. The product was found to be an air- and light-stable dark blue powder that could be stored for several months without observed decomposition [216]. By elemental analysis it was suspected that the product was wet with trace amounts of water (FcBF<sub>4</sub>•¼H<sub>2</sub>O) which presumably originated from the HBF<sub>4</sub> aqueous reagent. It is likely that the ionic FcBF<sub>4</sub> salt is hygroscopic, therefore the powder was stored in a vacuum desiccator when not in use. Efforts to further dry the product in a vacuum oven at ≥70 °C resulted in an observed decomposition of the powder (a darkening of the powder and a loss of the blue colour), thus the product was dried under vacuum for at least one day at more ambient temperatures (25-40 °C) before use.

The solubility of each oxidation state was measured by use of UV-vis Beer-Lambert calibrations (Appendix C). The solubility limit of Fc and FcBF<sub>4</sub> in pure MeCN is 0.16 and 1.20 M respectively, therefore the neutral Fc oxidation state is an order of magnitude less soluble than the ionic FcBF<sub>4</sub> due to its lower polarity. The low solubility of Fc therefore limits the battery application to concentrations of up to 0.16 M, assuming the supporting electrolyte does not lower the Fc solubility. In the present work, flow-cell validation using the Fc/FcBF<sub>4</sub> redox couple was performed up to concentrations of 10 mM Fc, thus the Fc solubility is sufficiently high for battery testing at dilute concentrations.

To investigate the fundamental electrochemical properties of the Fc/FcBF<sub>4</sub> redox couple, voltammetry methods on Fc were performed. As shown in Figure 30a, cyclic voltammetry of 10 mM Fc gives symmetrical diffusion-limited peaks indicative of a one-electron reversible solution-phase redox couple. Also shown in

Figure 30a is the blank electrolyte voltammogram which shows that the Fc/FcBF<sub>4</sub> redox couple resides roughly central in the electrolyte stability region. Given that the Fc redox potential is  $\approx 1.5$  V lower than the observed onset of the electrolyte decomposition, the Fc/FcBF<sub>4</sub> single redox couple battery can be cycled with large upper and lower battery thresholds of  $\pm 1$  V without incurring unwanted decomposition of the supporting electrolyte. The Fc electrolyte was found to be electrochemically inert at cathodic potentials (in the range of -3 to 0 V vs Fc), but a second oxidation process was observed at approx. 1.5 V vs Fc (Figure 30b) which is attributed to the irreversible oxidation of Fc<sup>+</sup> to the unstable dication species [217]. The decomposition of this species affects the reversibility of the Fc/FcBF<sub>4</sub> redox couple such that the Fc<sup>+</sup> back-reduction peak becomes increasingly broad and shifted negatively, whereas the forward Fc oxidation peak remained unaffected. This behaviour was attributed to electrode fouling, which grew with successive voltammetry scans, severely decreasing the kinetics of the Fc<sup>+</sup> reduction. During battery operation the cell potential was restricted to  $\pm 1$  V to exclude the dication formation. To check that the Fc/FcBF<sub>4</sub> redox couple does not form an electrode film and affect its own redox kinetics, 100 consecutive CV scans were conducted in a narrow -0.4 to 0.4 V vs Fc potential region. Figure 30c shows that the electrode surface was indeed unaffected and in addition, the FcBF<sub>4</sub> species within the diffusion layer appears stable for long periods of time.

The Fc/FcBF<sub>4</sub> redox couple was studied as a function of scan-rate in the range of 0.01 to 1 V s<sup>-1</sup> as shown in Figure 31a. Peak analysis showed that the Fc/FcBF<sub>4</sub> redox couple has a relatively large peak separation of 100 mV at 0.01 V s<sup>-1</sup> which increased with scan-rate to 330 mV at 1 V s<sup>-1</sup> (Figure 31b). Despite the high peak separations, the Fc/FcBF<sub>4</sub> redox couple gave peak current ratios close to unity (0.98 to 1.08) which suggested high stability of the FcBF<sub>4</sub> oxidation state. Thus, the Fc/FcBF<sub>4</sub> redox couple is characterised as a quasi-reversible redox process such that the mass transport coefficient of the redox couple is comparable in magnitude to the standard electrochemical rate constant. To investigate this, the peak current

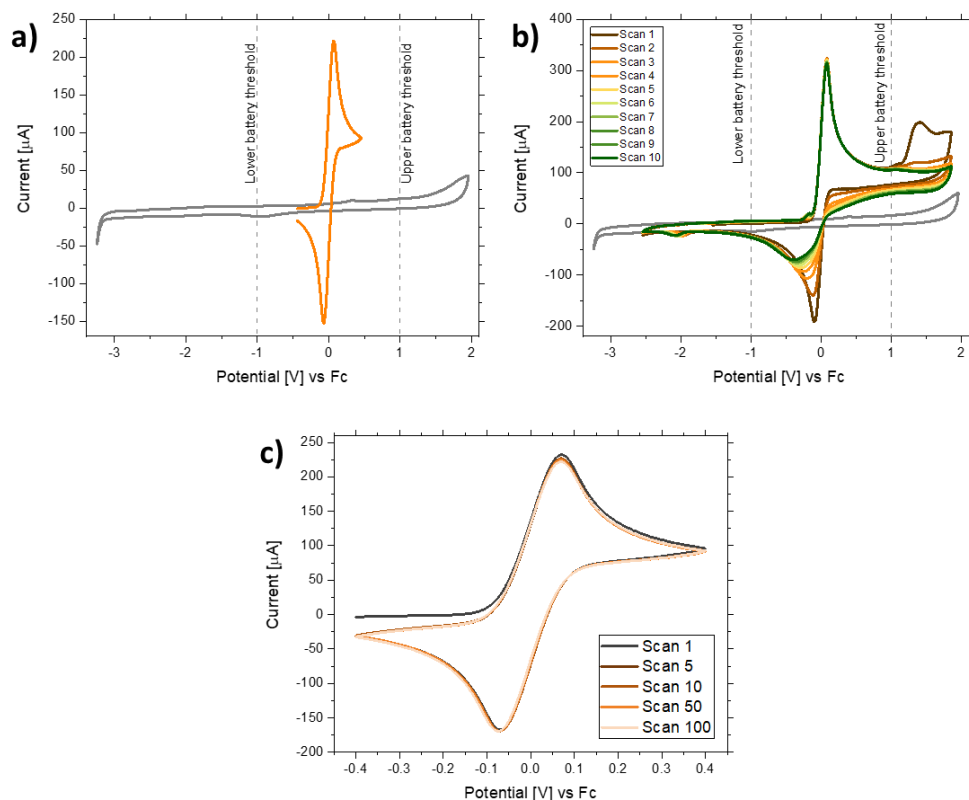


**Figure 30. Cyclic voltammetry of 10 mM Fc in 0.1 M TEA BF<sub>4</sub>, MeCN. Blank voltammetry of the supporting electrolyte is given in grey and vertical dashed lines represent the upper and lower battery potential thresholds at  $\pm 1$  V. a) Fc redox potential in comparison to the supporting electrolyte. ( $50 \text{ mV s}^{-1}$ ). b) CV of Fc in a wider potential range. 10 scans shown ( $100 \text{ mV s}^{-1}$ ). c) CVs as a function of scan number up to 100 scans.**

was analysed by Randles-Sevcik analysis at slow scan-rates ( $\leq 100 \text{ mV s}^{-1}$ ) to give linear dependencies on the square root of scan-rate, with intercepts of less than  $2.7 \times 10^{-6} \text{ A}$  (Figure 31b and c). The corresponding diffusion coefficient for the oxidation of Fc was calculated as  $2.10 \times 10^{-5} \text{ cm}^2 \text{ s}^{-1}$ , assuming that the Randles-Sevcik equation ( 2.3.3 ) is valid. The redox couple was then characterised by Koutecký-Levich analysis as shown in Figure 32 to attain kinetic information. LSVs as a function of rotation rate gave limiting current plateaus at overpotentials of  $\geq 100 \text{ mV}$ , however above  $400 \text{ mV}$  overpotential, the plateaus showed increasing currents characteristic of a background current. The analysis in the region of 0 to  $300 \text{ mV}$  overpotential gave well defined linear relationships of the inverse current against the inverse square-root of rotation rate. A corresponding standard electrochemical rate constant of  $2.40 \times 10^{-2} \text{ cm s}^{-1}$  and transfer coefficient of 0.63

were calculated indicating fast electrochemical kinetics of the Fc/FcBF<sub>4</sub> redox couple.

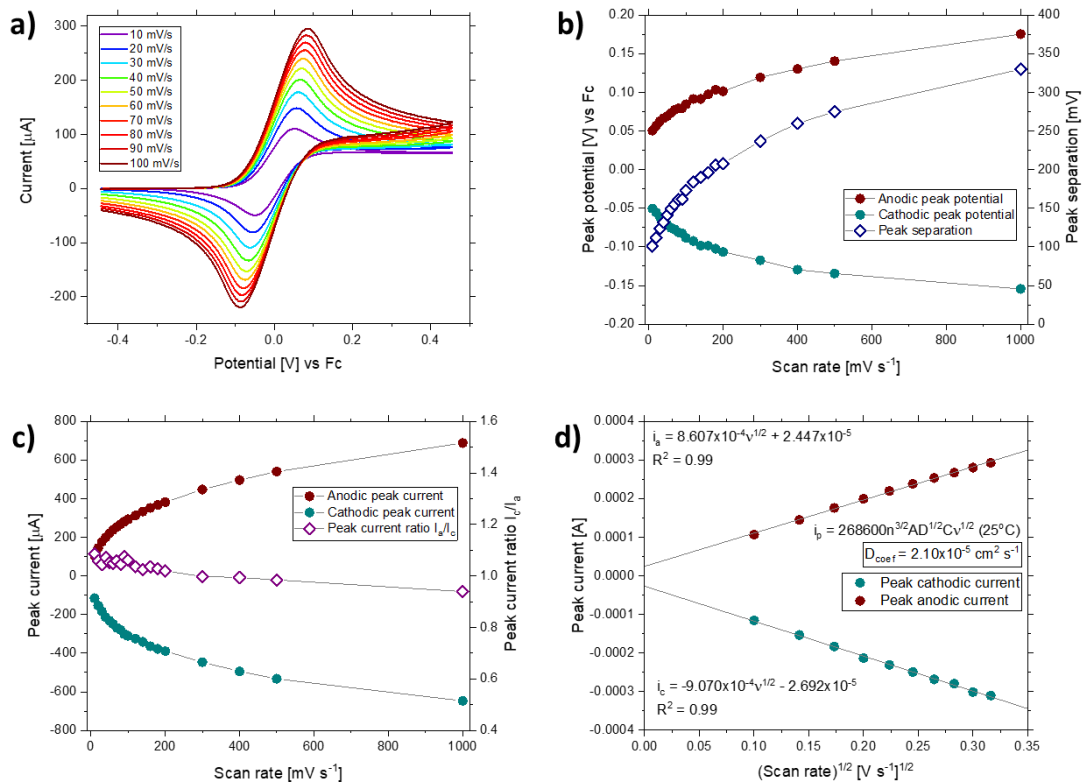


**Figure 31. a) CVs as a function of scan-rate in the range of 10 to 100 mV s<sup>-1</sup> of 10 mM Fc. First scans shown. b) Peak potentials and separations for the Fc/FcBF<sub>4</sub> redox couple. c) Peak currents and current ratios ( $I_c/I_a$ ). d) Randles-Sevcik analysis for the forward Fc oxidation. The peak analysis for the back FcBF<sub>4</sub> is also given.**

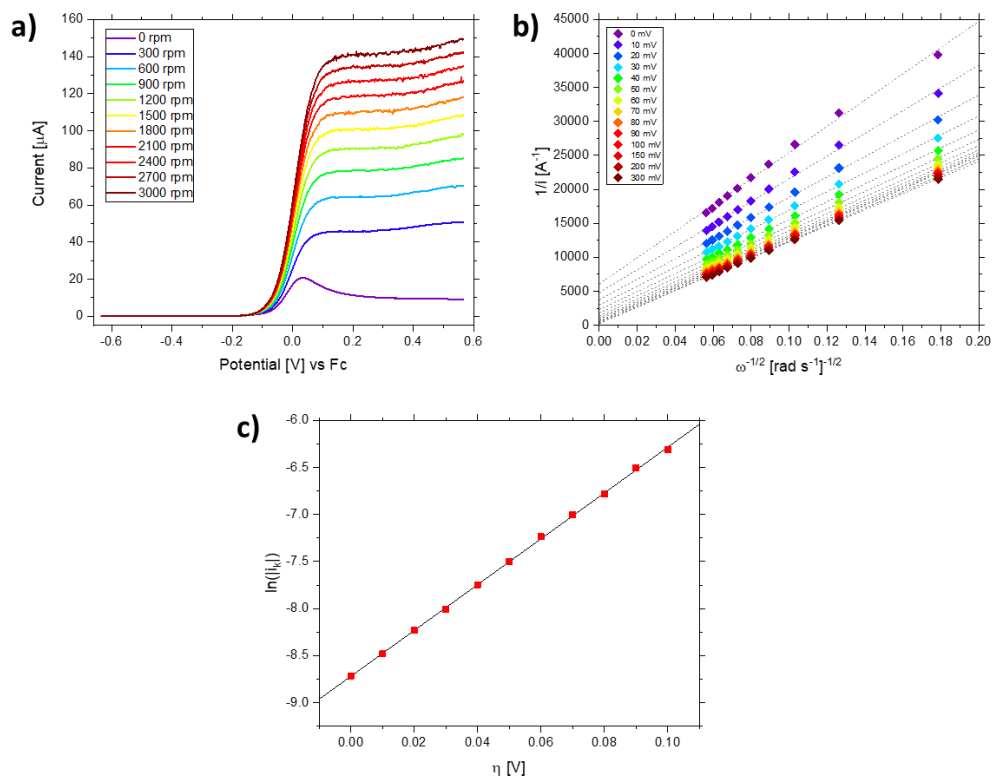


**Figure 32.** Koutecký-Levich analysis of 1 mM Fc in 0.1 M TEA BF<sub>4</sub>, MeCN electrolyte. a) RDE LSVs as a function of rotation rate. b) Koutecký-Levich plots as a function of overpotential. c) plot of the logarithm of the kinetically limited current against overpotential.

### 4.3.2 Cell characterisation by use of the Fc/FcBF<sub>4</sub> chemistry

#### 4.3.2.1 Flow-cell

By use of the Fc/FcBF<sub>4</sub> redox couple, cell level phenomena can be studied to quantify the flow-cell performance without requiring a reference electrode because similar processes occur at both electrodes. Here the cell is assembled in a single-electrolyte configuration, whereby the flow-cell is connected to a single electrolyte reservoir (Figure 21) at 50 % SOC. This methodology means that the effects of physical processes such as membrane crossover, that ordinarily affect the electrolyte composition, are nullified because the overall electrolyte concentration of Fc and FcBF<sub>4</sub> are always constant. Therefore, cell-level polarization and EIS can be conducted at steady-state giving reliable measurements of cell resistances and IV-characteristics [97]. Thus, the effects of flow-rate and differences in electrode/membrane configurations can be studied to

optimise the flow-cell towards minimising cell resistances [97]. In addition, when the conversion through the cell is low, this technique accurately mimics a full RFB at 50 % SOC and therefore the polarization curves can be used to predict appropriate current densities for efficient battery cycling in full-cell experiments. Here, a battery electrolyte concentration of 5 mM Fc/FcBF<sub>4</sub> was chosen to model the other flow-cell experiments in this thesis, which were typically operated at 1 mM concentration. Thus, the flow-cell performance of the Fc/FcBF<sub>4</sub> redox couple can be directly compared to novel chemistries.

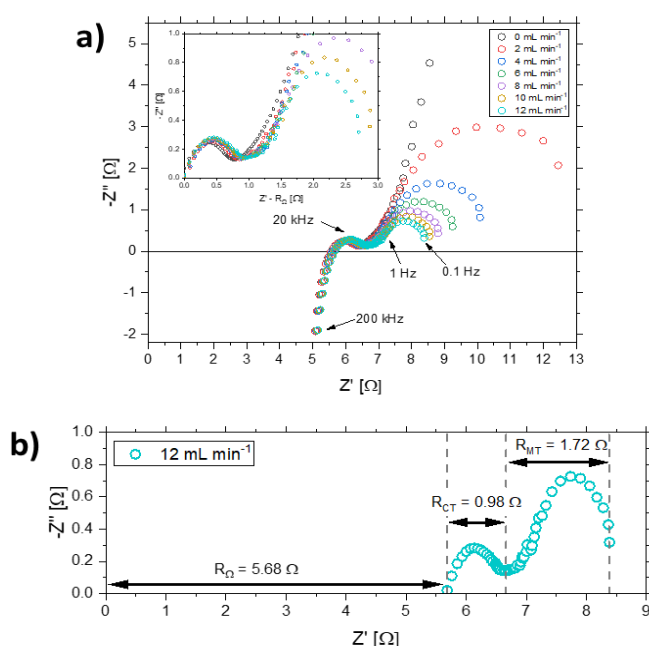


**Figure 33. Electrochemical impedance of the FC-II flow-cell. a) EIS as a function of flow-rate. b) analysis of the EIS spectrum of the flow-cell at 12 mL min<sup>-1</sup>. The ohmic resistance (R<sub>Ω</sub>), charge-transfer resistance (R<sub>CT</sub>) and mass transport resistance (R<sub>MT</sub>) are shown.**

The EIS Nyquist plots of the FC-II flow-cell as a function of flow-rate are shown in Figure 33. Considering the EIS waveform, for each flow-rate two semicircles and a Z' intercept is observed. Whereas the diameter of the first semicircle is invariant with flow-rate, the second decreases in size as flow-rate increases and can be attributed to mass-transport. Therefore, the EIS data can be rationalised as the sum of ohmic, charge-transfer and mass-transfer resistances, corresponding to the x-intercept, semicircle one and two. Analysis of the EIS data (Figure 33b) gives an

ohmic resistance of  $5.68 \Omega$  ( $11.81 \Omega \text{ cm}^2$ ), whereas the charge-transfer resistance was estimated at  $0.98 \Omega$  ( $2.04 \Omega \text{ cm}^2$ ) by measuring the diameter of the first semicircle. The large ohmic resistance was attributed to the low electrolyte conductivity and membrane resistance, however the ohmic resistance here is reasonable given that the supporting electrolyte concentration is only 0.1 M. For comparison, a  $R_{\Omega}$  of  $\approx 2 \Omega \text{ cm}^2$  was reported by Milshtein et al [97] for a flow-cell utilising a Daramic separator and 1 M Fc1N112<sup>+</sup>, 0.5 M TEA TFSI, MeCN electrolyte. In comparison, the charge-transfer resistance is a much smaller contributor to the cell resistance than ohmic, because of the fast kinetics of the Fc/FcBF<sub>4</sub> redox couple. As noted by others too, in stark contrast to aqueous RFBs where the redox kinetics dominate the cell resistance, here it is the ohmic resistance which dominates the cell resistance in NA RFBs [97].

The polarization curves in Figure 34a give the cell potential as a function of current density for various flow-rates, allowing the cell resistance to be interpreted under different operating conditions. For each curve a linear relationship at low overpotentials is observed which gives a resistance equivalent to the flow-cell ASR of  $21.16 \Omega \text{ cm}^2$  [159]. This gradient was observed to decrease slightly as the flow-rate increased which indicates that the cell ASR decreases due to enhanced reactant transport to the porous electrodes. At high overpotentials the polarization curves become vertical indicating significant increases in cell resistance. This behaviour can be rationalised as the point where the flow-cell depletes the redox species via full conversion, thus starving the flow-cell of reactants and giving a maximum current density. However as shown by the faster flow-rates in Figure 34a, full conversion occurs at higher cell potentials as the flow-rate increases, thus allowing the cell to achieve higher current densities. The data clearly shows that it is advantageous to increase the flow-rate to attain higher power densities. As observed by Milshtein et al. [97], this has a diminishing rate of return because the power density approaches a maximum as flow-rate is increased, as shown in Figure 34b.

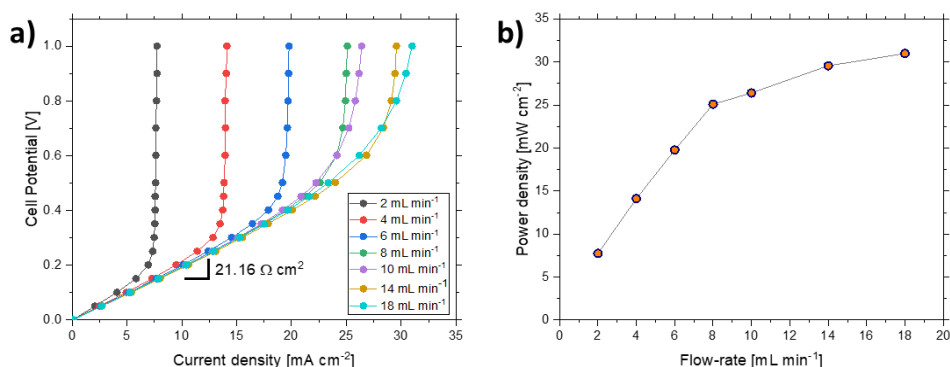


**Figure 34. a) Polarization curves as a function of flow-rate for the FC-II flow-cell. B) Maximum power density (at 1 V cell potential) as a function of flow-rate.**

Based on the polarization data, a flow-rate of 10 mL min<sup>-1</sup> was adopted as the default flow-rate for battery experiments in this thesis because it corresponds to the complete circulation of the 10 mL battery electrolyte every minute, and because 10 mL min<sup>-1</sup> is a reasonable compromise between cell performance and reliability. At higher flow-rates, the leakage rate from the flow-cell is accelerated due to increased electrolyte pressure on the flow-cell seals and gaskets. Furthermore, higher pumping rates cause faster wear of the peristaltic pump tubing.

#### 4.3.2.2 Glass cells

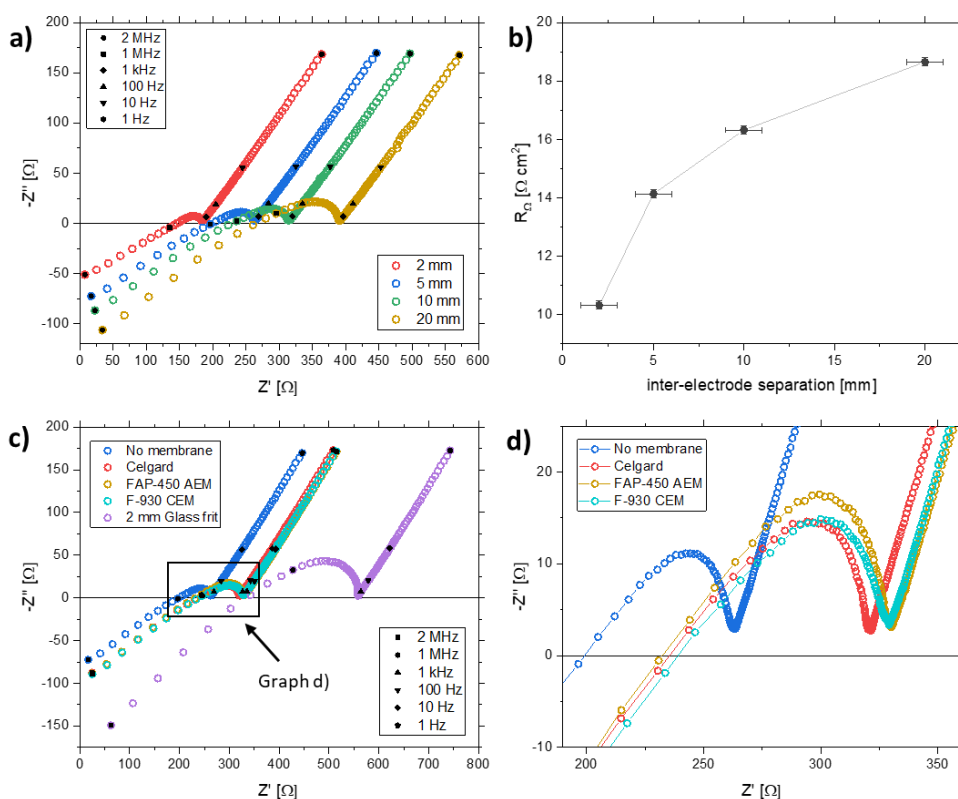
For comparison to the FC-II flow-cell, EIS was performed on the GC-II glass cell to quantify the ohmic resistance. Relatively larger ohmic resistances are expected in glass cell experiments because the inter-electrode separation is much larger than in zero-gap flow-cells.

Figure 35a shows the effect of varying the electrode separation on the cell resistance when no membrane is present. As shown, the measured ohmic resistance (x-axis intercept) increases with electrode separation due to the increasing solution resistance. Typically, this solution resistance will increase linearly with electrode separation as given by

$$\rho = \frac{RA}{l} \quad (4.3.1)$$

where  $\rho$  is the resistivity, however here the dependence was non-linear (Figure 35b). This unexpected behaviour was attributed to the difficulty in measuring  $R_{\Omega}$  because the EIS data does not conform to conventional equivalent circuits. As shown, the data shows linearity at high frequencies and the observed semi-circle diameter increased with distance. Given that the electrode area and electrolyte concentrations were controlled, it is unlikely that  $R_{CT}$  increases at larger electrode separations and therefore the observed semi-circle most likely has additional resistance contributions. To confirm the validity of this argument, the  $R_{CT}$  was estimated from the semi-circle diameter of the 2 mm EIS in Figure 35a, and was found to be  $\sim 2.7 \Omega \text{ cm}^2$ , which is comparable to the FC-II. Regardless, the data shows that large electrode separations cause considerable solution resistance and therefore increased ohmic resistance. At 20 mm the ohmic resistance is  $\sim 18.5 \Omega \text{ cm}^2$  which far exceeds the FC-II ohmic resistance, despite no membrane being present in Figure 35a.

To quantify the membrane contribution on the ohmic resistance, EIS of the cell with different separators was recorded as shown in Figure 35c. In each case the ohmic resistance was higher than the control (no membrane), however the glass frit imparted significantly more resistance compared to the polymeric separators. To estimate these contributions, the shift of  $Z'$  of the low frequency diffusion tail (at 1 Hz) relative to the control was recorded; 62, 69, 68 and 297  $\Omega$  for the Celgard® MPS, FAP-450 AEM, F-930 CEM and glass frit respectively. Thus, the MPS is significantly less resistive compared to the other separators.



**Figure 35. a) EIS of the GC-II cell as a function of electrode separation (no membrane). b) The variation of ohmic resistance with electrode separation. c) EIS of the GC-II cell with different separator configurations. The electrodes are separated by 10 mm of electrolyte. d) Zoomed perspective of graph c as shown.**

### 4.3.3 Charge-discharge studies of the Fc/FcBF<sub>4</sub> redox couple

Battery-like experiments can be conducted whereby the oxidation of Fc in one electrolyte is coupled to the reduction of FcBF<sub>4</sub> in the other electrolyte. The cell can be repeatedly ‘charged’ and ‘discharged’, such that the electrolytes are reversibly converted from 0 – 100 % SOC, however these are arbitrary definitions for the process of passing positive/negative current until a positive/negative potential limit is reached. Thus, the experiment is considerably simplified compared to full-cell experiments as only one redox material and two oxidation states are used [156,159]. Although the cell setup here is strictly speaking not a battery (does not store energy), these charge-discharge experiments allow battery properties to be easily investigated such as overpotentials and redox material stability. A typical charge-discharge curve is shown in Figure 36a whereby charge and discharge

plateaus are observed slightly above and below the cell potential of 0 V. Although voltaic efficiency is not mathematically defined for this experiment type, due to the 0 V cell potential, the efficiency of the system can be assessed by considering the overpotential on charge/discharge. Taking the average cell potential as a measure of the overpotential, battery overpotentials of only 58 and 60 mV were observed on charge and discharge respectively, at a current density of  $2.40 \text{ mA cm}^{-2}$ , which indicates the high efficiency of the system. In consideration of the capacity, the cell also performs impressively as 100 % capacity is achieved on the first discharge as shown in Figure 36c. Thereafter the capacity retention is remarkable as the cell can be continuously cycled for several days and after 200 cycles (7.8 days), 80 % of the initial capacity is retained. In addition, coulombic efficiencies  $\geq 97\%$  are recorded, which indicates high stability of the system in MeCN electrolyte.

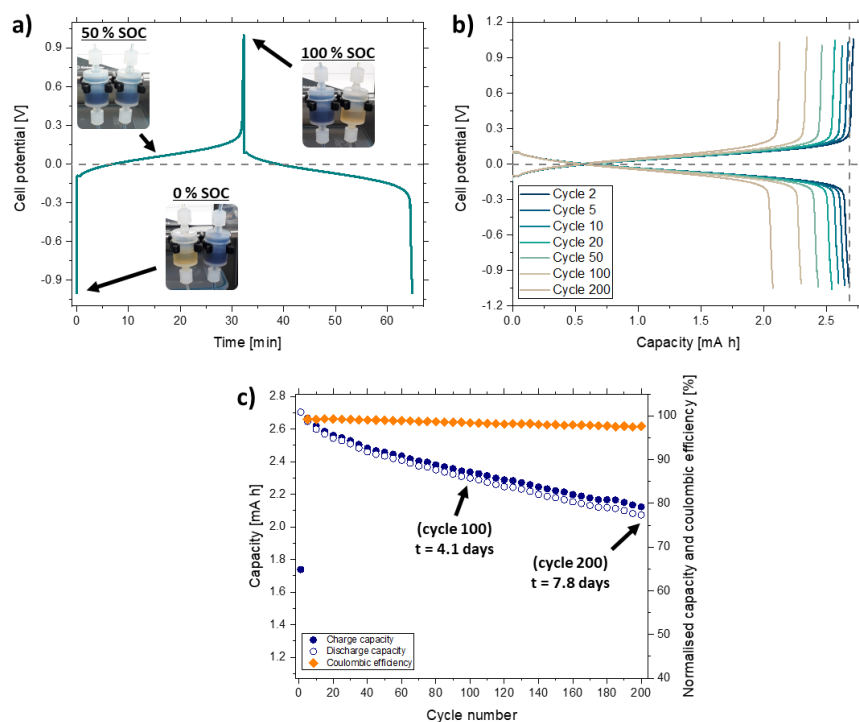


**Figure 36. a) Typical charge-discharge curve of the Fc/FcBF<sub>4</sub> single redox couple cell. Photographs are shown of the electrolyte reservoirs at 0, 50 and 100 % SOC. b) Selected charge-discharge curves during battery cycling. The vertical dashed line indicates the 2.68 mA h cell capacity. c) Capacity and coulombic efficiency as a function of cycle number (cell cycled from an initial SOC of 50 %). 5 mM Fc/FcBF<sub>4</sub>, 0.1 M TEA BF<sub>4</sub>, MeCN electrolyte at 10 mL min<sup>-1</sup>, 2.40 mA cm<sup>-2</sup> (1.87 C).**

Figure 37 shows the same experiment repeated using a PC-based electrolyte under otherwise identical experimental conditions for MeCN (Figure 36). Here the PC-electrolyte cycled with average potentials of 250 and -210 mV on charge and discharge respectively; a much higher overpotential than in the comparable MeCN-based experiment. This difference was mostly attributed to the higher ohmic resistance arising from the viscous PC solvent [97] which initially prevented cycling such that the cell required  $\approx 12$  h to equilibrate. The cell also cycled at much lower capacities, from 81 to 31 %, as shown in Figure 37b. The capacity loss mechanism was not studied here because PC is a less desirable solvent choice for NA RFBs, however the initial low capacity was attributed to the long equilibration time.

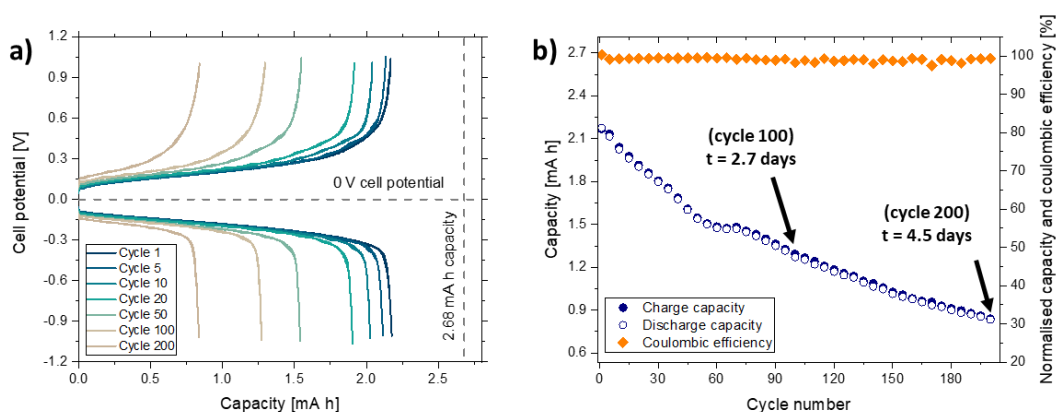


**Figure 37. a) Selected charge-discharge curves during battery cycling of PC-based electrolyte at  $2.40 \text{ mA cm}^{-2}$  ( $1.87 \text{ C}$ ). b) Capacity and coulombic efficiency as a function of cycle number (cell cycled from an initial SOC of 100 % after  $\sim 12$  hour equilibration).  $5 \text{ mM Fc/FcBF}_4$ ,  $0.1 \text{ M TEA BF}_4$ , PC electrolyte at  $10 \text{ mL min}^{-1}$ .**

Next, the system was studied as a function of current density, in the range of  $2.40$  to  $12.02 \text{ mA cm}^{-2}$  in MeCN electrolyte, as shown in Figure 38. Here the effect of overpotential becomes apparent because the accessible capacity decreases as the current density increases. In addition, the cell cycled at higher potentials; at  $12.02 \text{ mA cm}^{-2}$ , the average potential is  $\pm 220 \text{ mV}$ . In consideration of the cell characterisation in section 4.3.2 and section 2.4.2, it can be concluded that the overpotential here arises from both the finite mass transport and the ohmic resistance. At high current densities the flux of  $\text{Fc/FcBF}_4$  reagent to the electrodes

is limiting, thus increasing the overall cell resistance. Regardless, Figure 38c shows that high C-rates of up to  $\approx 10C$  can be achieved with minimal overpotential and high accessible capacities ( $\sim 75\%$  for  $12.02 \text{ mA cm}^{-2}$ ). However, the cell was unable to reliably cycle at the maximum current density indicated by polarization ( $\sim 27 \text{ mA cm}^{-2}$ , Figure 34), as charge-discharge experiments at  $24 \text{ mA cm}^{-2}$  gave large overpotentials of  $500 \text{ mV}$  and a maximum capacity of  $20\%$ .

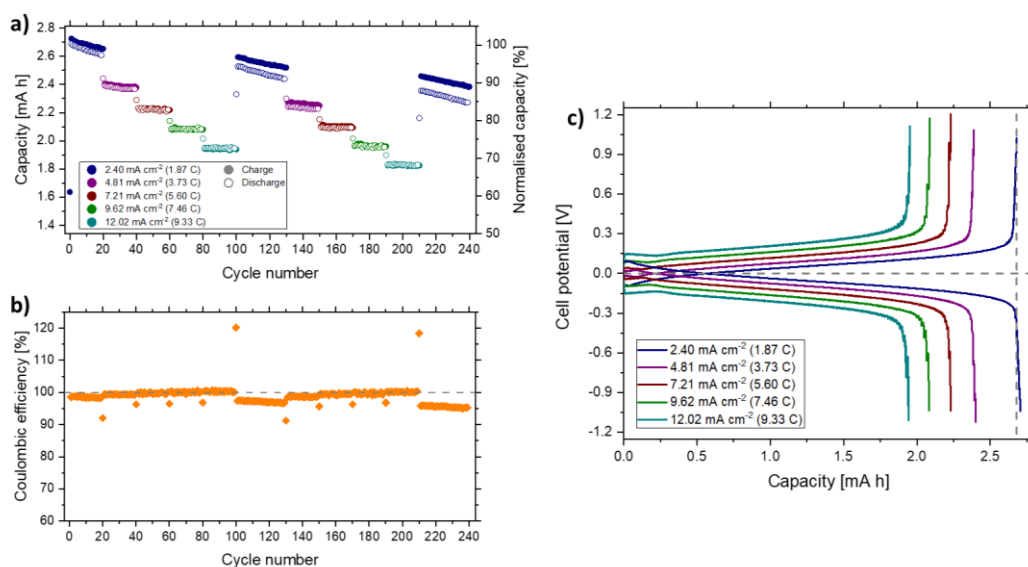


**Figure 38.** Cycling of the Fc/FcBF<sub>4</sub> single redox couple cell as a function of current density. a) Capacity and b) coulombic efficiency against cycle number. c) An overlay of charge-discharge curves at different current densities. Cycles 2, 22, 42, 62 and 82 are shown. The vertical dashed line shows the theoretical 2.68 mA h capacity. (5 mM Fc/FcBF<sub>4</sub> in 0.1 M TEA BF<sub>4</sub>, MeCN electrolyte).

Given that the performance of the FC-II flow-cell has been validated using the Fc/FcBF<sub>4</sub> redox couple, similar experiments were conducted using a glass H-cell (GC-III glass cell, Chapter 3, Figure 22cii) in MeCN electrolyte (Figure 39). Here the performance is considerably poorer than in the flow-cell as the average cell potential is  $\sim 600 \text{ mV}$  (at  $1 \text{ mA}$ ) and only very low currents are possible, giving low C-rates of  $\leq 0.75 \text{ C}$ . Despite this, the cell achieved  $98\%$  capacity on charge/discharge which suggests that the observed overpotentials are mainly due to the large ohmic resistance of the glass cell with a minor contribution from limited mass transport. This conclusion is supported by Figure 39a whereby the

same capacity is achieved at both 0.5 and 1 mA applied currents, in contrast to Figure 38 where the flow-cell capacity is dependent on the applied current density. Therefore, in comparison the superior flow-cell can charge the electrolyte in significantly less time with much lower overpotential, despite using twice the electrolyte volume of the H-cell.

(Flow-cell: 60 mV overpotential at 5 mA and 29.5 min 100 % electrolysis time for 10 mL electrolytes. H-cell: 600 mV overpotential at 1 mA and 1.28 h 100 % electrolysis time for 5 mL electrolytes.).

This difference is most significant when comparing the C-rates achieved by each cell; at maximum the H-cell achieves 0.75 C, whereas the flow-cell manages 9.33 C, with 75 % capacity. Thus, the flow-cell is most suited towards battery studies, whereas the H-cell is more appropriate for bulk electrolysis methods where the cell overpotentials occur in the sacrificial electrolyte.

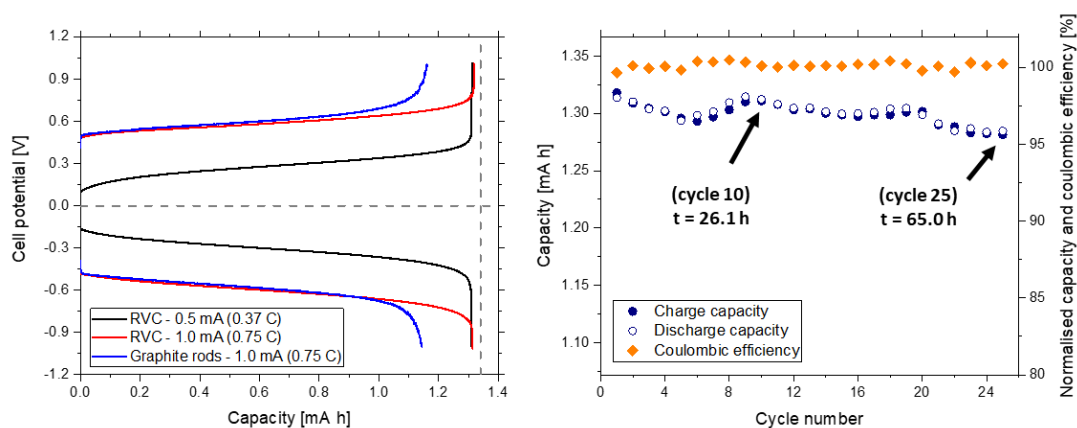


**Figure 39. a) Typical Fc/FcBF<sub>4</sub> charge-discharge curves for the GC-III glass H-cell, using RVC and graphite rod electrodes. b) Representative cell capacities for the GC-III glass H-cell (RVC electrodes at 1 mA). (5 mM Fc/FcBF<sub>4</sub> in 0.1 M TEA BF<sub>4</sub>, MeCN electrolyte).**

#### 4.3.4 Capacity loss investigations

Thus far, the cell designs were studied in terms of their performance to assess their capabilities, however as is evident in Figure 36c, a significant capacity fade was observed across all experiments over long periods of time. In addition, the initial capacity on first cycle and the capacity loss rate was found to vary across different experiments. The mechanism for the capacity loss was not immediately

obvious, so experiments were conducted to identify the mechanism. Generally speaking, all capacity loss in RFBs can be attributed to a loss of redox material from the electrolytes, however the mechanism for this loss can be either due to a physical or a chemical process, as shown in Figure 40.

Cell leakage is the simplest mechanism for capacity loss as any leakage will decrease the total moles of redox material in the electrolytes. Although the FC-II flow-cell has been developed and optimised to prevent the leakage of the liquid electrolytes, losses still occur because there is a tendency for MeCN-based electrolytes to diffuse through the gaskets and evaporate off solvent. This process slowly decreases the electrolyte volume and leaves behind crystalline formations on the gasket edges composed of the redox materials and supporting salt. Despite this, the total volume loss after 7 day experiments was insignificant and furthermore, capacity loss occurs in the GC-III glass cell which is fully sealed. In addition, to ensure that the capacity loss was not due to electrolyte soaking into the flow-cell polymer/rubber materials, an experiment was conducted whereby the flow-cell was preconditioned by pumping supporting electrolyte for 24 h and then conducting battery cycling. Here the capacity loss and cell performance were near-identical to experiments conducted from an as-assembled dry flow-cell, which indicated no benefits to pre-conditioning the flow-cell in other experiments. Thus, cell leakage is not responsible for the observed capacity fade.

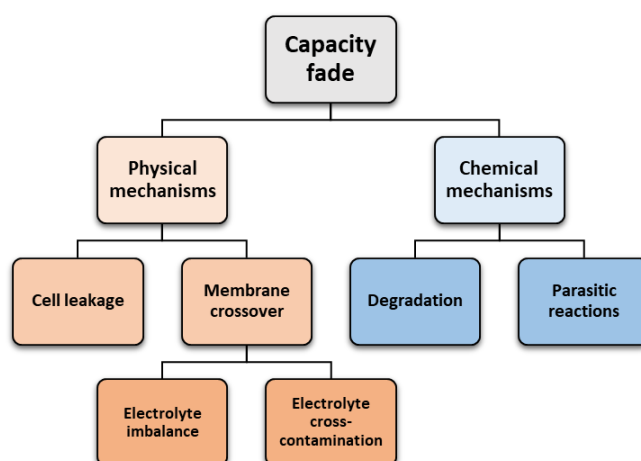
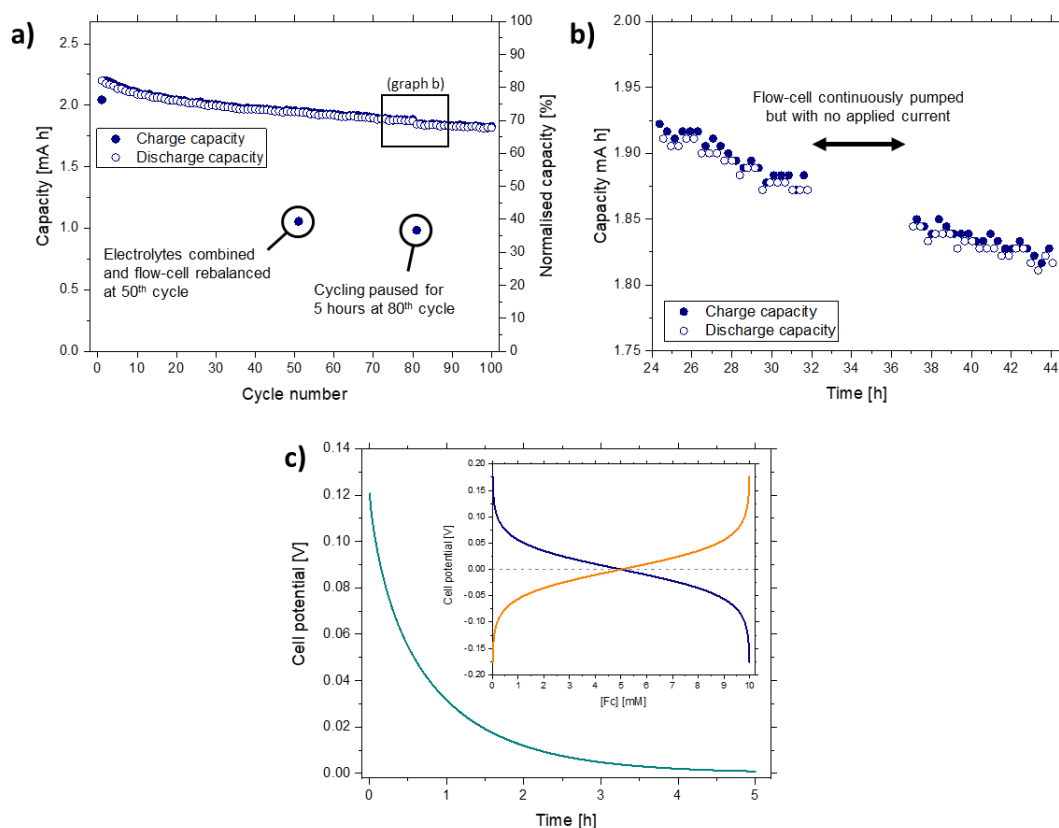


Figure 40. characteristic capacity loss mechanisms in RFBs.

Next, an experiment was devised whereby the electrolytes were rebalanced midway through cycling to examine whether the capacity loss was due to membrane crossover with time. As only one redox couple was used in these experiments, membrane crossover cannot cross-contaminate the electrolytes, however it is possible that unequal pressure on the membrane could force an electrolyte imbalance such that the concentrations of Fc/FcBF<sub>4</sub> or the total volume of electrolytes become non-equal. As shown in Figure 41a, the recombination of the electrolytes did not restore the cell capacity to the initial capacity, which indicates that the capacity loss is not due to membrane crossover and associated electrolyte imbalance.

Capacity loss must therefore be attributed to chemical or electrochemical processes occurring in the battery. To discern whether the capacity loss was due to the electrochemical reactions at the electrode surfaces, an experiment was conducted whereby the electrolyte pumping was maintained but no battery cycling was conducted for 5 h, as shown in Figure 41b. The capacity decreased linearly with time despite no applied currents, which proves that the capacity loss is not due to the battery cycling or parasitic reactions with the supporting electrolyte. Therefore, the capacity loss is most likely due to a slow chemical reaction which occurs in the electrolyte. Furthermore, this experiment proves that the capacity loss has a time-dependency rather than a dependency on the cycle number, as is observed in other battery technologies [218]. This time dependency is most obvious in Figure 38 whereby the capacity loss rate is fastest at 2.40 mA cm<sup>-2</sup> ( $3.31 \times 10^{-3}$  mA h cycle<sup>-1</sup>) and slowest at 12.02 mA cm<sup>-2</sup> ( $8.46 \times 10^{-5}$  mA h cycle<sup>-1</sup>) because the time taken to complete a cycle decreases as the current density increases. In fact, the overriding capacity loss in this experiment showed a linear relationship with time, giving a near-constant loss rate per hour at all current densities of  $1.07 \times 10^{-2}$  C h<sup>-1</sup>. Despite this, the capacity loss rate was found to vary between different experiments indicating a complexity to the mechanism.



**Figure 41. Capacity loss study of the Fc/FcBF<sub>4</sub> system in the FC-II flow-cell. a) capacity vs cycle number. The battery electrolytes were recombined and rebalanced at the 50<sup>th</sup> cycle whereas the cell cycling was paused for 5 h at the 80<sup>th</sup>. b) capacity vs time during the cycling pause (cycle time defined by the start of each charge/discharge step). c) OCP measurement of the flow-cell during the 5 h cycling pause. Inset graph – the cell potential as a function of Fc or FcBF<sub>4</sub> concentration as predicted by the Nernst equation. 5 mM Fc/FcBF<sub>4</sub>, 0.1 M TEA BF<sub>4</sub>, MeCN electrolyte at 10 mL min<sup>-1</sup>, 4.81 mA cm<sup>-2</sup> (3.73 C).**

Given that the neutral Fc oxidation state is known to be exceptionally stable [215], it was suspected that decomposition of the ferrocenium ion was the likely reaction. This was confirmed by conducting UV-vis analysis of each oxidation state in anaerobic MeCN solution at 1 mM concentration. Whereas the Fc solution showed no change after 11 days, the FcBF<sub>4</sub> solution (with and without supporting salt) showed considerable evolution of the UV-vis spectrum as shown in Figure 42, with the largest change occurring for the FcBF<sub>4</sub>-only solution over the first 24 h.

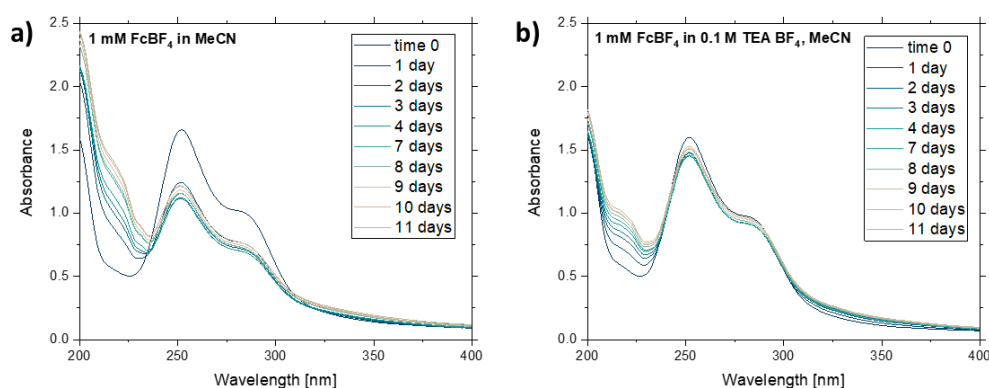
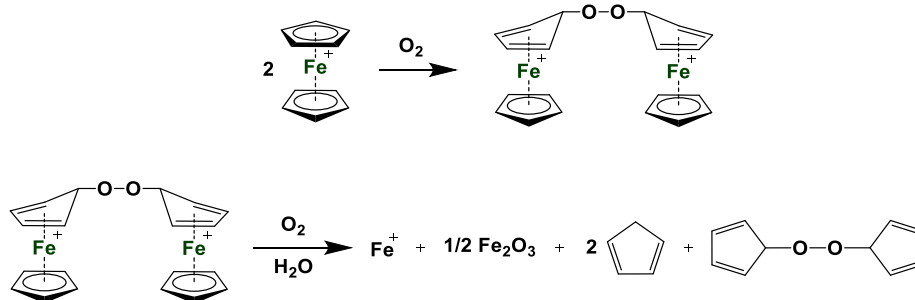


**Figure 42. The evolution with time of the UV-vis spectrum of a) 1 mM FcBF<sub>4</sub> in MeCN and b) 1 mM FcBF<sub>4</sub> in 0.1 M TEA BF<sub>4</sub>, MeCN.**

In addition, the instability of  $\text{FcBF}_4$  was visually observed in solutions of MeCN electrolyte; whereas solutions of  $\text{FcBF}_4$  in only MeCN gave a deep blue colour that persisted for at least one week, solutions of  $\text{FcBF}_4$  with TEA  $\text{BF}_4$  supporting salt were more blue-green in appearance and after several days the solutions were pale-green. This observation was also seen in the battery experiments whereby the combined  $\text{Fc}/\text{FcBF}_4$  green electrolyte appeared greener and more transparent after 7 days of cycling, indicating a loss of the  $\text{FcBF}_4$  species. The instability of  $\text{FcBF}_4$  in organic electrolytes is well known in the literature [219–221] as the ferrocenium ion is an oxidising agent and in particular, it rapidly decomposes in the presence of oxygen as shown in Scheme 4, to give iron oxide and cyclopentadienyl-decomposition products [220]. In the present work, the battery electrolytes were maintained in an anaerobic  $\text{N}_2$  glovebox with oxygen levels at 1 ppm maximum and therefore it is unlikely that the observed capacity fade can be attributed to oxygen. Furthermore, to ensure that trace oxygen was not responsible, a similar experiment to Figure 42 was conducted whereby an antioxidant, 2,6-diterbutyl-4-methyl phenol (ionol), was added at 1 mM concentration [220]. However, the UV-vis spectrum showed similar evolution with time as the controls.



**Scheme 4. The decomposition mechanism of ferrocenium cations in the presence of oxygen** [219–221].

Next, it was suspected that trace water in the electrolyte was possibly causing the observed capacity fade. In contrast to the oxygen content where it is easy to operate in anaerobic conditions, it was very challenging to achieve perfectly anhydrous conditions because the TEA  $\text{BF}_4$  salt and the  $\text{FcBF}_4$  product are hygroscopic materials. Furthermore, the synthesis of  $\text{FcBF}_4$  does not yield a fully anhydrous product (elemental analysis was consistent with  $\frac{1}{4}\text{H}_2\text{O}$ ) which could not be fully dried in the solid phase. Therefore, it was anticipated that the battery electrolytes contained near stoichiometric quantities of water to  $\text{FcBF}_4$ . Regardless, to examine whether the ferrocenium ion is reactive towards water, experiments were conducted whereby 0.9 mM  $\text{FcBF}_4$  solutions were prepared with varying quantities of water (0.56 M to 2.78 M) in anaerobic conditions. As shown in Figure 43b, a slow loss of the characteristic  $\text{FcBF}_4$  absorbance peaks was observed with time, however this rate was roughly equal to the control. Interestingly, the addition of water caused the precipitation of a small quantity of yellowish substance from each solution which accounts for the difference in magnitude between the water-containing solutions and the control (dashed grey line in Figure 43a). Regardless, this work proves that the  $\text{FcBF}_4$  is not directly reactive towards water as the water content was in very large excess, and furthermore  $\text{FcBF}_4$  has been routinely manipulated in aqueous solutions in the literature [216,221]. In addition, efforts to produce anhydrous battery electrolytes, such as drying the supporting electrolyte over 4 Å molecular sieves for several days, did not yield any better capacity retention. The role of water in the decomposition of  $\text{FcBF}_4$  is not clear, however it has been proposed that water (or alternative protic electrolytes) catalyse the

decomposition of  $\text{FcBF}_4$  in oxygenated solutions (Scheme 4). Therefore, the presence of water in the battery electrolytes may catalyse the anaerobic  $\text{FcBF}_4$  decomposition or provide a source of dissolved oxygen.

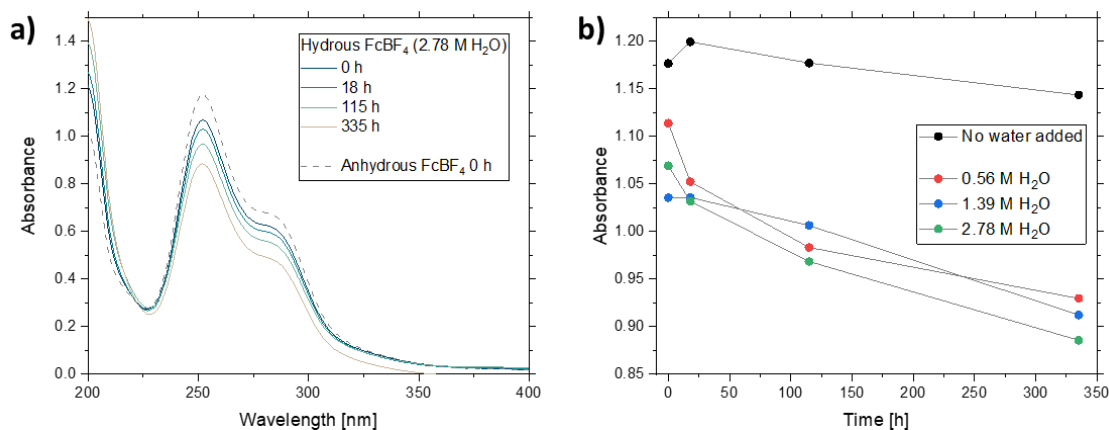


**Figure 43. a) The evolution with time of the UV-vis spectrum of 0.9 mM  $\text{FcBF}_4$  in MeCN with 2.78 M  $\text{H}_2\text{O}$  (1 mL  $\text{H}_2\text{O}$  in 20 mL volume). b) The variation in peak absorbance at  $\lambda_{\text{max}} = 252$  nm with time for different quantities of added water.**

To rationalise the observed instability of the  $\text{FcBF}_4$ , the voltammetry of Fc and  $\text{FcBF}_4$  as a function of scan-rate were compared as shown in Figure 44. Although each compound gives similar current response, it is evident that the peak currents for  $\text{FcBF}_4$  are lower in magnitude than for Fc. This is more obvious for the  $\text{Fc} \rightarrow \text{FcBF}_4$  peak than the  $\text{FcBF}_4 \rightarrow \text{Fc}$  peak. This observation could be explained by an inaccuracy of the  $\text{FcBF}_4$  concentration, due to partial decomposition prior to the experiment, however it is also possible that the ferrocenium ion could possess a lower diffusion coefficient, thus accounting for lower observed peak currents. The ionic ferrocenium species is expected to have a larger solvation radius than the neutral Fc and therefore a lower diffusion coefficient [97].

Upon close inspection of Figure 44 the baseline current before reduction of  $\text{FcBF}_4$  was observed to increase with scan rate. To study this phenomenon further, the  $\text{FcBF}_4$  solution was studied at an RDE as shown in Figure 45. Whereas zero current response was observed before oxidation of Fc in Figure 32, here the baseline current before reduction of  $\text{FcBF}_4$  is non-zero and it increased linearly with the square-root of rotation rate. This unexpected behaviour proves that the blue  $\text{FcBF}_4$  solution contains a small quantity of the neutral Fc oxidation state,

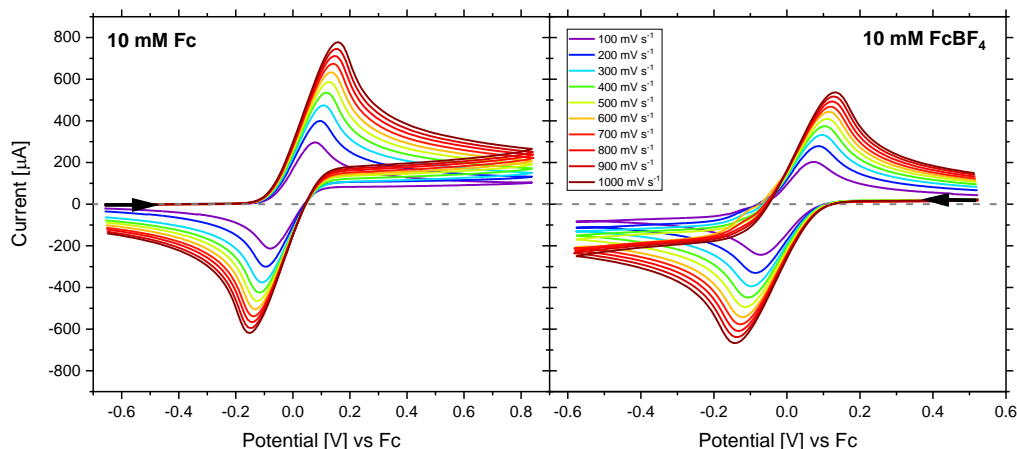


**Figure 44. The scan-rate dependence of 10 mM Fc and FcBF<sub>4</sub> in 0.1 M TEA BF<sub>4</sub>, MeCN electrolyte. First scans shown.**

despite preparing the solution with only FcBF<sub>4</sub> and using the solution as soon as possible. The decomposition of FcBF<sub>4</sub> to give Fc has been previously observed in aerobic solutions of DMF or DMSO [220], however this has not been observed in anaerobic MeCN electrolytes. Based on this conclusion, the gradual conversion of FcBF<sub>4</sub> to Fc in the battery electrolytes accounts for the measured battery capacity loss and the visual observations of the electrolyte colours with time. In addition, if the FcBF<sub>4</sub> solutions contain Fc, then it is expected that the addition of water would cause precipitation of the water-insoluble Fc, thus accounting for the observations in Figure 43.

Based upon the apparent chemical reduction of FcBF<sub>4</sub> to give Fc in MeCN solution, it was expected that the concentration of FcBF<sub>4</sub> and Fc would decrease/increase respectively with time in the battery electrolyte. Furthermore, it is likely that the decomposition would proceed in the electrolyte regardless of whether it is in the flow-cell or not. To examine this, a fresh solution of battery electrolyte was prepared and then battery cycling was conducted immediately. The remaining solution was then stored for three months in a sealed glass bottle over 4 Å molecular sieves and then the same battery experiment was conducted again under identical conditions. As shown in Figure 46 the initial battery experiment gave 100 % capacity on first cycle, however the aged electrolyte gave only 80 %,

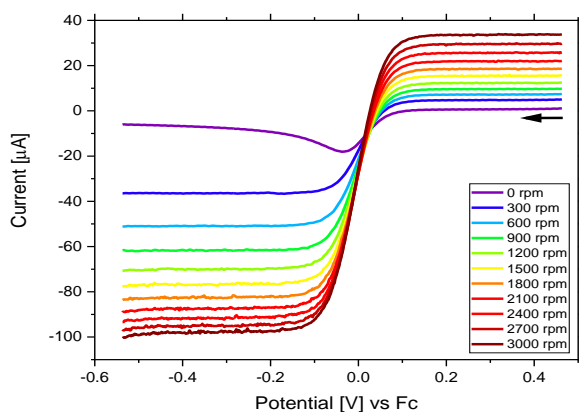


**Figure 45. RDE LSVs of 1 mM FcBF<sub>4</sub> in 0.1 M TEA BF<sub>4</sub>, MeCN electrolyte at 50 mV s<sup>-1</sup> on GC electrode. The effect of increasing the rotation rate is shown.**

thus, indicating that decomposition of the electrolyte occurred during storage. Despite this, the fresh electrolyte gave faster capacity decay and a lower final capacity after 200 cycles. This experiment shows that the capacity loss rate of the Fc/FcBF<sub>4</sub> electrolyte occurs faster in the flow-cell than when stored and not in use. In addition, the capacity retention appears to be very sensitive to the battery conditions.

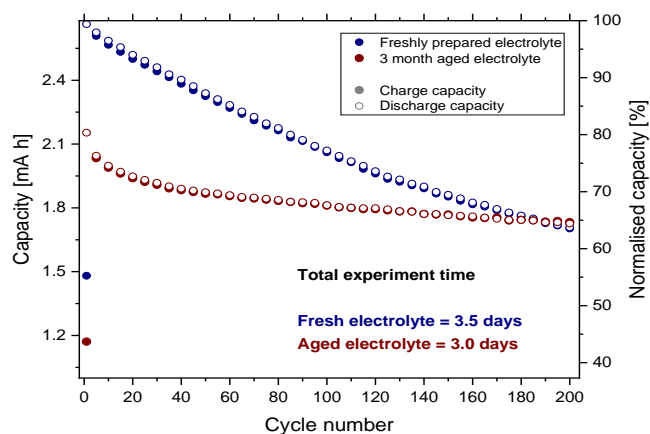


**Figure 46. Cycling of the Fc/FcBF<sub>4</sub> single redox couple cell at 4.81 mA cm<sup>-2</sup>. (5 mM Fc/FcBF<sub>4</sub> in 0.1 M TEA BF<sub>4</sub>, MeCN electrolyte). The capacity retention of the freshly prepared electrolyte (blue) is compared to the three month old electrolyte (red). The total experiment time for the completion of 200 cycles is given for reference.**

In a separate set of experiments, the battery electrolyte was studied by cyclic voltammetry before and after use, as shown in Figure 47. The results show that, the unused fresh electrolyte appears identical to a different electrolyte that has been aged by three months, and that the concentrations of Fc and FcBF<sub>4</sub> both decrease during battery cycling. Based on the peak currents for Fc oxidation and FcBF<sub>4</sub> reduction, it is evident that the concentration of FcBF<sub>4</sub> decreases more than the Fc and in addition, the FcBF<sub>4</sub> content decreases more during longer battery experiments. This result is consistent with the observation that the battery electrolyte become pale-green in appearance after cycling. Interestingly, the total amount of Fc + FcBF<sub>4</sub> appears to decrease with battery cycling, which suggests that the decomposition of FcBF<sub>4</sub> does not proceed via chemical reduction back to Fc, and instead a decomposition to iron oxide or other Fe species is likely occurring.

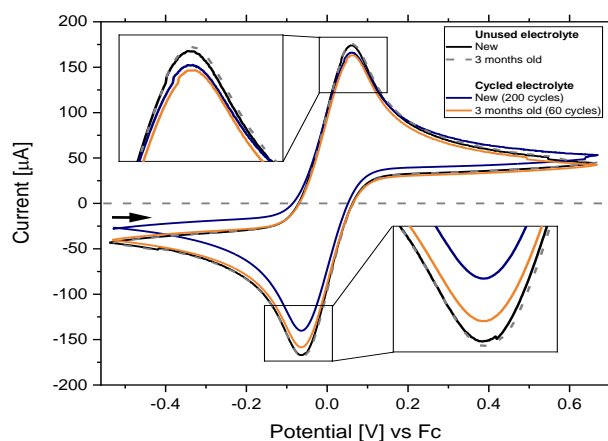


**Figure 47. Cyclic voltammetry of Fc/FcBF<sub>4</sub> battery electrolytes (5 mM Fc and 5 mM FcBF<sub>4</sub> in 0.1 M TEA BF<sub>4</sub>, MeCN) at 50 mV s<sup>-1</sup>. The current response of a freshly prepared electrolyte is compared to a three month old electrolyte, as well as electrolytes recovered from battery studies.**

## 4.4 Conclusions

To quantify the performance of the cell designs developed in Chapter 3, the Fc/FcBF<sub>4</sub> redox couple was adopted as a model chemistry. Due to the fast redox kinetics and high stability, the redox couple enabled cell-level diagnostic studies to measure the cell ASR and to choose an appropriate electrolyte flow-rate. By use of

the model chemistry in battery-like experiments, the flow-cell design was validated by conducting long-term experiments (> 1 week) and cycling at a range of current densities. Therefore, the present work serves as a direct comparison for the novel redox materials developed in the following chapters. Although the Fc/FcBF<sub>4</sub> redox couple displays exceptional stability compared to other proposed NA RFB redox materials, questions remain as to the mechanism for capacity loss in battery experiments. Specifically, the FcBF<sub>4</sub> oxidation state is unstable in the electrolyte which causes a loss of the total amount of Fc/FcBF<sub>4</sub> with time, thus limiting the capacity. The mechanism for the decomposition of FcBF<sub>4</sub> is not fully understood as neither the oxygen or water content in the electrolyte appear to be responsible. In addition, the capacity loss rate was found to vary between experiments which suggests that the chemistry is sensitive to the quality and purity of the electrolyte, the battery conditions (perhaps temperature and UV-light) or the battery architecture. It is important to note that capacity loss has been observed in all NA RFB studies employing Fc [136,205,214] or its derivatives [138,145], however the capacity loss mechanisms were never studied. Therefore, the implications of this work are important for the research field and more generally for the vast number of ferrocene applications in energy technologies and beyond. Future work could examine the stability of FcBF<sub>4</sub> more directly to identify the decomposition mechanism, however to avoid this issue, alternative Fc derivatives could be applied. Specifically, the ferrocenium ion of Fc derivatives with large alkyl substituents are known to be more stable, such as decamethylferrocene, because the Fe core is less accessible due to steric hinderance [215,220].

# Chapter 5

## Co(II) Complexes with Azole-Pyridine Ligands

The work presented in this chapter is published in [1].

### 5.1 Introduction

2,2':6',2''-Terpyridine (tpy) is a classical ligand which forms numerous homoleptic coordination complexes with transition metal centres of general formula  $[M(\text{tpy})_2]^n(\text{A}^-)_n$ . Being composed of three pyridyl donor groups, tpy is a chelating ligand which forms more thermodynamically and kinetically stable octahedral complexes compared to analogous bpy complexes. Their application in NA RFBs has been done previously giving similar properties to bpy complexes, however lower MCC solubility was typically observed [1,95,105]. Therefore, higher solubility analogues of tpy complexes which exploit the stabilising effect of tridentate ligands are expected to be good candidates for application in NA RFBs. Azole-pyridine ligands are analogues of bpy and tpy whereby some of the pyridyl donors are replaced with heterocyclic azoles such as a pyrazole, 1,2,3-triazole or 1,2,4-triazole [222]. Given that azoles are weaker  $\sigma$ -donating/ $\pi$ -accepting ligand groups compared to pyridyl groups, the electrochemistry of the MCC can be considerably affected by substitution of a pyridine group with an azole [223]. Therefore, by designing the ligand as a combination of different pyridyl and azole donors, a vast number of different ligands are possible, hence allowing the MCC properties such as redox potentials to be finely tuned by subtle changes of the ligand structure. This methodology therefore enables the MCC electrochemistry and solubility to be improved without considerable increases in the molecular weight.

A literature review identified azole-pyridine complexes of cobalt [223,224], ruthenium [224,225] rhenium [226] and iridium [227], which were developed for applications in dye-sensitized solar cells; where similar electrochemical properties to RFBs are desirable. Although the electronic properties of Ru, Re and Ir MCCs are of interest, the low abundance and high cost of these elements make them impractical for application in RFBs. In contrast, Co is much more earth-abundant and offers three stable oxidation states (I,II and III), thus allowing a symmetric RFB to be constructed. Herein Co(II) complexes with azole-pyridine ligands are applied in a symmetric NA RFB. The properties of ligands with 3,5-dimethyl pyrazole and 1,2,4-triazole substitutions are compared to the tpy complex.

## 5.2 Experimental

### 5.2.1 Chemicals and reagents

All chemicals were analytical or reagent grade and used as received from the supplier without further purification. Sigma Aldrich, UK; DMSO (anhydrous,  $\geq 99.9$  %),  $\text{CoCl}_2 \cdot 6\text{H}_2\text{O}$  (ACS reagent, 98 %), 2,6-dibromopyridine (98 %),  $\text{KPF}_6$  (98 %). TCI Europe; 1,2,4-triazole ( $>98.0$  %), 6-bromo-2,2'-bipyridine ( $>97.0$  %),  $t\text{BuOK}$  ( $>97.0$  %), TBA  $\text{PF}_6$  ( $>98.0$  %). Fisher; MeCN (HPLC grade,  $>99.9$  %), MeOH (Analytical grade, 99.99 %). ACROS Organics; MeCN (AcroSeal<sup>®</sup>, anhydrous, extra dry over molecular sieves, 99.9 %). Fluka Analytical; 3,5-dimethylpyrazole (Produced by Wacker,  $\geq 99.0$  %). Alfa Aesar; 2,2':6',2''-terpyridine (97 %).

### 5.2.2 Synthesis of azole-pyridine ligands

Complexes **1-4** were prepared by a simplified procedure based upon the method reported in Ref. [223] such that reactions were not conducted in an inert environment or purified by chromatography. Ligand **L1** was purchased whereas ligands **L2-L5** were synthesised by non-catalysed C-N coupling of an azole with a halo-pyridine in the presence of potassium tert-butoxide, in anhydrous DMSO. Corresponding complexes **1-4** were produced by reaction of  $\text{CoCl}_2 \cdot 6\text{H}_2\text{O}$  with excess of ligand **L1-L4** in methanol before precipitation in aqueous  $\text{KPF}_6$  solution to give the hexafluorophosphate salt. All products were characterised by  $^1\text{H}$  NMR.

**General procedure:** Excess of substituted azole and potassium tert-butoxide were dissolved in 4-6 mL of DMSO causing a slight exothermic reaction to occur. The mixtures were stirred for 15 min to allow the reactions to finish and cool to room temperature. 6-Bromo-2,2'-bipyridine or 2,6-dibromopyridine was then added and heated under reflux for 24 h at either 110 °C, for **L2**, or 140 °C, for **L3-5**. Yellow to dark brown oils were produced which were cooled to room temperature before water (50 ml) was added, giving white to peach suspensions. The mixtures were then cooled further in an ice bath for 1 h to encourage precipitation before Buchner filtration under vacuum. The solids were then washed with cold water (10 ml) before being dried under vacuum and recovered. **L4** required purification by recrystallization; product dissolved in hot methanol (6 ml) and ice-cold water was added to the point of precipitation. The product was then recovered by filtration and dried under vacuum as before. No further purification was deemed necessary as <sup>1</sup>H NMR indicated high purity. Ligand products were dried under high vacuum and stored in a desiccator for 24 h before complexation with cobalt(II) to remove any remaining water, methanol or DMSO.

**L2 = 6-(N-3,5-dimethylpyrazoyl)-2,2'-bipyridine:** 3,5-Dimethylpyrazole (299 mg, 3.11 mmol), <sup>t</sup>BuOK (342 mg, 3.05 mmol) and 6-Bromo-2:2'-bipyridine (306 mg, 1.30 mmol) gave a white powder solid: 207 mg (0.83 mmol, 63 %). Calc. for C<sub>15</sub>H<sub>14</sub>N<sub>4</sub> (MW 250.30). <sup>1</sup>H NMR (400 MHz, CDCl<sub>3</sub>): δ = 8.68 (d, J = 4.81 Hz, 1H), 8.33 (d, J = 7.94 Hz, 1H), 8.32-8.27 (m, 1H), 7.93-7.88 (m, 2H), 7.81 (td, J = 7.76 Hz, 1.83 Hz, 1H), 7.33-7.29 (m, 1H), 6.03 (s, 1H), 2.79 (d, J = 0.66 Hz, 3H, Pyrazole CH<sub>3</sub>), 2.31 (s, 3H, Pyrazole CH<sub>3</sub>) ppm.

**L3 = 2,6-bis-(N-3,5-dimethylpyrazoyl)pyridine:** 3,5-Dimethylpyrazole (937 mg, 9.75 mmol), <sup>t</sup>BuOK (1099 mg, 9.79 mmol) and 2,6-dibromopyridine (1001 mg, 4.22 mmol) gave a white powder solid: 798 mg (2.99 mmol, 70 %). Calc. for C<sub>15</sub>H<sub>17</sub>N<sub>5</sub> (MW 267.34). <sup>1</sup>H NMR (400 MHz, CDCl<sub>3</sub>): δ = 7.88 (t, J = 8.01 Hz, 1H, Pyridine para-H), 7.68 (d, J = 7.92 Hz, 2H, Pyridine meta-H), 6.00 (s, 1H, Pyrazole H), 2.58 (s, 6H, Pyrazole CH<sub>3</sub>), 2.30 (s, 6H, Pyrazole CH<sub>3</sub>) ppm.

**L4 = 6-(N-1,2,4-triazoyl)-2,2'-bipyridine:** 1,2,4-Triazole (207 mg, 3.00 mmol), <sup>t</sup>BuOK (341 mg, 3.04 mmol) and 6-Bromo-2:2'-bipyridine (309 mg, 1.31 mmol)

gave a pale peach powder solid: 118 mg (0.53 mmol, 40 %). Calc. for  $C_{12}H_9N_5$  (MW 223.23).  $^1H$  NMR (400 MHz,  $CDCl_3$ ):  $\delta$  = 9.31 (s, 1H), 8.71 (d,  $J$  = 4.81 Hz, 1H), 8.47-8.42 (m, 2H), 8.13 (s, 1H), 8.03 (t,  $J$  = 7.83 Hz, 1H), 7.93 (d,  $J$  = 8.10 Hz, 1H), 7.88 (td,  $J$  = 7.77, 1.82 Hz, 1H), 7.40-7.35 (m, 1H) ppm.

**L5 = 2,6-bis-(N-1,2,4-triazoyl)pyridine:** 1,2,4-Triazole (671 mg, 9.72 mmol),  $t$ BuOK (1090 mg, 3.04 mmol) and 2,6-dibromopyridine (1001 mg, 4.22 mmol) gave a white solid: 853 mg (4.00 mmol, 95 %). Calc. for  $C_9H_7N_7$  (MW 213.20).  $^1H$  NMR (400 MHz, toluene- $d_8$ ):  $\delta$  = 8.50 (s, 2H, Triazole H), 7.88 (s, 2H, Triazole H), 7.36 (d,  $J$  = 8.01 Hz, 2H Pyridine meta-H), 6.92 (t,  $J$  = 7.99 Hz, 1H Pyridine para-H) ppm.

### 5.2.3 Synthesis of Co(II) complexes

**General Procedure:** Complexes **1-4** were produced by first dissolving the corresponding ligand (small excess) in methanol (5 ml) and heating to 60 °C under reflux until all the solid dissolved. To which,  $CoCl_2 \cdot 6H_2O$  was added, producing red to Yellow solutions. After a further 2 h of stirring, the mixtures were cooled to room temperature before they were pipetted drop-wise into a stirred solution of  $KPF_6$  (large excess) in 30 ml of water, in order to convert the complex to the hexafluorophosphate salt. In each case, the complex precipitated instantly to give dark red to peach suspensions. After stirring in an ice bath for 30 min to facilitate precipitation, the solids were then recovered by Buchner filtration under vacuum, washed with water to remove inorganic salts and dried under vacuum. The solids were then stored in a desiccator for at least 24 h to promote drying of the solids. All compounds were found to be air- and moisture-stable and showed no degradation due to light. Synthesis of complex **5** by the same procedure could not be accomplished.

**1 = [Co(2,2':6',2''-Terpyridine) $_2$ ](PF $_6$ ) $_2$ :**  $CoCl_2 \cdot 6H_2O$  (151 mg, 0.63 mmol) and 2,2':6',2''-Terpyridine (307 mg, 1.31 mmol) gave dark red/ brown solid: 404 mg (0.49 mmol, 79 %). Calc. for  $C_{30}H_{22}CoF_{12}N_6P_2$  (MW 815.41).  $^1H$  NMR (400 MHz, acetone- $d_6$ ): a single set of aromatic H was not observed;  $\delta$  = 97.77 (s, 4H), 56.25 (s, 4H), 47.27 (s, 4H), 33.48 (s, 4H), 21.36 (s, 2H), 8.35 (s, 4H) ppm.

**2** = [Co(6-(N-3,5-dimethylpyrazoyl)-2,2'-bipyridine)<sub>2</sub>](PF<sub>6</sub>)<sub>2</sub>: CoCl<sub>2</sub>.6H<sub>2</sub>O (90.4 mg, 0.38 mmol) and **L2** (201 mg, 0.80 mmol) gave orange-cream solid: 383 mg (0.45 mmol, 56 %). Calc. for C<sub>30</sub>H<sub>28</sub>CoF<sub>12</sub>N<sub>8</sub>P<sub>2</sub> (MW 849.46). <sup>1</sup>H NMR (400 MHz, acetone-d<sub>6</sub>): a single set of aromatic H was not observed; δ = 82.37 (s, 2H), 77.44 (s, 2H), 77.35 (s, 2H), 71.22 (s, 2H), 50.27 (s, 2H), 15.10 (s, 6H), 12.14 (s, 2H), 7.00 (s, 2H), 1.24 (s, 2H), 2.02 (s, 2H), -0.90 (s, 6H) ppm.

**3** = [Co(2,6-bis-(N-3,5-dimethylpyrazoyl)pyridine)<sub>2</sub>](PF<sub>6</sub>)<sub>2</sub>: CoCl<sub>2</sub>.6H<sub>2</sub>O (262 mg, 1.10 mmol) and **L2** (603 mg, 2.25 mmol) gave orange-cream solid: 1749 mg (1.98 mmol, 78 %). Calc. for C<sub>30</sub>H<sub>34</sub>CoF<sub>12</sub>N<sub>10</sub>P<sub>2</sub> (MW 883.53). <sup>1</sup>H NMR (400 MHz, acetone-d<sub>6</sub>): a single set of aromatic H was not observed; δ = 83.99 (s, 2H), 62.10 (s, 4H), 12.85 (s, 12H), 4.74 (m, 12H), 1.20 (s, 4H) ppm.

**4** = [Co(6-(N-1,2,4-triazoyl)-2,2'-bipyridine)<sub>2</sub>](PF<sub>6</sub>)<sub>2</sub>: CoCl<sub>2</sub>.6H<sub>2</sub>O (67.0 mg, 0.28 mmol) and **L4** (118 mg, 0.53 mmol) gave peach solid: 186 mg (0.23 mmol, 28 %). Calc. for C<sub>24</sub>H<sub>18</sub>CoF<sub>12</sub>N<sub>10</sub>P<sub>2</sub> (MW 795.33). <sup>1</sup>H NMR (400 MHz, acetone-d<sub>6</sub>): a single set of aromatic H was not observed; δ = 119.00 (s, 2H), 95.78 (s, 2H), 93.13 (s, 2H), 78.41 (s, 2H), 43.08 (s, 2H), 31.18 (s, 2H), 20.67 (s, 2H), 18.23 (s, 2H), 12.10 (s, 2H) ppm.

#### 5.2.4 Voltammetry studies

CV experiments were performed in deaerated 1 mM solutions of each complex, with 0.1 M TBA PF<sub>6</sub> supporting electrolyte, in HPLC-grade MeCN. A three-electrode cell was employed consisting of a Pt CE, Ag wire quasi-reference and either a Au or GC disk working electrode (1.6 and 3.0 mm diameter respectively, BASi, Alvatek, UK). WEs were polished before use with two grades of diamond slurries (3 mm and 0.25 mm, Buehler) and alumina suspension (0.05 mm, Buehler) prior to sonication in deionized water, MeOH rinsing and drying under compressed nitrogen. The quasi-reference was stabilized by galvanostatic deposition of AgPF<sub>6</sub> from saturated KPF<sub>6</sub> solution and all redox potentials were reported against Fc. Measurements were recorded using a PC-controlled Compactstat (IVIUM Technologies) and redox-couple reversibility was assessed as a function of increasing scan rate in the range of 10-1280 mV s<sup>-1</sup>.

### 5.2.5 Battery methods

Initial battery cycling experiments were conducted on 1 mM solutions of each complex in anhydrous MeCN with 0.5 M TBA PF<sub>6</sub> electrolyte in a nitrogen glove-box (MBRAUN). A H-type glass cell was employed (GC-I) consisting of two graphite rod electrodes (Goodfellow Cambridge Limited, 99.997 %, 5.0 mm diameter, ≈4 cm separation), an AEM (Fumatech, Fumasep FAP-450, 1.33 cm<sup>2</sup> area) and a magnetic stir-bar per half-cell. Prior to assembly, the electrodes were polished with fine sand paper and tissue to give a reflective surface, whereas the membrane was soaked in the test solution for at least 24 h. Precisely 9 mL of test solution was added to each compartment to be used as both the posolyte and negolyte during battery cycling. The graphite rods were then immersed to give a 22.8 cm<sup>2</sup> electroactive area. Cycling was then performed using a constant  $\pm 4.4 \mu\text{A cm}^{-2}$  current density between upper and lower thresholds  $\approx (V_{\text{cell}} - 0.6 \text{ V}) \leq V_{\text{cell}} \leq (V_{\text{cell}} + 0.6 \text{ V})$ ; where the cell potential  $V_{\text{cell}}$  is defined as the potential difference between the cathodic and anodic redox couples.

The charge-discharge performance of complex **2** was examined in the FC-I flow-cell in a nitrogen glovebox (MBRAUN) as a function of applied current density. Graphite felt was used as the electrodes (SGL Group, 8.0 cm<sup>2</sup> geometrical surface area) whereas graphite plate (C-Tech Innovation, 4 mm thickness)/brass sheet (K&S Engineering, 0.25 mm thickness) served as current collectors. An AEM (Fumatech, Fumasep FAP-450, 8.0 cm<sup>2</sup> area) was used to separate the two half-cells. The cell was filled with exactly 50 mL of 1 mM complex **2** in anhydrous 0.5 M TBA PF<sub>6</sub> MeCN electrolyte per half-cell and pumped cyclically through the cell using a peristaltic pump (Cole Parmer, MasterFlex<sup>®</sup> L/S<sup>®</sup> series fitted with Easy-Load<sup>®</sup> II pump head) at a constant flowrate of 60 mL min<sup>-1</sup>. Battery cycling was then conducted at constant current densities of 0.125 and 1.25 mA cm<sup>-2</sup> between 2.0 and 0.8 V upper and lower thresholds respectively. The same experiment was repeated using the FC-II flow-cell employing an interdigitated flow field, 1 mm carbon paper electrodes and a porous Celgard separator. 10 mL of 10 mM complex **3** in 0.1 M TBA PF<sub>6</sub> anhydrous MeCN was used in each half-cell and pumped

cyclically through the flow-cell at  $10 \text{ mL min}^{-1}$ . The cell was then cycled at  $\pm 2.4$  and  $0.48 \text{ mA cm}^{-2}$  between 2.0 and 0.8 V upper and lower thresholds respectively.

### 5.2.6 Solubility measurements

The solubility of each complex in pure MeCN was estimated by a gradual solvent addition method. The exact mass of a small sample of complex ( $\approx 10\text{-}20 \text{ mg}$ ) was initially measured using a five-decimal place balance (Mettler Toledo, UK). To which,  $\approx 10\text{-}20 \text{ }\mu\text{L}$  aliquots of anhydrous MeCN were added, by use of a  $2\text{-}200 \text{ }\mu\text{L}$  pipettor, until the solid dissolved by visual inspection. The total mass of solvent added was then measured and used to calculate the solvent volume, assuming a MeCN density of  $0.786 \text{ g cm}^{-3}$ . The saturation concentrations were then calculated and averaged over three repetitions.

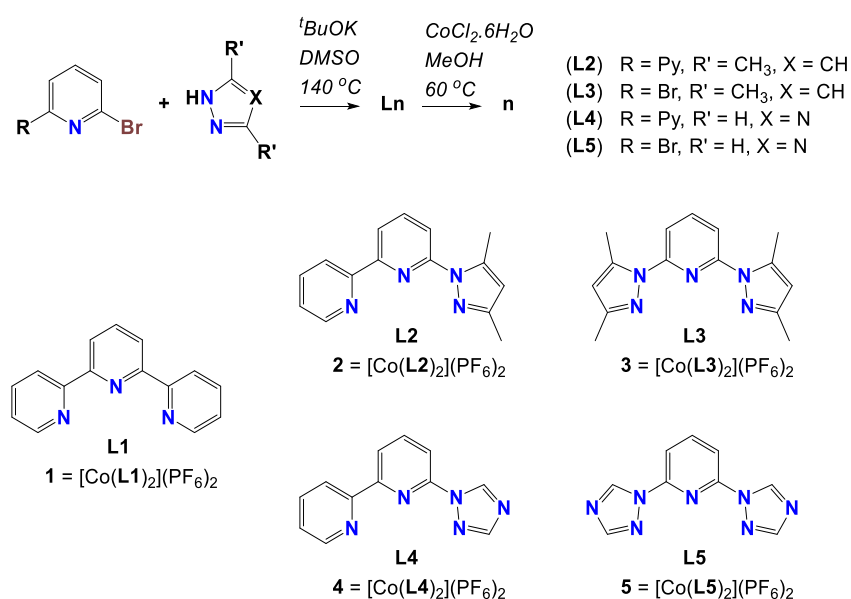
## 5.3 Results and discussion

### 5.3.1 Synthesis and characterisation

Ligands **L2-L5** and complexes **1-4** were prepared as shown in Scheme 5. Complexes **1-2** and **4** and ligand **L3** were previously reported [95,222,223,226,228,229], however complex **3** and ligand **L5** from this study were new. Synthetic yields for ligand synthesis varied in the range of 40 to 95 % which was attributed to differences in the strength of ligand precipitation from the DMSO/water mix and in the case of **L4**, the need to purify the product.  $^1\text{H}$  NMR spectra of ligands **L2** and **L4** in  $\text{CDCl}_3$  gave proton signals consistent with literature [223], whereas that of **L3** and **L5** (in  $\text{CDCl}_3$  and toluene- $d_8$  respectively) gave proton environments with the expected signal multiplicities and integrations for the symmetrical ligand structures.  $^1\text{H}$  NMR spectra of complexes **1-4** gave sharp singlets ranging from  $\delta = -0.09$  to  $119.00 \text{ ppm}$  due to the paramagnetic cobalt(II) metal centre. Chemical shifts of **2** and **4** were also consistent with literature [223] whereas **1** and **3** exhibited the expected number of proton environments. Synthetic yields for preparation of the Co(II) complexes were in the range of 28 to 79 % which was attributed to incomplete reaction of the ligands with cobalt chloride,

indicating that the reaction conditions could be further optimised to increase the synthetic yields.

Ligands **L1-L4** were all methanol-soluble white to cream solids, whereas **L5** was significantly more insoluble and required hot DMSO, THF, toluene or benzene to solvate the non-polar structure. Complexes **1-4** were air-, light- and moisture-stable dark red to pale-brown solids, which were soluble in MeCN. Complex **5** could not be produced in this study despite successful synthesis of the **L5** ligand and pyrazole analogues reported here and elsewhere [222,223,225,226,228]. It was suspected that the complexation with cobalt(II) was hindered by a combination of limiting ligand solubility, possible thermodynamic restraints such as weaker electron deficient 1,2,4-triazole  $\sigma$ -donating/ $\pi$ -accepting bonding and a significant kinetic barrier associated with the initial bonding of a terminal 1,2,4-triazole with the cobalt metal centre. However, it was speculated that its synthesis might be possible by use of a highly activated cobalt starting material featuring weakly coordinating ligands in anhydrous inert conditions.



**Scheme 5.** Synthesis of ligands **L1-L5** and cobalt(II) complexes **1-5**.

### 5.3.2 Solubilities in MeCN

The solubilities of complexes **1-4** are  $\approx 0.18$ ,  $0.22$ ,  $0.50$  and  $0.16\text{ mol dm}^{-3}$  respectively. Comparatively low solubilities to other published MCCs were

expected due to the low polarity of the tridentate ligands. As such, measured values were found to be of similar magnitude, however a 0.34 M variation was observed across the set due to structural differences of the ligands. Solubility of complexes in series **1**, **2**, **3** increased with the number of substituted 3,5-dimethylpyrazole groups (from 0 to 2 to 4) due to more favourable interactions between the ligand methyl groups and the polar MeCN solvent. In contrast, substitution with 1,2,4-triazoles resulted in a loss of ligand polarity and complex solubility. It was therefore speculated that complex **5** would have been the least soluble in this study making its use undesirable. Corresponding theoretical energy densities for complexes **1-4** were calculated to be 2.58, 4.03, 12.80 and 3.24 W h L<sup>-1</sup> respectively (equation ( 2.4.6 )). Thus, the highest theoretical energy density was achieved by complex **3** due to a combination of its higher cell potential and superior solubility. Therefore, full substitution with 3,5-dimethylpyrazoles resulted in a five-fold increase of energy density compared to the initial 2,2':6',2''-terpyridine complex.

### 5.3.3 Voltammetry behaviour of Co(II) complexes

The electrochemical behaviour of complexes **1-4** was investigated as a function of scan rate and electrode material. As shown in Figure 48, complexes **1** and **2** exhibited three redox couples whereas complexes **3** and **4** exhibited only two. Starting from a Co(II) oxidation state, the complexes can be oxidised or reduced to the Co(III) and Co(I) oxidation states respectively, however for complexes **1** and **2** a further reduction at lower potentials was observed. Given that the second reduction would yield a formal Co(0) oxidation state, it was concluded that this process corresponds to reduction of the ligand as pyridine and bipyridine are known to be redox active organic molecules [189]. Extra redox couples for cobalt complexes with bis(acetylaceton)ethylenediamine and 1,10-phenanthroline ligands have been reported but not assigned [122,132,139], hence it is also likely that these processes are ligand-centric reductions which result in radical anion formation. Therefore, the electrochemistry of the Co complexes can be generalised as:

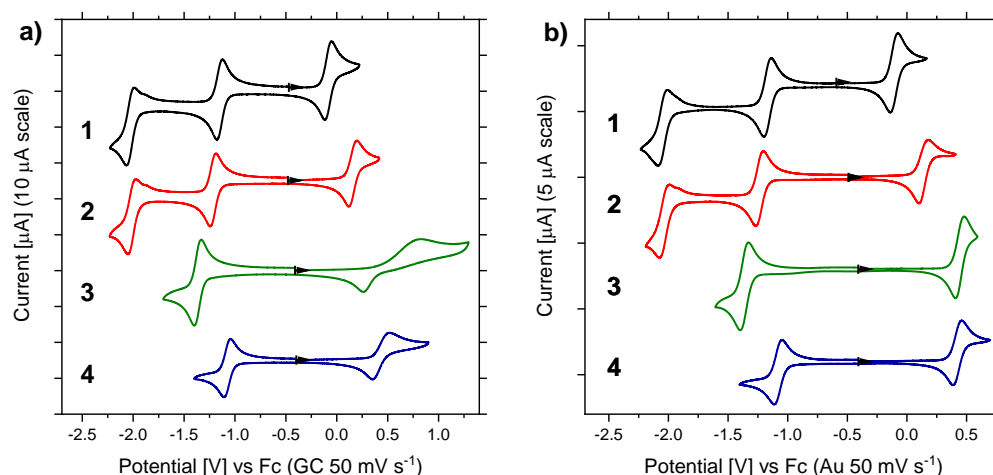
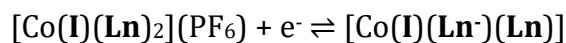
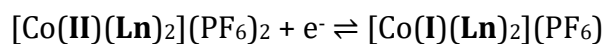
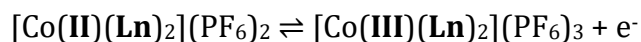


**Figure 48.** First cyclic voltammograms of 1 mM cobalt(II) complexes 1-4 on a) GC and b) Au electrode in 0.1 M TBA PF<sub>6</sub> MeCN solution at 50 mV s<sup>-1</sup>. Arrows indicate the start point of cyclic voltammetry.

A NA-RFB can be constructed by utilising the Co(III/II) redox couple in the posolyte and either Co(II/I) or L/L<sup>-</sup> in the negolyte, to give cell potentials,  $V_{\text{cell}}$ , in the region of 1.06-2.17 V. Complex **2** gave the largest cell potential (2.17 V) when cycled between the Co(III) and L<sup>-</sup> oxidation states, however complex **3** gave the largest potential difference between the cobalt oxidation states of 1.81 V. Utilisation of ligand redox couples would therefore yield higher cell potentials however undesirable initial electrolysis of the Co(II) electrolyte, akin to the VRFB, would be required to produce the Co(I) electrolyte. Furthermore, given that only complexes **1** and **2** presented with reversible ligand reductions, (**4** gave irreversible response and **3** completely lacked any ligand response) it is likely that the L<sup>-</sup> oxidation state is less stable than the Co oxidation states. This behaviour suggests that the reversible azole-pyridine ligand response originates from the reduction of the bipyridine unit [122,189], however its stability is dependent on the electron deficiency of the terminal group; 1,2,4-triazole is significantly more

electron deficient than pyridine, therefore it destabilises the bipyridine reduced species. Thus, azole-pyridine ligands are capable of non-innocent behaviour as long as they comprise a bipyridine unit and their terminal donor group is not significantly electron deficient [223].

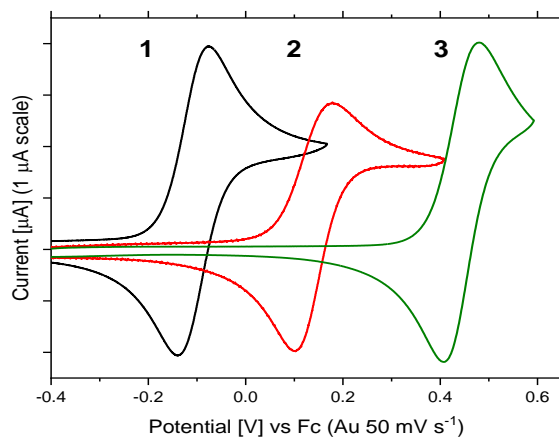


**Figure 49. Overlay of the first scan CVs of the Co(III/II) redox couple, of complexes 1-3, representing the stepwise substitution of terminal 2,2':6',2''-terpyridine pyridyl groups with 3,5-dimethylpyrazole donor groups. 1 mM complex in 0.1 M TBA PF<sub>6</sub> MeCN solution at 50 mV s<sup>-1</sup> on Au electrode.**

Redox potentials of the cobalt couples were found to be dependent on the ligand structure and electron deficiency of its terminal azole donors [223,228], whereas ligand potentials have been shown to vary little with changes in structure [223]. Successive replacement of terminal pyridine donors with weaker  $\sigma$ -donating/ $\pi$ -accepting 3,5-dimethylpyrazoles (in series **1**, **2**, **3**) positively shifts the Co(III/II) couple by approximately 275 mV per substitution (Figure 49), whereas the Co(II/I) couples are negatively shifted  $\approx$  100 mV (on average). In contrast, replacement with electron-deficient 1,2,4-triazole resulted in significant positive shifts of both cobalt redox couples and a dramatic loss of the Co(III/II) reversibility on GC. As a result of these potential shifts, the potential difference between the cobalt redox couples also increases; from 1.07 to 1.37 to 1.81 V for complexes **1**, **2** and **3** respectively (on GC). It was therefore expected that complex **5** would have produced the largest potential difference between the cobalt oxidation states, and likely the largest cell potential, as the cobalt potential difference of complex **4** was

larger than that of **3**; 1.51 and 1.37 V respectively. Despite this, the trend of Co(III/II) reversibility as a function of terminal ligand donor strength, means that the Co(III/II) redox couple of complex **5** would likely be irreversible or at least less reversible than that of complex **3**.

In general, the redox couples were reversible processes giving forward and reverse diffusion limited peaks which were highly symmetric. Whereas the redox potentials of each process were found to be invariant of the electrode material, their electrochemical reversibility were found to be dependent as shown in Figure 48. Taking the peak separation of each redox couple (Table 7) as a simple measure of electrochemical reversibility, a clear trend is observed: the Co(II/I) redox couples were found to be the most reversible processes giving peak separations of less than 70 mV which showed little variation on either GC or Au. In contrast, the Co(III/II) and L/L<sup>-</sup> couples gave larger peak separations in excess of 70 mV, consistent with quasi-reversible behaviour, and more significant variation with electrode material. This trend was in agreement with previous literature whereby the Co(III/II) couples were more reversible on Au while Co(II/I) and L/L<sup>-</sup> were better on GC [223]. This behaviour was the most extreme for complex **3** and **4** where the peak separations of the Co(III/II) redox couple on GC electrode were much larger; 566 and 165 mV respectively. This behaviour can be rationalised as a significant decrease in the standard electrochemical rate constant on GC in comparison to the more catalytic Au, thus giving irreversible or severely quasi-reversible electrochemistry for **3** and **4** respectively. Such behaviour is undesirable for application in RFBs as the battery architecture typically uses carbon-based electrodes to minimise the technology cost.

**Table 7. Redox potentials, as measured from cyclic voltammograms at 50 mV s<sup>-1</sup>, of cobalt(II) complexes in 0.1 M TBA PF<sub>6</sub> MeCN solution, reported relative to Fc. Peak separations are given in parentheses and redox potentials are rounded to three significant figures.**

Complex	Electrode	L/L <sup>-</sup> E <sub>1/2</sub> [V] vs Fc	Co(II/I) E <sub>1/2</sub> [V] vs Fc	Co(III/II) E <sub>1/2</sub> [V] vs Fc	ΔE [V], Co(II) Co(III)   L L <sup>-1</sup>	ΔE [V], Co(II) Co(III)  Co(II) Co(I)
1	GC	-2.03 (79)	-1.15 (57)	-0.09 (63)	1.94	1.06
	Au	-2.05 (77)	-1.17 (59)	-0.11 (64)		
2	GC	-2.01 (78)	-1.22 (55)	0.16 (79)	2.17	1.38
	Au	-2.03 (83)	-1.24 (61)	0.14 (77)		
3	GC	-	-1.37 (69)	0.54 (566)	-	1.81
	Au	-	-1.37 (68)	0.44 (74)		
4	GC	-	-1.08 (64)	0.43 (165)	-	1.50
	Au	-	-1.08 (65)	0.42 (71)		

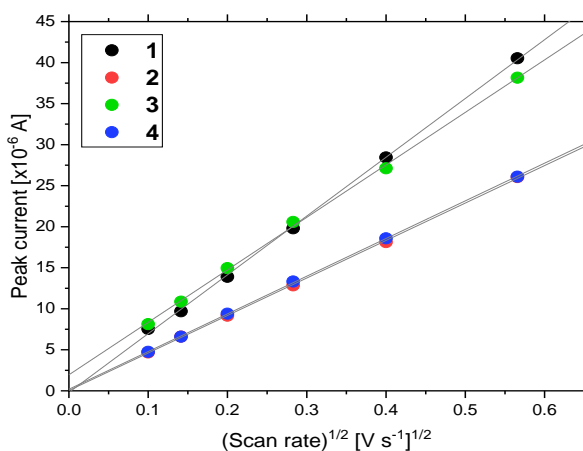


**Figure 50. Randles-Sevcik plot for complexes 1 – 4 at 1 mM concentration in 0.1 M TBA PF<sub>6</sub>, MeCN electrolyte at room temperature. Peak currents were measured via baseline extrapolation of the Co(II/I) cathodic peakon on first scan.**

To assess the reversibility of the cobalt redox couples, the electrochemistry was investigated as a function of scan rate in the range of 10 to 1280 mV s<sup>-1</sup> as shown in Figure 51. In general, the peak potentials showed little variation with scan rate, giving near constant peak separations, which indicated fully reversible to slight quasi-reversible behaviour. In exception, the Co(III/II) redox couples on GC

showed increasingly divergent peak potentials as a function of scan rate suggesting quasi-reversible to irreversible behaviour. By use of the most reversible redox couples (Co(II/I) on GC), the diffusion coefficient of each complex was measured by use of the Randles-Sevcik equation in the range of 10 to 320  $\text{mV s}^{-1}$ . Plots of the peak cathodic current against the square-root of scan rate gave linear relationships with intercepts less than 2  $\mu\text{A}$  and  $R^2$  greater than 0.99 as shown in Figure 50. Corresponding diffusion coefficients were calculated to be  $1.45 \times 10^{-5}$ ,  $5.91 \times 10^{-6}$ ,  $1.16 \times 10^{-5}$  and  $5.97 \times 10^{-6} \text{ cm}^2 \text{ s}^{-1}$  for complexes **1** - **4** respectively. Such diffusion coefficients were found to be comparable or in excess of similar MCCs in the literature under similar electrolyte conditions;  $2.9 \times 10^{-6} \text{ cm}^2 \text{ s}^{-1}$  for  $\text{V}(\text{acac})_3$  [129] and  $4.35 \times 10^{-6} \text{ cm}^2 \text{ s}^{-1}$  for  $[\text{Co}(\text{phen})_2](\text{PF}_6)_2$  [131].

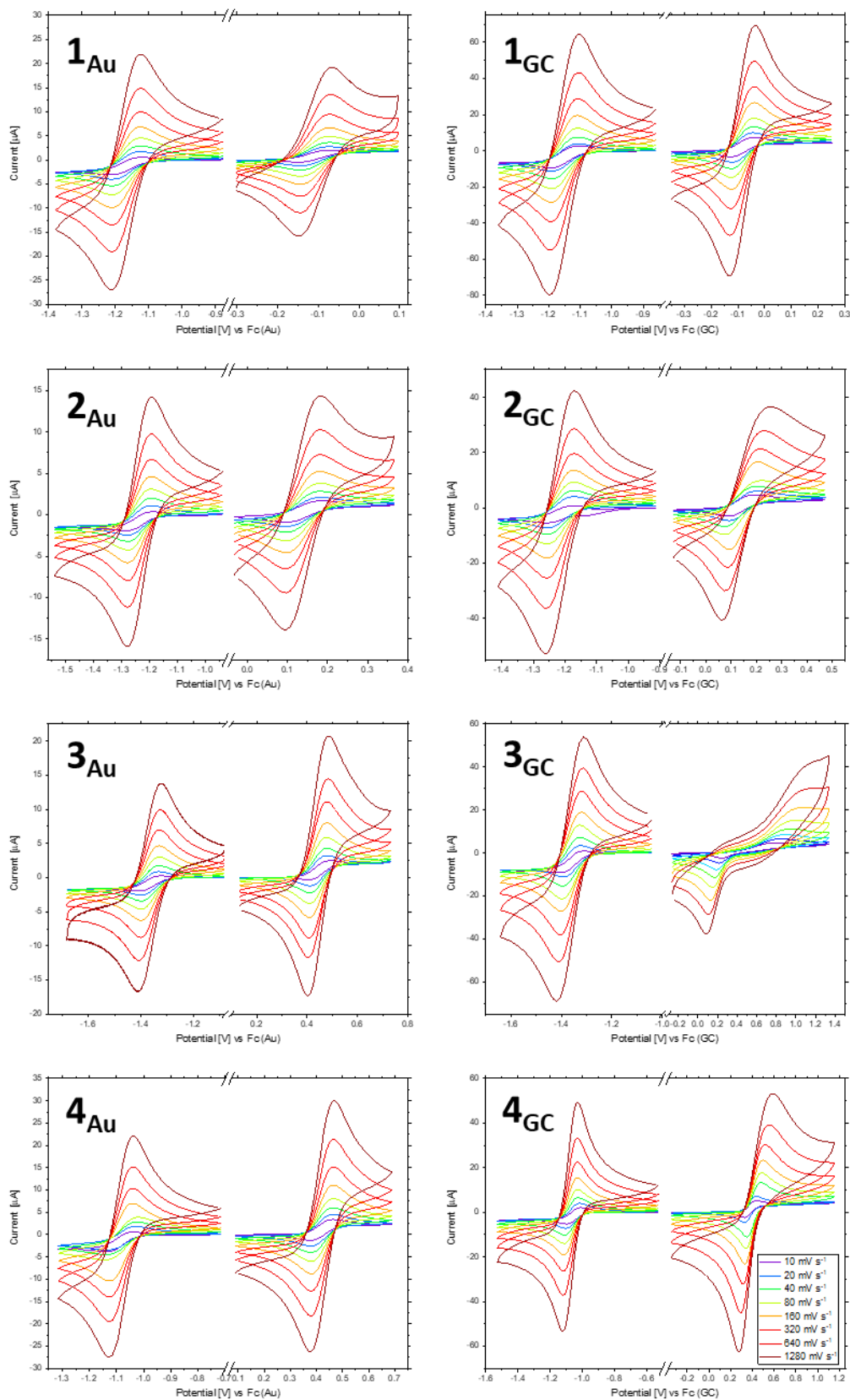


**Figure 51. Second scan CVs of 1 mM complex in 0.1 M TBA PF<sub>6</sub> MeCN solution as a function of scan rate. Left) Co(II/I) redox couple. Right) Co(III/II) redox couple.**

### 5.3.4 Electrochemical kinetics

Standard electrochemical rate constants were measured by use of the Koutecký-Levich method as shown in Figure 53 to Figure 55. Linear sweep voltammograms at rotation rates in the range of 300 to 3000 rpm were recorded at  $50 \text{ mV s}^{-1}$  on both Au and GC electrodes. In the case of the Co(II/I) redox couples for complexes **1-4** (and for the L/L<sup>-</sup> of complexes **1** and **2**), well defined plateaus and convection limited currents were observed on both GC and Au electrode. These plateaus gave reliable Koutecký-Levich plots and corresponding rate constants in the range of  $8.43 \times 10^{-3}$  to  $1.38 \times 10^{-2} \text{ cm s}^{-1}$  were measured. With the exception of complex **3**, the rate constants on GC and Au were approximately equal, indicating that the electrochemistry of the Co(II/I) redox couples is generally invariant of the electrode material. In contrast, the Co(III/II) redox couples were less consistent and showed dependency on the electrode material; whereas complex **1** gave similar Co(III/II) response on both Au and GC, complexes **2-4** generally gave limiting currents on Au but not on GC. This behaviour can be attributed to the much lower rate constants of these redox couples on GC (approximately one order-of-magnitude less than on Au) and their corresponding quasi-reversible/irreversible electrochemistry, such that significantly higher overpotentials are required to give convection-limited currents. Corresponding Koutecký-Levich plots were less reliable such that the linear fits were of poor quality and unexpected behaviour in the data was observed at high rotation rates.

The unusual behaviour of the Co(III/II) redox couples was attributed to the visible adsorption of the Co species to the electrode surface. As observed by Shavaleev et al. [223], the reversibility of the Co(III/II) couples was found to be dependent on the electrode history such that their reproducibility was lost when the Co(II/I) couple was cycled in the same scan due to adsorbed reduced Co species [223]. The same behaviour was observed in the present work during cyclic voltammetry experiments, particularly for complexes **3** and **4**, however in the enhanced hydrodynamic RDE studies, a similar effect was observed for the Co(III/II) redox couples despite only operating the WE at anodic potentials. Starting from a freshly polished electrode, the RDE LSVs of the Co(II/I) couples

could be reliably and reproducibly recorded without further polishing. In contrast, the Co(III/II) RDE studies gave less reproducible voltammograms such that polishing between each scan was required to prevent the accumulation of Co adsorbates, which would otherwise affect the current response on future scans.

**Table 8. Standard electrochemical rate constants for complexes 1-4 on Au and GC electrode as measured by the Koutecký-Levich method. Meaningful RDE LSVs of the Co(III/II) redox couple for complex 3 could not be achieved due to (a) excessive overpotential and (b) irreproducible results due to high sensitivity of the kinetics on the electrode surface. (c) The quality of the data and analysis was poor, giving an unreliable rate constant and an unlikely transfer coefficient.**

Complex	Electrode	Co(II/I) $k^0$ [cm s <sup>-1</sup> ] ( $\beta$ )	Co(III/II) $k^0$ [cm s <sup>-1</sup> ] ( $\alpha$ )
1	GC	$1.37 \times 10^{-2}$ (0.62)	$8.91 \times 10^{-3}$ (0.46)
	Au	$1.31 \times 10^{-2}$ (0.70)	$1.50 \times 10^{-2}$ (0.72)
2	GC	$1.35 \times 10^{-2}$ (0.64)	$3.54 \times 10^{-3}$ (0.36)
	Au	$1.38 \times 10^{-2}$ (0.66)	$1.49 \times 10^{-2}$ (0.76)
3	GC	$8.43 \times 10^{-3}$ (1.03)	(a)
	Au	$7.66 \times 10^{-3}$ (1.51) (c)	(b)
4	GC	$1.24 \times 10^{-2}$ (0.77)	$1.27 \times 10^{-3}$ (0.26)
	Au	$1.37 \times 10^{-2}$ (0.70)	$1.10 \times 10^{-2}$ (0.50)

This behaviour indicated that the rate constant for the Co(III/II) redox couples are very sensitive to the nature of the electrode surface such that the presence of adsorbed Co(I) or Co(III) species passivates the electrode surface or makes the electrode less-catalytic. Therefore, under mass-transport enhanced high-current conditions such as in a flow battery, it is expected that the Co(III/II) redox couple will limit the battery performance due to its slower kinetics and sensitivity to the electrode surface. This effect is further demonstrated in Figure 63 (section 5.3.6) whereby the voltammetry of a recovered battery electrolyte of complex 2 shows irreversible kinetics of the Co(III/II) redox couple at a freshly polished GC electrode. This indicates that the Co(I) and/or Co(III) oxidation states immediately adsorb to the electrode surface whenever present in solution.

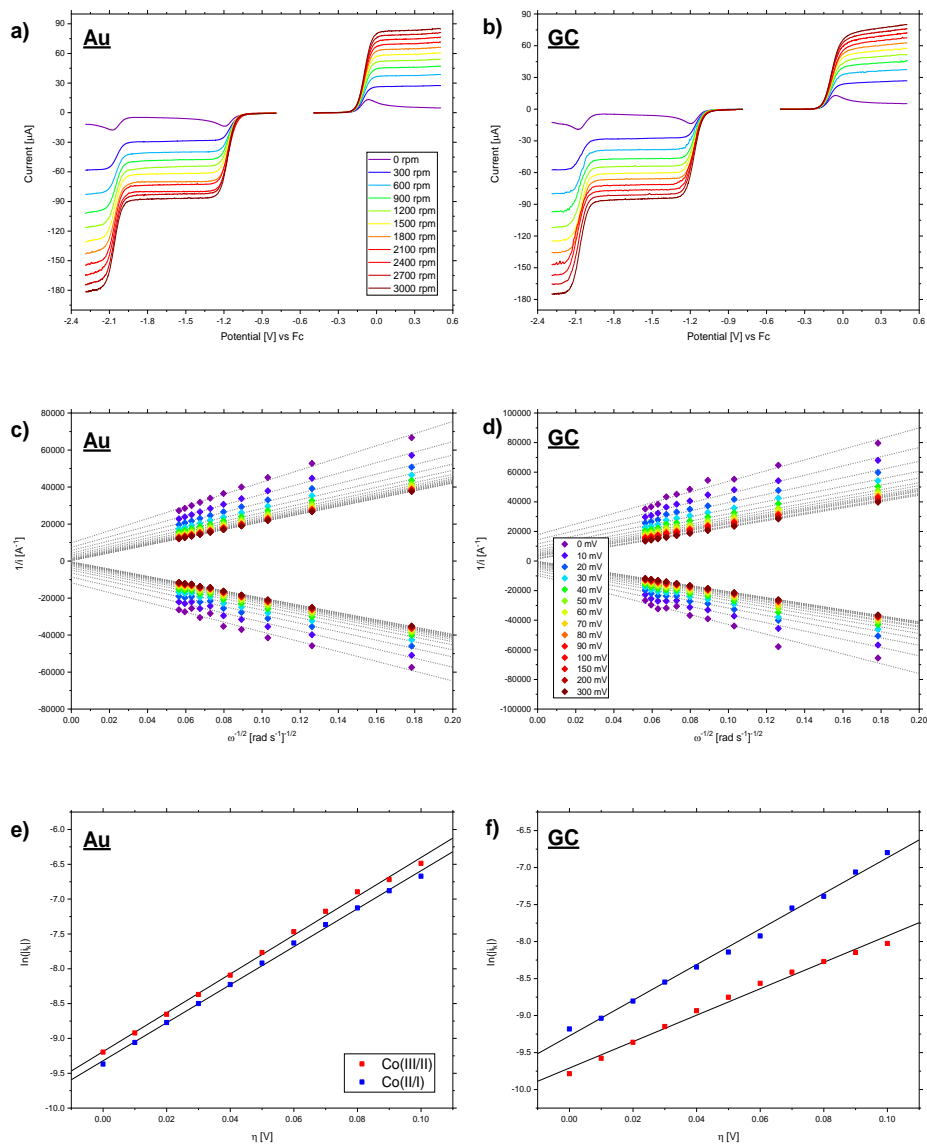


**Figure 52. Koutecký-Levich analysis of 1 mM complex 1 in 0.1 M TBA PF<sub>6</sub> at Au (graphs a, c and e) and GC (graphs b, d and f) electrode. a/b) RDE LSVs as a function of rotation rate. c/d) Koutecký-Levich graphs for overpotentials 0 to 300 mV. e/f) logarithm of the kinetically limited current as a function of overpotential.**

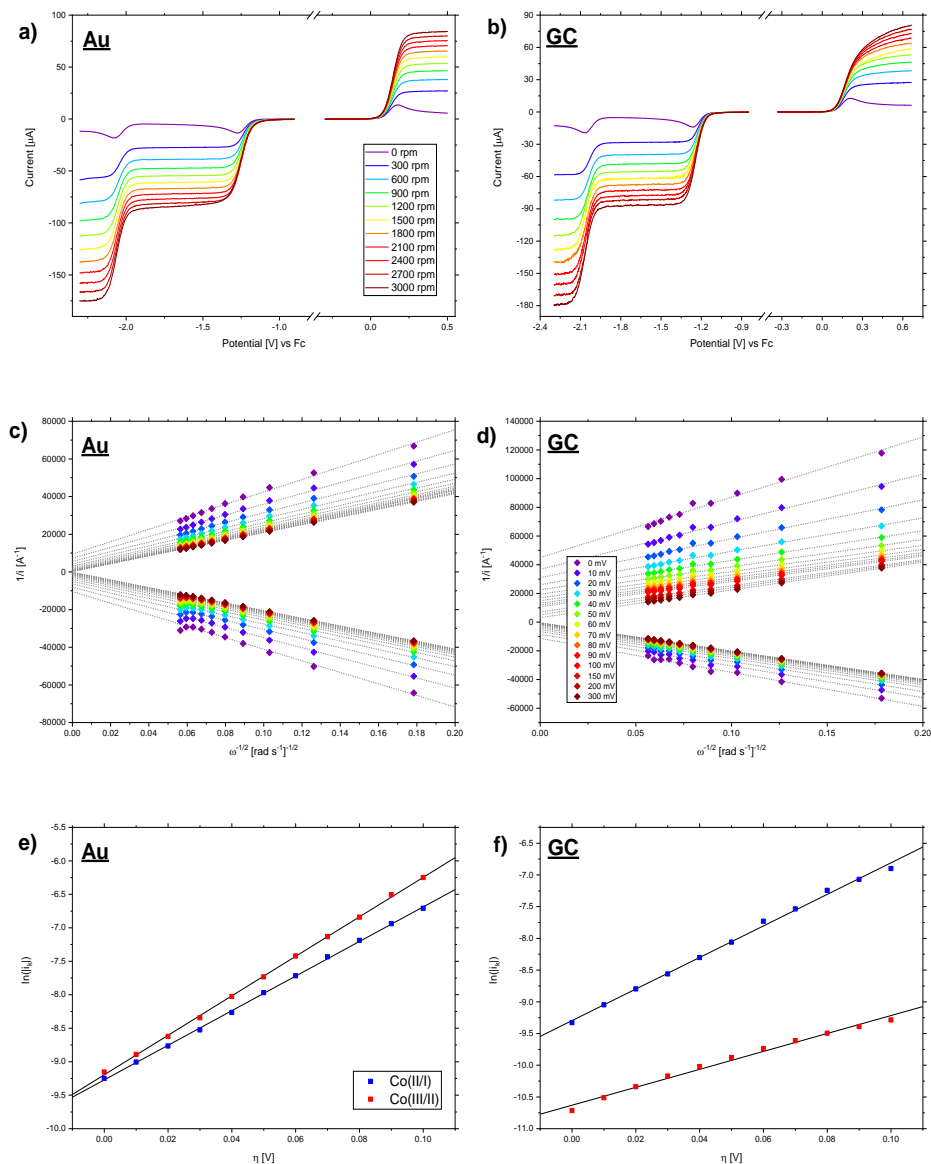


**Figure 53. Koutecký-Levich analysis of 1 mM complex 2 in 0.1 M TBA PF<sub>6</sub> at Au (graphs a, c and e) and GC (graphs b, d and f) electrode. a/b) RDE LSVs as a function of rotation rate. c/d) Koutecký-Levich graphs for overpotentials 0 to 300 mV. e/f) logarithm of the kinetically limited current as a function of overpotential.**

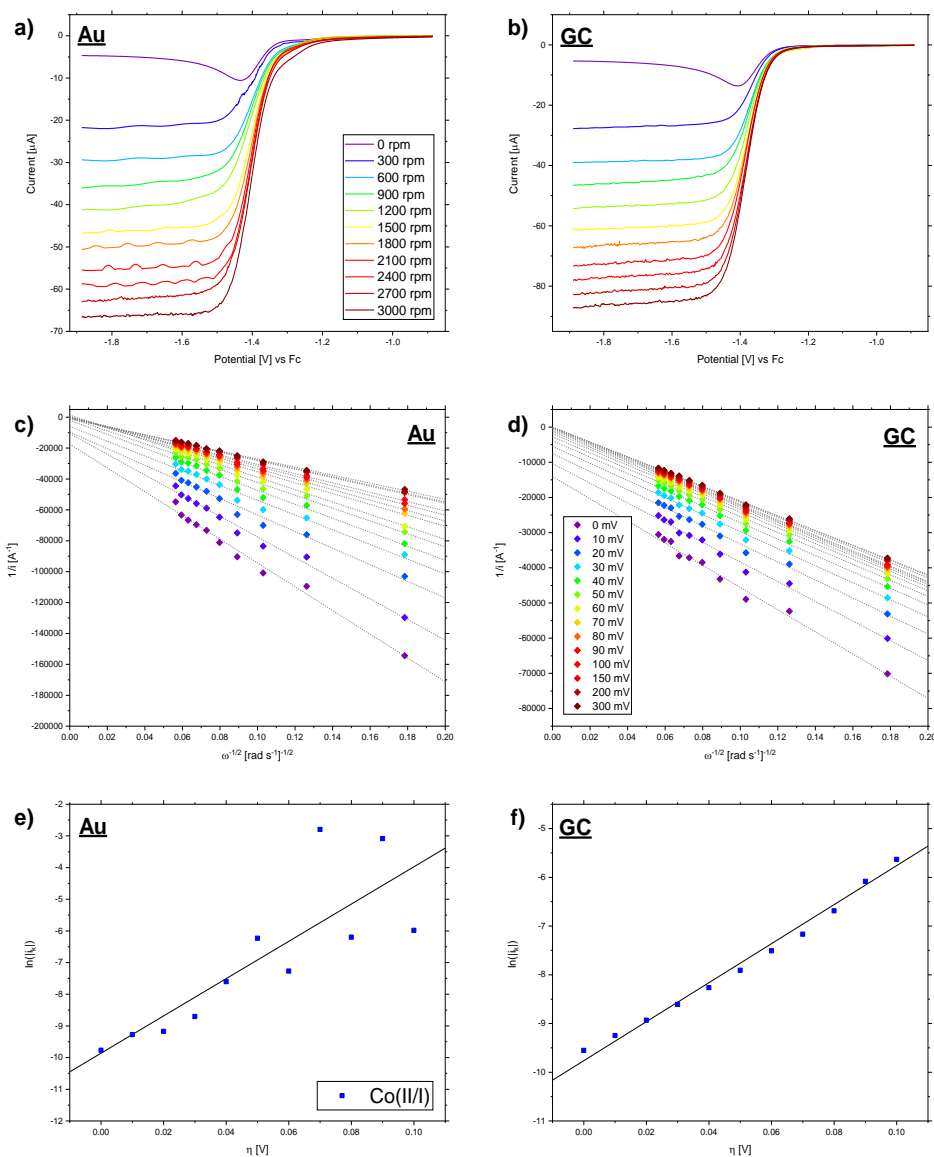


**Figure 54. Koutecký-Levich analysis of 1 mM complex 3 in 0.1 M TBA PF6 at Au (graphs a, c and e) and GC (graphs b, d and f) electrode. a/b) RDE LSVs as a function of rotation rate. c/d) Koutecký-Levich graphs for overpotentials 0 to 300 mV. e/f) logarithm of the kinetically limited current as a function of overpotential.**

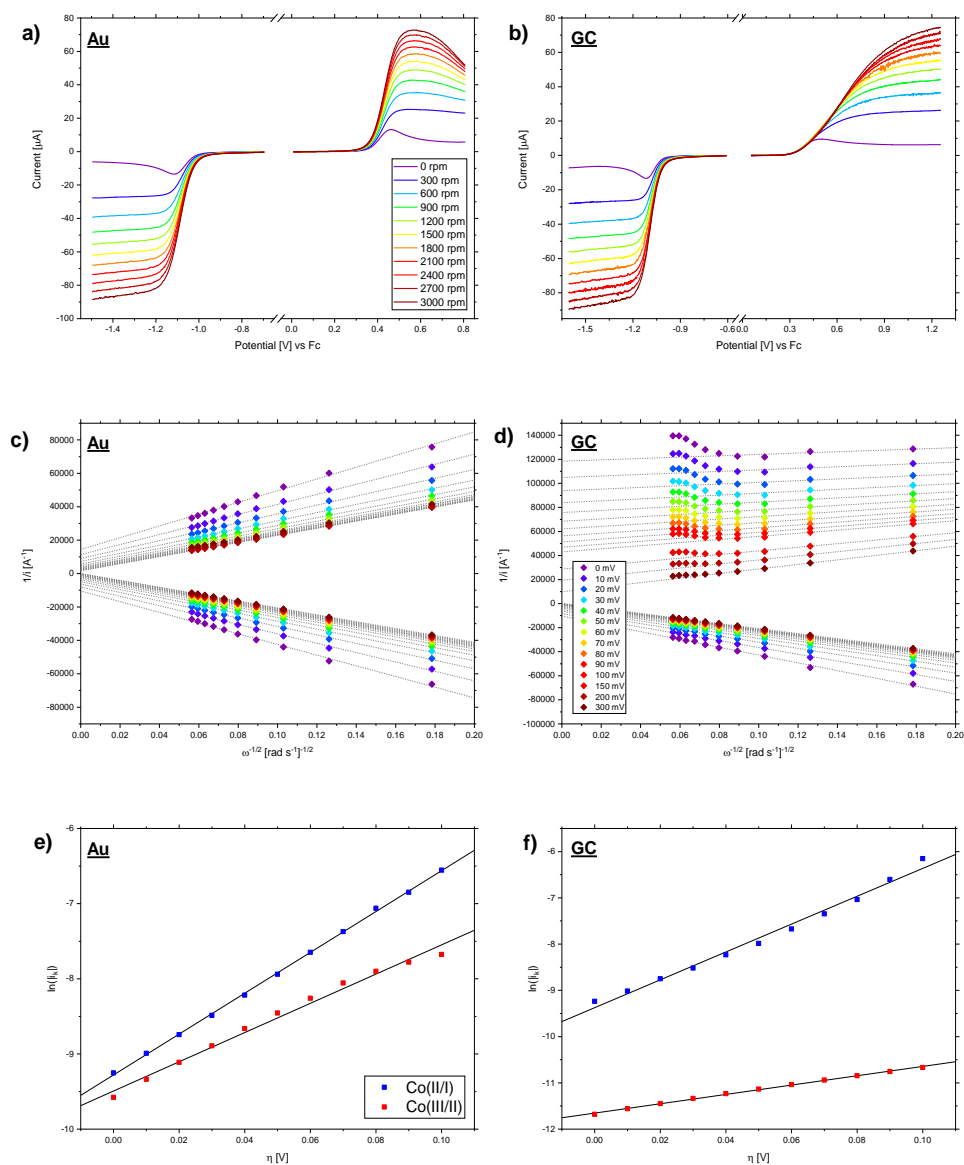


**Figure 55.** Koutecký-Levich analysis of 1 mM complex 4 in 0.1 M TBA PF<sub>6</sub> at Au (graphs a, c and e) and GC (graphs b, d and f) electrode. a/b) RDE LSVs as a function of rotation rate. c/d) Koutecký-Levich graphs for overpotentials 0 to 300 mV. e/f) logarithm of the kinetically limited current as a function of overpotential. The linear fits of the Co(III/II) on GC in d) are based on rotation rates of 300 to 1500 rpm.

The electrochemical behaviour of the Co complexes and the observed rate constants can be rationalised by considering the electronic structure of the Co complexes as shown in Figure 56. The two tridentate ligands coordinate with the

metal centre to create a pseudo-octahedral environment which results in a classic electronic structure consisting of three nonbonding  $t_{2g}$ -like molecular orbitals (MOs) [ $d(xy)$ ,  $d(yz)$  and  $d(zx)$ ] and two  $e_g$ -like antibonding MOs [ $d(z^2)$  and  $d(x^2-y^2)$ ]. These orbitals are populated with the d-electrons in either a high- or low-spin configuration which depends on the strength of the crystal field splitting and therefore the field strength of the ligands. In the Co(III) oxidation state, the complexes exist as a stable 18-electron Co(III)- $d^6$  low-spin electronic configuration because the crystal field splitting energy exceeds the pairing energy of the low-spin electrons [140]. When this is reduced, an electron is injected into the LUMO to give a 19-electron Co(II)- $d^7$  low-spin configuration in which the axial Co-N bonds are lengthened and the  $d(z^2)$ -based  $\sigma^*$ -MO is lowered in energy (a Jahn-Teller distortion). However, this structure is expected to be unstable because of geometrical strain and because the elongated Co-N bonds may be easily cleaved. Instead, like other first-row transition metals, the complex undergoes spin-crossover [229] into the more energetically-favourable Co(II)- $d^7$  high-spin configuration. Thus, the exchange energy between the unpaired electron-spins lowers the total energy of the complex and results in a less-strained and a less-reactive complex.

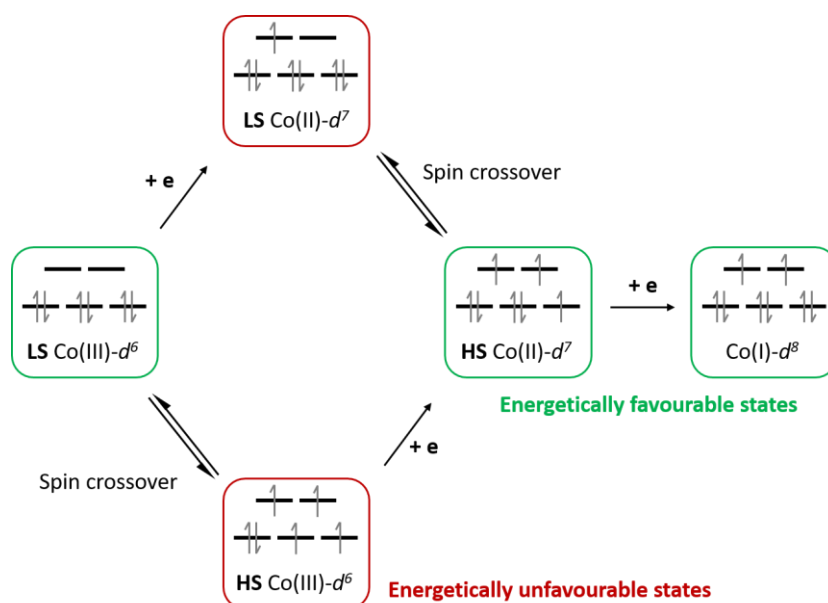


**Figure 56. Conceptual diagram for the spin crossover of the  $[\text{Co(III/II)(Ln)}_2]^{2+/3+}$  redox couple.**

This spin crossover phenomenon has been known to occur in many complexes of Co(III/II) such as the terpyridine complex **1** [229,230] and has been proven experimentally by various spectroscopic techniques and theoretical calculations. In contrast, the reduction of Co(II)-d<sup>7</sup> to Co(I)-d<sup>8</sup> is more straight forward because the octahedral geometry gives only one possible electronic configuration, and therefore no spin crossover occurs. The difference in the measured electrochemical rate constants between the Co(III/II) and Co(II/I) redox couples can therefore be attributed to the change in electronic configuration and associated geometry changes of the Co(III/II) redox transition [140].

### 5.3.5 Charge-discharge performance in H-type glass cell

Battery cycling of complexes **1-4** in a H-type glass cell was evaluated using 1 mM of complex in 0.5 M TBA PF<sub>6</sub> electrolyte as shown in Figure 57 to Figure 60. Charging of the orange Co(II) electrolytes gave yellow Co(III) polysolutes and red or green Co(I) negolytes for complexes **1** and **2-4** respectively. On discharge, the original orange electrolyte was recovered indicating that the Co redox couples could be reversibly cycled in the battery. Each complex was cycled 10 times between upper and lower thresholds which were sufficiently over/under the cell potential to allow complete charge/discharge, but not too large as to avoid charge transfer to unwanted processes such as the ligand reduction. Due to the large ohmic resistance and inferior mass transport as compared to a flow-cell, a low 100  $\mu\text{A}$  ( $\pm 4.4 \mu\text{A cm}^{-2}$ ) current, corresponding to a C-rate of 0.41C, was required to charge-discharge the cell. Attempts to cycle the H-cell at higher current densities resulted in considerable overpotential and inefficient battery cycling because upper/lower potential thresholds were reached before complete charge/discharge occurred.

Battery cycling curves, shown in Figure 57b to Figure 60b displayed very well-defined charge-discharge plateaus which corresponded to the expected cell potentials thus indicating that the cell was utilising the intended Co(III/II) and Co(II/I) redox couples. For complexes **1,2** and **4** the cell potential showed an approximately Nernstian dependence, indicating that the cell potential was almost

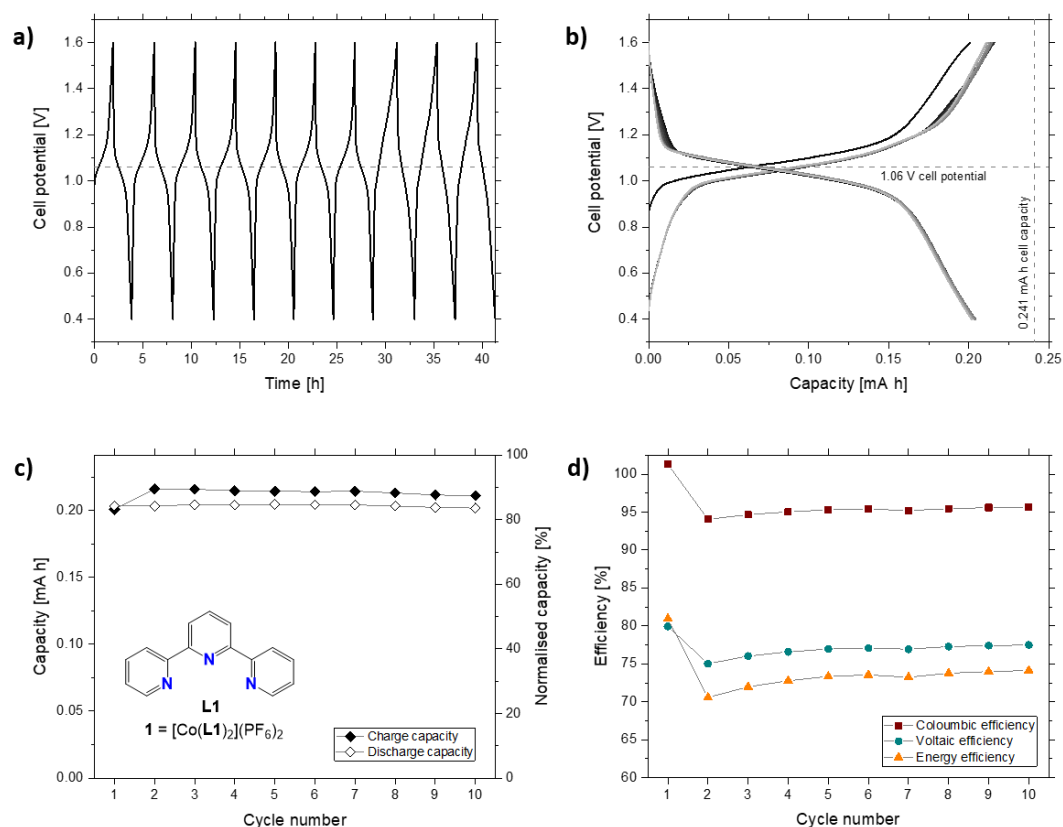


**Figure 57. a) Charge-discharge cycles of 1 mM complex 1 in 0.5 TBA PF<sub>6</sub> MeCN solution at  $\pm 4.4 \mu\text{A cm}^{-2}$  between 1.6 and 0.4 V upper and lower potential thresholds in GC-I. b) evolution of charge-discharge curves as a function of capacity. c) Charge-discharge capacities as a function of cycle number. d) Cycling efficiencies as a function of cycle number.**

exclusively dependent on the state-of-charge, and without significant contributions from kinetic or mass-transport overpotential. However, in the case of complex **3**, significantly more overpotential was observed such that the charge/discharge plateaus were approx. 200 mV above/below the cell potential respectively. Given that the same convection within the H-cell was used for each complex, the mass transport of each complex to the electrode surface was approximately equal. Therefore, the observed overpotential must be attributed to slower electrochemical kinetics of complex **3** compared to the others. This is supported by the cyclic voltammetry in Figure 48, whereby the GC electrode was significantly less catalytic towards the Co(III/II) redox couple as compared to the other complexes, hence the observed overpotential during battery cycling can be

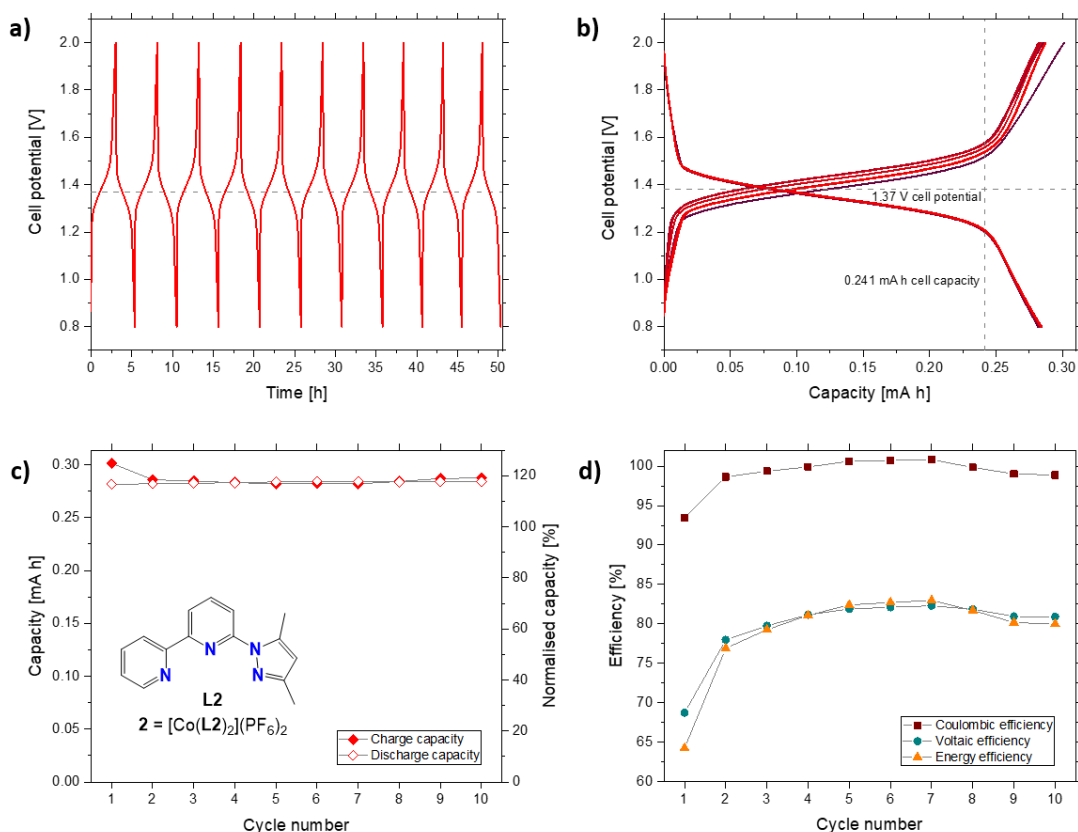
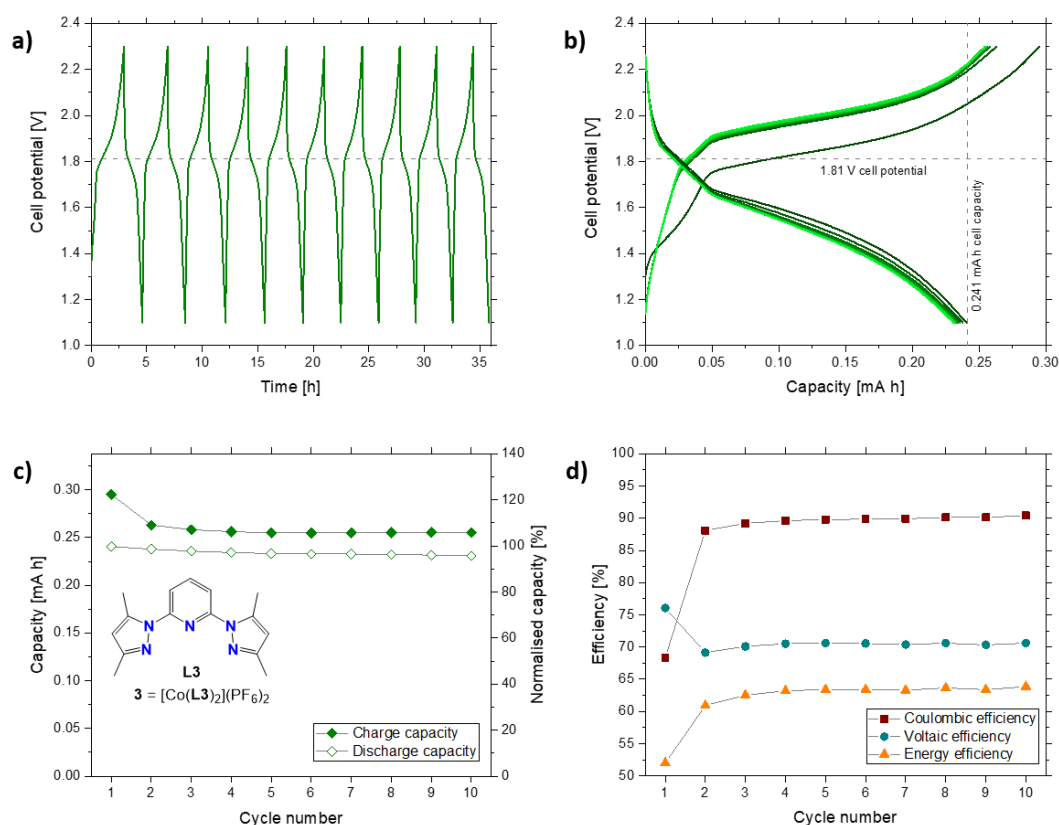


**Figure 58.** a) Charge-discharge cycles of 1 mM complex 2 in 0.5 TBA PF<sub>6</sub> MeCN solution at  $\pm 4.4 \mu\text{A cm}^{-2}$  between 2.0 and 0.8 V upper and lower potential thresholds in GC-I. b) evolution of charge-discharge curves as a function of capacity. c) Charge-discharge capacities as a function of cycle number. d) Cycling efficiencies as a function of cycle number.

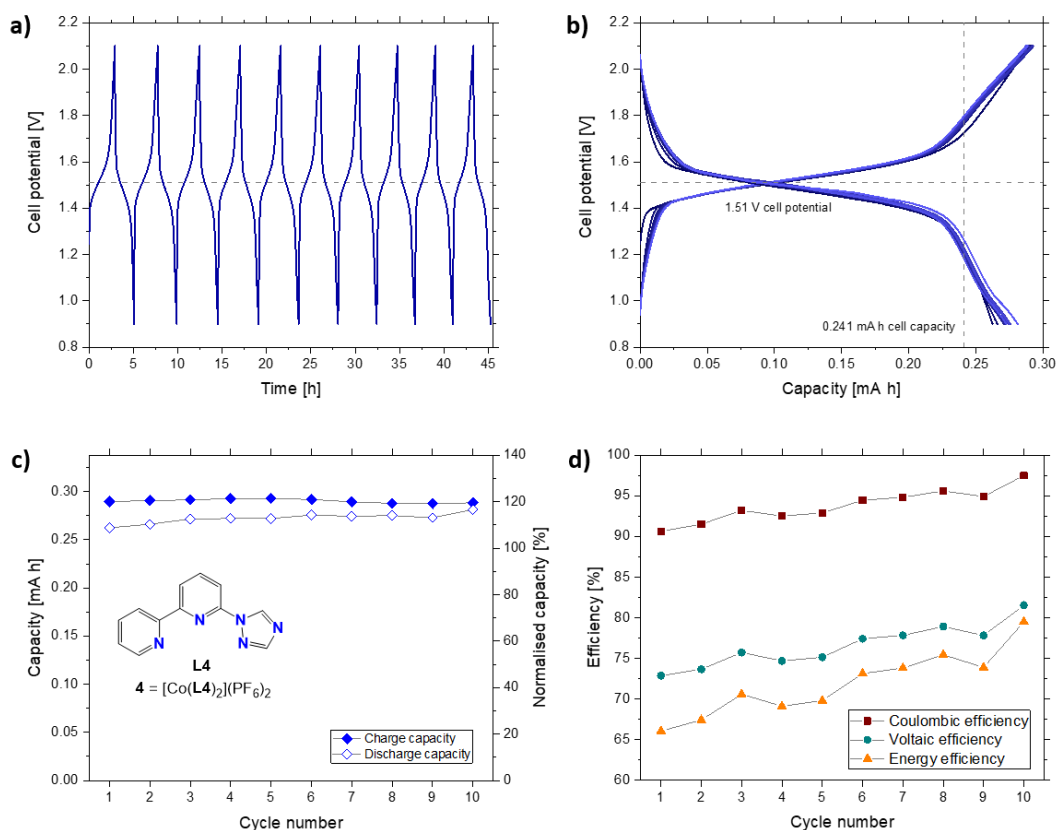
attributed to the slow Co(III/II) kinetics on the applied graphite electrodes. Poor performance of complex 3 at the low current density applied is not promising for application, however the kinetic response may be improved via utilising a more catalytic electrode material.

Figure 57c to Figure 60c shows the capacity achieved by each complex with respect to the theoretical capacity of 0.24 mA h. Complexes 1 to 4 all achieved capacities which were consistent with the theoretical capacity ( $> 0.2$  mA h) which indicated that SOC close to 100 and 0 % on charge and discharge were accessed, respectively. Whereas complex 1 cycled below the theoretical capacity (approx. 90 % on charge), complexes 2-4 all exceeded the theoretical capacity during cycling, giving  $\approx 120$ , 105 and 120 % on charge respectively. This discrepancy can be

attributed to self-discharge of the charged electrolytes through the membrane over the long cycling timescales ( $\approx 4.8$  h per cycle) which caused self-discharge during cycling. This phenomenon also explains the observed hysteresis between the charge and discharge capacity for each complex during cycling because membrane crossover in a symmetric RFB causes the charge/discharge capacity to be lengthened/shortened respectively. Despite the inconsistent capacities, the results demonstrate the high capacity retention of each complex, such that near-constant capacity on charge and discharge was observed over 10 cycles, corresponding to high capacity retention of each complex for at least 35 to 50 hours.



**Figure 59. a) Charge-discharge cycles of 1 mM complex 3 in 0.5 TBA PF<sub>6</sub> MeCN solution at  $\pm 4.4 \mu\text{A cm}^{-2}$  between 2.3 and 1.1 V upper and lower potential thresholds in GC-I. b) evolution of charge-discharge curves as a function of capacity. c) Charge-discharge capacities as a function of cycle number. d) Cycling efficiencies as a function of cycle number.**



**Figure 60. a) Charge-discharge cycles of 1 mM complex 4 in 0.5 TBA PF<sub>6</sub> MeCN solution at  $\pm 4.4 \mu\text{A cm}^{-2}$  between 2.1 and 0.9 V upper and lower potential thresholds in GC-I. b) evolution of charge-discharge curves as a function of capacity. c) Charge-discharge capacities as a function of cycle number. d) Cycling efficiencies as a function of cycle number.**

The performance of each complex was also assessed in terms of the coulombic, voltaic and energy efficiencies as shown in Figure 57d to Figure 60d. Coulombic efficiencies were exceptionally high (over 90 %) and in addition the voltaic efficiencies were in excess of 70 % which gave corresponding high energy efficiencies between 60 and 80 %. The efficiencies were also consistent across the whole experiment timescale and across the 10 cycles, with the exception of complex 4 whereby a gradual efficiency rise was observed suggesting that the system required more time to reach equilibration. Generally, all four complexes gave comparable performance such that mean coulombic efficiencies at lowest 89.7 % and voltaic efficiencies in the range of 70.3 to 81.0 % were achieved. A lower energy efficiency of 63.1 % was observed for complex 3 which resulted from

significantly more overpotential during charging and discharging, compared to the other complexes. This overpotential can be attributed to the slower electron-transfer kinetics of the Co(III/II) redox couple which was observed on carbon-based electrodes, hence limiting the performance of the full battery.

### 5.3.6 Flow-cell battery studies

To assess the battery performance of the Co complexes, a prototype unoptimized flow-cell consisting of graphite felt electrodes and an anion-exchange membrane was employed (FC-I). Based upon the measured cell potentials, solubilities and electrochemical kinetics of complexes **1-4**, complex **2** was initially chosen for further study in lab-scale flow-cell experiments whereby higher current densities are possible due to enhancements in mass transport. Although complex **3** would have given a theoretically higher energy density, the poor kinetics on carbon electrodes of its Co(III/II) redox couple was undesirable. Battery performance of 1 mM complex **2** in 0.5 M TBA PF<sub>6</sub> electrolyte was examined as a function of constant cycling current density at  $\pm 0.125$  and  $1.25 \text{ mA cm}^{-2}$ , corresponding to a charge rate of 0.75 and 7.46C respectively. At higher current densities the battery cycled with significantly more overpotential hence giving low voltaic efficiencies of approx. 60 and 50 % at  $0.125$  and  $1.25 \text{ mA cm}^{-2}$  respectively. A significant capacity fade was also observed in both experiments such that at  $0.125 \text{ mA cm}^{-2}$  the charge capacity decreased from 95 to 51 % over 17.7 h, whereas at  $1.25 \text{ mA cm}^{-2}$  the charge capacity decreased faster over a shorter time; from 72 to 13 % (over 1.2 h).

In comparison to the H-cell experiment in Figure 58 which maintained high capacity over 50.3 h, the trend in capacity suggests that the capacity loss in the flowing experiments is not due to chemical instability but rather the inefficient cycling or loss of battery electrolyte. Due to the unsuitable polymer materials and poor current collector design used in the prototype cell, electrolyte loss via leakage or soaking into the plastic/rubber materials was severe and was likely a significant contribution for the observed capacity loss. In addition, the difference in capacities of the two experiments indicates that the overpotential during cycling is also a

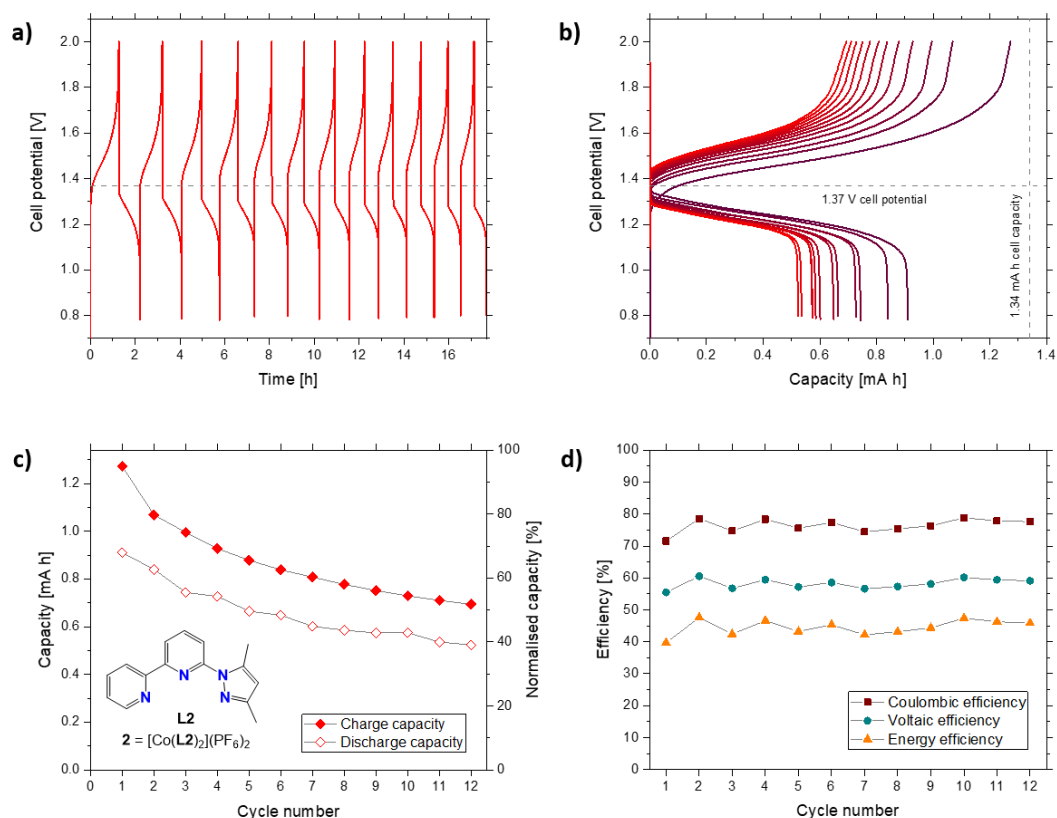


**Figure 61.** a) Charge-discharge cycles of 1 mM **2** in 0.5 TBA PF<sub>6</sub> MeCN solution at ± 0.125 mA cm<sup>-2</sup> between 2.0 and 0.8 V upper and lower potential thresholds in prototype flow-cell. b) evolution of charge-discharge curves as a function of capacity. c) Charge-discharge capacities as a function of cycle number. d) Cycling efficiencies as a function of cycle number.

contribution for the capacity fade. This is supported by the observation of electrolyte colour such that the cell was visibly not discharged to a zero SOC each cycle. Given that the mass-transport in the flow-cell design was sufficiently high, the source of this overpotential was attributed to the kinetics of the Co(III/II) redox couple; the **2** Co(III/II) rate constant was considerably lower than the Co(II/I) rate constant on carbon electrode. Therefore, the performance of the flow-cell and overpotentials are principally limited by the kinetics of the Co(III/II) redox couple. As a post-mortem investigation, the combined battery electrolyte after a similar flow-cell experiment of complex **2** was studied by voltammetry, as shown in Figure 63. The experiment shows that the presence of Co(III) and/or Co(I) oxidation states in the electrolyte causes a severe decrease of the Co(III/II) redox

couple kinetics at the GC electrode, whereas the Co(II/I) and L/L<sup>-</sup> kinetics appeared unaffected. Therefore, the rate constants for the Co(III/II) redox couples of **1-4** are likely slower in the flow-cell than those measured in section 5.3.3. This conclusion is further supported by Figure 64 (discussed in the following paragraphs) which compares the performance of complex **3** to Fc/FcBF<sub>4</sub> in Chapter 4.

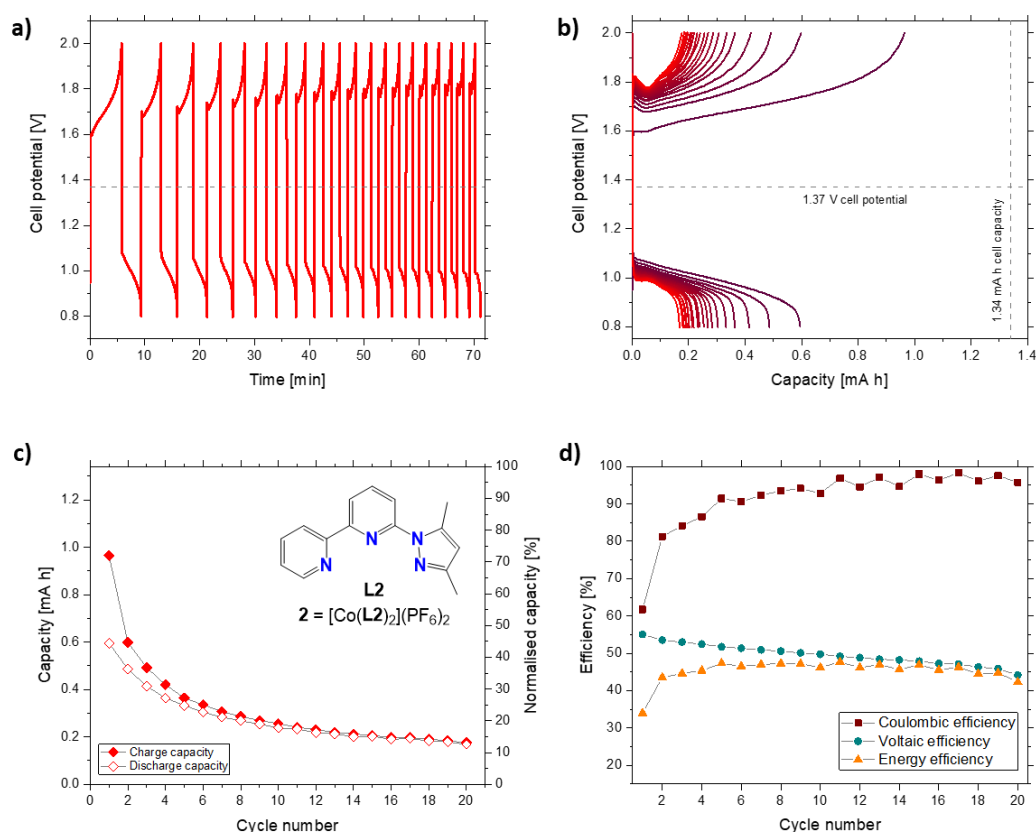


**Figure 62.** a) Charge-discharge cycles of 1 mM **2** in 0.5 TBA PF<sub>6</sub> MeCN solution at  $\pm 1.25$  mA cm<sup>-2</sup> between 2.0 and 0.8 V upper and lower potential thresholds in prototype flow-cell. b) evolution of charge-discharge curves as a function of capacity. c) Charge-discharge capacities as a function of cycle number. d) Cycling efficiencies as a function of cycle number.

Despite the design flaws of the prototype flow-cell and electrolyte loss, it is obvious from the well-defined plateaus in the charge/discharge curves in Figure 61b that the cell was able to access high/low SOC on charge/discharge respectively, thus the battery operated better than similar non-aqueous RFBs utilising MCCs in the literature. Frequently, poor battery cycling with large

overpotentials in excess of 1 V have been reported [127–129,131,132,139] which can be attributed to unoptimization of the cell design. A high cell resistance is likely the reason why these studies have typically also used a tenfold lower current on discharge than charge [127–129] and often the requirement to drive the cell to very low potentials (frequently to 0 V) to force the cell to discharge [129]. Therefore, it was speculated that further optimisation of the flow-cell design used here would improve the battery performance of the Co(II) complexes by minimising the other sources of cell resistance.

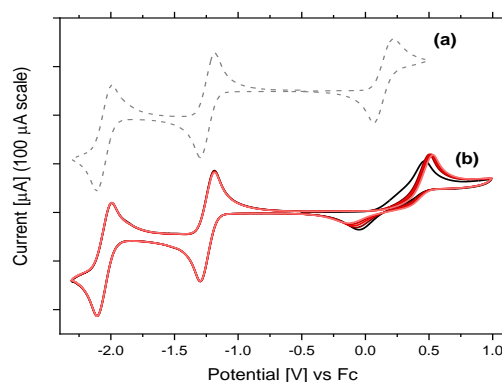


**Figure 63. Cyclic voltammograms of 10 mM complex 2 in 0.1 M TBA PF<sub>6</sub>, MeCN at GC electrode, 50 mV s<sup>-1</sup>. a) fresh and unused Co(II) electrolyte. b) an electrolyte of complex 2 recovered from a battery experiment by combining the posolyte and negolyte.**

Revision experiments using the FC-II flow-cell were performed to improve the performance of the Co(II) complexes and to benchmark the performance against the Fc/FcBF<sub>4</sub> model chemistry explored in Chapter 4. Given that the FC-II flow-cell has been optimised to minimise cell resistances, complex 3 was chosen for application due to its superior cell potential and solubility in order to test the compound at a higher concentration and current density. The battery was operated at 50 mM concentration giving a capacity of 13.4 mA h (a tenfold increase than in Figure 61 and Figure 62) and at a current density of 9.62 mA cm<sup>-2</sup>, corresponding to 1.49 C, as shown in Figure 64. The cell was cycled for 100 cycles and a corresponding total experimental time of 56.3 h. At this current density, an overpotential of  $\approx$ 200 mV was observed on first charge/discharge giving 84 % capacity, however the cell performance worsened with time giving  $\approx$ 500 mV

overpotential and only 28 % capacity remaining after 100 cycles. In this case, the capacity loss was not attributed to poor design of the flow-cell or electrolyte leakage. It is therefore likely that a chemical reaction of the **3** chemistry with time or cycle number occurred. This behaviour is evident in the charge/discharge curves in Figure 64b whereby the battery overpotential significantly increases with cycle number such that the charge plateaus do not curve completely vertical before hitting the upper threshold potential. This therefore indicates that the cell was unable to fully charge each cycle before reaching the 2.4 V upper threshold potential despite fully discharging each cycle, as evidenced by the constant > 98 % coulombic efficiency. The increasing overpotential with cycle suggests that either the quantity of **3** redox material decreased with time (due to chemical degradation) or the kinetics of the **3** electrochemistry worsened with time. A decrease of the **3** Co(III/II) rate constant is a plausible explanation as the voltammetry investigations have generally showed that the Co(III/II) kinetics are sensitive to the electrode material, surface and history. As shown in the comparable experiment in Figure 63, the formation of high concentrations of the Co(I) and/or Co(III) oxidation states of **3** is likely to cause adsorption of these species to the electrode surface, thus decreasing the Co(III/II) kinetics further.

The performance of complex **3** in the FC-II flow-cell can be directly compared to that of the model Fc/FcBF<sub>4</sub> chemistry explored in Chapter 4 as similar operational conditions were used in both experiments. At 10 mM concentration of the Fc/FcBF<sub>4</sub> model chemistry, the flow-cell is capable of the same current density as the 50 mM complex **3** experiment described here in Figure 64, with less overpotential. Therefore, under the similar mass transport conditions of the flow-cell experiments, the Co complex performs considerably worse due to the kinetic limitations of the Co(III/II) redox couples on carbon-based electrodes.

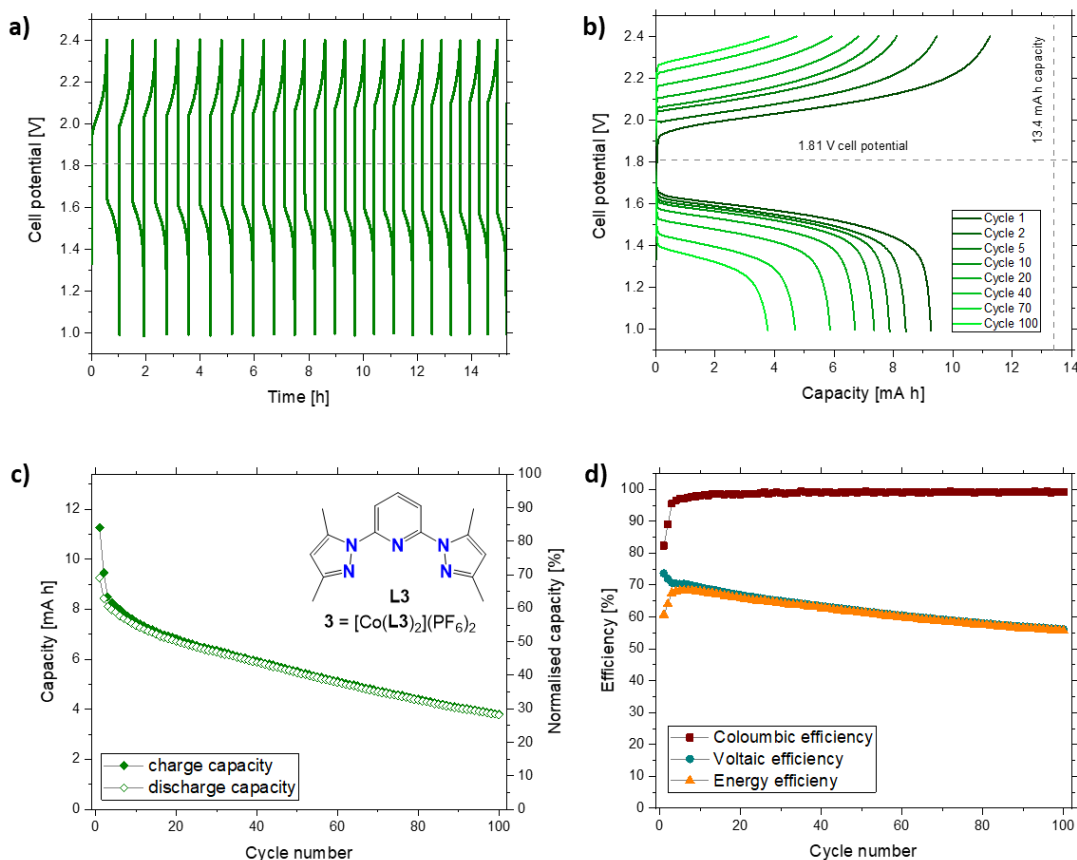


**Figure 64.** a) Charge-discharge cycles of 50 mM 3 in 0.5 TEA BF<sub>4</sub> MeCN solution at  $\pm 9.62 \text{ mA cm}^{-2}$  between 2.4 and 1.0 V upper and lower potential thresholds in FC-II flow-cell (first 20 of 100 cycles shown). b) evolution of charge-discharge curves as a function of capacity. c) Charge-discharge capacities as a function of cycle number. d) Cycling efficiencies as a function of cycle number.

## 5.4 Conclusions

In summary, a new class of cobalt(II) complexes with ‘tunable’ tridentate azole-pyridine type ligands were evaluated for use in a novel symmetric non-aqueous redox-flow battery. Four different structures were synthesised and their electrochemical, physical and battery properties were investigated as a function of successive substitution of the terminal pyridyl groups of 2,2':6',2''-terpyridine with 3,5-dimethylpyrazoles or 1,2,4-triazoles. Cyclic voltammetry of the complexes showed that such complexes undergo reversible Co(III/II) and Co(II/I) redox couples, as well as ligand-centred redox couples, allowing symmetric RFB to be

created. The redox potentials of the Co(III/II) and Co(II/I) redox couples were found to be dependent on the structure of the ligand because the substitution of terminal pyridine groups with weaker  $\sigma$ -donating/ $\pi$ -accepting 3,5-dimethylpyrazole donors shifts the Co redox potentials. This allowed the battery cell potential to be preferentially increased from 1.07 to 1.91 V because the Co(III/II) and Co(II/I) redox potentials were shifted positively and negatively respectively. In correlation, the solubility of the complexes was also increased from 0.18 to 0.50 M due to more favourable polar methyl interactions with the MeCN solvent. As a result, the theoretical energy density of 2,2':6',2''-terpyridine cobalt(II) hexafluorophosphate complex was five-fold increased from 2.58 to 12.80 Wh L<sup>-1</sup> for that of 2,6-bis-(N-3,5-dimethylpyrazoyl)pyridine cobalt(II) hexafluorophosphate.

Battery cycling experiments on 1 mM complexes in 0.5 M TBA PF<sub>6</sub> MeCN electrolyte, as both posolyte and negolyte, in a H-type glass cell gave high coulombic and energy efficiencies of 89.7-99.8 % and 63.1-80.8 % respectively, when cycled at a very low 0.41 C charge rate. These experiments demonstrated that the Co complexes **1-4** can be reversibly cycled in a battery and that they are stable over long time periods. At higher current densities in a flow-cell the complexes gave reasonable performance however significant capacity fade was observed suggesting poor cyclability of the Co complexes. The mechanism for the capacity loss was not formally identified, however the limiting kinetics of the Co(III/II) redox couple is a plausible explanation for the observed increase in overpotential. The standard electrochemical rate constants of the Co(III/II) redox couples were found to be typically an order of magnitude lower than the corresponding Co(II/I) redox couples due to spin-crossover during the Co(III/II) redox process. Furthermore, the Co(III/II) kinetics are also dependent on the electrode material and are very sensitive to the presence of adsorbed Co species on the electrode surface. Therefore, the production of the Co(III) posolyte on charge (or the Co(I) negolyte, assuming it crosses the membrane) is expected to adsorb to the posolyte electrode and further decrease the Co(III/II) rate constant during battery operation.

The present work demonstrates a methodology for increasing the cell potential and solubility of a symmetric MCC NA RFB. Crucially, the direct modification of the ligand donor groups allows for the MCC properties to be tuned without substantially increasing the molecular weight or cost of the symmetric redox material. Furthermore, the synthetic route for the complexes is simplistic, reliable and can be easily adapted to produce many possible ligand candidates by simply using different azole and pyridyl starting materials. Therefore, future work could develop an optimised molecule by designing and synthesising many different azole-pyridine ligands to tune the redox properties and solubilising interactions with the battery solvent. In addition, it is possible that the Co metal centre may be exchanged for a more earth-abundant element such as Fe or Mn to decrease the material cost. Despite this, these Co complexes at present have several drawbacks for application which require attention. Firstly, the cell potentials are relatively small ( $< 2$  V) compared to similar MCCs already applied for NA RFBs and do not fully exploit the solvent stability range. Although the cell potential was increased from 1.07 to 1.81 V, it is unlikely that it can be substantially increased towards 3 V because the largest redox potential shifts were accompanied by worsening electrochemistry and irreversible behaviour. Secondly, the complexes suffer from undesirably low diffusion coefficients and electrochemical rate constants due to their large size and the spin-crossover phenomena, respectively. These issues are problematic for application as they will limit the RFB performance in terms of the battery power density and energy efficiency.

Since this research was conducted and published, a similar article applying Co(II) complexes with azole-pyridines was published by Yang et al. [140]. The study examined the use of similar pyridine-pyrazole complexes in both a full symmetric NA RFB and in a hybrid Li-RFB. Here the concentration of the complexes was up to 0.4 M and experimental timescales were much longer. Despite this, the findings were in agreement with the results presented here and further demonstrates the stability of the Co complexes.



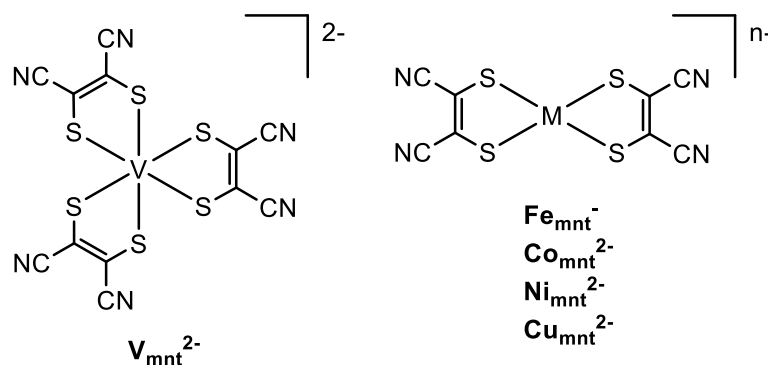
# Chapter 6

## Dithiolene Complexes of First-Row Transition Metals

The work presented in this chapter is published in [3].

### 6.1 Introduction

As introduced in the previous chapter, MCCs are good candidates for NA RFB electrolytes because they can be stable in multiple oxidation states, hence allowing symmetric RFBs to be easily designed [1,133,135,140]. Despite this, low solubility of most MCCs such as the Co(II) complexes in Chapter 5 limits practical application at present. Previous research has shown that smaller MCCs, such as  $M(\text{acac})_3$  complexes are generally more soluble, which is presumably due to higher polarity. To address this challenge, a literature review was performed to identify lower molecular weight MCCs which would give enhanced solubility. Complexes with 'dithiolene' ligands were identified as promising MCCs because they are non-innocent when bound to transition metal ions. Such complexes are known to undergo multiple redox events through oxidation and reduction centred on either the metal or dithiolene ligand [231–234]. Recently, the vanadium complex of the dithiolene ligand 1,2-dicyanoethylene-1,2-dithiolate (maleonitriledithiolate,  $\text{mnt}^{2-}$ ), namely  $(\text{TEA})_2\text{V}_{\text{mnt}}$  was studied as a symmetric electrolyte for NA RFBs [148] (Scheme 6).  $\text{V}_{\text{mnt}^{2-}}$  undergoes two reversible metal-centred one-electron reductions and one reversible ligand-centred one-electron oxidation in MeCN solution [234]. Despite poor battery cycling in a static H-cell experiments, the electrochemistry was promising for further study. Herein, the application of  $\text{V}_{\text{mnt}}$  is extended to flow-cell experiments and the wider family of bis-mnt complexes of Fe, Co, Ni and Cu are studied.



**Scheme 6. The chemical structures of metal dithiolene complexes studied for symmetric NA RFBs in this work.**

## 6.2 Experimental

### 6.2.1 Synthesis of sodium maleonitriledithiolate

All chemicals were used as received from the supplier without further purification. NMR spectra were recorded on a Bruker Ultrashield 400 Plus spectrometer at 298 K. CHNS elemental analyses were performed on an Elementar vario MICRO cube. High resolution mass assignment was performed using a Shimadzu LCMS-IT-TOF with electrospray ionisation.

**Disodium cis-1,2-dicyanoethylene-1,2-dithiolate (Na<sub>2</sub>mnt).** The synthetic method was adapted from [235] with modifications. To a suspension of NaOH (10.17 g, 254 mmol) in 30 mL DMF, sulfur was slowly added (8.15 g, 254 mmol) over 40 min. The dark red reaction mixture was cooled to 0 °C and a solution of chloroacetonitrile (6.392 g, 84.7 mmol) in 6 mL DMF was added dropwise over 1 h. The tan-brown reaction mixture was slowly warmed to room temperature under stirring for 1.5 h. Isopropanol (iPrOH) (50 mL) was then added and the reaction warmed to ~60 °C, hot filtered, and washed with 40 mL of boiling iPrOH. 100 mL of diethyl ether was then added to the cooled filtrate and the solution was cooled to -20 °C. Scratching the flask with a spatula caused crystallisation of the sodium cyanodiformate intermediate ( $\cdot$ 3DMF solvate, NCCS<sub>2</sub>Na $\cdot$ 3DMF, 20.1 g, 69 %), which was isolated by filtration, washed with 100 mL diethyl ether, and air dried. Next, NCCS<sub>2</sub>Na $\cdot$ 3DMF was dissolved in 170 mL H<sub>2</sub>O to give a brown solution which was left for 3 days, in which time dimerization of the intermediate NCCS<sub>2</sub>Na $\cdot$ 3DMF

resulted in a light brown solution with a sulfur precipitate. The mixture was filtered through celite and washed with aliquots of 50 mL H<sub>2</sub>O. The light brown filtrate was dried to a brown oil by rotary evaporator, taken up in 100 mL EtOH and again evaporated to give a tan-brown powder, which was further dried under high-vacuum at 80 °C for 5 h to yield 6.8 g (approx. quantitative from NCCS<sub>2</sub>Na·3DMF) of crude product. This was suspended in 40 mL boiling EtOH, hot filtered, and washed with 40 mL boiling EtOH. To the cooled filtrate was added 50 mL diethyl ether, and cooled to 0 °C, to produce a bright yellow powder precipitate, which was filtered and washed with 100 mL of diethyl ether, then dried under high-vacuum to yield **Na<sub>2</sub>mnt·1<sup>3</sup>/<sub>4</sub>H<sub>2</sub>O** (2.978 g, 14.27 mmol, 34 %). <sup>13</sup>C NMR (D<sub>2</sub>O, 100 MHz): δ = 126.30, 122.74. Anal calcd. for C<sub>4</sub>N<sub>2</sub>Na<sub>2</sub>S<sub>2</sub>·1<sup>3</sup>/<sub>4</sub>H<sub>2</sub>O: C 22.07, H 1.62, N 12.87, S 29.46 %; found: C 22.34, H 1.48, N 12.63, S 29.47 %. Repeated syntheses returned yields of 11-34 % with solvent water content of ·<sup>3</sup>/<sub>4</sub>H<sub>2</sub>O to ·3H<sub>2</sub>O. <sup>13</sup>C NMR data consistent with that reported in the literature [236].

### 6.2.2 Synthesis of metal maleonitriledithiolate complexes

**(TEA)<sub>2</sub>[V(mnt)<sub>3</sub>]·<sup>1</sup>/<sub>2</sub>H<sub>2</sub>O = (TEA)<sub>2</sub>V<sub>mnt</sub>**. The synthesis of (TEA)<sub>2</sub>[V(mnt)<sub>3</sub>] has been described previously [148] however the method here makes use of an adapted procedure for the related [(C<sub>6</sub>H<sub>5</sub>)<sub>4</sub>As]<sub>2</sub>[V(mnt)<sub>3</sub>] complex [237]. To a yellow suspension of Na<sub>2</sub>mnt·3H<sub>2</sub>O (1.11 g, 4.62 mmol) in 20 mL dry THF was added solid VCl<sub>3</sub> (242 mg, 1.54 mmol) resulting in a dark green suspension. Upon stirring the green solution for 40 min, a solution of TEA Cl in 2 mL of EtOH was added dropwise. After stirring overnight, the solution was filtered and washed with 20 mL dry THF. The filtrate was evaporated to dryness, washed with 2-propanol and the residual green solid taken up in 5 mL hot acetone/15 mL boiling iPrOH then cooled on ice. Black microcrystalline material was isolated by filtration, then recrystallized by dissolving in 5 mL acetone and 10 mL iPrOH, then reduced in volume to 10 mL by heating. Black needle crystals were filtered and dried in air then under high vacuum yielding **(TEA)<sub>2</sub>[V(mnt)<sub>3</sub>]·<sup>1</sup>/<sub>2</sub>H<sub>2</sub>O** 315 mg, 0.43 mmol, 28 %. Anal calcd. for C<sub>28</sub>H<sub>40</sub>N<sub>8</sub>S<sub>6</sub>V·<sup>1</sup>/<sub>2</sub>H<sub>2</sub>O: C 45.38, H 5.58, N 15.12, S 25.96 %; found: C 45.54, H 5.51, N 15.11, S 26.32 %; HRMS (ESI<sup>-</sup>): m/z = 600.9548 {(TEA)[V(mnt)<sub>3</sub>]}<sup>-</sup> (calcd = 600.9550), 235.3978 [V(mnt)<sub>3</sub>]<sup>2-</sup> (calcd = 235.3980). UV-vis: λ<sub>max</sub> / cm (ε /

$\text{L mol}^{-1} \text{ cm}^{-1}$ ) = 223.5 (40187), 258.5 (39152), 307.5 (19508), 427.5 (6038), 579.5 (4475).

**(TEA)[Fe(mnt)<sub>2</sub>] = (TEA)Fe<sub>mnt</sub>.** The synthesis was adapted from that previously described with modifications [238]. To a yellow solution of Na<sub>2</sub>mnt·1 $\frac{3}{4}$ H<sub>2</sub>O (648 mg, 2.98 mmol) in 20 mL 1:1 H<sub>2</sub>O/EtOH was added a solution of FeCl<sub>3</sub> (242 mg, 1.49 mmol) in 1.5 mL H<sub>2</sub>O resulting immediately in a dark brown-red solution. The reaction was stirred for 30 min, filtered through celite and washed with 10 mL 1:1 H<sub>2</sub>O/EtOH. To the filtrate was added a 4 mL EtOH solution of TEA Cl (494 mg, 2.98 mmol) dropwise to give a dark precipitate. After stirring for 30 min, the sticky black solid mass was filtered, washed with 10 mL water then 10 mL ice cold 1:1 H<sub>2</sub>O/EtOH, then recrystallized by dissolving in 15 mL hot acetone, adding 20 mL hot iPrOH then reducing the volume to 20 mL by heating, and cooling to 0 °C. The resulting black microcrystalline solid was filtered, washed with 20 mL ice cold iPrOH, and dried in air then in vacuo to yield **(TEA)[Fe(mnt)<sub>2</sub>]** (358 mg, 0.77 mmol, 52 %). Anal calcd. for C<sub>16</sub>H<sub>20</sub>FeN<sub>5</sub>S<sub>4</sub>: C 41.20, H 4.32, N 15.01, S 27.50 %; found: C 40.83, H 4.23, N 15.09, S 27.54 %; HRMS (ESI<sup>-</sup>): m/z = 335.8354 [Fe(mnt)<sub>2</sub>]<sup>-</sup> (calcd = 335.8361). UV-vis:  $\lambda_{\text{max}}$  / cm ( $\epsilon$  / L mol<sup>-1</sup> cm<sup>-1</sup>) = 241.0 (19904), 270.0 (26699), 300.0 (15561), 358.5 (12060), 451.0 (9118).

**(TEA)<sub>2</sub>[Co(mnt)<sub>2</sub>] = (TEA)<sub>2</sub>Co<sub>mnt</sub>.** The synthesis was adapted from that previously described with modifications [239]. Under an atmosphere of N<sub>2</sub> Na<sub>2</sub>mnt·1 $\frac{1}{4}$ H<sub>2</sub>O (400 mg, 1.92 mmol) was dissolved 1:1 H<sub>2</sub>O/EtOH (6 mL, degassed with N<sub>2</sub>) to give a bright yellow solution. A purple solution of CoCl<sub>2</sub>·6H<sub>2</sub>O (228 mg, 0.96 mmol) in 1:1 H<sub>2</sub>O/EtOH (3 mL, degassed with N<sub>2</sub>) under N<sub>2</sub> was added to the Na<sub>2</sub>mnt solution via syringe, causing a colour change to dark red. After stirring for 30 min, a solution of TEA Cl (319 mg, 1.92 mmol) in 1:1 H<sub>2</sub>O/EtOH (2 mL, degassed with N<sub>2</sub>) under N<sub>2</sub> was added via syringe giving an immediate black precipitate. After stirring for 20 min, the precipitate was filtered under a stream of N<sub>2</sub>, washed with ice cold 1:1 H<sub>2</sub>O/EtOH and dried under high-vacuum to yield **(TEA)<sub>2</sub>[Co(mnt)<sub>2</sub>]· $\frac{1}{2}$ H<sub>2</sub>O** (397 mg, 0.65 mmol, 68 %) as a black microcrystalline solid. Anal calcd. for C<sub>24</sub>H<sub>40</sub>CoN<sub>6</sub>S<sub>4</sub>· $\frac{1}{2}$ H<sub>2</sub>O: C 47.35, H 6.79, N 13.80, S 21.06 %; found: C 47.35, H 6.70, N 13.86, S 21.42 %; HRMS (ESI<sup>-</sup>): m/z = 338.8339

[Co(mnt)<sub>2</sub>]<sup>-</sup> (calcd = 338.8343). UV-vis:  $\lambda_{\max}$  / cm ( $\epsilon$  / L mol<sup>-1</sup> cm<sup>-1</sup>) = 233.5 (25897), 262.5 (32615), 316.0 (20708), 416.0 (7328), 458.5 (6015), 549 (3128).

**(TEA)<sub>2</sub>[Ni(mnt)<sub>2</sub>] = (TEA)<sub>2</sub>Ni<sub>mnt</sub>**. The synthesis was adapted from that previously described with modifications [239]. To a yellow solution of Na<sub>2</sub>mnt·1¼H<sub>2</sub>O (812 mg, 3.89 mmol) in 15 mL 1:1 H<sub>2</sub>O/EtOH was added a green solution of NiCl<sub>2</sub>·6H<sub>2</sub>O (462 mg, 1.94 mmol) in 2 mL 1:1 H<sub>2</sub>O/EtOH resulting immediately in a red solution. After stirring for 20 min a 2 mL solution of TEA Cl (806 mg, 4.86 mmol) in 1:1 H<sub>2</sub>O/EtOH was added dropwise to give an orange precipitate. The reaction was stirred for a further 40 min, filtered and washed with 10 mL H<sub>2</sub>O then 4 mL ice cold 1:1 H<sub>2</sub>O/EtOH and air dried. The collected orange solid was then dissolved in 12 mL hot acetone and 20 mL of iPrOH slowly with heating to boiling, then the red solution was cooled to 0 °C. Dark red crystals were filtered, washed with 10 mL ice-cold iPrOH, then dried in vacuo at 60 °C to yield **(TEA)<sub>2</sub>[Ni(mnt)<sub>2</sub>]** (918 mg, 1.53 mmol, 79 %). Anal calcd. for C<sub>24</sub>H<sub>40</sub>N<sub>6</sub>NiS<sub>4</sub>: C 48.08, H 6.72, N 14.02, S 21.39 %; found: C 47.70, H 6.48, N 13.98, S 21.64 %; HRMS (ESI): m/z = 467.9957 {(TEA)[Ni(mnt)<sub>2</sub>]<sup>-</sup> (calcd = 467.9960), 337.8360 [Ni(mnt)<sub>2</sub>]<sup>-</sup> (calcd = 337.8365).  $\lambda_{\max}$  / cm ( $\epsilon$  / L mol<sup>-1</sup> cm<sup>-1</sup>) = 215.5 (22980), 270.5 (43074), 316.0 (27320), 380.5 (6483), 473.5 (3567).

**(TEA)<sub>2</sub>[Cu(mnt)<sub>2</sub>] = (TEA)<sub>2</sub>Cu<sub>mnt</sub>**. The synthesis was adapted from that previously described with modifications [239]. To a yellow solution of Na<sub>2</sub>mnt·1¾H<sub>2</sub>O (686 mg, 3.15 mmol) in 20 mL 1:1 H<sub>2</sub>O/EtOH was added a solution of CuCl<sub>2</sub> (212 mg, 1.58 mmol) in 2 mL H<sub>2</sub>O resulting immediately in a dark brown solution. The reaction was stirred for 30 min, filtered through celite and washed with 10 mL 1:1 H<sub>2</sub>O/EtOH. To the filtrate was added a 4 mL EtOH solution of TEA Cl (522 mg, 3.15 mmol) dropwise to give a maroon precipitate. After stirring for 45 min the maroon powder was filtered, washed with 5 mL water then 3 mL ice cold 1:1 H<sub>2</sub>O/EtOH, and dried in air. The powder was recrystallized by dissolving in 15 mL hot acetone, adding 20 mL hot iPrOH then reducing the volume to 20 mL by heating, and cooling to 0 °C. The resulting maroon microcrystalline solid was filtered, washed with 20 mL ice cold iPrOH, and dried in air then in vacuo to yield **(TEA)<sub>2</sub>[Cu(mnt)<sub>2</sub>]** (425 mg, 0.70 mmol, 45 %). Anal calcd. for C<sub>24</sub>H<sub>40</sub>CuN<sub>6</sub>S<sub>4</sub>: C

47.69, H 6.67, N 13.90, S 21.22 %; found: C 47.38, H 6.68, N 13.97, S 21.61 %; HRMS (ESI<sup>-</sup>): m/z = 472.9913 {(TEA)[Cu(mnt)<sub>2</sub>]}<sup>-</sup> (calcd = 472.9903), 342.8304 [Cu(mnt)<sub>2</sub>]<sup>-</sup> (calcd = 342.8307).  $\lambda_{\max} / \text{cm} (\epsilon / \text{L mol}^{-1} \text{cm}^{-1}) = 281.0 (22442), 319.5 (14976), 350.0 (10051), 370.0 (10153), 477.0 (4131)$ .

### 6.2.3 UV-vis spectroscopic methods

UV-vis spectra were recorded on an Agilent Cary 60 spectrophotometer. Spectra of the as-synthesized materials were recorded for 50  $\mu\text{M}$  solutions in MeCN. Spectra of charged electrolytes were recorded on solutions prepared as follows: In a N<sub>2</sub> filled glovebox, an initial battery charge was first performed on a solution of 1mM complex in 0.1 M TBA PF<sub>6</sub> MeCN solution in each half cell. 50  $\mu\text{M}$  solutions of each charged electrolyte were then prepared by extracting 250  $\mu\text{L}$  from the battery electrolytes and diluting to 5 mL (5 mM TBA PF<sub>6</sub> supporting salt concentration). The solutions were transferred to sealed quartz cuvettes (Starna Scientific, 1 cm path length), removed from the glovebox, and UV-vis spectra were recorded immediately. The time of t = 0 presented in the results represents approximately 5 minutes after the initial charge of the flow-cell was completed.

### 6.2.4 Solubility measurements

The solubility of each complex in pure MeCN was measured by UV-vis spectroscopy. The absorbance of stock solutions of the complex at 10, 20, 30, 40, and 50  $\mu\text{M}$  was measured at the following wavelengths: (TEA)<sub>2</sub>V<sub>mnt</sub>, 258.5 nm; (TEA)Fe<sub>mnt</sub>, 241.0 nm; (TEA)<sub>2</sub>Co<sub>mnt</sub>, 262.5 nm; (TEA)<sub>2</sub>Ni<sub>mnt</sub>, 270.5 nm; (TEA)<sub>2</sub>Cu<sub>mnt</sub>, 281.0 nm. In each case a Beer-Lambert calibration relating concentration and absorbance ( $R^2 > 0.99$ ) was achieved and used to calculate the concentration of unknown solutions (Appendix C). A saturated solution of each complex was prepared by making a suspension of 150-300 mg of complex in 0.3-0.5 mL MeCN, which was sonicated for at least one hour, then quickly filtered through cotton wool, and series-diluted into the calibration range by taking 20  $\mu\text{L}$  into 20 mL MeCN (200 fold dilution) then 250  $\mu\text{L}$  into 10 mL MeCN (40 fold dilution).

### 6.2.5 Voltammetry studies

Voltammetry experiments were performed in anaerobic 1 mM solutions of each complex, with 0.1 M TBA PF<sub>6</sub> supporting electrolyte, in HPLC grade MeCN. All voltammetry experiments were performed under an inert N<sub>2</sub> atmosphere; solutions were fully purged before use and a N<sub>2</sub> headspace was maintained throughout the experiments. CV was performed by using a standard 20 mL 3-electrode glass cell (BASi®) consisting of a Pt CE, Ag/AgPF<sub>6</sub> RE (Ag wire in a glass fritted tube of 0.1 M TBA PF<sub>6</sub> in MeCN) and a GC disk working electrode (3.0 mm diameter, BASi, Alvatek, UK). Redox-couple reversibility and diffusion coefficients, calculated by Randles–Sevcik analysis, were assessed by variation of the scan rate. RDE studies were performed using a 60 mL RRDE-3A apparatus (ALS Co., Ltd) with a 3 mm diameter GC working electrode at rotation rates in the range of 300 to 3000 rpm. Electrochemical rate constants were derived from the RDE data by Koutecký-Levich analysis. Working electrodes were polished before use with two grades of diamond slurries (3 μm and 0.25 μm, Buehler) and alumina suspension (0.05 μm, Buehler) prior to sonication in deionized water, acetone rinsing and air drying. Redox potentials were reported against Fc as an internal standard. Measurements were recorded using a PC-controlled Emstat<sup>3+</sup> (PalmSens) with a minimum resolution of 1 mV.

### 6.2.6 Battery methods

Galvanostatic battery experiments were performed using the FC-II flow-cell described in chapter 3 with FTFFs. 1 mm carbon paper electrodes (TFP Ltd. PVA binder, 2.08 cm<sup>2</sup> active area) and either a Celgard separator (Celgard® 2500 MPS, 25 μm thickness) or F-930 CEM (fumapem® F-930, FuMA-Tech GmbH, 30 μm thickness). Battery experiments were conducted on 10 mL solutions per half-cell of 1 mM redox material in 0.1 M TBA PF<sub>6</sub> (TCI chemicals) electrolyte in either MeCN (99.9 %, Extra Dry over Molecular Sieve, AcroSeal™, ACROS Organics™) or propylene carbonate (99.5 %, anhydrous, AcroSeal™, ACROS Organics™) at a flow-rate of 10 mL min<sup>-1</sup> by use of a Masterflex L/S peristaltic pump (Cole-Parmer). Experiments were conducted within a N<sub>2</sub> glovebox (Saffron Scientific Ltd. or MBRAUN) which was maintained at oxygen and water levels at a maximum 1 ppm.

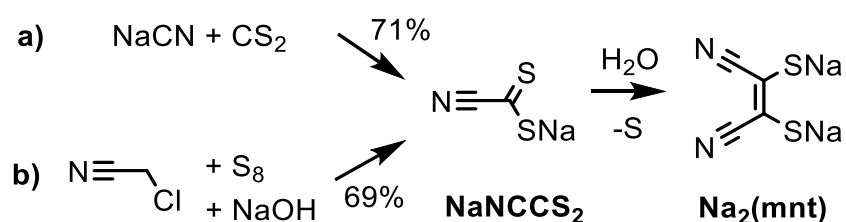
Charge-discharge cycles were performed at constant current density until the defined upper and lower potential thresholds were reached. The same magnitude of current was used upon both the charge and discharge. Charge-discharge cycling was controlled by either an Autolab (Metrohm AG) or Compactstat (Ivium Technologies) potentiostat. For the independent redox couple experiments the following example procedure was performed; to examine the negolyte, a symmetric flow-cell with  $M_{mnt}^{2-}$  initial starting electrolyte in each half cell was charged at constant current to access the  $M_{mnt}^{3-}$  as the negolyte and  $M_{mnt}^{1-}$  as the posolyte. The posolyte was then replaced with fresh  $M_{mnt}^{2-}$  electrolyte, before battery cycling at constant current between upper/lower potential thresholds just above/below 0 V. To examine the posolyte, the  $M_{mnt}^{3-}$  negolyte was instead replaced with fresh  $M_{mnt}^{2-}$  electrolyte after the initial electrolysis.

## 6.3 Results and discussion

### 6.3.1 Synthesis and characterisation

All compounds were synthesized according to literature procedures [148,235,237–239], however with modifications. The widely used synthetic method for the  $mnt^{2-}$  ligand, first reported by Bähr and Schleitzer in 1957, proceeds first by formation of the sodium cyanodithioformate ( $NaNCCS_2$ ) intermediate from sodium cyanide and carbon disulfide, followed by dimerization/desulfurization to give  $Na_2mnt$  (Scheme 7a) [239–241]. However, in the interests of accessing  $Na_2mnt$  from more environmentally benign and less toxic starting materials, an alternative method reported by Hoepfing and co-workers was followed (Scheme 7b) [235]: the intermediate  $NaNCCS_2$  is prepared from chloroacetonitrile with  $NaOH$  and sulfur in DMF. The yield achieved here was identical to the more hazardous route (69 % in this work. 71 % from  $NaCN + CS_2$  in [239]), however the method has been reported as near-quantitative (88-97 %) in the literature [235]. The isolated intermediate is then dissolved in water and allowed to stand for 12 hours to dimerize to  $Na_2mnt$ , which is isolated by filtration to remove sulfur followed by evaporation of the filtrate to give a tan-brown solid, in quantitative yield from  $NaNCCS_2$ . The  $Na_2mnt$  crude product was purified by

first drying under high vacuum at 80 °C for several hours before recrystallization from EtOH/Et<sub>2</sub>O to give a bright yellow microanalytically clean powder in moderate yield (49 % from NaNCCS<sub>2</sub>, 34 % overall). The principals of green chemistry are infrequently applied in the RFB literature; however, it is important to critically assess the synthetic origins of potential redox materials for sustainability and safety. Here, the alternative method is significantly less hazardous, and the synthetic yield is comparable to the more commonly used reaction utilising NaCN and CS<sub>2</sub>, hence the application of the M<sub>mnt</sub> complexes for RFB energy storage is justified.



**Scheme 7. Synthetic pathways to the Na<sub>2</sub>mnt ligand: a) from NaCN and CS<sub>2</sub> in DMF [239–241] and b) from chloroacetonitrile, NaOH and sulfur in DMF [235].**

Anionic complexes of mnt were synthesized with TEA<sup>+</sup> cations in order to ensure good solubility of the electrolyte species in MeCN. Complexation reaction procedures were adapted from those previously reported to produce tris-mnt (TEA)<sub>2</sub>V<sub>mnt</sub> [148,237], and bis-mnt (TEA)Fe<sub>mnt</sub> [238], (TEA)<sub>2</sub>Co<sub>mnt</sub> [239], (TEA)<sub>2</sub>Ni<sub>mnt</sub> [239] and (TEA)<sub>2</sub>Cu<sub>mnt</sub> [239]. All complexes were synthesized using the corresponding metal chloride and TEA Cl and recrystallized from boiling acetone/iPrOH to yield analytically clean microcrystalline solids. Synthetic yields for the preparation of the metal complexes varied in the range of 28 to 79 % due to the differences in the work-up of the products, however it is likely that the methods could be optimised towards higher yields and less wastage of the transition metal starting materials.

The solubility of each complex was measured in MeCN solvent by use of UV-vis Beer-Lambert calibrations (Appendix C). In each case linear fits with high R-squared values above 0.999 were achieved for multiple wavelengths. The maximal solubility of the complexes was in the range of 0.03 M to 0.91 M, indicating

generally low solubility for the complexes. Corresponding theoretical energy densities were calculated in the range of 0.6 to 16 W h L<sup>-1</sup> as shown in Table 10. Despite the relatively large cell potentials realised by **V<sub>mnt</sub>**, **Co<sub>mnt</sub>** and **Ni<sub>mnt</sub>**, the low solubility resulted in undesirably low energy densities. Thus, the **M<sub>mnt</sub>** complexes are comparable to similar MCCs applied in early NA RFB literature [124]. The exceptionally low solubility of (TEA)**Fe<sub>mnt</sub>** makes this complex unsuitable for application, however it is important to note that in general the monoanions of the **M<sub>mnt</sub>** complexes are expected to be less soluble than the corresponding **M<sub>mnt</sub>** dianions or trianions. Therefore, it is possible that the 0.03 M solubility of (TEA)**Fe<sub>mnt</sub>** is representative of the other **M<sub>mnt</sub>** monoanions whereas the (TEA)<sub>2</sub>**Fe<sub>mnt</sub>** species is likely to have a higher solubility comparable to the other **M<sub>mnt</sub>** dianions. The (TEA)<sub>2</sub>**Cu<sub>mnt</sub>** species gave the highest recorded solubility of 0.91 M which is comparable or higher than other MCCs in the literature [124,129].

### 6.3.2 Voltammetry behaviour of metal complexes

Voltammetry of the five complexes in relevant conditions, was performed on GC electrode to assess suitability of the **M<sub>mnt</sub>** complexes as candidates for NA RFB electrolytes (Figure 65, Table 9). In each case at least two redox processes were observed meaning that each **M<sub>mnt</sub>** complex can be applied as a symmetric RFB electrolyte. As shown in Figure 65, the complexes **Ni<sub>mnt</sub>**, **Co<sub>mnt</sub>**, **Cu<sub>mnt</sub>** and **Fe<sub>mnt</sub>** presented with two reversible redox couples whereas **V<sub>mnt</sub>** gave three. The half-wave potentials were measured for each reversible process and corresponding theoretical cell potentials were calculated as 1.08, 1.12, 1.42, 1.68 and 1.92 V for **V<sub>mnt</sub>**, **Cu<sub>mnt</sub>**, **Fe<sub>mnt</sub>**, **Co<sub>mnt</sub>** and **Ni<sub>mnt</sub>** respectively (Table 9). Thus, **V<sub>mnt</sub>** gave the lowest cell potential whereas **Ni<sub>mnt</sub>** gave the highest when using the **M<sub>mnt</sub><sup>2-/1-</sup>** and **M<sub>mnt</sub><sup>2-/3-</sup>** redox couples as the negolyte and posolyte respectively. However, if the additional **V<sub>mnt</sub><sup>3-/4-</sup>** redox couple is used as the negolyte, then **V<sub>mnt</sub>** gives the highest cell potential of 2.26 V and a favourable theoretical energy density of 16 W h L<sup>-1</sup>. Beyond the potential regions shown in Figure 65, the complexes all exhibit at least one irreversible oxidation process at approximately 0.5-1 V vs Fc, which are attributed to oxidative degradation of the complexes, as shown in Figure 67a to Figure 70a. In the cases of **V<sub>mnt</sub>**, **Co<sub>mnt</sub>** and **Ni<sub>mnt</sub>** the irreversible processes are

well-defined diffusion limited oxidations that lack back-reduction reactions. These oxidations are characteristic of EC mechanisms, however back-reduction peaks and increased current response of the  $M_{mnt}^{1-}$  reduction peaks are observed, which suggests that the EC processes has slow kinetics for the chemical reaction or that the decomposition yields electroactive products (overall ECE mechanism). Regardless, during battery operation the upper threshold potentials of the  $M_{mnt}$  complexes were deliberately restricted to avoid these irreversible oxidation processes. This was most challenging for  $Cu_{mnt}$  whereby the irreversible processes occur only  $\sim 250$  mV after the  $Cu_{mnt}^{2-/1-}$  redox couple.

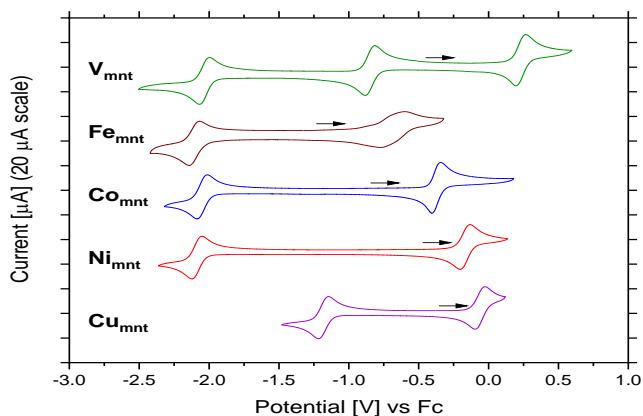


**Figure 65. Cyclic voltammograms of 1 mM  $M_{mnt}$  complexes in 0.1 M TBA PF<sub>6</sub>, MeCN electrolyte on GC electrode at 100 mV s<sup>-1</sup>. Black arrows indicate the starting point and direction for voltammetry. Second scans shown.**

All redox processes observed for the five complexes gave small peak separations ( $\Delta E = 69$ -77 mV, Table 9) close to the theoretical 59 mV separation expected for a fully-reversible one electron process, suggesting highly reversible redox behaviour, with the exception of (TEA) $Fe_{mnt}$ . For the Fe complex, the process at -0.689 V vs Fc has an abnormally large peak separation of 177 mV and the peaks appear much broader than for the reduction process at -2.016 V. This redox couple was investigated as a function of scan-rate and also at an RDE (Figure 66). The results showed no evidence of a two-electron process; thus, the large peak separation was attributed to sluggish kinetics and possible electrode adsorption. While the other four complexes are synthesized as dianions, the complex anion of

(TEA) $\text{Fe}_{\text{mnt}}$  is monoanionic. Attempts to improve the reversibility of the Fe complex redox activity by accessing the dianionic complex, i.e.  $\text{Fe}_{\text{mnt}}^{2-}$ , were unsuccessful despite using Fe(II) halide starting materials and working under dry, anaerobic (Schlenk) conditions.

**Table 9. Redox potentials vs Fc, as measured by CV at 100 mV s<sup>-1</sup> on GC electrode on 1 mM solutions of complex in 0.1 M TBA PF<sub>6</sub> MeCN electrolyte. The theoretical cell potential,  $V_{\text{cell}} = E_{1/2}(\text{M}_{\text{mnt}}^{2-/1-}) - E_{1/2}(\text{M}_{\text{mnt}}^{3-/2-})$ , for a symmetric battery of the corresponding electrolyte is given. (a) The larger cell potential for a battery employing the more negative  $\text{M}_{\text{mnt}}^{4-/3-}$  redox couple of  $\text{V}_{\text{mnt}}$ .**

Complex	$E_{1/2}(\text{M}_{\text{mnt}}^{2-/1-})$ [V]	$E_{1/2}(\text{M}_{\text{mnt}}^{3-/2-})$ [V]	$E_{1/2}(\text{M}_{\text{mnt}}^{4-/3-})$ [V]	$V_{\text{cell}}$ [V]
(TEA) <sub>2</sub> $\text{V}_{\text{mnt}}$	0.23 (73)	-0.85 (69)	-2.03 (74)	1.08, 2.26 <sup>(a)</sup>
(TEA) $\text{Fe}_{\text{mnt}}$	-0.69 (177)	-2.11 (77)	-	1.42
(TEA) <sub>2</sub> $\text{Co}_{\text{mnt}}$	-0.38 (61)	-2.05 (74)	-	1.68
(TEA) <sub>2</sub> $\text{Ni}_{\text{mnt}}$	-0.17 (70)	-2.09 (69)	-	1.92
(TEA) <sub>2</sub> $\text{Cu}_{\text{mnt}}$	-0.06 (69)	-1.18 (71)	-	1.12

Variable scan-rate CV was conducted for all complexes which showed that the peak separations of the redox couples show little increase with increasing scan-rate, indicating high reversibility (Figure 67b to Figure 70b). Randles–Sevcik analyses were performed to measure diffusion coefficients in the range of  $8.6 \times 10^{-6}$  –  $1.4 \times 10^{-5}$  cm<sup>2</sup> s<sup>-1</sup>, (Table 10) which are favourable for facile mass transport. These values are comparable to those reported for high-performing non-aqueous electrolytes based on Fc and cobaltocene ( $1.41$ – $2.23 \times 10^{-5}$  cm<sup>2</sup> s<sup>-1</sup>) [205] and higher than the widely studied  $\text{V}(\text{acac})_3$  ( $1.8$ – $2.9 \times 10^{-6}$  cm<sup>2</sup> s<sup>-1</sup>) [129] and iron tris-bpy ( $1.56 \times 10^{-6}$  cm<sup>2</sup> s<sup>-1</sup>) [123] systems.

RDE studies on  $\text{M} = \text{V}, \text{Co}, \text{Ni},$  and  $\text{Cu}$  complexes were also performed to evaluate electrochemical rate constants. Well-defined limiting currents which obey the Levich theory were observed which allowed Koutecký-Levich analysis. Standard electrochemical rate constants in the range of  $1.00$ – $1.66 \times 10^{-2}$  cm s<sup>-1</sup> (Table 10) were recorded which justify the observed electrochemical reversibility of all the redox couples. Kinetic analysis was not achieved for the  $\text{Fe}_{\text{mnt}}$  complex because at high rotation rates, a limiting current was not observed, (even at 500 mV overpotential) which indicates non-ideal behaviour at the electrode surface and possible electrode adsorption.

**Table 10. Solubilities in MeCN, theoretical maximum RFB energy densities, diffusion coefficients, and standard electrochemical rate constants for the  $M_{mnt}$  complexes. (a) the theoretical energy density assuming that the  $V_{mnt}^{3-/4-}$  redox couple was used as the battery negolyte vs the  $V_{mnt}^{2-/1-}$  redox couple as the posolyte. (b) the diffusion coefficient and rate constant for  $Fe_{mnt}$  were not calculated because the data does not obey the Randles-Sevcik and Koutecký-Levich equations respectively.**

Complex	Solubility [M]	Energy density [W h L <sup>-1</sup> ]	Diffusion coefficient $M_{mnt}^{2-/1-} / M_{mnt}^{2-/3-}$ [cm <sup>2</sup> s <sup>-1</sup> ]	Standard rate constant $M_{mnt}^{2-/1-} / M_{mnt}^{2-/3-}$ [cm s <sup>-1</sup> ]
(TEA) <sub>2</sub> V <sub>mnt</sub>	0.53	7.7/16 <sup>(a)</sup>	$8.8 \times 10^{-6} / 8.6 \times 10^{-6}$	$1.66 \times 10^{-2} / 1.53 \times 10^{-2}$
(TEA)Fe <sub>mnt</sub>	0.03	0.6	- (b)	- (b)
(TEA) <sub>2</sub> Co <sub>mnt</sub>	0.39	8.8	$1.3 \times 10^{-5} / 1.1 \times 10^{-5}$	$1.16 \times 10^{-2} / 1.35 \times 10^{-2}$
(TEA) <sub>2</sub> Ni <sub>mnt</sub>	0.30	7.7	$1.4 \times 10^{-5} / 1.3 \times 10^{-5}$	$1.63 \times 10^{-2} / 1.00 \times 10^{-2}$
(TEA) <sub>2</sub> Cu <sub>mnt</sub>	0.91	14	$9.3 \times 10^{-6} / 9.0 \times 10^{-6}$	$1.39 \times 10^{-2} / 1.45 \times 10^{-2}$

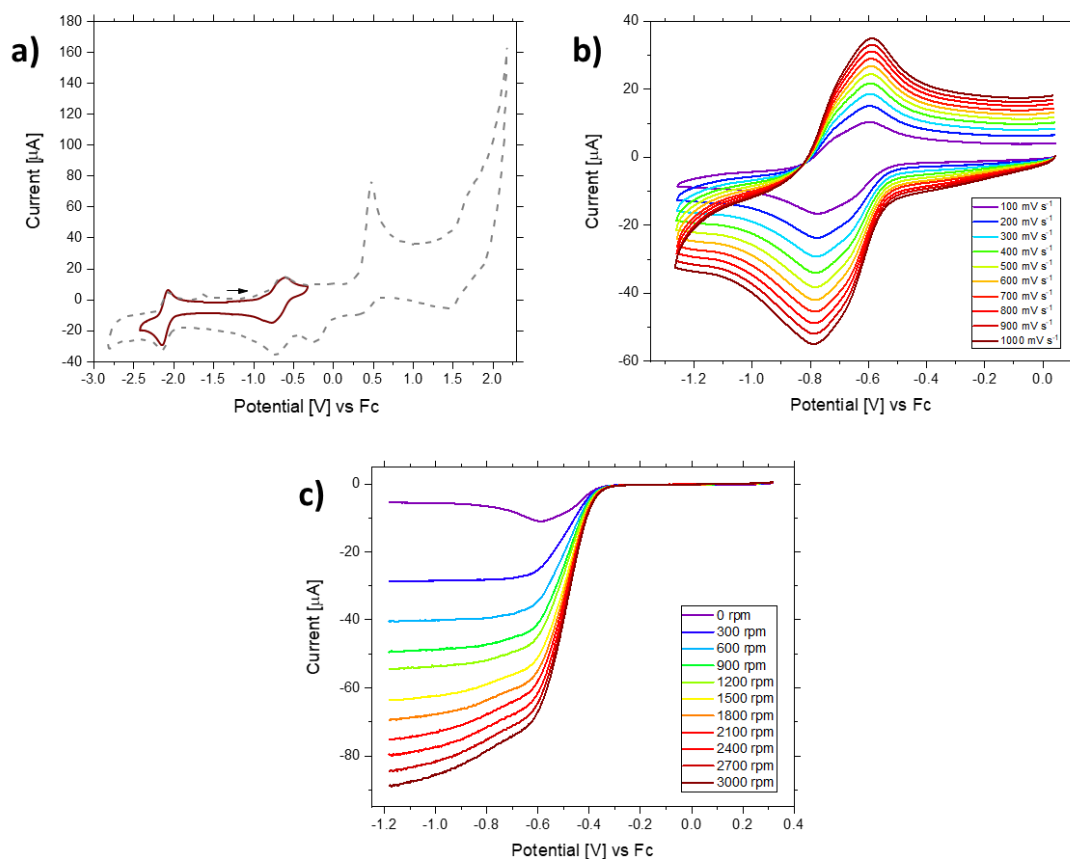


**Figure 66. Voltammetry analysis of 1 mM  $Fe_{mnt}$  in 0.1 M TBA PF<sub>6</sub> MeCN electrolyte on GC electrode. a) Second scan cyclic voltammograms at 100 mV s<sup>-1</sup>. The full region and restricted region scans are represented by the dashed and solid lines respectively. b) Scan-rate behaviour. First scans shown. c) RDE LSVs as a function of rotation rate at 50 mV s<sup>-1</sup>.**

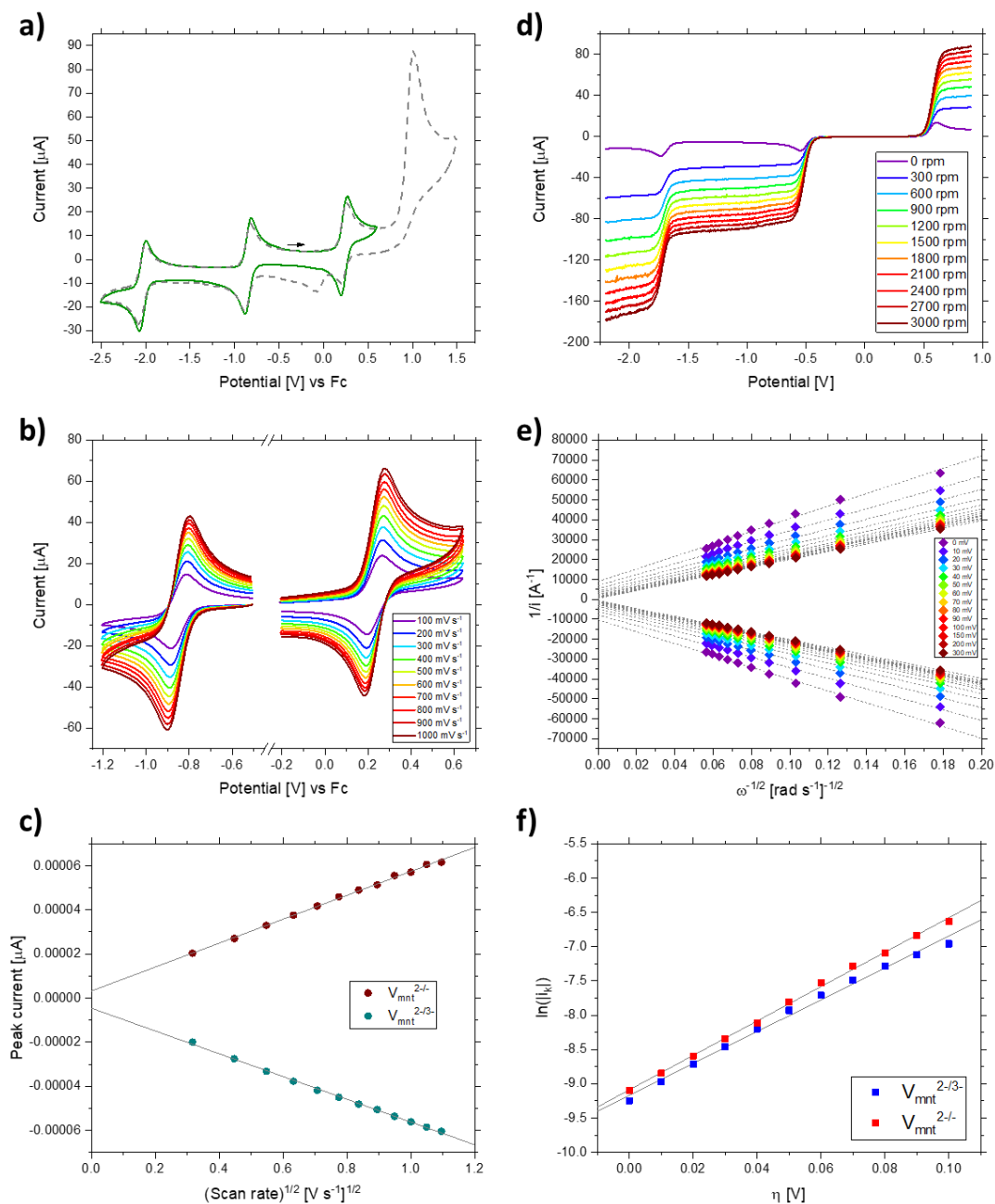


**Figure 67.** Voltammetry analysis of 1 mM  $V_{mnt}$  in 0.1 M TBA  $PF_6$  MeCN electrolyte on GC electrode. a) Second scan cyclic voltammograms at  $100 \text{ mV s}^{-1}$ . The full region and restricted region scans are represented by the dashed and solid lines respectively. b) Scan-rate behaviour. First scans shown. c) Peak current as a function of the square-root of scan rate. d) RDE LSVs as a function of rotation rate at  $50 \text{ mV s}^{-1}$ . e) Koutecký-Levich plot as a function of overpotential. f) The logarithm of the kinetically limited current vs overpotential.

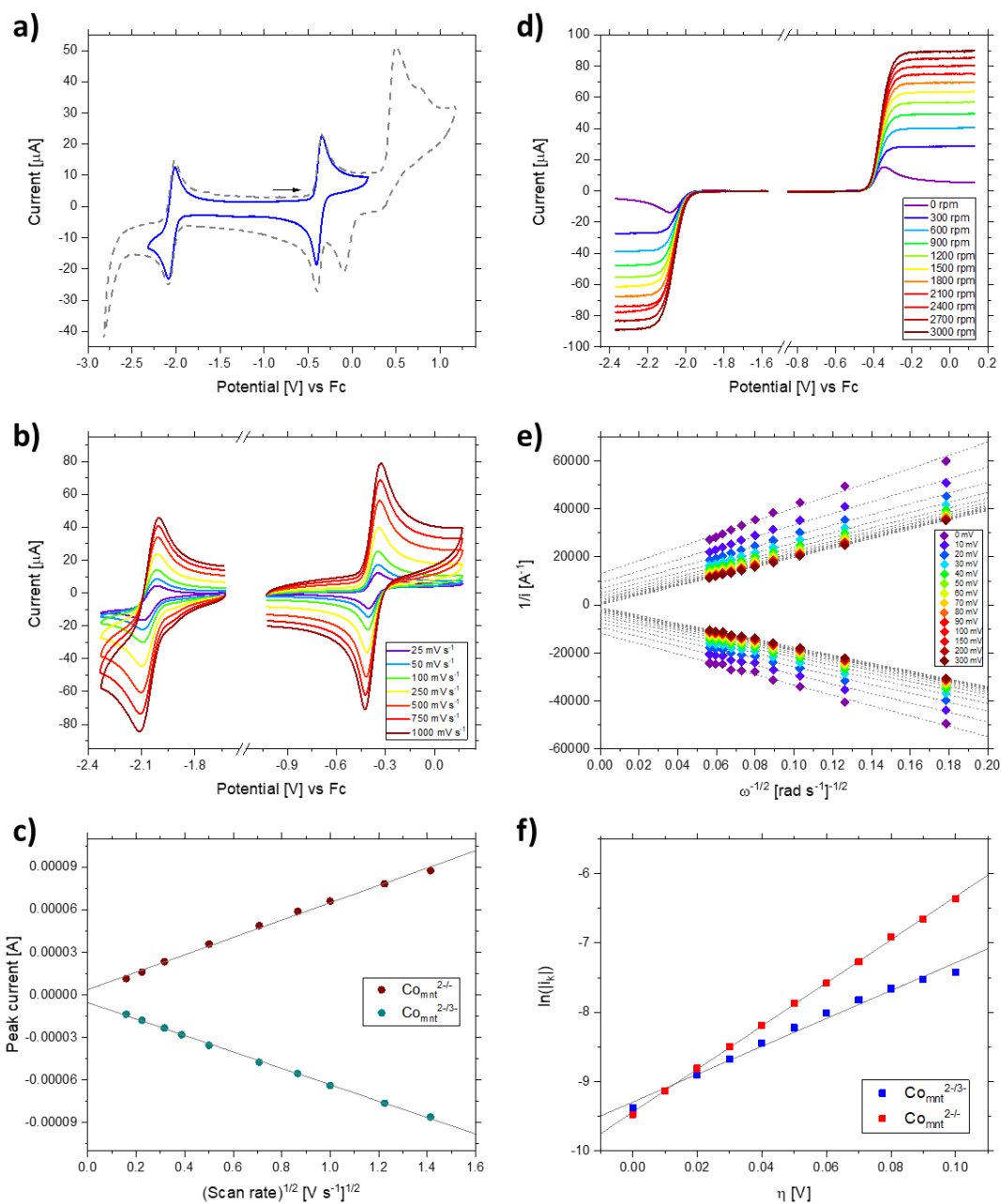


**Figure 68.** Voltammetry analysis of 1 mM  $\text{Co}_{\text{mnt}}$  in 0.1 M TBA  $\text{PF}_6$  MeCN electrolyte on GC electrode. a) Second scan cyclic voltammograms at  $100 \text{ mV s}^{-1}$ . The full region and restricted region scans are represented by the dashed and solid lines respectively. b) Scan-rate behaviour. First scans shown. c) Peak current as a function of the square-root of scan rate. d) RDE LSVs as a function of rotation rate at  $50 \text{ mV s}^{-1}$ . e) Koutecký-Levich plot as a function of overpotential. f) The logarithm of the kinetically limited current vs overpotential.

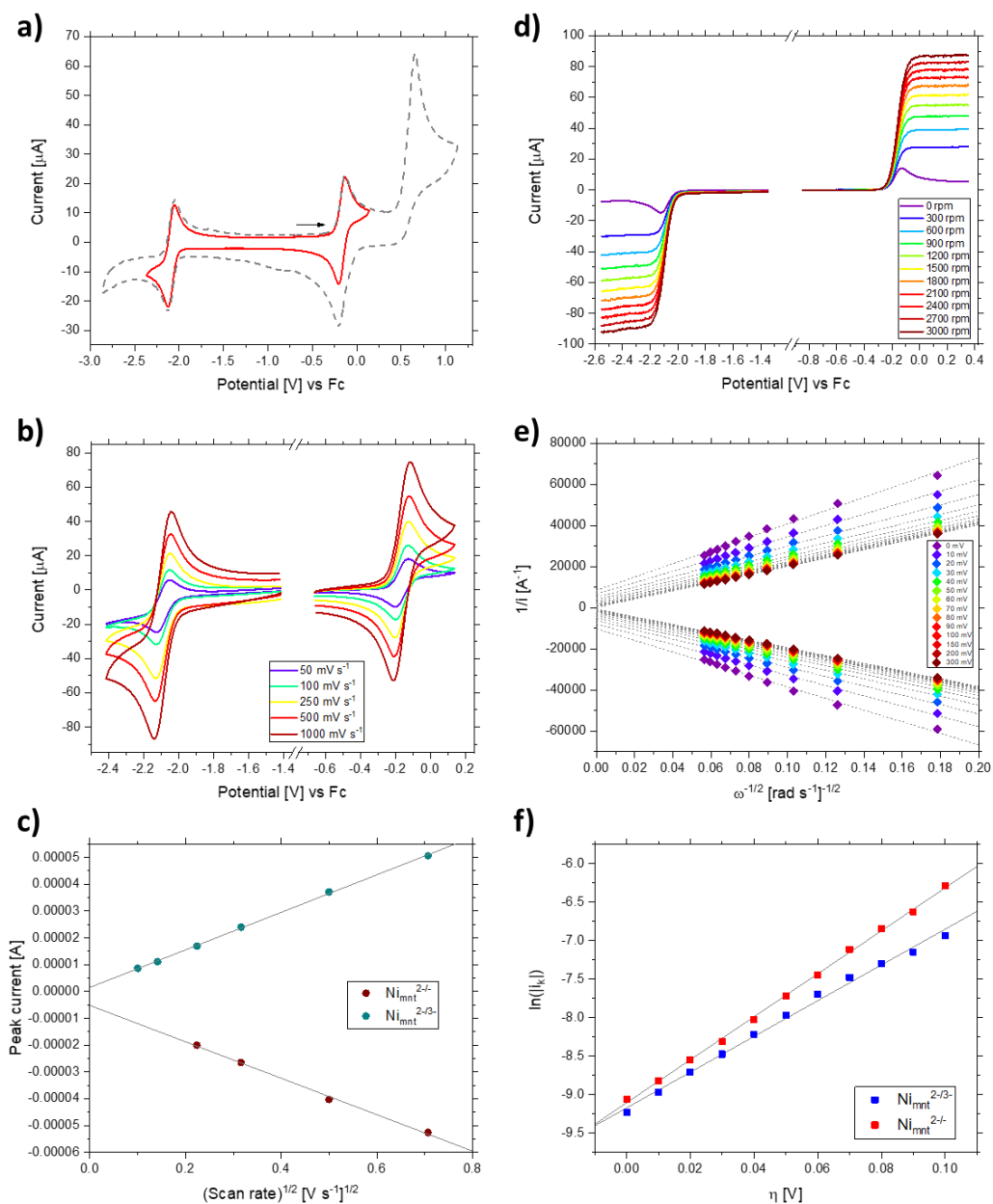


**Figure 69.** Voltammetry analysis of 1 mM  $\text{Ni}_{\text{mnt}}$  in 0.1 M TBA  $\text{PF}_6$  MeCN electrolyte on GC electrode. a) Second scan cyclic voltammograms at  $100 \text{ mV s}^{-1}$ . The full region and restricted region scans are represented by the dashed and solid lines respectively. b) Scan-rate behaviour. First scans shown. c) Peak current as a function of the square-root of scan rate. d) RDE LSVs as a function of rotation rate at  $50 \text{ mV s}^{-1}$ . e) Koutecký-Levich plot as a function of overpotential. f) The logarithm of the kinetically limited current vs overpotential.

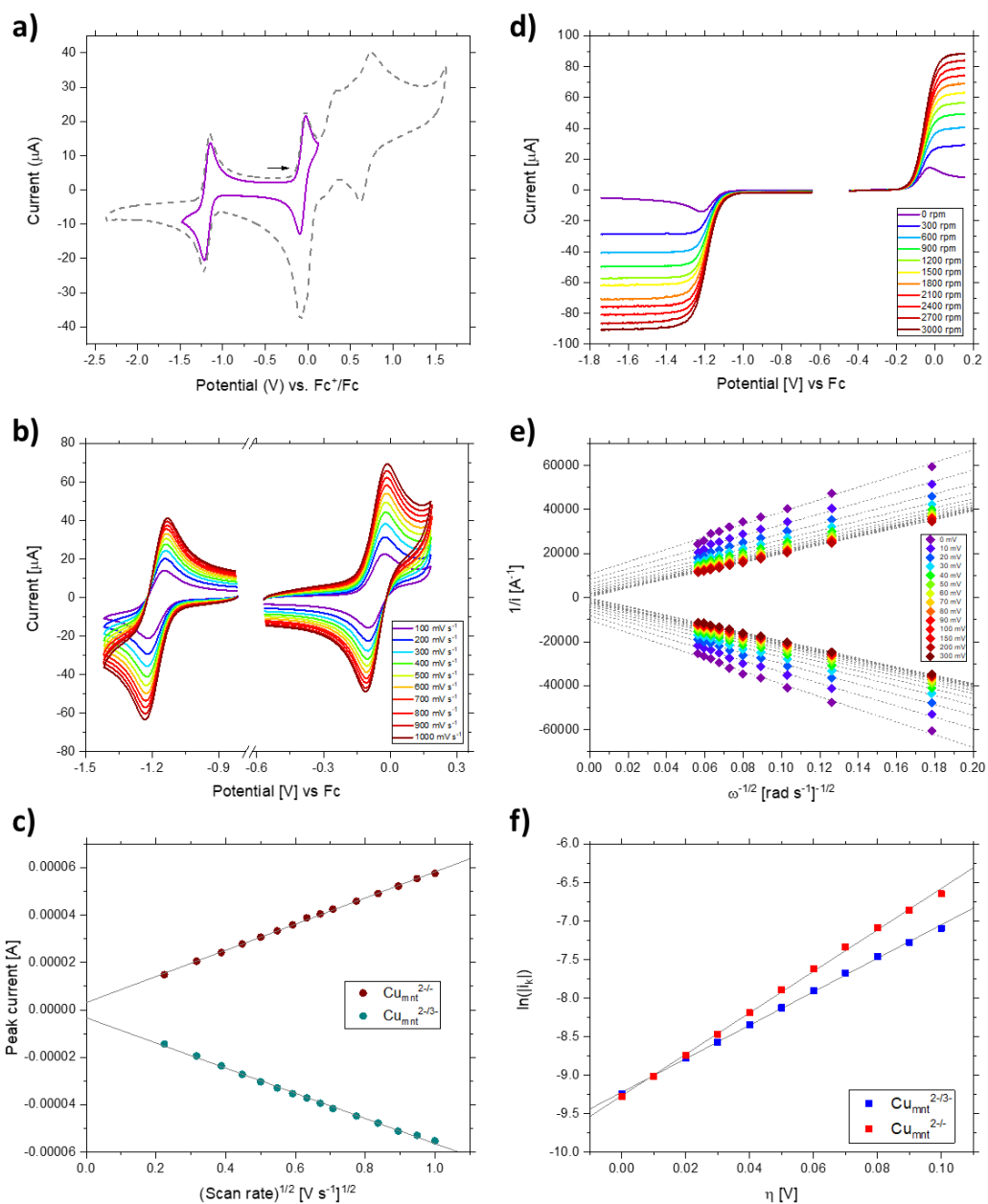


**Figure 70.** Voltammetry analysis of 1 mM  $\text{Cu}_{\text{mnt}}$  in 0.1 M TBA  $\text{PF}_6$  MeCN electrolyte on GC electrode. a) Second scan cyclic voltammograms at  $100 \text{ mV s}^{-1}$ . The full region and restricted region scans are represented by the dashed and solid lines respectively. b) Scan-rate behaviour. First scans shown. c) Peak current as a function of the square-root of scan rate. d) RDE LSVs as a function of rotation rate at  $50 \text{ mV s}^{-1}$ . e) Koutecký-Levich plot as a function of overpotential. f) The logarithm of the kinetically limited current vs overpotential.

### 6.3.3 $V_{\text{mnt}}$ battery studies

In a previous report by Cappillino et al. [148],  $(\text{TEA})_2V_{\text{mnt}}$  was shown to have promising charge-discharge performance in H-cell experiments at 20 mM concentration. Here, it was anticipated that improved performance in a flow-cell could be achieved, due to the enhanced mass transport and decreased cell resistances arising from pumped electrolytes and smaller inter-electrode separations, respectively. Assessment of 1 mM  $(\text{TEA})_2V_{\text{mnt}}$  in MeCN as a symmetric electrolyte was performed in the FC-II flow-cell employing a porous Celgard separator. 100 charge-discharge cycles were recorded at a constant current density of  $\pm 0.48 \text{ mA cm}^{-2}$  with the threshold potential set to 1.5 V for charge cycles to avoid accessing the irreversible oxidation process at  $\sim 1 \text{ V vs Fc}$ , and 0.3 V for discharge (Figure 71a). On the initial charge, a plateau at  $\sim 1.1 \text{ V}$  is observed, indicating that charging is occurring about the expected cell potential for the one electron transfer process of 1.08 V, until a maximum capacity of 0.253 mA h which corresponds to 94 % of the 0.268 mA h theoretical capacity for a one electron process. Upon discharge, a voltage plateau from  $\sim 1.1$ -1.0 V was observed, corresponding to a high voltaic efficiency of 95 % for cycle 2 (Figure 71b). Despite this, a lower discharge capacity of 0.158 mA h (59 %), was observed, indicating a low coulombic efficiency of 62 % for cycle 2, resulting in an energy efficiency of 59 %. The charge-discharge behaviour was consistent for ten cycles, but by the 20<sup>th</sup> cycle a second discharge plateau was observed at around 0.8 V, indicating that the battery composition has changed such that alternative redox processes were occurring. Although charge-discharge was achieved up to 100 cycles, good performance was only achieved up to around 20 cycles. In contrast, very little battery cycling data was reported by Cappillino et al. such that only 16 cycles were achieved. Furthermore, in [148] the discharge curves did not give plateaus at the expected potential despite using a tenfold lower current on discharge, and low < 30 % voltaic efficiency was observed indicating poor battery performance. Therefore, by operating in a flow-cell, enhanced performance is achieved here in comparison to the previously reported non-flowing H-cell charge-discharge experiments [148]. While coulombic efficiency decreased from  $\approx 90 \%$  to  $\approx 60$ -70 %, the voltaic efficiency was markedly increased from  $\approx 25 \%$  to 95 %, resulting in a

tripling of the energy efficiency  $\approx 20\%$  to  $\approx 60\%$ , highlighting the importance of testing proposed RFB electrolytes in flow conditions.

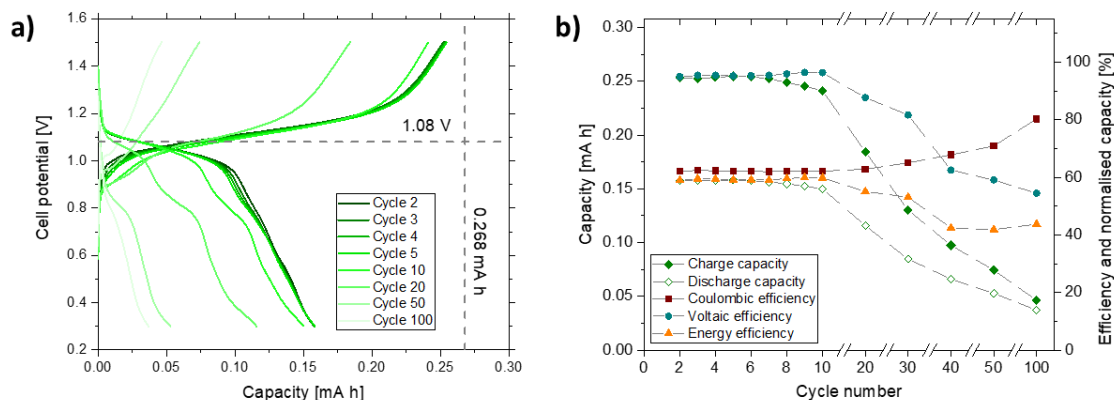


**Figure 71. a) Cell potential vs capacity and b) capacities and efficiencies for selected charge-discharge cycles at  $\pm 0.48 \text{ mA cm}^{-2}$  current density for  $1 \text{ mM } (\text{TEA})_2\text{V}_{\text{mnt}}$  in  $0.1 \text{ M TBA PF}_6$  MeCN solution with Celgard separator. Dashed grey lines in a) indicate the theoretical cell potential and capacity.**

Next, the effects of changing the flow-cell separator as well as electrolyte solvent on the battery cycling performance was investigated. Switching the Celgard for a Fumapem F-930 CEM gave slightly diminished performance with similar discharge capacities but energy efficiencies approximately 10 % lower for F-930 than for Celgard as shown in Figure 72. The poorer performance of the applied CEM was attributed to its smaller thickness ( $30 \mu\text{m}$ ) and the undesirable physical properties of the membrane material in MeCN solvent. Switching the battery solvent for PC solvent gave similar performance, with slightly better coulombic and slightly worse voltaic efficiencies, resulting in energy efficiencies just below 50 % (Figure 73), however the current was only half that of the MeCN experiments in Figure 71 and Figure 72. The poorer battery performance was attributed to the lower conductivity and higher viscosity of PC, which results in higher cell resistances. However, again the efficiencies obscure the overall poor performance of  $(\text{TEA})_2\text{V}_{\text{mnt}}$  in PC as the discharge capacities are in fact much lower than in MeCN at 28 % and 59 % respectively on cycle 2. The capacity loss after the first charge was very dramatic as the cell retained only 33 % of the capacity after the initial full

charge. Thereafter the capacity faded gradually with cycling until less than 10 % was retained in the cell.

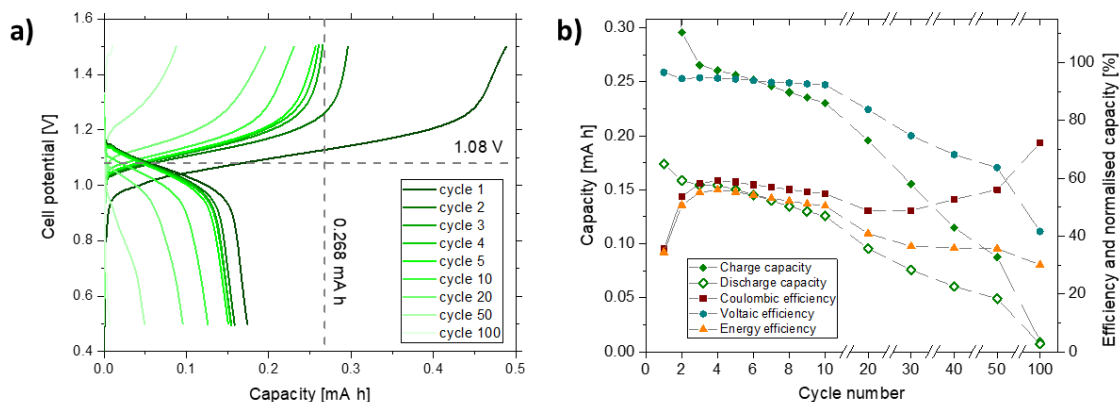


**Figure 72. a) Cell potential vs capacity and b) capacities and efficiencies for selected charge-discharge cycles at  $\pm 0.48 \text{ mA cm}^{-2}$  current density for  $1 \text{ mM (TEA)}_2\text{V}_{\text{mnt}}$  in  $0.1 \text{ M TBA PF}_6$  MeCN solution with Fumapem F-930 CEM. Dashed grey lines in a) indicate the theoretical cell potential and capacity.**

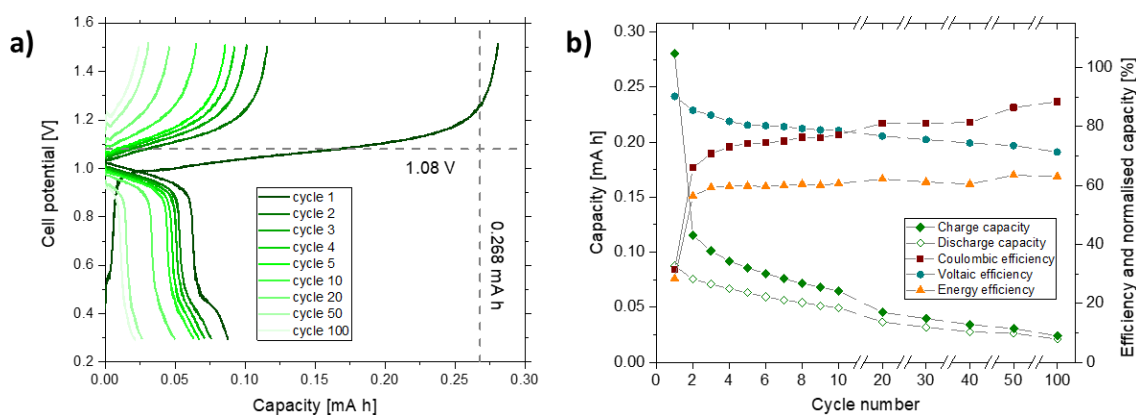


**Figure 73. a) Cell potential vs capacity and b) capacities and efficiencies for selected charge-discharge cycles at  $\pm 0.24 \text{ mA cm}^{-2}$  current density for  $1 \text{ mM (TEA)}_2\text{V}_{\text{mnt}}$  in  $0.1 \text{ M TBA PF}_6$  PC solution with Celgard separator. Dashed grey lines in a) indicate the theoretical cell potential and capacity.**

Despite the evident instability issues of the  $\text{V}_{\text{mnt}}$  battery, the larger  $2.26 \text{ V}$  battery was attempted by use of the  $\text{V}_{\text{mnt}}^{4-/3-}$  redox couple. In order to access the second reduction process in an RFB, first a battery of  $\text{V}_{\text{mnt}}^{2-}$  in each half cell was charged to  $1.5 \text{ V}$ , to give  $\text{V}_{\text{mnt}}^{3-}$  negolyte and  $\text{V}_{\text{mnt}}^{1-}$  posolyte solutions. The  $\text{V}_{\text{mnt}}^{1-}$

posolyte was then discarded and replaced with fresh starting material, giving  $V_{mnt}^{3-}$  negolyte and  $V_{mnt}^{2-}$  posolyte initial solutions, which were then subjected to charge-discharge cycling up to 2.7 V. Performing this experiment in both MeCN and PC gave initial charging curves with plateaus at 2.2-2.5 V around the expected potential of 2.26 V, however essentially zero capacity was observed upon discharge and subsequent charge cycles and the capacity vastly exceeded the theoretical capacity (Figure 74). Given that zero capacity was retained after fully charging the cell to 2.7 V, it was speculated that the  $V_{mnt}^{4-}$  is very reactive towards the solvent or the irreversible oxidation in Figure 67a began to occur in the posolyte. The complexity of this experiment makes it very challenging to diagnose the specific cause for the cell not discharging.

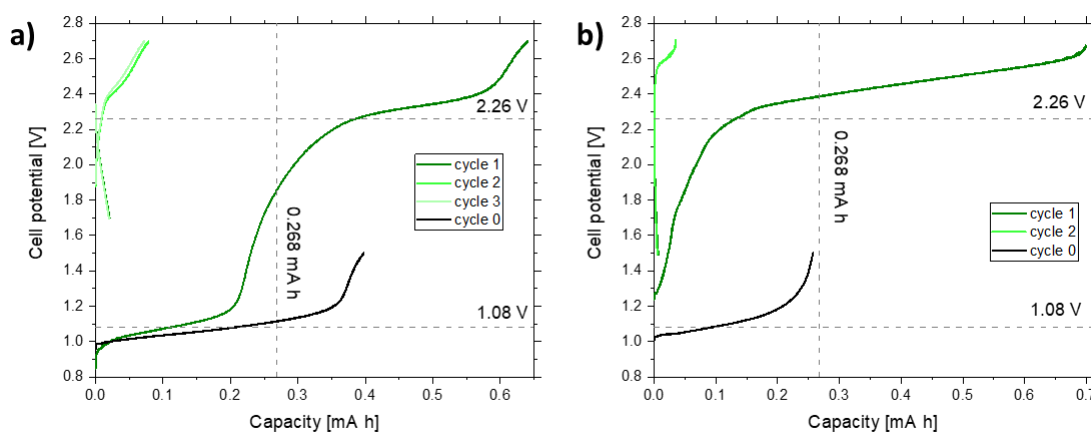


**Figure 74.** Cell potential vs capacity for the first three charge-discharge cycles for the 2.26 V potential battery of 1 mM  $(TEA)_2V_{mnt}$  in 0.1 M TBA  $PF_6$  electrolyte. a) MeCN solvent with fumapem F-930 CEM at  $\pm 0.48 \text{ mA cm}^{-2}$ . b) PC solvent with Celgard separator at  $\pm 0.24 \text{ mA cm}^{-2}$ . Also shown are 'cycle 0', the initial charge cycle to 1.5 V before the posolyte was replaced with fresh  $(TEA)_2V_{mnt}$  solution.

To diagnose why the  $(TEA)_2V_{mnt}$  was giving poor capacity retention in the battery experiments, the stability of each oxidation state was investigated by independent single redox couple cycling whereby the cell potential is 0 V. It is reasonable to assume that the starting  $(TEA)_2V_{mnt}$  oxidation state is indefinitely stable as the electrolyte showed no signs of degradation after long-term storage and usage in non-anhydrous electrolyte during bench-top experiments. Therefore,

the capacity retention of the single redox couple cycling experiments can be used to directly assess the stability of the charged oxidation state under study. Flow-cell experiments were performed for both the negolyte and posolyte for 1 mM  $(\text{TEA})_2\text{V}_{\text{mnt}}$  in 0.1 M TBA PF<sub>6</sub> MeCN solution with Celgard separator. The negolyte experiment, whereby the  $\text{V}_{\text{mnt}}^{3-/2-}$  redox couple is charged/discharged, reveals good performance up to 100 cycles (Figure 76a) with low overpotentials ( $\approx 0.1$  V) and discharge capacity fading from 63 % on cycle 1 to 36 % cycle 100 (Figure 76b). The posolyte experiment, cycling of  $\text{V}_{\text{mnt}}^{2-/1-}$  showed poorer performance compared to the negolyte, with capacity fading much faster to almost zero capacity remaining by cycle 30 (Figure 76b and c). These independent battery cycling experiments show that in the symmetric RFB the posolyte, i.e. the  $\text{V}_{\text{mnt}}^{2-/1-}$  redox process, is less stable and is mostly responsible for the significant capacity fade observed by cycle 50.

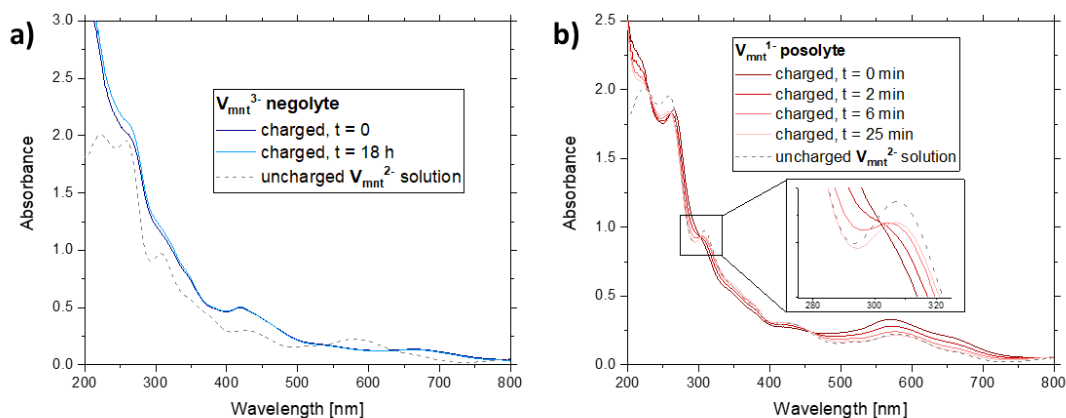


**Figure 75. Time evolution of the UV-vis spectra of the a)  $\text{V}_{\text{mnt}}^{3-}$  negolyte and b)  $\text{V}_{\text{mnt}}^{1-}$  posolyte solutions diluted to 50  $\mu\text{M}$  concentration in 5 mM TBA PF<sub>6</sub> MeCN solution, of the 1.09 V battery of  $(\text{TEA})_2\text{V}_{\text{mnt}}$  after an initial charge to 1.5 V. Also shown is the uncharged starting solution (grey); 50  $\mu\text{M}$   $(\text{TEA})_2\text{V}_{\text{mnt}}$  MeCN solution.**

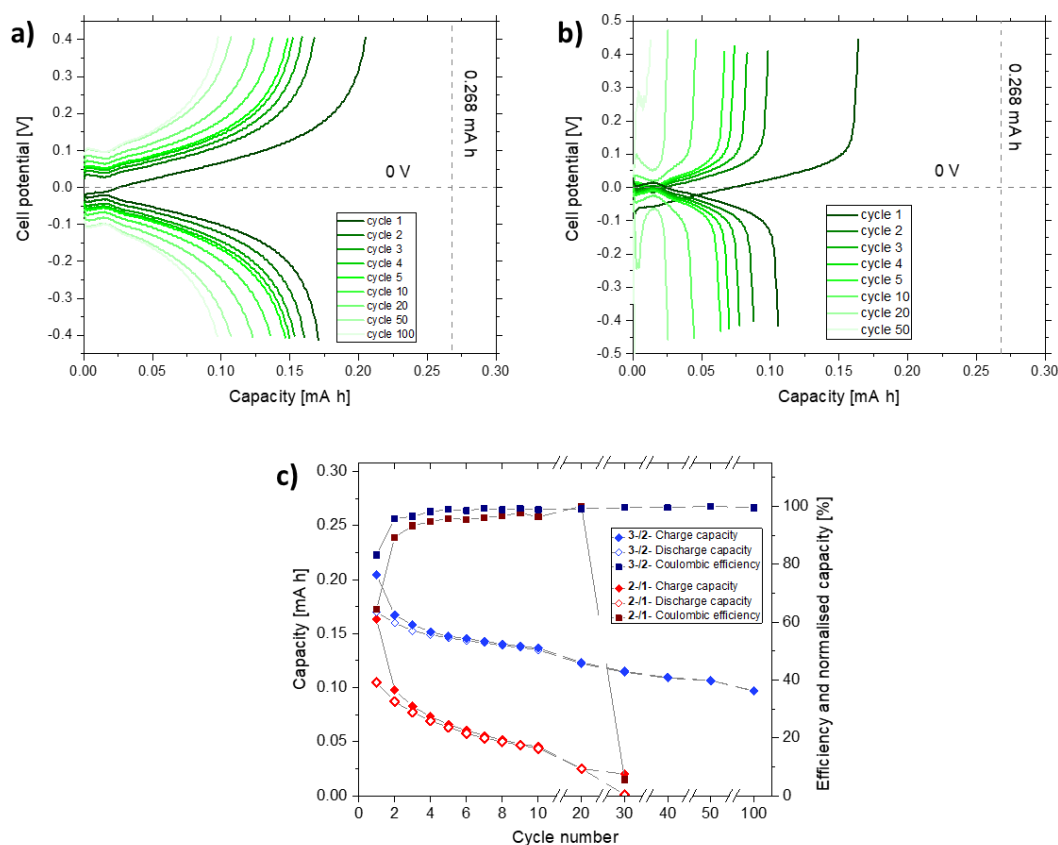


**Figure 76.** Cell potential vs capacity for the independent redox couple battery cycling of a)  $V_{mnt}^{3-/2-}$  and b)  $V_{mnt}^{2-/1-}$ . Dashed grey lines indicate the theoretical potential and capacity. c) Charge-discharge capacities for selected cycles of independent redox couple battery cycling of  $V_{mnt}^{3-/2-}$  and  $V_{mnt}^{2-/1-}$ . Conditions: 1mM  $(TEA)_2V_{mnt}$  in 0.1 M TBA PF<sub>6</sub> MeCN solution,  $\pm 0.96$  mA cm<sup>-2</sup> constant current density,  $\pm 0.4$  V charge-discharge voltage thresholds, Celgard separator.

For each of the  $M = V, Co, Ni, Cu$  complexes the posolyte and negolyte solutions were extracted from the symmetric RFB charge-discharge experiments after the first charge cycle and measured by UV-vis spectroscopy to observe their stability over time. For  $(TEA)_2V_{mnt}$  the charged negolyte solution ( $V_{mnt}^{3-}$ ) gives a distinct spectrum from the uncharged electrolyte with most notably the absence of the peaks at 308 and 580 nm. This solution also appeared to be stable with minimal change in the spectrum over 18 hours (Figure 75a). The posolyte  $V_{mnt}^{1-}$  solution also gave a distinct spectrum immediately after the initial charge cycle, with the loss of the 308 nm peak and an increase in intensity/shift to lower wavelength of

the 580 nm peak. However, over 25 min the spectrum evolved, most notably with the reappearance of the peak at 308 nm, to give an almost identical spectrum to that of the initial uncharged  $\text{V}_{\text{mnt}}^{2-}$  electrolyte (Figure 75a). This result is in agreement with the symmetric single-redox couple flow-cell data (Figure 76), with the  $\text{V}_{\text{mnt}}^{3-}$  negolyte being more stable than the  $\text{V}_{\text{mnt}}^{1-}$  posolyte. Furthermore, the spectra revealed that the posolyte solution self-discharged to the initial  $\text{V}_{\text{mnt}}^{2-}$  dianion, and that this process occurred over short time-scales. The mechanism for the self-discharge of the  $\text{V}_{\text{mnt}}^{1-}$  species is unclear however it is evident that a reducing agent (possibly trace water) must be present in the electrolyte in order to chemically reduce  $\text{V}_{\text{mnt}}^{1-}$ .

### 6.3.4 $\text{Co}_{\text{mnt}}$ battery studies

$(\text{TEA})_2\text{Co}_{\text{mnt}}$  charge-discharge cycling revealed voltage plateaus centred around the expected  $V_{\text{cell}}$  of 1.68 V and excellent voltaic efficiencies of 96 % for the first ten cycles (Figure 77). Coulombic and energy efficiencies were 63-69 % and 61-66 % over the first ten cycles, with discharge capacity fading from 56 % to 37 %. Despite good performance initially, the discharge capacity faded steadily to 14 % on cycle 50, and to essentially zero capacity (6 %) by the 100<sup>th</sup> cycle. In addition, an unexpected second plateau near the 2.2 V threshold was observed on charge, which became more prominent with cycling, indicating that the battery chemistry evolved with increasing cycle number.

In the independent  $\text{Co}_{\text{mnt}}^{3-/2-}$  negolyte single redox couple battery cycling, there is steady, almost complete, capacity fade in 50 cycles from 38 % to 1 % (Figure 79a and c). The posolyte in this case, i.e. the  $\text{Co}_{\text{mnt}}^{2-/1-}$  redox couple, appears more stable to multiple charge-discharge cycles, with almost zero overpotential, and a capacity fade from 75 % to 54 % over 50 cycles (Figure 79b and c).

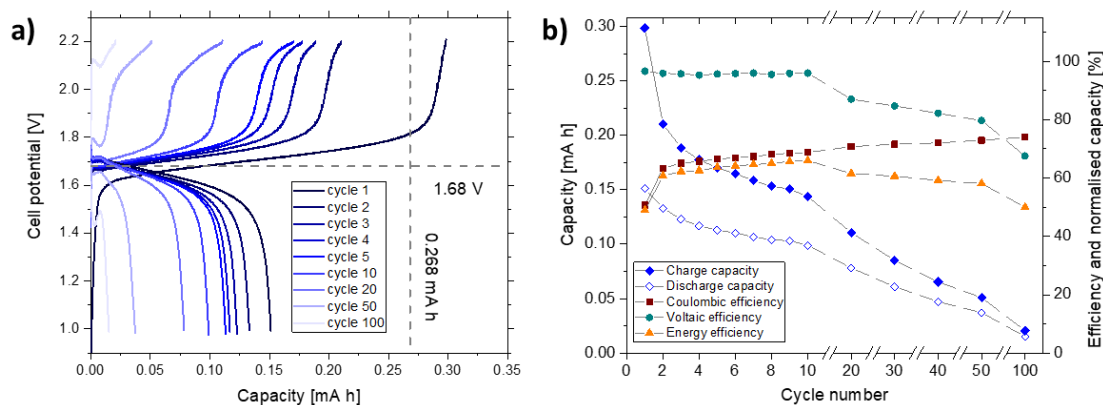


**Figure 77. a) Cell potential vs capacity for selected charge-discharge cycles for  $(\text{TEA})_2\text{Co}_{\text{mnt}}$ . Dashed lines indicate the theoretical cell potential and capacity. b) Capacities and efficiencies for selected charge-discharge cycles for  $(\text{TEA})_2\text{Co}_{\text{mnt}}$ . Conditions: 1 mM  $(\text{TEA})_2\text{Co}_{\text{mnt}}$  in 0.1 M TBA PF<sub>6</sub> MeCN solution, Celgard separator,  $\pm 0.48 \text{ mA cm}^{-2}$  constant current density, 2.2/1.0 V potential thresholds.**

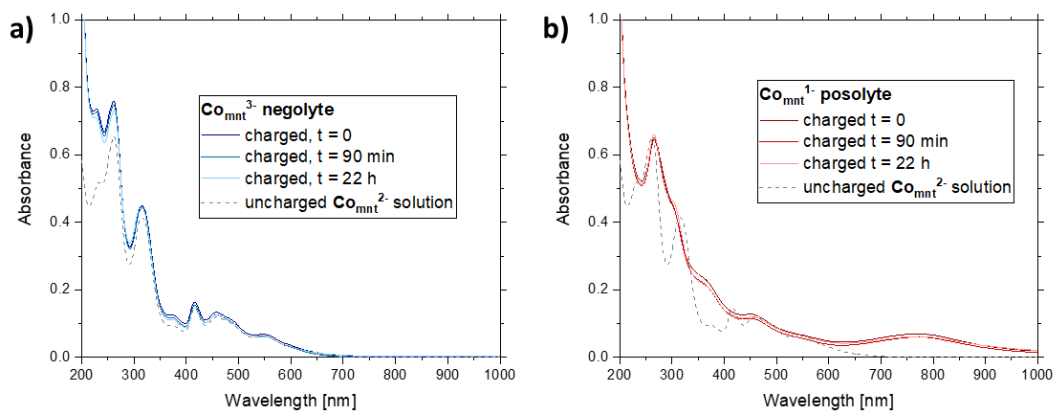


**Figure 78. Time evolution of the UV-vis spectra of the a)  $\text{Co}_{\text{mnt}}^{3-}$  negolyte and b)  $\text{Co}_{\text{mnt}}^{1-}$  posolyte solutions diluted to  $50 \mu\text{M}$  concentration in 5 mM TBA PF<sub>6</sub> MeCN solution, after initial charge of  $(\text{TEA})_2\text{Co}_{\text{mnt}}$  to 2.2 V. Also shown is the uncharged starting solution (grey);  $50 \mu\text{M}$   $(\text{TEA})_2\text{Co}_{\text{mnt}}$  in 5 mM TBA PF<sub>6</sub> MeCN solution.**

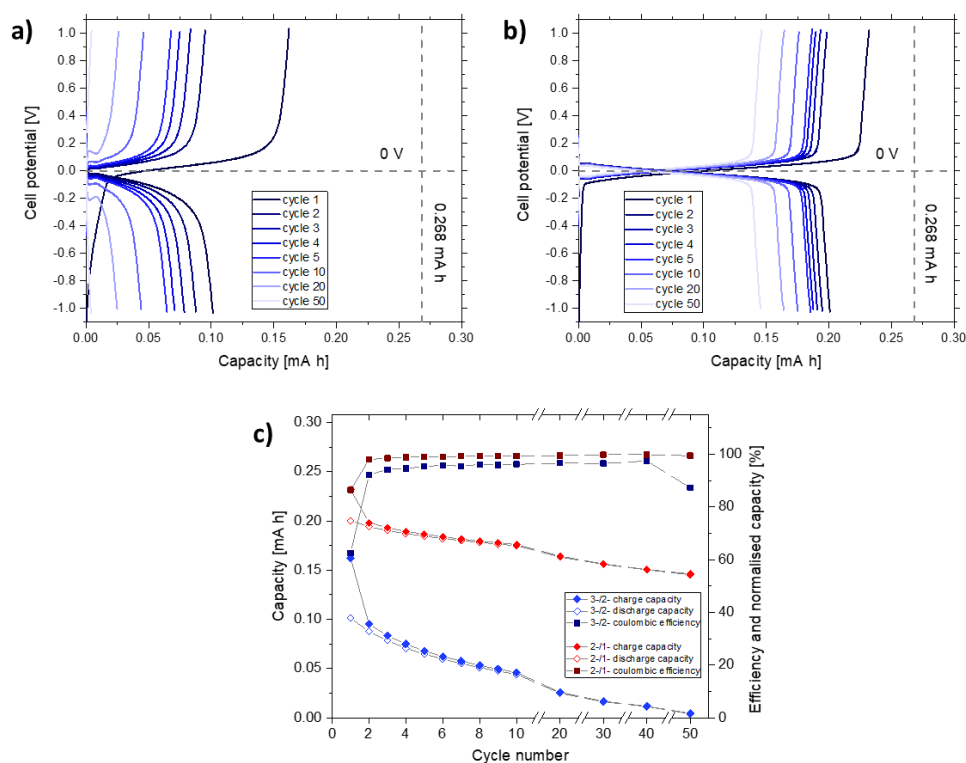


**Figure 79. Cell potential vs capacity for the independent redox couple battery cycling of a)  $\text{Co}_{\text{mnt}}^{3-/2-}$  and b)  $\text{Co}_{\text{mnt}}^{2-/1-}$ . Dashed grey lines indicate the theoretical potential and capacity. c) Charge-discharge capacities for selected cycles of independent redox couple battery cycling of  $\text{Co}_{\text{mnt}}^{3-/2-}$  and  $\text{Co}_{\text{mnt}}^{2-/1-}$ . Conditions: 1 mM  $(\text{TEA})_2\text{Co}_{\text{mnt}}$  in 0.1 M TBA  $\text{PF}_6$  MeCN solution,  $\pm 0.48 \text{ mA cm}^{-2}$  constant current density,  $\pm 1 \text{ V}$  charge-discharge voltage thresholds, Celgard separator.**

UV vis spectra of  $(\text{TEA})_2\text{Co}_{\text{mnt}}$  (Figure 78), indicate that the charged  $\text{Co}_{\text{mnt}}^{3-}$  negolyte solution is unstable, giving an almost identical spectrum to the initial  $\text{Co}_{\text{mnt}}^{2-}$  solution after only a few minutes. The posolyte  $\text{Co}_{\text{mnt}}^{1-}$  species is much more robust in solution, giving a distinct UV-vis spectrum which is almost unchanged over 22 hours. This is in line with the symmetric single redox couple battery cycling data, for which the posolyte-only  $\text{Co}_{\text{mnt}}^{2-/1-}$  battery significantly outperformed the negolyte-only  $\text{Co}_{\text{mnt}}^{3-/2-}$  system.

### 6.3.5 $\text{Ni}_{\text{mnt}}$ battery studies

Battery cycling of  $(\text{TEA})_2\text{Ni}_{\text{mnt}}$  achieved 91.5 % capacity on first charge with a well-defined plateau at the expected 1.92 V cell potential, as shown in Figure 80,

however thereafter the cell cycled with less than 20 % capacity. Moreover, the charge-discharge curves lacked any defined shape which indicated that the cell was not maintaining capacity. This result suggested that the charged electrolytes were very reactive towards the electrolyte, however it was unclear which oxidation states were unstable. The experiment was repeated using PC as the solvent to investigate whether the complex was reacting with MeCN. The experiment in PC resulted in a great improvement in battery cycling performance (Figure 81), with the initial charge cycle showing a long plateau around 1.92 V up to a capacity of 97 %. Despite this, the coulombic efficiency of the first cycle was very low (40 %) and the capacity faded to less than 10 % by the 50<sup>th</sup> cycle, indicating instability of the system.

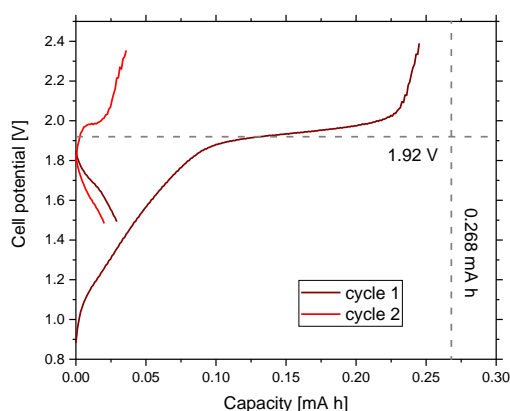


**Figure 80.** Cell potential vs capacity for the first two charge-discharge cycles at  $\pm 0.24 \text{ mA cm}^{-2}$  for  $1 \text{ mM (TEA)}_2\text{Ni}_{\text{mnt}}$  in  $0.1 \text{ M TBA PF}_6 \text{ MeCN}$  solution with Celgard separator. Dashed grey lines indicate the theoretical cell potential and capacity.

The independent redox couple RFB experiments of  $(\text{TEA})_2\text{Ni}_{\text{mnt}}$  in MeCN are perhaps the most insightful, with the negolyte retaining almost no capacity and the posolyte showing very robust performance with respect to long term cycling (Figure 82). The  $\text{Ni}_{\text{mnt}}^{3-/2-}$  negolyte system showed a poor initial discharge capacity of 16 % which rapidly faded to 4 % after just 10 cycles (Figure 82a), indicating that  $(\text{TEA})_2\text{Ni}_{\text{mnt}}$  is unstable as the negolyte, and would account for the very poor battery cycling performance of the MeCN symmetric RFB which displayed almost zero discharge capacity on the first cycle (Figure 80). In contrast, the  $\text{Ni}_{\text{mnt}}^{2-/1-}$

posolyte system is very stable to charge-discharge cycling with a capacity fade from only 66 % to 51 % over 100 cycles and an average coulombic efficiency of > 99 % (Figure 82c). The relatively low capacity was attributed to in part the method, such that charge imbalance of the electrolytes is inevitable, however the high coulombic efficiency indicates that the  $\text{Ni}_{\text{mnt}}^{1-}$  is significantly stable in the electrolyte. Despite  $(\text{TEA})_2\text{Ni}_{\text{mnt}}$  being shown to be ineffective as a single-species electrolyte in MeCN for symmetric RFBs, the  $\text{Ni}_{\text{mnt}}^{2-/1-}$  redox couple appears to be very stable over multiple charge-discharge cycles, so could be utilized as a posolyte material in an asymmetric RFB.

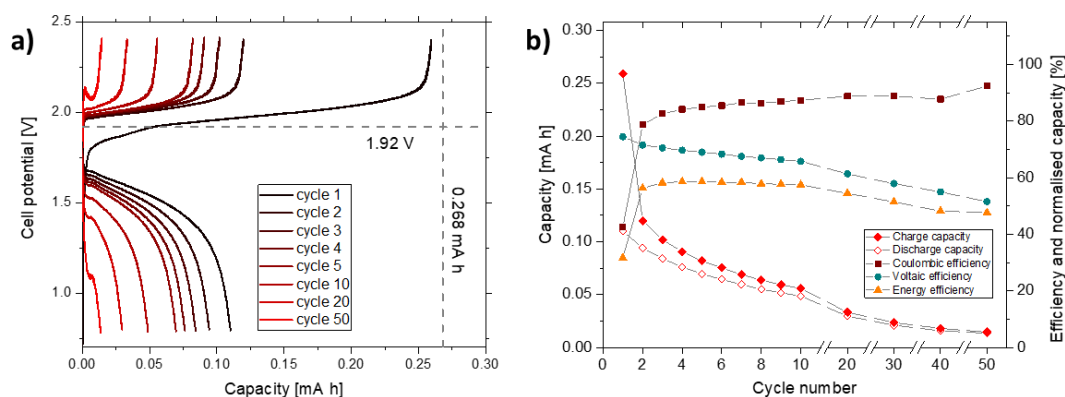


**Figure 81. a) Cell potential vs capacity for selected charge-discharge cycles for  $(\text{TEA})_2\text{Ni}_{\text{mnt}}$ . Dashed lines indicate the theoretical cell potential and capacity. b) Capacities and efficiencies for selected charge-discharge cycles for  $(\text{TEA})_2\text{Ni}_{\text{mnt}}$ . Conditions: 1 mM  $(\text{TEA})_2\text{Ni}_{\text{mnt}}$  in 0.1 M TBA  $\text{PF}_6$  PC solution, Celgard separator,  $\pm 0.48 \text{ mA cm}^{-2}$  constant current density, 2.4/0.8 V potential thresholds.**

UV-vis spectra of charged electrolyte solutions of  $(\text{TEA})_2\text{Ni}_{\text{mnt}}$  (Figure 83), indicate that the charged  $\text{Ni}_{\text{mnt}}^{3-}$  negolyte solution is very unstable, giving an almost identical spectrum to the starting  $\text{Ni}_{\text{mnt}}^{2-}$  electrolyte solution after only a few minutes. The reduced species  $\text{Ni}_{\text{mnt}}^{3-}$  in MeCN and DME solutions, have previously been observed to be air-sensitive and unstable in solution [242] – indicating that in our battery system, even trace amounts of oxygen may be causing rapid discharge of the  $\text{Ni}_{\text{mnt}}^{3-}$  species to the starting  $\text{Ni}_{\text{mnt}}^{2-}$  state resulting in very small capacity retention for the symmetric cell. Despite this, the posolyte

$\text{Ni}_{\text{mnt}}^{4-}$  species is far more stable in solution, giving a distinct UV-vis spectrum which shows little change over 22 hours.

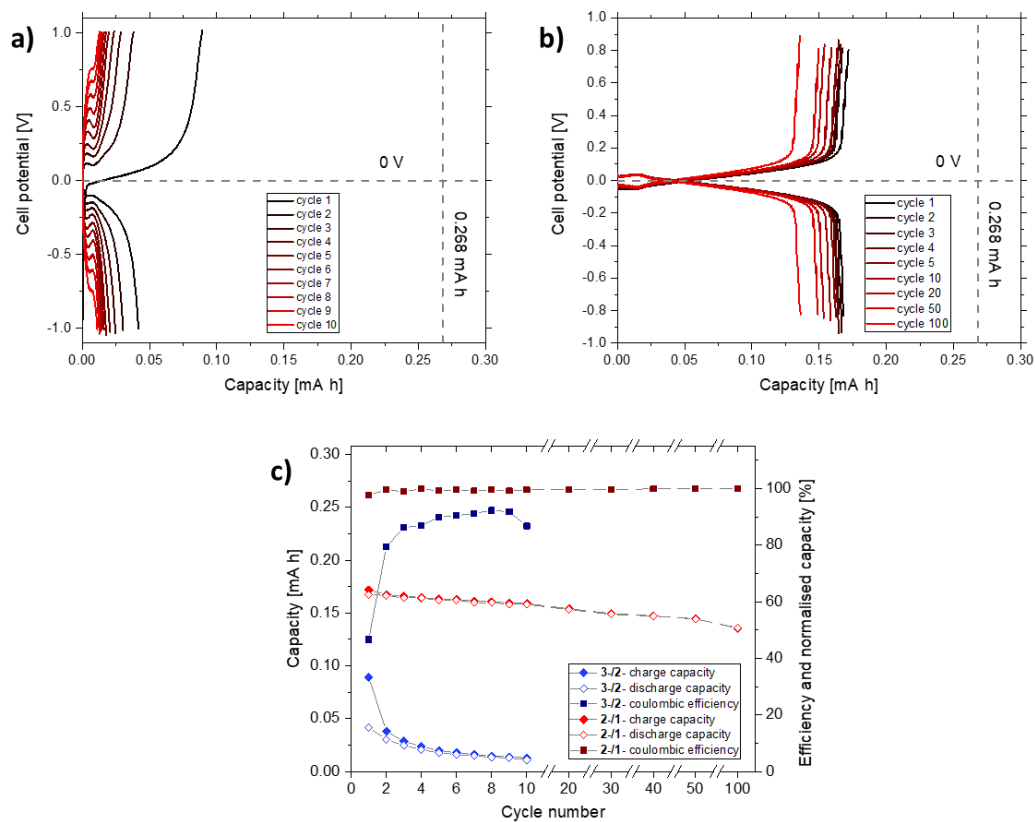


**Figure 82.** Cell potential vs capacity for the independent redox couple battery cycling of a)  $\text{Ni}_{\text{mnt}}^{3-/2-}$  and b)  $\text{Ni}_{\text{mnt}}^{2-/1-}$ . Dashed grey lines indicate the theoretical potential and capacity. c) Charge-discharge capacities for selected cycles of independent redox couple battery cycling of  $\text{Ni}_{\text{mnt}}^{3-/2-}$  and  $\text{Ni}_{\text{mnt}}^{2-/1-}$ . Conditions: 1 mM  $(\text{TEA})_2\text{Ni}_{\text{mnt}}$  in 0.1 M TBA PF<sub>6</sub> MeCN solution,  $\pm 0.48$  mA cm<sup>-2</sup> constant current density, Celgard separator.

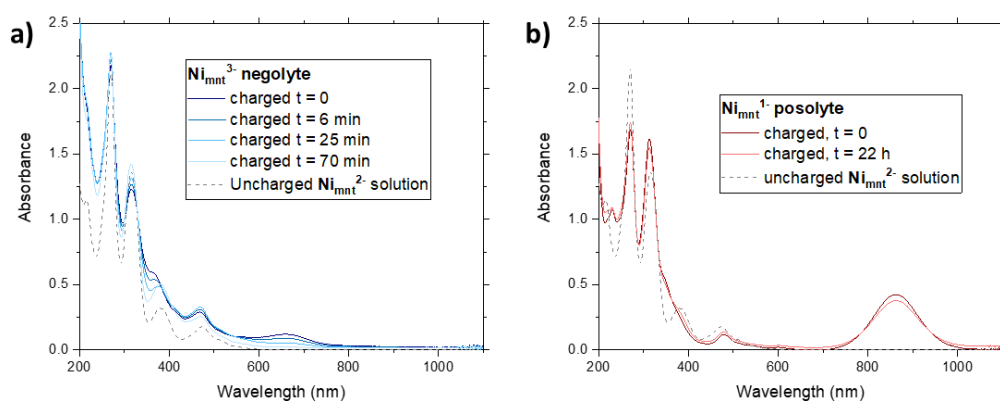


**Figure 83. Time evolution of the UV-vis spectra of the a)  $\text{Ni}_{\text{mnt}}^{3-}$  negolyte and b)  $\text{Ni}_{\text{mnt}}^{1-}$  posolyte solutions diluted to 50  $\mu\text{M}$  concentration in 5 mM TBA  $\text{PF}_6$  MeCN solution, after initial charge of  $(\text{TEA})_2\text{Ni}_{\text{mnt}}$  to 2.4 V. Also shown is the uncharged starting solution (grey); 50  $\mu\text{M}$   $(\text{TEA})_2\text{Ni}_{\text{mnt}}$  in 5 mM TBA  $\text{PF}_6$  MeCN solution.**

### 6.3.6 $\text{Cu}_{\text{mnt}}$ battery studies

$(\text{TEA})_2\text{Cu}_{\text{mnt}}$  was tested under 100 charge-discharge cycles at  $\pm 0.48 \text{ mA cm}^{-2}$  constant current density in MeCN with either a Celgard separator (Figure 84) or Fumapem F-930 CEM (Figure 85). The initial charge cycle with Celgard reached a capacity of 0.358 mA h (134 %), suggesting that self-discharge occurred during charging. The charge-discharge cycles exhibit voltage profiles with plateaus slightly above and below  $V_{\text{cell}} = 1.12 \text{ V}$  at 1.1-1.3 V on charge and 1.1-0.85 V on discharge, giving a consistent voltaic efficiency of 85 % over 100 cycles (Figure 84b). The coulombic efficiency and hence also energy efficiency remained near-constant at 60-68 % and 51-58 % respectively over cycles 2-100. The overall energy efficiency of this system is comparable to  $(\text{TEA})_2\text{V}_{\text{mnt}}$  and  $(\text{TEA})_2\text{Co}_{\text{mnt}}$  under the same conditions, however, the capacity retention of  $(\text{TEA})_2\text{Cu}_{\text{mnt}}$  is far superior, with the discharge capacity only fading from 65 % to 53 % from cycle 1 to 50 and retaining 43 % at the 100<sup>th</sup> cycle. Moreover, the excellent solubility of  $(\text{TEA})_2\text{Cu}_{\text{mnt}}$  in MeCN (0.91 M) makes this complex the highest performing complex studied here. Using the Fumapem F-930 CEM, under otherwise identical conditions, resulted in much poorer battery performance for the  $(\text{TEA})_2\text{Cu}_{\text{mnt}}$  system (Figure 85), with energy efficiency of 38-33 % for cycles 2-10 and rapid capacity fade with a discharge capacity of only 0.7 % on cycle 20. In addition, an

unexpected charge plateau starting at approx. 1.5 V was observed in this experiment, which was attributed to the irreversible oxidation at approx. 0.25 V vs Fc occurring in the polysolite. It is unclear why the same plateaus were not observed in Figure 84a, however it is possible that the increased cell resistance (due to the CEM) caused the irreversible oxidation to become a competing reaction in the battery.

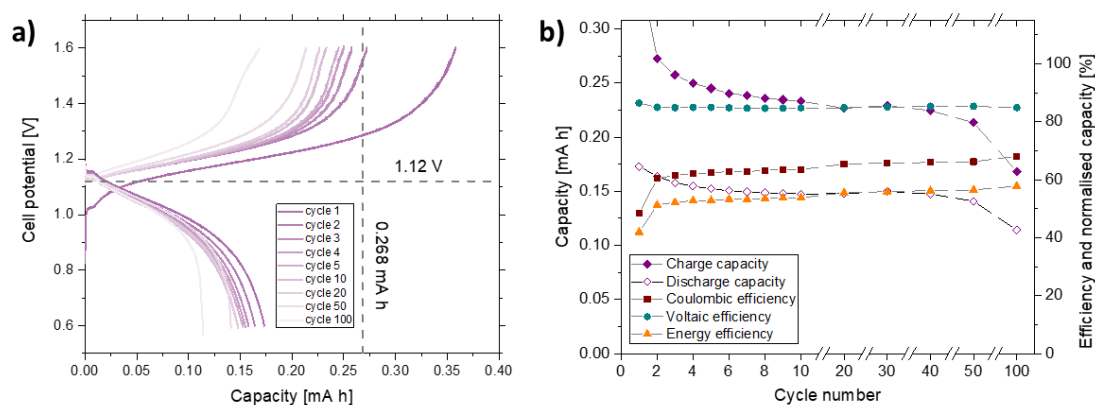


**Figure 84. a) Cell potential vs capacity for selected charge-discharge cycles for  $(\text{TEA})_2\text{Cu}_{\text{mnt}}$ . Dashed lines indicate the theoretical cell potential and capacity. b) Capacities and efficiencies for selected charge-discharge cycles for  $(\text{TEA})_2\text{Cu}_{\text{mnt}}$ . Conditions: 1 mM  $(\text{TEA})_2\text{Cu}_{\text{mnt}}$  in 0.1 M TBA PF<sub>6</sub> MeCN solution, Celgard separator,  $\pm 0.48 \text{ mA cm}^{-2}$  constant current density, 1.6/0.6 V potential thresholds.**

For  $(\text{TEA})_2\text{Cu}_{\text{mnt}}$ , as is seen with the other bis-mnt complexes  $(\text{TEA})_2\text{Co}_{\text{mnt}}$  and  $(\text{TEA})_2\text{Ni}_{\text{mnt}}$ , the negolyte is less stable with poor discharge capacity of 23 % and steady fade over 100 cycles to 9 % (Figure 87a). Despite this, the  $(\text{TEA})_2\text{Cu}_{\text{mnt}}$  polysolite single redox couple battery, i.e. cycling of  $\text{Cu}_{\text{mnt}}^{2-/1-}$  shows more stable performance (Figure 87b and c), with discharge capacities approximately twice that of the negolyte over the first 10 cycles before fading to a similar capacity by cycle 100.

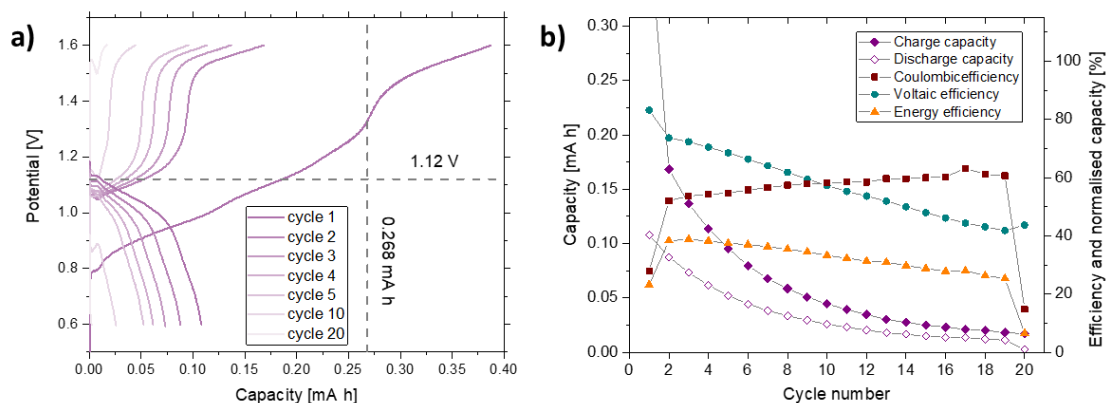


**Figure 85. a) Cell potential vs capacity for selected charge-discharge cycles for  $(\text{TEA})_2\text{Cu}_{\text{mnt}}$ . Dashed lines indicate the theoretical cell potential and capacity. b) Capacities and efficiencies for selected charge-discharge cycles for  $(\text{TEA})_2\text{Cu}_{\text{mnt}}$ . Conditions: 1 mM  $(\text{TEA})_2\text{Cu}_{\text{mnt}}$  in 0.1 M TBA  $\text{PF}_6$  MeCN solution, fumapem F-930 CEM,  $\pm 0.48 \text{ mA cm}^{-2}$  constant current density, 1.6/0.6 V potential thresholds.**

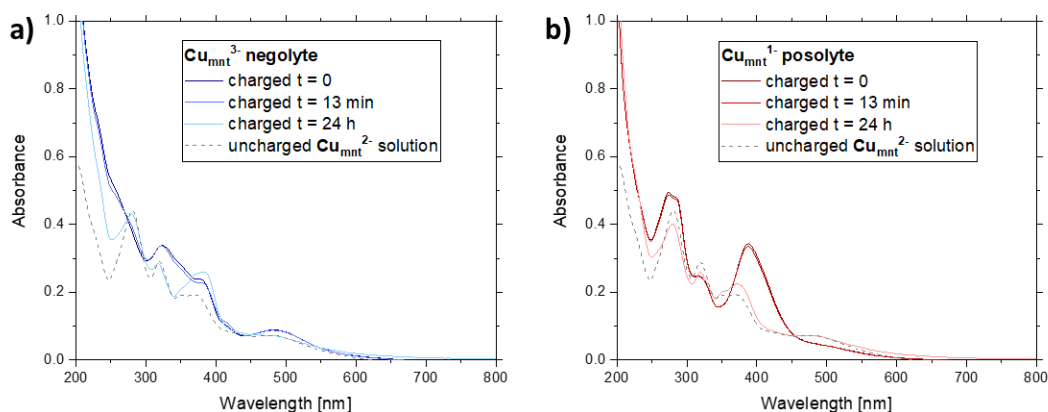


**Figure 86. Time evolution of the UV-vis spectra of the a)  $\text{Cu}_{\text{mnt}}^{3-}$  negolyte and b)  $\text{Cu}_{\text{mnt}}^{1-}$  posolyte solutions diluted to 50  $\mu\text{M}$  concentration in 5 mM TBA  $\text{PF}_6$  MeCN solution, after initial charge of  $(\text{TEA})_2\text{Cu}_{\text{mnt}}$  to 1.6 V. Also shown is the uncharged starting solution (grey); 50  $\mu\text{M}$   $(\text{TEA})_2\text{Cu}_{\text{mnt}}$  in 5 mM TBA  $\text{PF}_6$  MeCN solution.**

For  $(\text{TEA})_2\text{Cu}_{\text{mnt}}$  both the posolyte and negolyte solutions gave distinct spectra to the initial electrolyte and are stable for at least a few minutes (Figure 86). However, both charged electrolytes appear to self-discharge over 24 hours to give spectra resembling that of the initial  $\text{Cu}_{\text{mnt}}^{2-}$  electrolyte. This was consistent with the independent single redox couple battery cycling experiments whereby both the

posolyte and negolyte have similar discharge capacities after 100 cycles. Unlike the  $M = V, Co, Ni$  complexes which each had one oxidation state observed by UV-vis to rapidly self-discharge, both the charged oxidation states of  $Cu_{mnt}$  appear unstable, however the timeframe for self-discharge is much slower, thus allowing 100 charge-discharge cycles in the symmetric RFB to be conducted with low capacity fade.

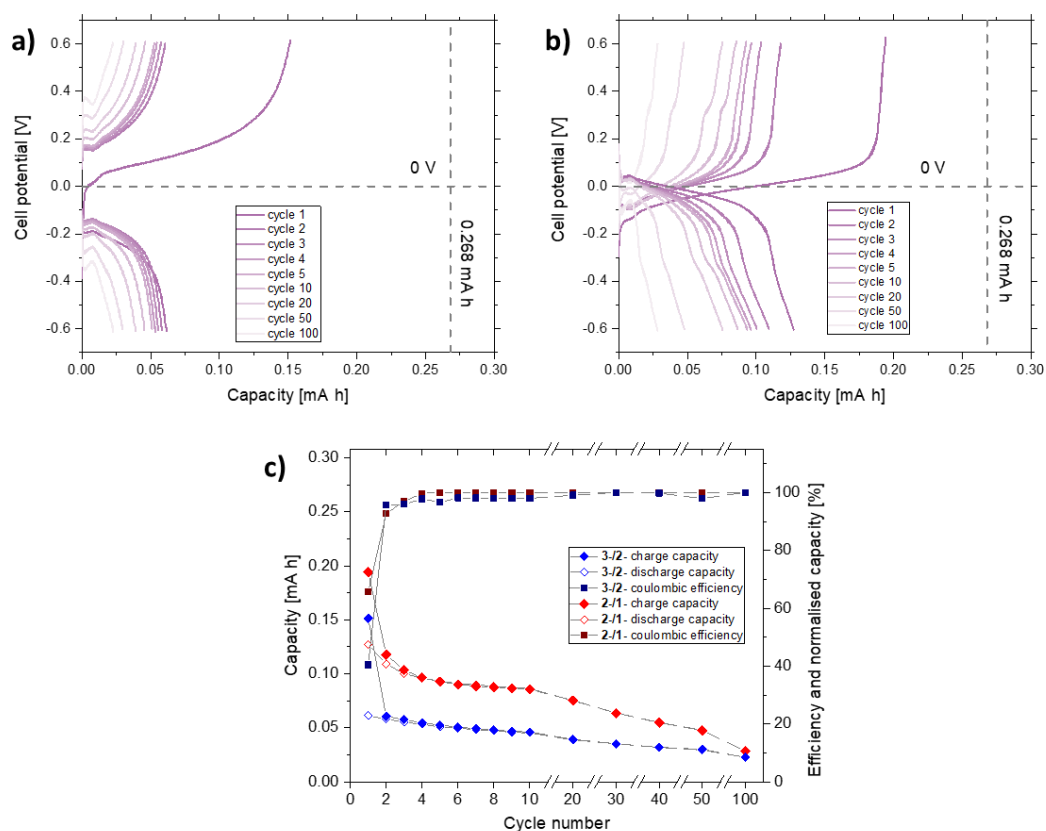


**Figure 87.** Cell potential vs capacity for the independent redox couple battery cycling of a)  $Ni_{mnt}^{3-/2-}$  and b)  $Ni_{mnt}^{2-/1-}$ . Dashed grey lines indicate the theoretical potential and capacity. c) Charge-discharge capacities for selected cycles of independent redox couple battery cycling of  $Ni_{mnt}^{3-/2-}$  and  $Ni_{mnt}^{2-/1-}$ . Conditions: 1mM  $(TEA)_2Ni_{mnt}$  in 0.1 M TBA  $PF_6$  MeCN solution,  $\pm 0.48$  mA  $cm^{-2}$  constant current density, Celgard separator.

### 6.3.7 $\text{Fe}_{\text{mnt}}$ battery studies

Despite the  $\text{Fe}_{\text{mnt}}$  complex giving a low solubility and small cell potential, a fair assessment of its battery performance was made. This experiment was challenging as the  $\text{Fe}_{\text{mnt}}$  complex was synthesised as the monoanion and therefore the  $(\text{TEA})\text{Fe}_{\text{mnt}}$  solution cannot be directly used for a symmetric electrolyte. Therefore, the  $(\text{TEA})_2\text{Fe}_{\text{mnt}}$  complex must first be accessed before then charging to the  $(\text{TEA})_3\text{Fe}_{\text{mnt}}$  and  $(\text{TEA})\text{Fe}_{\text{mnt}}$  oxidation states in the negolyte and posolyte respectively. A 2 mM solution of  $(\text{TEA})\text{Fe}_{\text{mnt}}$  was first electrolysed to  $(\text{TEA})_2\text{Fe}_{\text{mnt}}$  in the flow-cell against the irreversible oxidation reaction, shown in Figure 66a. The 2 mM  $(\text{TEA})_2\text{Fe}_{\text{mnt}}$  solution was then diluted to 1 mM concentration and used in both half-cells of the flow-cell. Charge-discharge was then attempted under the same conditions as the other complexes as shown in Figure 88. The cell charged to 0.423 mA h (158 %) but then discharged and cycled with approx. 16 % capacity thereafter. In addition, the cell did not charge at the intended 1.42 V cell potential, but rather at a lower 0.9 V cell potential. Due to the complexity of the experiment and the possible instability of the  $\text{Fe}_{\text{mnt}}$  oxidation states, it is difficult to diagnose what processes were occurring within the flow-cell. Regardless, the small cell potential, low solubility and irregular  $\text{Fe}_{\text{mnt}}^{2-/1-}$  redox couple make the complex completely unsuitable for application.

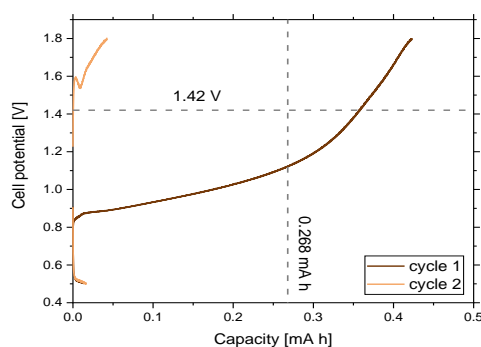


**Figure 88. Cell potential vs capacity for the first two charge-discharge cycles at  $\pm 0.24 \text{ mA cm}^{-2}$  for 1 mM  $(\text{TEA})_2\text{Fe}_{\text{mnt}}$  in 0.1 M TBA  $\text{PF}_6$  MeCN solution with Celgard separator. Dashed grey lines indicate the theoretical cell potential and capacity.**

### 6.3.8 $M_{\text{mnt}}$ battery comparison

In a symmetric full-cell RFB,  $(\text{TEA})_2\mathbf{V}_{\text{mnt}}$  and  $(\text{TEA})_2\mathbf{Co}_{\text{mnt}}$  showed modest performance, with the initial 10 cycles displaying high voltaic efficiencies of 95-96 % each, however long-term cycling was not possible with significant discharge capacity fade to 20 % and 14 % respectively by cycle 50.  $(\text{TEA})_2\mathbf{Cu}_{\text{mnt}}$  displays comparable performance over 10 charge-discharge cycles, however, it showed superior capacity retention with a smaller capacity fade to 43 % over 100 cycles, and is the best performing symmetric RFB studied here. For  $(\text{TEA})_2\mathbf{Ni}_{\text{mnt}}$ , which displayed the largest cell potential for a simple one-electron disproportionation symmetric electrolyte, almost zero discharge capacity could be achieved in MeCN, however a switch to PC solvent did allow for charge-discharge cycling, albeit with poor performance.

Independent single redox couple flow-cell experiments revealed that for  $(\text{TEA})_2\mathbf{V}_{\text{mnt}}$  the negolyte  $\mathbf{V}_{\text{mnt}}^{3-/2-}$  is more robust than the posolyte  $\mathbf{V}_{\text{mnt}}^{2-/1-}$  with greater capacity retention achieved for the negolyte-only experiment, despite both processes being reversible on a CV timescale. A previous study on the  $\mathbf{V}_{\text{mnt}}$  redox series, using X-ray absorption spectroscopy and DFT calculations, determined that oxidation of  $\mathbf{V}_{\text{mnt}}^{2-} = [\text{V}^{\text{IV}}(\text{mnt}_3^{6-})]^{2-}$  is a ligand-centred process to the diradical  $[\text{V}^{\text{IV}}(\text{mnt}_3^{5\cdot})]^- = \mathbf{V}_{\text{mnt}}^{1-}$  species and involves a change in geometry from distorted octahedral to trigonal prismatic, while reduction to  $\mathbf{V}_{\text{mnt}}^{3-}$  is metal-centred, i.e. V(IV) to V(III) [234]. While no conclusions on the stability of the redox products were made in the above report, and both redox processes are reversible by CV [234], two different processes (ligand- vs. metal-centred redox) appear to give RFB electrolytes of contrasting stability.

Conversely, for the square planar bis-mnt complexes ( $M = \text{Co}, \text{Ni}, \text{Cu}$ ) it was the posolyte which showed greater capacity retention over multiple charge-discharge cycles of the single redox couple, while the negolyte in each case was unstable. A previous study, in THF solution, found that metal-centred reduction of  $\mathbf{Co}_{\text{mnt}}^{2-}$  gives the air-sensitive unstable  $\mathbf{Co}_{\text{mnt}}^{3-}$  trianion, while ligand-centred oxidation to the  $\mathbf{Co}_{\text{mnt}}^{1-}$  monoanion is more robust [243]. Similarly, for  $\mathbf{Ni}_{\text{mnt}}^{2-}$  the reduction is metal-centred and the  $\mathbf{Ni}_{\text{mnt}}^{3-}$  product has been observed to be unstable in air

reverting back to the dianion [242]. Trace amounts of oxygen present in the solvent, despite working in glovebox conditions, could well be responsible for the rapid capacity fade of the negolytes of the  $\text{Co}_{\text{mnt}}$  and  $\text{Ni}_{\text{mnt}}$  RFBs as the concentration of the  $\text{M}_{\text{mnt}}$  complexes was only 1 mM in this study. Another previous dithiolene study has observed that weak protic acids oxidize the basic and strongly reducing  $\text{Co}_{\text{mnt}}^{3-}$  and  $\text{Ni}_{\text{mnt}}^{3-}$  species in THF solution, either directly to  $\text{M}_{\text{mnt}}^{2-}$ , or through protonation to  $[\text{M}(\text{H})(\text{mnt})_2]^{2-}$  hydrides followed by subsequent decomposition to  $\text{M}_{\text{mnt}}^{2-}$  and  $\text{H}_2$  [244]; this could be another possible mechanism for the self-discharge of  $\text{Co}_{\text{mnt}}^{3-}$  and  $\text{Ni}_{\text{mnt}}^{3-}$  negolytes observed by UV-vis in the present study. More recently, sulfur K-edge X-ray absorption spectroscopy has been used to determine  $\text{Ni}_{\text{mnt}}^{2-}$  oxidation to  $\text{Ni}_{\text{mnt}}^{1-}$  is ligand-centred [233], and results in a very stable  $\text{Ni}_{\text{mnt}}^{2-/1-}$  posolyte system in the present study. Again, it is noted that a contrast between ligand- vs metal-centred redox processes exists in terms of the stability of the resulting RFB electrolytes; however, conversely to six-coordinate tris-mnt  $\text{V}_{\text{mnt}}$  where metal-centred reduction gives a stable negolyte, for four-coordinate bis-mnt  $\text{Co}_{\text{mnt}}$  and  $\text{Ni}_{\text{mnt}}$  it is the ligand-centred oxidation that results in the more stable posolytes. The posolyte of  $\text{Cu}_{\text{mnt}}$  displays poorer capacity retention than the posolytes of  $\text{Co}_{\text{mnt}}$  and  $\text{Ni}_{\text{mnt}}$ ; interestingly, oxidation of  $\text{Cu}_{\text{mnt}}^{2-}$  to  $\text{Cu}_{\text{mnt}}^{1-}$  is a metal-centred Cu(II) to Cu(III) process [233], in contrast to the ligand-centred oxidation of  $\text{Co}_{\text{mnt}}^{2-}$  and  $\text{Ni}_{\text{mnt}}^{2-}$ .

The best performing electrolytes are the  $(\text{TEA})_2\text{V}_{\text{mnt}}^{3-/2-}$  negolyte, and the  $(\text{TEA})_2\text{Co}_{\text{mnt}}^{2-/1-}$  and  $(\text{TEA})_2\text{Ni}_{\text{mnt}}^{2-/1-}$  posolytes which retain ~40-50 % capacity after 100 charge-discharge cycles and are therefore promising for use in asymmetric RFBs.

## 6.4 Conclusions

Five transition metal complexes of the dithiolene ligand mnt have been assessed for application as redox-active materials for single-species electrolytes in symmetric non-aqueous RFBs. The V, Co, Ni, and Cu complexes all exhibit at least two reversible redox-couples and have favourable diffusion coefficients/electrochemical rate constants suitable for RFB charge-discharge

battery cycling in MeCN solvent. While  $(\text{TEA})_2\text{Ni}_{\text{mnt}}$  and  $(\text{TEA})\text{Fe}_{\text{mnt}}$  MeCN electrolytes displayed poor performance and stability in symmetric RFBs,  $(\text{TEA})_2\text{V}_{\text{mnt}}$ ,  $(\text{TEA})_2\text{Co}_{\text{mnt}}$ , and  $(\text{TEA})_2\text{Cu}_{\text{mnt}}$  were able to be charged-discharged for up to 100 cycles with high voltaic efficiencies. However, capacity retention over multiple cycles proved challenging, with 43 % retention the best achieved over 100 cycles for  $(\text{TEA})_2\text{Cu}_{\text{mnt}}$ . Analysing the negolyte and posolyte solutions separately, by independent single redox couple battery cycling, revealed that in each case one oxidation state was far more robust to long term cycling. This was especially insightful for  $(\text{TEA})_2\text{Ni}_{\text{mnt}}$  which could not be charged-discharged in a symmetric MeCN RFB; the negolyte suffers immediate capacity fade, while the posolyte is robust to 100 charge-discharge cycles. Monitoring of the UV-vis spectra of freshly charged negolyte and posolyte solutions of each complex over time, agreed with the observations of posolyte/negolyte stability from the single redox couple RFB experiments, and indicated that unstable redox states were self-discharging to the starting dianionic state. The self-discharging mechanism results in a cell imbalance, inherently limiting capacity of the symmetric RFBs.

Although the dithiolene complexes studied here are not suitable as materials for single-species symmetric RFBs, longer-term stability was observed for  $(\text{TEA})_2\text{V}_{\text{mnt}}^{3-/2-}$  negolyte and  $(\text{TEA})_2\text{Co}_{\text{mnt}}^{2-/1-}$  and  $(\text{TEA})_2\text{Ni}_{\text{mnt}}^{2-/1-}$  posolyte solutions and are therefore applicable as single electrolytes in asymmetric RFBs. The development of ion-selective membranes which are suitable for use with non-aqueous electrolytes is at present a limitation in the field of NA RFBs and as such hinders the use of the studied dithiolene metal complexes in asymmetric battery designs.

It is evident from the present study that chemical instability is inherent to the mnt ligands. It is likely that the small size of the ligands means that the metal centre is accessible to other molecules because of a lack of steric protection. Indeed, for the planar bis-mnt complexes, it is expected that the metal centre will easily coordinate with other ligands to form 5 coordinate complexes which are likely to be intermediate species in reaction mechanisms. Perhaps for this reason, the  $\text{M}_{\text{mnt}}$  complexes are reactive because the solvents like MeCN are known to be

weak ligands [245]. In addition, the bidentate ligands may be undesirably labile in solution and may exchange with MeCN or other species. Future work could target derivatized dithiolene ligands which are more protecting of the metal centre or less labile. Such effects are expected to increase the stability of the oxidized and reduced states of the complexes.

# Chapter 7

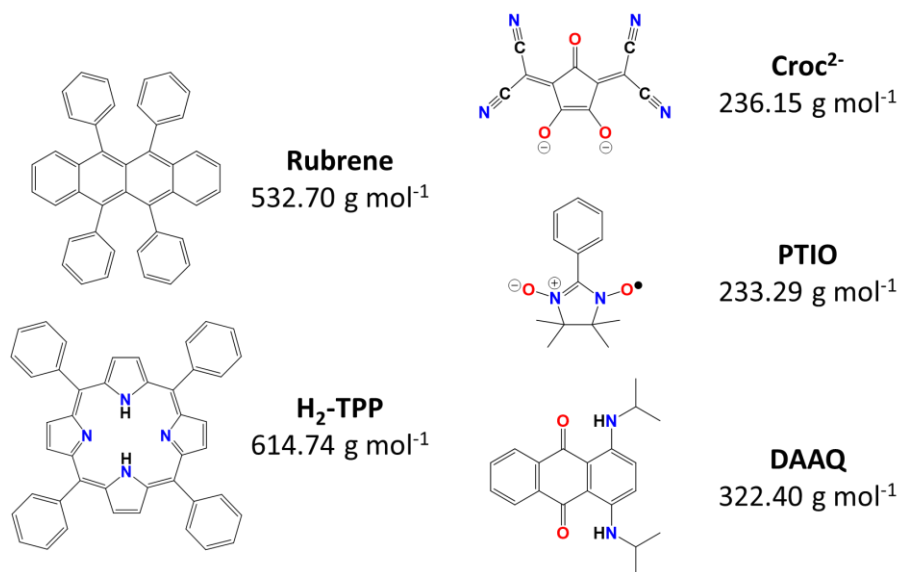
## Symmetric Organic Electrolyte: Croconate Violet

The work presented in this chapter is published in [4] and contributed to [2].

### 7.1 Introduction

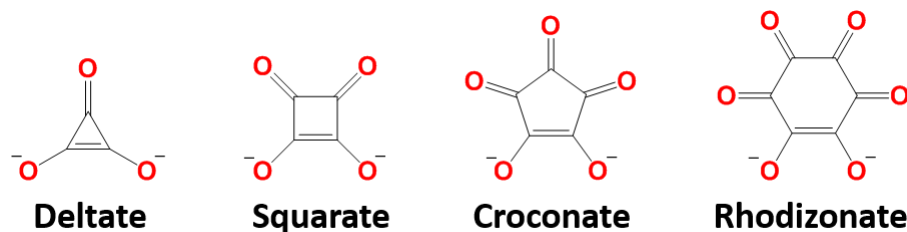
The MCCs described in Chapters 5 and 6 demonstrate the ease at which symmetric RFBs based on inorganic redox materials can be constructed, due to the multiple stable oxidation states of the metal centre and large potential difference between them. In contrast it is considerably more challenging to realise a symmetric NA RFB based upon a single organic redox material because ROMs typically undergo fewer redox transitions and exist in a limited number of stable oxidation states (most commonly only one redox couple). Furthermore, in the cases where ROMs present with two redox couples, such as quinoxalines [158,164,246], p-phenylenediamines [174], anthraquinones [165,187], phenothiazines [165] and pyridiniums [160,182], the potential difference between the two redox couples is typically small ( $\leq 0.8$  V), meaning that the RFB cell potential is restricted. For these reasons only four symmetric ROM flow batteries have been reported to date. In 2007 the cyclic voltammetry of rubrene (Scheme 8) was reported by Chakrabarti et al. giving a 2.33 V potential difference, however due to the very poor solubility of rubrene in MeCN (a 3:1 mixture of MeCN to toluene was required to dissolve rubrene at 0.25 mM) and high cost (> £45 per gram) this ROM was not applied for RFBs [94]. The first successful application of a symmetric ROM in a NA RFB was by Duan et al. in 2016 whereby 2-phenyl-4,4,5,5-tetramethylimidazoline-1-oxyl-3-oxide (PTIO, Scheme 8) was used to achieve a one-electron battery with a 1.73 V cell potential [169,179]. Also in 2016, Potash et al. demonstrated a two-electron symmetric RFB (4 redox couples) with a 1.76 V

cell potential (or 2.72 V if using all four redox couples) by use of diaminoanthraquinones (DAAQ, Scheme 8) [152]. More recently, a porphyrin derivative was applied by Ma et al. demonstrating a high 2.83 V two-electron RFB ( $H_2$ TPP, Scheme 8) which, despite a maximal solubility of 10 mM (highest in the DCM solvent used compared to more polar conventional solvents), achieved good capacity retention [99].



**Scheme 8. Chemical structures and molecular weights of symmetric ROMs for NA RFBs.**

A general survey of redox chemistry literature identified oxocarbons and their pseudooxocarbon derivatives as possible ROMs for applications in RFBs. Oxocarbons are a family of compounds composed of only carbon and oxygen atoms;  $C_xO_y$  where X and Y are integers. Radialene-type cyclic polyketones are a sub-class of oxocarbons with formula  $C_nO_n$ , where n is an integer, which are regarded as cyclic polymers of carbon monoxide. Given their structure, each carbonyl of a cyclic oxocarbon is in theory reducible to an enolate ion, thus giving a redox series from the neutral state to the n<sup>th</sup> anionic state. Therefore, given their low molecular weights and solubility and polar solvents, oxocarbons such as deltate, squarate, croconate and rhodizonate (Scheme 9) are expected to be good ROM candidates for applications in RFBs.

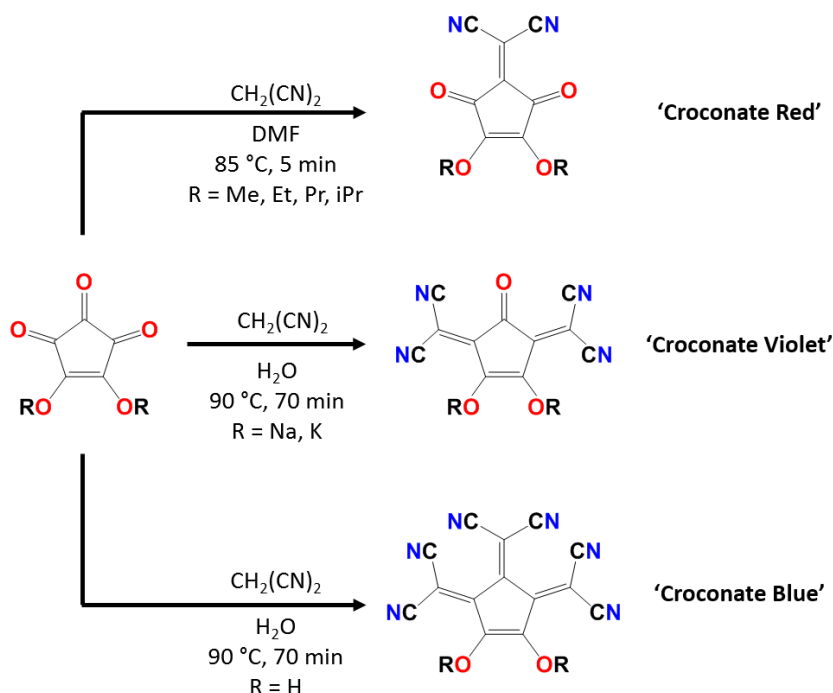


**Scheme 9. Radialene-type oxocarbon dianion structures.**

Although there is significant literature regarding the chemistry of oxocarbons and pseudooxocarbons [247–255], there is relatively little reported electrochemistry to use as a basis for application in a NA RFB [256–258]. Despite this, the pseudooxocarbon croconate violet ( $\text{Croc}^{2-}$ , Scheme 8) stands out as giving promising electrochemistry [259–261] and has featured in several publications [259–266] including those whereby the molecule is used as a bidentate ligand in an MCC [259,266].  $\text{Croc}^{2-}$  is a pseudooxocarbon derivative of croconic acid whereby two carbonyl groups have been substituted with dicyanomethylene substituents, however similar molecules croconate red and blue also exist which possess one or three dicyanomethylene groups respectively (Scheme 10).

These croconate pseudooxocarbons were first prepared in 1978 [262,264] and then later studied by voltammetry in 1982 by L. Doane and A. Fatiadi [260,261]. Because of the unusually high proportion of redox-active functional groups and the molecular resonance, the croconate dyes display an exceptionally rich amount of electrochemistry despite their low molecular weight. Previous literature has shown that the croconate dianions are capable of a four-electron redox series via one-electron processes, from the neutral to the tetra-anion oxidation state, thus giving four redox couples which may be exploited for a symmetric NA RFB design [260]. In addition, the molecules display many other properties desirable for application; the croconate derivatives are low molecular weight, significantly polar, soluble in a range of solvents, and their molecular bonding is significantly delocalised across the whole molecule [264] which should enhance the stability of the molecule's oxidation states via resonance. Furthermore, in comparison to the previously reported symmetric ROM electrolytes, which are neutral compounds that disproportionate to anionic and cationic species in the battery electrolyte and

posolyte respectively,  $\text{Croc}^{2-}$  is dianionic and therefore the one-electron disproportionation of  $\text{Croc}^{2-}$  yields anionic oxidation states. Such a common-ion symmetric electrolyte (akin to the VRFB) is more preferential for application as it would allow a conventional CEM to be used to inhibit crossover of the anionic Croc chemistry. Based on these properties, the croconate dyes were targeted as promising candidates for a symmetric ROM electrolyte for NA RFBs.



**Scheme 10. Preparation of croconate pseudooxocarbons via Knoevenagel condensation reactions with malononitrile [262,264].**

## 7.2 Experimental

### 7.2.1 Chemicals and reagents

All synthetic reagents, solvents and supporting salts were purchased and used as received without purification. MeCN (HPLC grade) was purchased from Fisher. Anhydrous MeCN (Acrosealed® extra-dry over molecular sieves), anhydrous DMF (Acrosealed®), anhydrous PC (Acrosealed®), and sodium rhodizonate dibasic (98 %) were purchased from Acros Organics. TBA  $\text{PF}_6$ , (>98 %), TEA  $\text{BF}_4$ , TBA Cl, (>98 %) and lithium bis(trifluoromethanesulfonyl)imide (Li TFSI, >98 %) were purchased from TCI UK Ltd. Activated manganese(IV) oxide (~85 %, <10  $\mu\text{m}$ ), Celite®,

benzothiadiazole (98 %), 7,7,8,8-Tetracyanoquinodimethane (98 %) and malononitrile ( $\geq 99$  %) were purchased from Sigma Aldrich.

### 7.2.2 Synthesis of Croconate Violet

The croconate violet dianion was prepared by a modified literature procedure to that given in refs [262,263].

**Preparation of Croconic acid disodium.** Sodium rhodizonate dibasic (9.54 mmol) was dissolved in 70 mL deionised water, to which activated magnesium(IV) oxide (57.24 mmol) was added. The solution was refluxed for two hours and then filtered over Celite® to remove the MnO<sub>2</sub> catalyst. The resulting yellow filtrate was then collected via rotary evaporation to yield the ring-contraction product croconic acid disodium trihydrate (8.65 mmol, 91 %). <sup>13</sup>C NMR (100 MHz, acetone-d<sub>6</sub>)  $\delta$  = 188.93 (-CO-CO-CO-) ppm.

**Preparation of sodium croconate violet hemipenta hydrate.** Croconic acid disodium trihydrate (2.69 mmol) was re-dissolved in 10 mL deionised water and a large excess of malononitrile (24.18 mmol) was added. The solution was then refluxed at 90 °C for 70 minutes and then the water was removed under high-vacuum. The product was recrystallised from hot water and filtered to yield the blue crystalline product sodium croconate violet hemipenta hydrate (Na<sub>2</sub>Croc·2.5H<sub>2</sub>O, 1.74 mmol, 64 %).

**Preparation of tetrabutylammonium croconate violet.** Na<sub>2</sub>Croc·2.5H<sub>2</sub>O (1.53 mmol) was dissolved in 4 mL water and then pipetting into a 45 mL aqueous solution of excess TBA Cl (6.12 mmol). The resulting green microcrystalline precipitate was then stored at 3 °C overnight before collecting by Buchner filtration under vacuum and drying, to give the tetrabutylammonium croconate violet product (TBA<sub>2</sub>Croc, 0.84 mmol, 55 %). The product was then dried under high vacuum to remove water before use. Product analysis via NMR is consistent with the literature procedure [262,263]. Calculated: C 70.74, H 10.08, N 11.51 %; found: C 70.50, H 10.40, N 11.74 %. <sup>1</sup>H NMR (400 MHz, acetone-d<sub>6</sub>)  $\delta$  = 0.97 (t, J = 7.3 Hz, 3H, -CH<sub>3</sub>), 1.43 (sx, J = 7.4 Hz, 2H, CH<sub>3</sub>CH<sub>2</sub>-), 1.81 (m, 2H, -CH<sub>2</sub>-CH<sub>2</sub>-CH<sub>2</sub>-), 3.44 (m, 2H, -CH<sub>2</sub>-N<sup>+</sup>) ppm. <sup>13</sup>C NMR (100 MHz, acetone-d<sub>6</sub>)  $\delta$  = 14.00 (-CH<sub>3</sub>, NBu<sub>4</sub><sup>+</sup>)

20.48 (CH<sub>3</sub>-CH<sub>2</sub>-, NBu<sub>4</sub><sup>+</sup>) 24.55 (-CH<sub>2</sub>-CH<sub>2</sub>-CH<sub>2</sub>-, NBu<sub>4</sub><sup>+</sup>) 48.78 (C(CN)<sub>2</sub>) 59.46 (-CH<sub>2</sub>-N<sup>+</sup>, NBu<sub>4</sub><sup>+</sup>) 120.16, 120.59 (CN) 149.51 (C3, C5: CC(CN)<sub>2</sub>); 181.18 (C1, C2, C4: CO) ppm.

### 7.2.3 Solubility measurement

The solubility of TBA<sub>2</sub>Croc in MeCN was measured by a UV-Vis methodology (Appendix C). A calibration curve was first measured by preparing series dilutions of TBA<sub>2</sub>Croc concentrations in the range of 1 to 10 μM. The resulting linear relationship between absorption at λ<sub>max</sub> = 554 nm and concentration obeyed the Beer-Lambert Law, thus allowing an unknown concentration to be calculated. A saturated solution of TBA<sub>2</sub>Croc was then prepared by mixing approximately 500 mg of TBA<sub>2</sub>Croc in 1 mL pure MeCN, heating to reflux and sonicating. After cooling to room temperature and allowing excess solid to precipitate out of solution, 0.5 mL of solution was extracted, and series diluted into the calibration range in order to back-calculate the concentration at the solubility limit. A 10 mm path-length quartz cuvette (Starna®) and Cary 60 UV-vis spectrometer (Agilent technologies) were used for all spectra acquired.

### 7.2.4 Voltammetry investigations

Electrolytes for voltammetry consisted of 1 mM of redox material in a solution of HPLC grade MeCN with 0.1 M supporting salt. CV was performed by using a standard 20 mL 3-electrode glass cell (BASi®) consisting of a 3 mm diameter GC WE, Pt CE and a Ag/Ag<sup>+</sup> RE containing the corresponding supporting electrolyte only. RDE studies were performed using a 60 mL RRDE-3A apparatus (ALS Co., Ltd) with a 3 mm diameter GC working electrode at rotation rates in the range of 300 to 3000 rpm. All voltammetry experiments were performed under an inert N<sub>2</sub> atmosphere; solutions were fully purged before use whereas during scans a N<sub>2</sub> headspace was maintained to prevent the ingress of oxygen. WEs were cleaned before use by polishing with diamond (3 μM then 0.25 μM particle size, nylon polishing pad) and alumina slurries (Buehler) (0.05 μM particle size, felt polishing pad), sonicating in de-ionised water, rinsing with MeOH and drying under compressed air. Data was recorded using either an EmStat<sup>3+</sup> (Palmsens),

Compactstat (IVIUM technologies) or PGSTAT204 (Metrohm) with a resolution of 1 mV. Potentials reported here are referenced against the Fc used as an internal standard.

### 7.2.5 Battery methods

Bulk electrolysis was performed using the GC-III glass cell. High surface area RVC foam electrodes and a Ag/Ag<sup>+</sup> RE were used for electrolysis whereas a GC WE was used for in-situ CV. Electrolysis of 6 mL of 1 mM TBA<sub>2</sub>Croc in 0.1 M TBA PF<sub>6</sub>, MeCN electrolyte was conducted at a constant 1 mA current until defined potential thresholds were reached. A 4 mL solution of supporting 0.1 M TBA PF<sub>6</sub>, MeCN electrolyte was used in the counter electrode compartment as sacrificial electrolyte.

Galvanostatic battery experiments were performed using the FC-II flow-cell. Experiments were conducted using IDFFs, 0.5 mm carbon paper electrodes (TFP Ltd. PVA binder) and a Fumapem<sup>®</sup> F-930 CEM or Celgard. Battery experiments were conducted on 10 mL solutions of 1 or 10 mM redox material in anhydrous MeCN with 0.1 or 0.5 M supporting salt at a flow-rate of 10 mL min<sup>-1</sup> by use of a Masterflex L/S peristaltic pump (Cole-Parmer). The batteries were then cycled at constant current density until the cell reached defined threshold potentials. Experiments were conducted within a N<sub>2</sub> glovebox (Saffron Scientific Ltd or MBRAUN) which was maintained at oxygen and water levels at a maximum of 1 ppm. Independent redox couple battery cycling experiments were conducted by: firstly, fully charging the symmetric battery via the one-electron disproportionation of Croc<sup>2-</sup> to produce charged electrolytes, then disposing of one electrolyte and replacing with fresh Croc<sup>2-</sup> electrolyte.

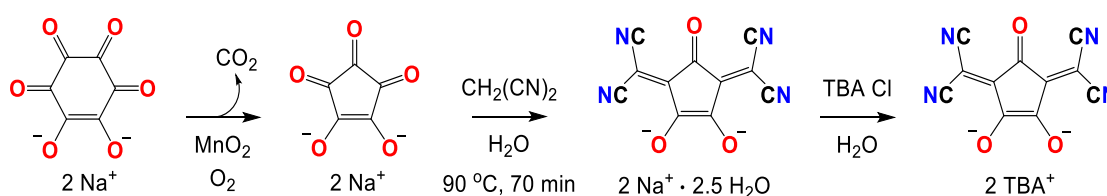
## 7.3 Results and discussion

The croconate dyes are intensely chromophoric organic dyes which are prepared by the substitution of the carbonyl groups of croconic acid with dicyanomethylene groups, as shown in Scheme 10. Based on the published literature, it was evaluated that Croc<sup>2-</sup> would be the simplest and most convenient

croconate dye to synthesise and that its electrochemistry would be sufficiently representative of the croconate dye group for an exploratory study.

### 7.3.1 Synthesis of TBA<sub>2</sub>Croc and solubility

Preparation of the Croc<sup>2-</sup> redox material is low-cost due to inexpensive starting materials (Material cost estimated as 7.23 GBP g<sup>-1</sup>) and involves simple reaction steps in aqueous solvent without requiring anaerobic conditions (Scheme 11). The Croc<sup>2-</sup> product is air- and moisture-stable and does not appear to photochemically decompose during long-term storage. The product is isolated as a pure crystalline powder which is easily handled despite being significantly skin staining.



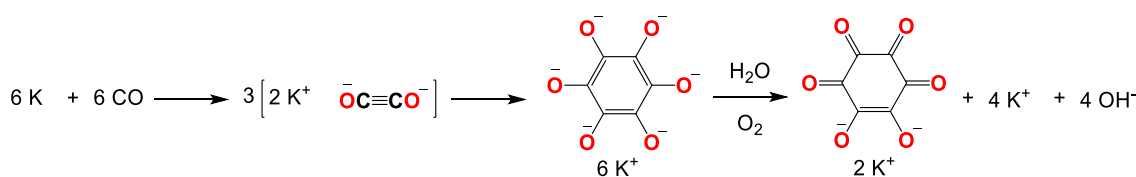
**Scheme 11. Synthetic scheme for the preparation of croconate violet**

Although commercially available, croconic acid disodium starting material is relatively expensive (~65 GBP g<sup>-1</sup>) however it is easily prepared by ring contraction of cheaper Sodium rhodizonate dibasic (~3 GBP g<sup>-1</sup>). Rhodizonate ring contraction occurs spontaneously in aerated water, however the reaction is sluggish due to limiting rhodizonate solubility and poor oxygen flux into the solution. Literature procedures suggested the use of NaOH to catalyse the sluggish reaction (r.t. 7 days), however the long reaction time was undesirable [263]. Despite efforts to accelerate the reaction such as bubbling compressed air through the solution, the use of NaOH was deemed unsatisfactory because isolation of croconic acid from the NaOH catalyst is challenging due to their high solubilities in water, making NaOH a poor choice. Activated manganese(IV) oxide was identified as a better catalyst as it considerably accelerates the reaction (2 hours) and is easily separated from the croconic acid product by filtration [251]. A high yield (91 %) was achieved for the ring contraction which gave little variation between different synthetic scales (500 mg vs 2 g scale), indicating that the step would be scalable for large-scale synthesis.

The reflux reaction of prepared croconic acid disodium salt with an excess of malononitrile yields the  $\text{Croc}^{2-}$  dianion as a hydrated sodium salt. The reaction was conducted using the optimised conditions (70 °C for 90 min) as described in [263] to avoid an apparent polymerisation reaction that results from excessive heating. After cooling the reaction mixture to room temperature and removing the water under high vacuum (without heating) the product was purified by recrystallisation from hot water to give a blue crystalline product at 64 % yield. The recrystallisation step was challenging for scale-up because the method required the removal of the water from the mixture under high vacuum at room temperature, however the removal of large volumes of water (>10 mL) becomes impractical on a standard laboratory high-vacuum manifold (fitted with a liquid nitrogen cold-trap), thus limiting the synthetic scale.

A salt metathesis of the hydrated salt was then performed to prepare the anhydrous tetrabutylammonium  $\text{Croc}^{2-}$  salt which is more preferential for anhydrous experiments in NA electrolyte. An undesirably low yield of 55 % was observed due to the  $\text{TBA}_2\text{Croc}$  species being sparingly soluble in water and the precipitate being microcrystalline. A one-pot methodology for the synthesis was attempted, in which croconic acid, malononitrile and TBA Cl was reacted under similar conditions, however the  $\text{TBA}_2\text{Croc}$  precipitate was not observed which can be attributed to the sensitive conditions required to crystallise the  $\text{Croc}^{2-}$  product.

The synthetic procedure is attractive for industrial application as the synthesis is water-based, gives reasonably high yields and in addition the rhodizonate starting material can be prepared through the reaction of an alkali metal with carbon monoxide; Scheme 12. Furthermore, the reagents are relatively low toxicity and are easy to handle; malononitrile and manganese (IV) oxide, being the most toxic compounds used, are easily-handled solids at room temperature and are already used in various industrial applications [267,268]. The scale-up practicalities of novel RFB materials is often over-looked in the literature as synthetic procedures with poor yields or undesirable work-ups are frequently reported [180].



**Scheme 12.** The preparation of rhodizonate via the reaction of an alkali metal with carbon monoxide [253].

The solubility of TBA<sub>2</sub>Croc in MeCN was measured by a UV/vis method in the micromolar concentration range. A well-defined absorption peak at 544 nm was observed which gave an extinction coefficient of  $9.17 \times 10^4 \text{ M}^{-1} \text{ cm}^{-1}$  in good agreement with the literature ( $8.77 \times 10^4 \text{ M}^{-1} \text{ cm}^{-1}$  at 534 nm in aqueous solution). The TBA<sub>2</sub>Croc solubility in MeCN is  $1.0 \pm 0.1 \text{ M}$  which is reasonably high compared to some other applied ROMs in MeCN; 20 mM for DB-134 [152], 0.47 M for an alkoxy anthraquinone derivative, 2.6 M for PTIO [179], 5.7 M for 2,1,3-benzothiadiazole [150] and 6.1 M for TEMPO [154].

### 7.3.2 Voltammetry investigations

CV of Croc<sup>2-</sup> in 0.1 M TBA PF<sub>6</sub> MeCN electrolyte at a GC electrode gave three reversible redox couples and an irreversible reduction indicating a total of five different oxidation states (Figure 89). Sweeping to anodic potentials from a bulk solution of Croc<sup>2-</sup> causes the sequential one-electron oxidations of Croc<sup>2-</sup> to firstly the semidione radical anion Croc<sup>•-</sup> and then to the neutral Croc species. These oxidation states appear stable on a voltammetry timescale as they give symmetric diffusion-limited redox couples which are fully-reversible. This is shown in Figure 90 and Figure 91 whereby the peak separations of these redox couples are small ( $\sim 70 \text{ mV}$  at  $100 \text{ mV s}^{-1}$ ) and show minimal increase with increasing scan rate; approx. 20 mV increase from 10 to  $1000 \text{ mV s}^{-1}$ . In addition, peak current ratios ( $I_a/I_c$ ) are close to unity ( $0.9 \leq I_a/I_c \leq 1.0$ ) and the peak anodic and cathodic currents give linear dependencies on the square root of the scan rate, allowing the Randles-Sevcik equation to be applied. The diffusion coefficient for the Croc<sup>2-</sup> species was calculated from the anodic/cathodic peak currents on first scan of Croc<sup>2-</sup> oxidation/reduction respectively, giving a D in the range of  $7.18$  to  $9.76 \times 10^{-6} \text{ cm}^2 \text{ s}^{-1}$ .

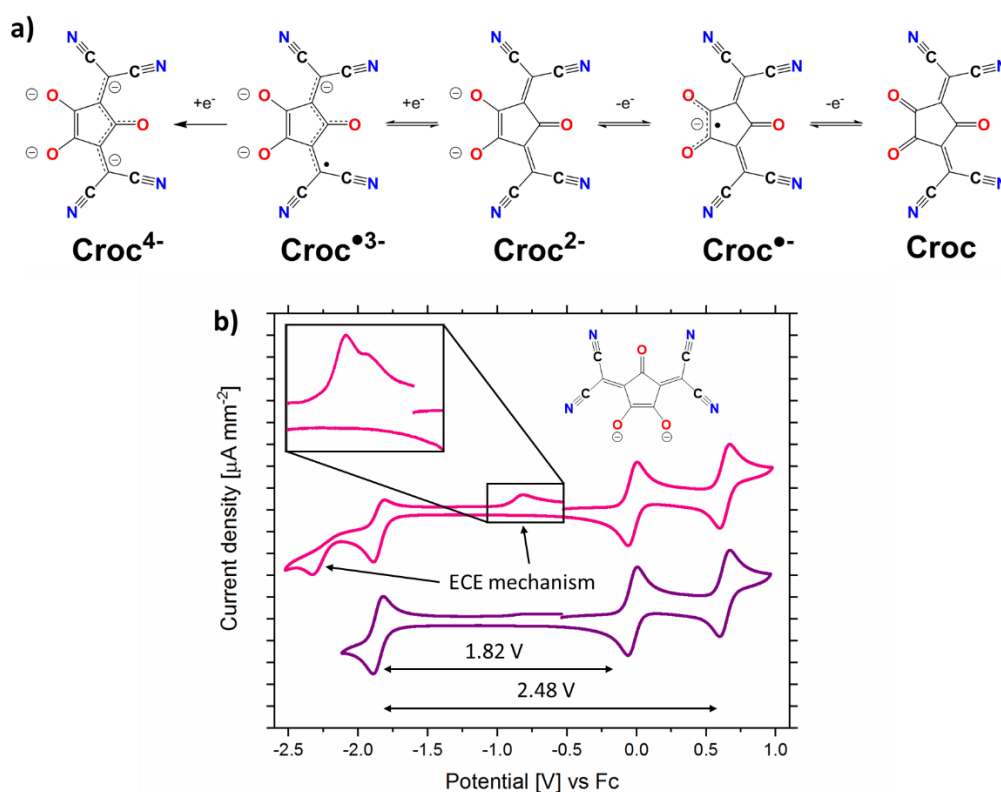


**Figure 89. a) the Croc redox series. b) Cyclic voltammetry of 1 mM TBA<sub>2</sub>Croc in 0.1 M TBA PF<sub>6</sub>, MeCN electrolyte at a GC electrode, 50 mV s<sup>-1</sup>. Full and partial electrochemical region scans are shown. First cycle shown.**

Sweeping to cathodic potentials causes the one-electron reduction of  $\text{Croc}^{2-}$  to the radical trianion  $\text{Croc}^{3-}$  and then a further one-electron reduction to presumably the  $\text{Croc}^{4-}$  tetraanion as shown in Figure 89. Whereas the first reduction appears reversible, giving a reverse oxidation peak, the second reduction gives no reverse oxidation peak indicating a chemically irreversible redox process. By limiting the voltammetry lower vertex to -2.1 V vs Fc to exclude the irreversible process, the reversible  $\text{Croc}^{2-}/\text{Croc}^{3-}$  redox couple appears stable giving a higher anodic peak current and a more symmetric redox couple, however when the voltammetry is swept more negatively, a lower anodic current for oxidation of  $\text{Croc}^{3-}$  is observed due to decomposition of the  $\text{Croc}^{4-}$  oxidation state. The  $\text{Croc}^{2-}/\text{Croc}^{3-}$  redox couple appears fully reversible, as shown in Figure 92, as characterised by a small  $\sim 70$  mV peak separation which is invariant of scan rate and  $I_a/I_c$  peak current ratio of approx. 0.7. A lower than usual ratio was observed

due to the lower vertex potential being restricted by the presence of the irreversible reduction process, thus giving a non-ideal anodic front-flank for extrapolation and measurement of the anodic peak current.

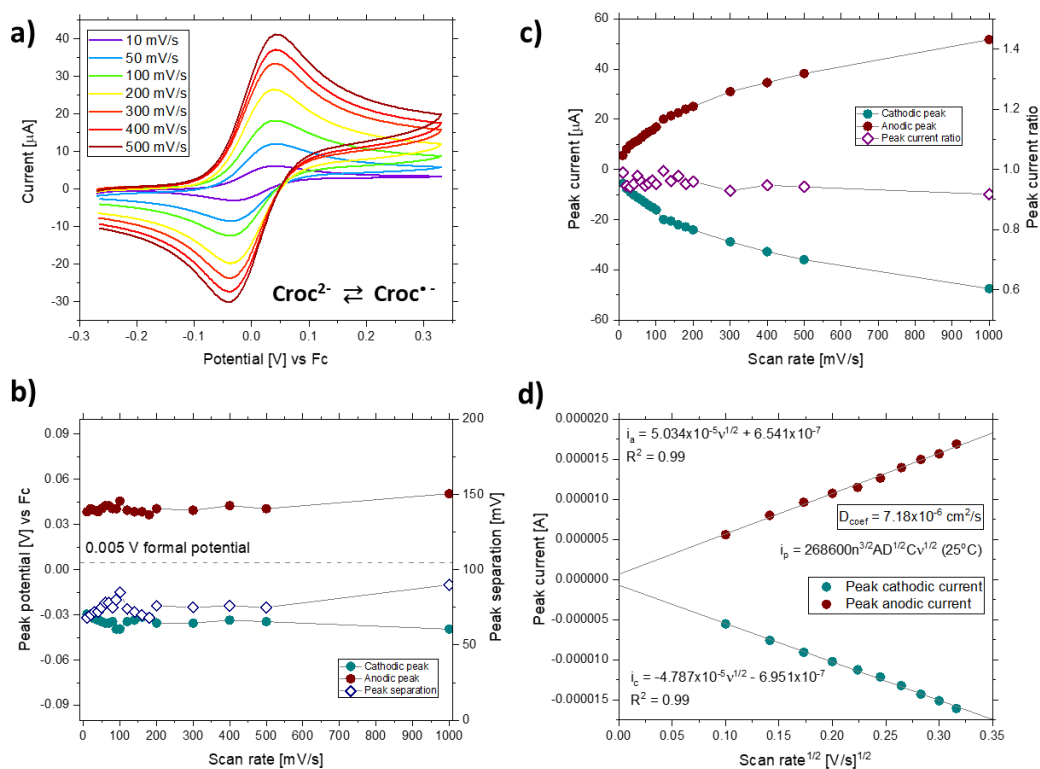


**Figure 90.** a) Cyclic voltammograms of the  $\text{Croc}^{2-}/\text{Croc}^{3-}$  redox couple as a function of scan rate (1 mM  $\text{TBA}_2\text{Croc}$  in 0.1 M TBA  $\text{PF}_6$ , MeCN). b) The variation of peak potentials and peak separation as a function of scan rate for the  $\text{Croc}^{2-}/\text{Croc}^{3-}$  redox couple. c) The variation of peak currents and peak current ratio as a function of scan rate for the  $\text{Croc}^{2-}/\text{Croc}^{3-}$  redox couple. d) Randles-Sevcik analysis of the  $\text{Croc}^{2-}/\text{Croc}^{3-}$  redox couple (the  $\text{Croc}^{2-}$  diffusion coefficient is given based upon the forward anodic reaction data on first scan).

Upon formation of  $\text{Croc}^{4+}$  at the electrode surface a rapid decomposition reaction occurs to produce products which are electrochemically inert at that potential. Upon sweeping the potential back towards 0 V vs Fc, a new anodic peak is observed at -0.8 V vs Fc which is attributed to the oxidation of the decomposed  $\text{Croc}^{4+}$  species. It can therefore be concluded that this process is an ECE mechanism, whereby the first electron-transfer is diffusion limited and the chemical reaction is irreversible. Upon closer inspection of the peak at -0.8 V vs Fc

(graph inset), the peak is composed of two similar peaks suggesting that the decomposition yields multiple products. Efforts to achieve a reversible  $\text{Croc}^{3-}/\text{Croc}^{4-}$  redox couple were unsuccessful as the process is chemically irreversible under various conditions: at Pt or Au electrodes, and in different solvents and

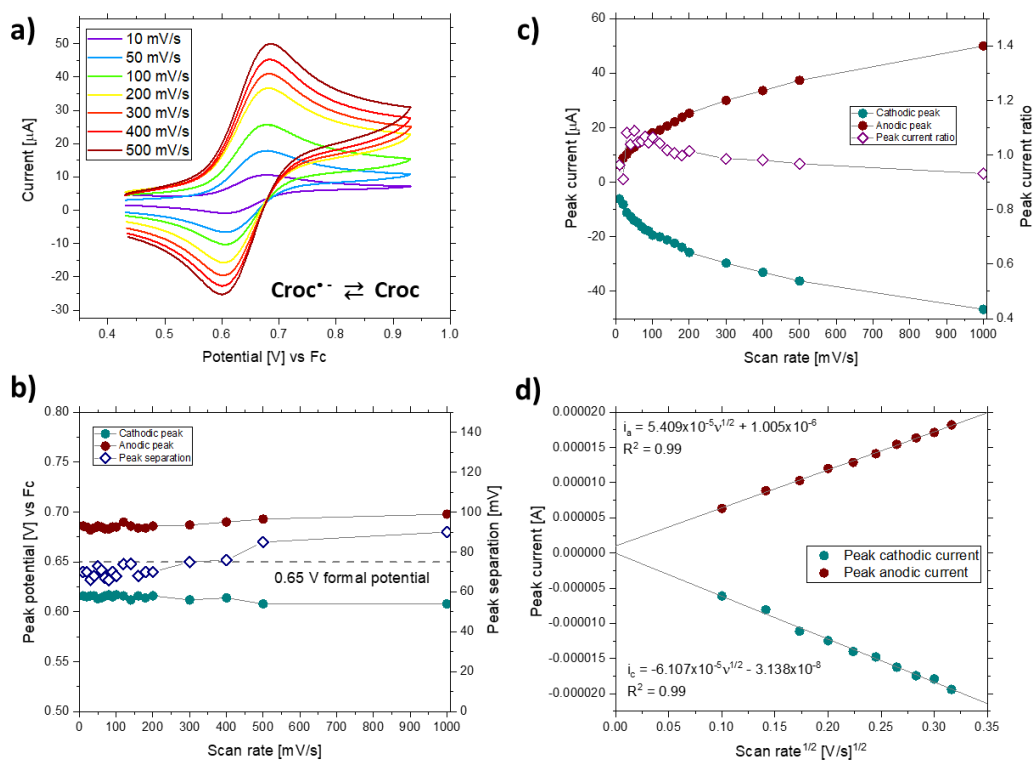


**Figure 91.** a) Cyclic voltammograms of the  $\text{Croc}^{3-}/\text{Croc}^{4-}$  redox couple as a function of scan rate (1 mM  $\text{TBA}_2\text{Croc}$  in 0.1 M  $\text{TBA PF}_6$ , MeCN). b) The variation of peak potentials and peak separation as a function of scan rate for the  $\text{Croc}^{3-}/\text{Croc}^{4-}$  redox couple. c) The variation of peak currents and peak current ratio as a function of scan rate for the  $\text{Croc}^{3-}/\text{Croc}^{4-}$  redox couple. d) The linear dependence of peak current on the square-root of scan rate for the  $\text{Croc}^{3-}/\text{Croc}^{4-}$  redox couple.

supporting salts (Figure 93). In particular, the conditions used by Doane and Fatiadi [260] to supposedly achieve reversibility were reproduced (anhydrous dimethylformamide at a gold electrode), however irreversibility was observed. Extreme measures to achieve an anhydrous electrolyte were used in the literature, suggesting that  $\text{Croc}^{4-}$  may be highly reactive towards trace water in the present experiments. Regardless, it is concluded that, due to the high charge density, the  $\text{Croc}^{4-}$  oxidation state is expected to be highly reactive towards electrophilic

species in solution and therefore far too unstable for any RFB application. The voltammetry response in different solvents and at different electrodes (Figure 93) was insightful as it showed that the  $\text{Croc}^{2-}$  electrochemistry is very dependent on the solvent and electrode material such that the electrochemistry is the most well behaved and consistent in MeCN. In contrast, voltammetry in PC and DMF gives

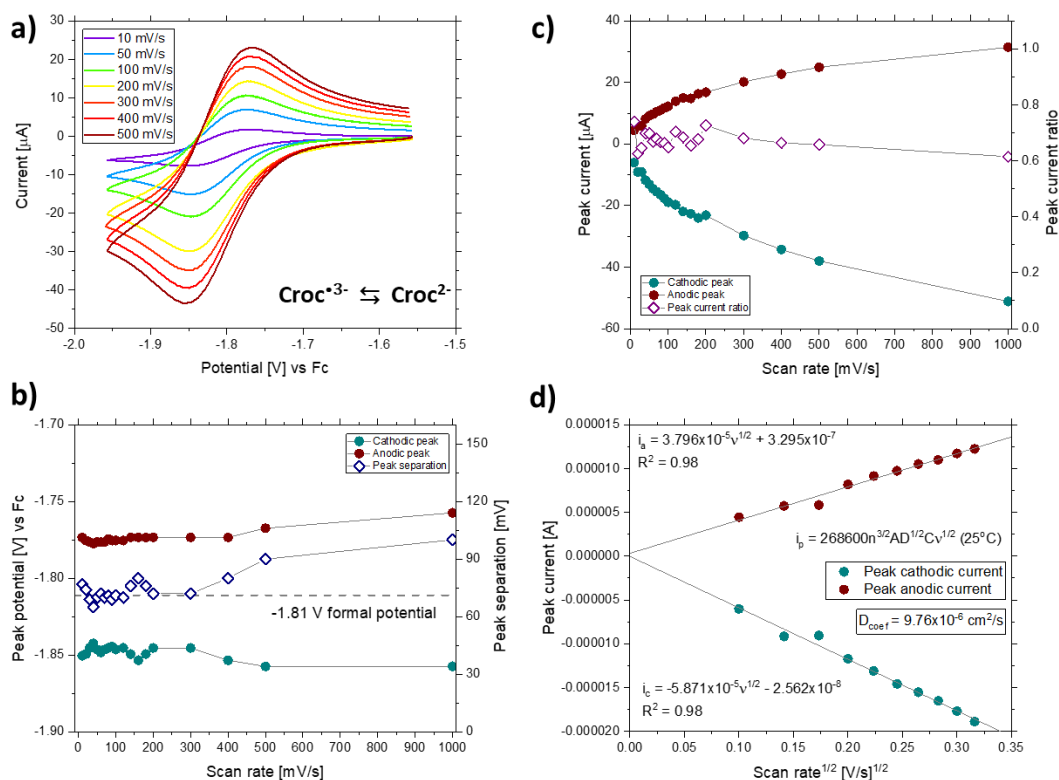


**Figure 92. a) Cyclic voltammograms of the  $\text{Croc}^{3-}/\text{Croc}^{2-}$  redox couple as a function of scan rate (1 mM  $\text{TBA}_2\text{Croc}$  in 0.1 M  $\text{TBA PF}_6$ , MeCN). b) The variation of peak potentials and peak separation as a function of scan rate for the  $\text{Croc}^{3-}/\text{Croc}^{2-}$  redox couple. c) The variation of peak currents and peak current ratio as a function of scan rate for the  $\text{Croc}^{3-}/\text{Croc}^{2-}$  redox couple. d) Randles-Sevcik analysis of the  $\text{Croc}^{3-}/\text{Croc}^{2-}$  redox couple (the  $\text{Croc}^{2-}$  diffusion coefficient is given based upon the forward cathodic reaction data on first scan).**

various other peaks observed which are dependent on the electrode used. The results indicated that the application of  $\text{Croc}^{2-}$  in MeCN at carbon-based electrodes was the most promising for battery application. Further work was then conducted to assess which supporting electrolyte salt would be most suitable for application with MeCN and carbon electrodes. The salts  $\text{TBA PF}_6$ ,  $\text{TBA BF}_4$  and  $\text{Li TFSI}$  were

examined, and the results showed that the electrochemistry was unchanged by switching the  $\text{PF}_6$  anion for  $\text{BF}_4$ , however when a lithiated salt (Li TFSI) was applied, the  $\text{Croc}^{2-}/\text{Croc}^{\bullet 3-}$  redox couple became chemically irreversible and a large sharp oxidative peak was observed at approx. 0 V vs Fc (Figure 94) which was attributed to the electrochemical stripping of an electrode film by oxidation.

This was proven by firstly observing the electrode film by eye and by also scanning in the positive potential region of the voltammogram (graph insert), whereby the deposited film from a previous experiment could be removed, thus returning the voltammetry of the  $\text{Croc}^{2-}$  oxidative redox couples.

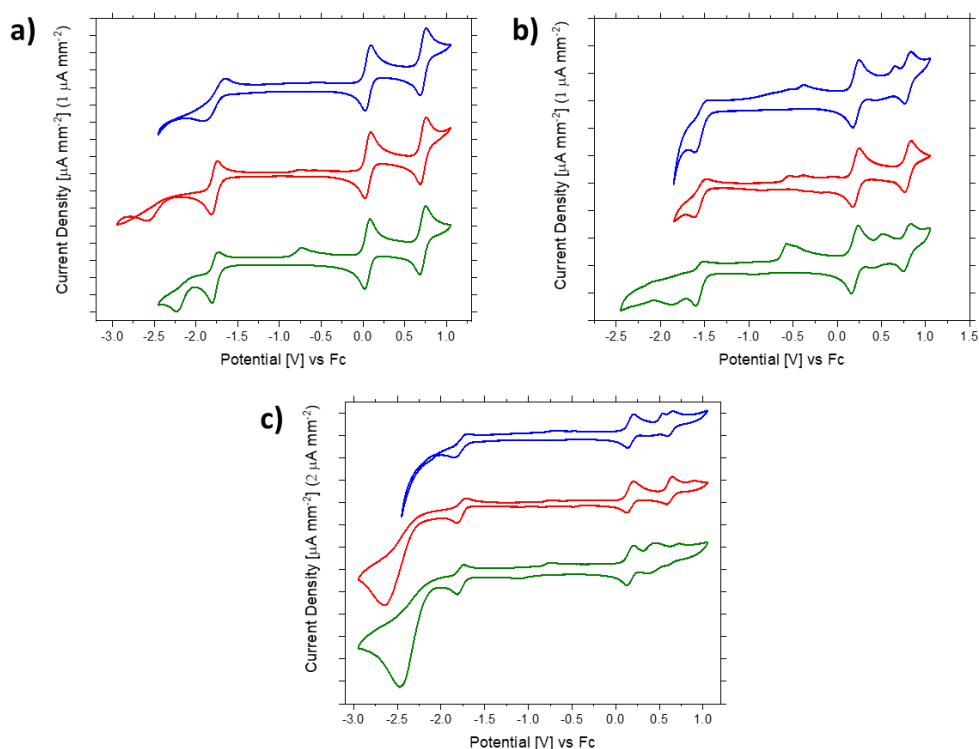


**Figure 93.** Cyclic voltammograms of 1 mM  $\text{TBA}_2\text{Croc}$  in 0.1 M  $\text{TBA PF}_6$  in solvent; a) MeCN. b) PC. c) DMF. Blue = 1.6 mm diameter Pt WE. Red = 1.6 mm diameter Au WE. Green = 3.0 mm diameter GC WE.  $50 \text{ mV s}^{-1}$ , second cycles shown.

To assess the electrochemical performance of croconate violet the kinetic parameters were measured by use of the Koutecký-Levich method (Figure 95). Standard electrochemical rate constants for the one-electron  $\text{Croc}^{2-}$  oxidation and reduction are  $k_0 = 1.54 \times 10^{-2}$  and  $1.37 \times 10^{-2} \text{ cm s}^{-1}$  respectively, which are

comparable to the rate constants of other high-performing ROMs studied for NA RFBs [150,154]. Limiting anodic current plateaus were achieved for both sequential electron transfers, whereas upon reduction of  $\text{Croc}^{2-}$ , sloping baselines and cathodic current plateaus were observed indicating a background current which was attributed to trace oxygen or water in the electrolyte. In addition, a broadening and asymmetry of the sigmoidal  $\text{Croc}^{4-}$  current response was observed which suggests that this process involves electrode adsorption. Given the complexity of the croconate violet electrochemistry it was concluded to be unsuitable to apply the Koutecký-Levich equation to the second oxidation and reduction reactions because of the instability issues of the charged oxidation states described in section 7.3.3, however the analysis is theoretically possible [201].

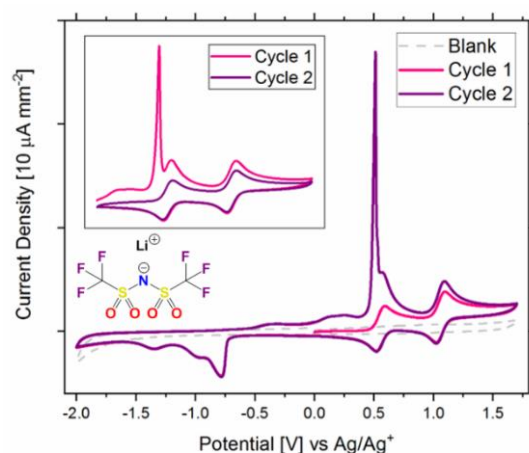


**Figure 94. Cyclic voltammetry of 1 mM TBA<sub>2</sub>Croc, 0.1 M Li TFSI, MeCN at GC WE, 50 mV s<sup>-1</sup>. First and second cycles are shown. Inset graph) Voltammetry in the anodic region after previously cycling the electrode in the cathodic region.**

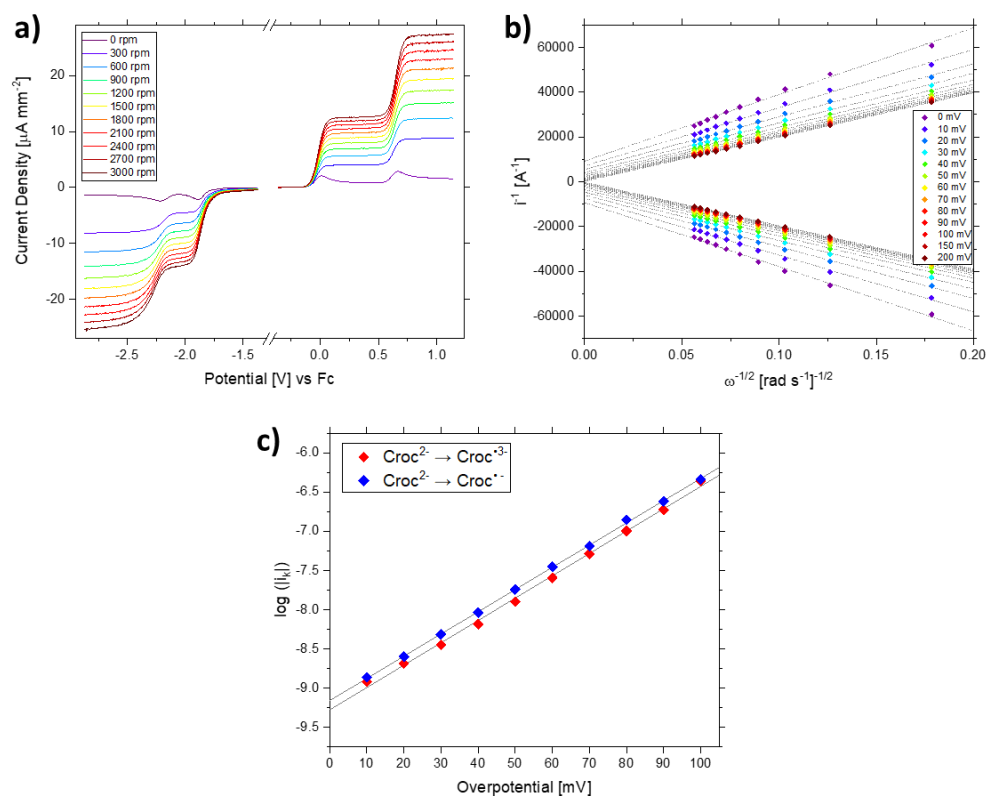


**Figure 95.** a) Linear sweep voltammograms of 1 mM Croc<sup>2-</sup> oxidation and reduction as a function of electrode rotation rate, at 50 mV s<sup>-1</sup> on GC electrode. b) Koutecký-Levich plots for the first one-electron oxidation and reduction of Croc<sup>2-</sup>; inverse current ( $i$ ) as a function of the inverse square root of the rotation rate ( $\omega$ ) at overpotentials ( $\eta$ ) 0 to 200 mV. c) Analysis of the kinetically-limited current ( $i_k$ ) dependency on  $\eta$  gives the exchange current at  $\eta = 0$ .

### 7.3.3 Battery application

By use of the croconate violet reversible redox couples, a symmetric RFB is possible with a 1.82 V cell potential, via the one-electron disproportionation of Croc<sup>2-</sup> to Croc<sup>•</sup> and Croc<sup>•3-</sup> (Figure 89), however by use of the additional Croc oxidation state, a 2.48 V cell potential is theoretically possible. Bulk electrolysis was performed to examine the radical and neutral oxidation states identified during cyclic voltammetry as shown in Figure 96. Electrolysis of Croc<sup>2-</sup> to Croc<sup>•3-</sup>, Croc<sup>•</sup> and Croc gave well defined plateaus at approximately -1.8, 0 and 0.65 V vs Fc respectively, corresponding to the three reversible redox couples of croconate violet. Inconsistent electrolysis times were observed (calc. 579 s per electrolysis), however this was attributed to crossover of Croc<sup>2-</sup> through the separator prior to

and during electrolysis. Immediately after electrolysis, cyclic voltammetry of the prepared solutions was conducted to examine the stability of each oxidation state with respect to time. Voltammetry of the  $\text{Croc}^{\bullet 3-}$  and  $\text{Croc}^{\bullet -}$  states gave similar electrochemistry to the stock  $\text{Croc}^{2-}$  solution and minimal evolution with respect to time, however a new redox couple at  $\sim 0.5$  V vs Fc was observed in the  $\text{Croc}^{\bullet 3-}$  solution whereas a prominent oxidative peak at  $\sim -0.1$  V vs Fc was observed in the  $\text{Croc}^{\bullet -}$  solution which was attributed to the stripping of an electrode film as previously discussed in section 7.3.2. Despite the appearance of new peaks, the voltammetry suggests that these oxidation states are relatively stable once formed, however voltammetry of the Croc species was significantly different to the  $\text{Croc}^{2-}$  electrochemistry, suggesting excessive decomposition of the neutral oxidation state. This is further evidenced in Figure 97 whereby the  $\text{Croc}^{\bullet -}/\text{Croc}$  redox couple was cycled in the bulk electrolysis cell. Although the  $\text{Croc}^{\bullet -}/\text{Croc}$  redox couple can be cycled, a new redox couple at approx. 0.25 V vs Fc began to dominate the cycling as a result of the Croc instability. Based on these results, the 1.82 V symmetric battery appeared plausible however the larger 2.48 V symmetric battery was unlikely to reversibly store charge.

Battery cycling at 10 mM  $\text{TBA}_2\text{Croc}$  concentration in a flow-cell gave charge/discharge plateaus around the expected 1.82 V cell potential, however, despite the first charge achieving 100 % theoretical capacity, only 10 % remained after the 10<sup>th</sup> cycle (Figure 98a). Capacity loss was attributed to the short lifetimes of the charged radical states, such that decomposition of the charged states occurs on a timescale longer than that of voltammetry. To identify which radical state was responsible for the rapid capacity loss, cyclic voltammetry was performed on the recovered electrolytes (Figure 98b). Analysis of the battery polysolite ( $\text{Croc}^{\bullet -}$ ) indicated minimal change, whereas it is evident that significant negolyte ( $\text{Croc}^{\bullet 3-}$ ) decomposition occurred because approx. 40 % of the croconate violet redox couple current density is absent compared to fresh  $\text{TBA}_2\text{Croc}$  electrolyte. In addition, new peaks in the voltammetry were observed and a significant current response around -0.8 V was observed corresponding to the decomposition products of the previously described  $\text{Croc}^{4-}$  oxidation state. Given that the upper potential

threshold was deliberately restricted during battery cycling to prevent formation of the  $\text{Croc}^{4-}$  species and that only one charge plateau was observed, it was concluded that  $\text{Croc}^{3-}$  decomposition proceeds predominantly via radical

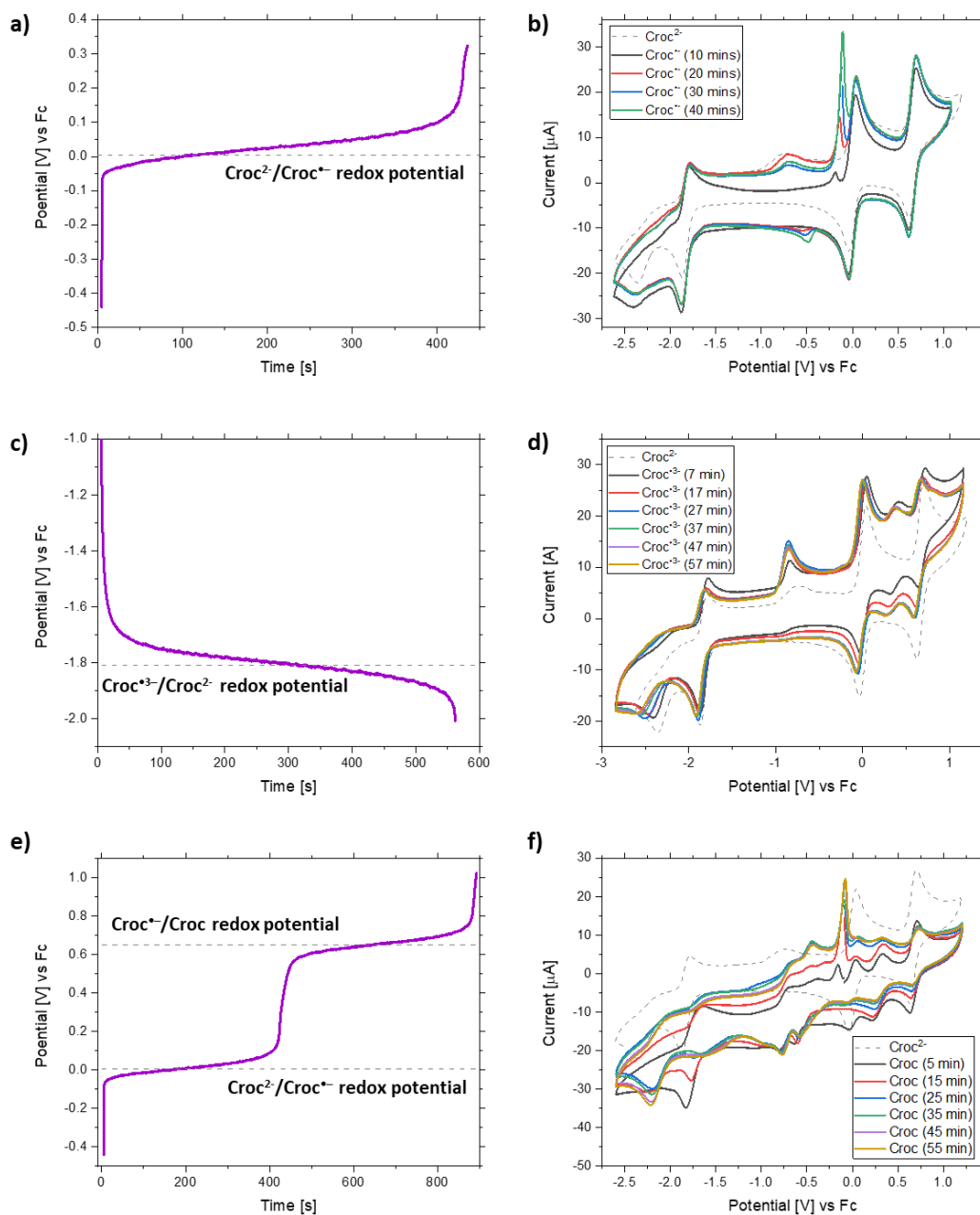


**Figure 96.** Bulk electrolysis of  $\text{Croc}^{2-}$  to a)  $\text{Croc}^{+}$ , c)  $\text{Croc}^{3-}$ , e) Croc oxidation states at 1 mA current (1 mM  $\text{TBA}_2\text{Croc}$  in 0.1 M TBA  $\text{PF}_6$ , MeCN) and Cyclic voltammetry of b)  $\text{Croc}^{+}$ , d)  $\text{Croc}^{3-}$ , f) Croc oxidation states as a function of time after formation via electrolysis. The approximate time of each voltammogram is indicated in the figure legend. (second scan shown,  $100 \text{ mV s}^{-1}$  at GC electrode).

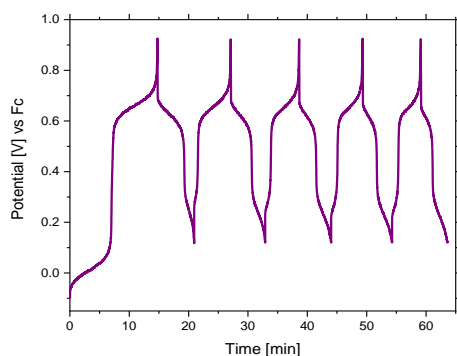


**Figure 97. Bulk electrolysis cycling of the Croc<sup>•-</sup>/Croc redox couple (1 mM TBA<sub>2</sub>Croc in 0.1 M TBA PF<sub>6</sub>, MeCN) at 1 mA.**

disproportionation to produce the starting Croc<sup>2-</sup> species and the unstable Croc<sup>4-</sup> state. This disproportionation reaction can be rationalised in terms of the difference in reduction potential between the Croc<sup>2-</sup>/Croc<sup>•3-</sup> and Croc<sup>•3-</sup>/Croc<sup>4-</sup> redox couples. As such, the ~0.5 V potential difference provides a large thermodynamic driving force for the disproportionation reaction. Although the instability of the Croc<sup>•3-</sup> oxidation state has been previously reported, by use of spectroelectrochemistry and electron spin resonance spectroscopy in DMF electrolyte (≈5 min lifetime) [265], the decay mechanism was not identified. The cyclic voltammetry results given in section 7.2.4 showed that in a lithiated electrolyte, the Croc<sup>2-</sup>/Croc<sup>•3-</sup> redox couple is chemically irreversible on a voltammetry timescale, therefore it is speculated that the presence of excess TBA<sup>+</sup>/TEA<sup>+</sup> ions inhibits the radical disproportionation reaction. Due to the low surface charge-density of tetraalkylammonium ions, TBA<sup>+</sup> ions are essentially unsolvated in non-aqueous solvents [269] and as such it is speculated that the association of TBA<sup>+</sup> with Croc<sup>•3-</sup> ions in solution provides steric protection from other Croc<sup>•3-</sup> ions, thus hindering the radical disproportionation reaction. This likely increases the Croc<sup>•3-</sup> lifetime sufficiently that the Croc<sup>•3-</sup> oxidation state appears stable on a cyclic voltammetry timescale.



↓

**decomposition**

The impact of the proposed radical disproportionation mechanism on battery operation is expected to make the negolyte the capacity-limiting electrolyte, thus accounting for the rapid capacity fade. Further evidence of  $\text{Croc}^{\bullet 3-}$  radical disproportionation was observed in Figure 89 whereby, despite limiting the voltammetry lower vertex potential to exclude  $\text{Croc}^{4-}$  formation, a small degree of current response at  $-0.8\text{ V}$  is still observed corresponding to the  $\text{Croc}^{4-}$  decomposition products which can only happen if the  $\text{Croc}^{\bullet 3-}$  disproportionation occurs.

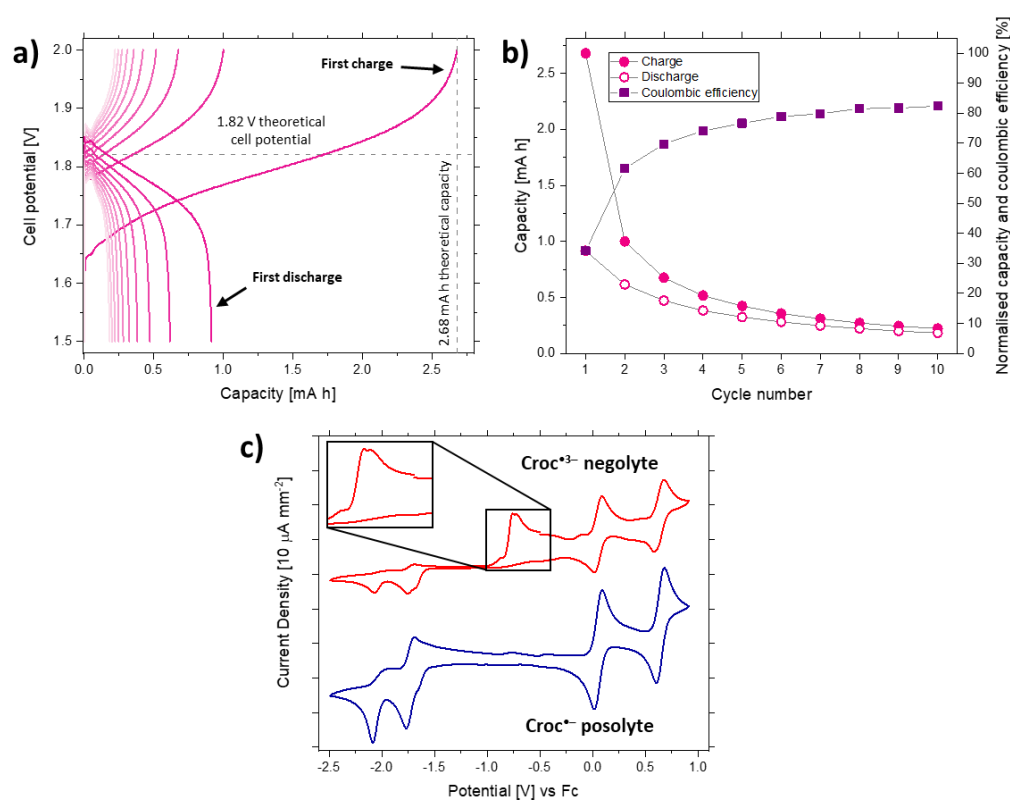


**Figure 98. a) Symmetric battery charge-discharge curves of 10 mM TBA<sub>2</sub>Croc in 0.5 M TEA BF<sub>4</sub>, MeCN electrolyte at  $\pm 2.4\text{ mA cm}^{-2}$ . The upper and lower threshold potentials are 2.0 and 1.5 V respectively. First 10 cycles are shown. Fumapem<sup>®</sup> F-930 CEM. b) Battery cycling capacities and coulombic efficiency of the 1.82 V symmetric RFB. c) Post-battery cycling voltammetry of used  $\text{Croc}^{\bullet 3-}$  and  $\text{Croc}^{\bullet -}$  electrolytes.  $50\text{ mV s}^{-1}$  at a GC electrode.**

To assess whether the  $\text{Croc}^{\bullet -}$  state is stable, independent battery cycling experiments were conducted whereby only one redox couple is used, i.e. the reduction process is coupled to the oxidation process, giving a 0 V cell potential.

The results of the  $\text{Croc}^{\bullet 3-}/\text{Croc}^{2-}$  cycling experiment were consistent with the post-cycling voltammetry analysis such that zero capacity was retained by the cell after only 10 cycles ( $\approx 14$  mins) as shown in Figure 99b, whereas the  $\text{Croc}^{2-}/\text{Croc}^{\bullet -}$  cycling showed reasonable capacity retention over 100 cycles (10 hours). From these results, it was concluded that both the  $\text{Croc}^{\bullet 3-}$  and  $\text{Croc}^{\bullet -}$  oxidation states have limited stability in the electrolyte once formed, however the  $\text{Croc}^{\bullet 3-}$  lifetime is considerably shorter. The decomposition mechanism of the  $\text{Croc}^{\bullet -}$  oxidation state is yet to be identified, however previous literature has also observed the slow radical decay [261,265] and it has been suggested that a similar radical disproportionation mechanism is possible given that the neutral Croc species is unstable [261].



↓

**decomposition**

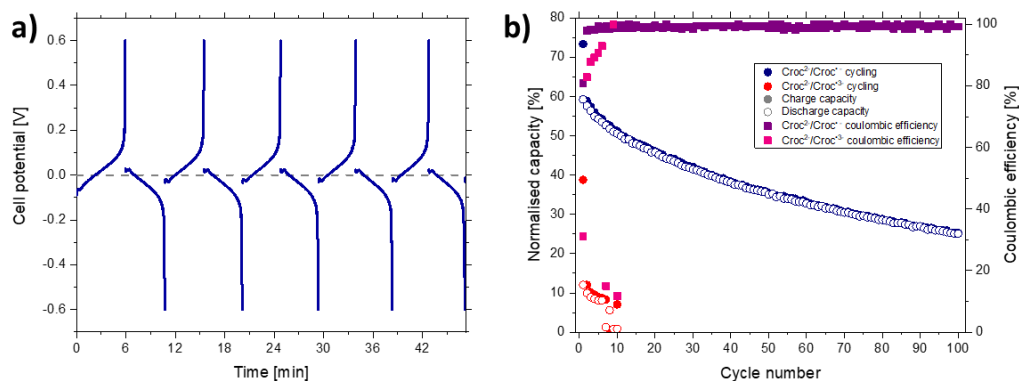


**Figure 99. Independent battery cycling experiments of single croconate violet redox couples. a) first five cycles of the  $\text{Croc}^{2-}/\text{Croc}^{\bullet -}$  cell, 1 mM  $\text{TBA}_2\text{Croc}$ , 0.1 M TBA  $\text{PF}_6$ , MeCN at  $\pm 0.96 \text{ mA cm}^{-2}$ . Celgard separator. b) Normalised capacity retention and coulombic efficiencies for the independent battery cycling of the  $\text{Croc}^{2-}/\text{Croc}^{\bullet -}$  and  $\text{Croc}^{2-}/\text{Croc}^{\bullet 3-}$  cells.**

Due to the short lifetime of the  $\text{Croc}^{\bullet 3-}$  oxidation state, it is concluded that croconate violet is an unsuitable electrolyte for RFB application. Despite this, it was hypothesised that the  $\text{Croc}^{\bullet -}$  state may still be suitable and therefore  $\text{Croc}^{2-}$  may be a good candidate for a NA RFB polysolite, when paired with a different ROM electrolyte in an asymmetric battery. To date, ROMs for NA RFB electrolytes/polysolites

have typically been neutral molecules which are reduced/oxidised to radical anions/cations respectively [2], thus the present work is the first anionic NA RFB ROM posolyte reported.

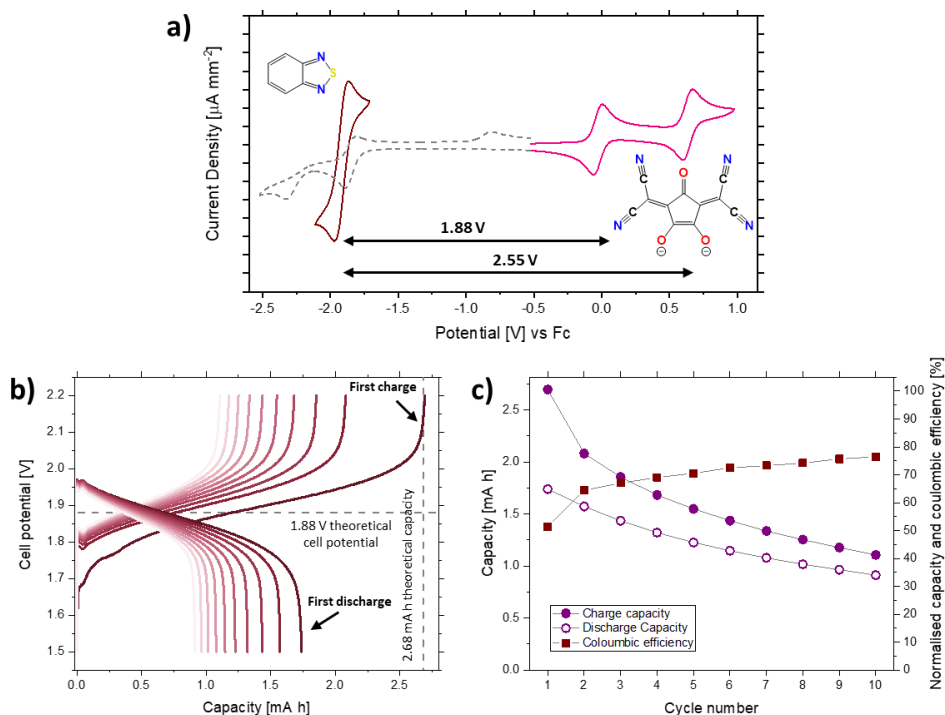


**Figure 100.** Battery cycling of the 1.88 V asymmetric BzNSN/Croc<sup>2-</sup> RFB; 10 mM TBA<sub>2</sub>Croc posolyte vs 10 mM BzNSN negolyte in 0.5 M TEA BF<sub>4</sub>, MeCN electrolyte at  $\pm 2.4$  mA cm<sup>-2</sup>. a) cyclic voltammogram of 1 mM BzNSN and TBA<sub>2</sub>Croc in 0.1 M TBA PF<sub>6</sub> MeCN electrolyte at GC electrode, 50 mV s<sup>-1</sup> b) First ten charge-discharge curves. The upper and lower threshold potentials are 2.2 and 1.5 V respectively. c) Battery cycling capacities and coulombic efficiency. Fumapem® F-930 CEM.

Based on recent NA RFB literature the long lifetime 2,1,3-benzothiadiazole (BzNSN) ROM was identified as a suitable negolyte to pair with a Croc<sup>2-</sup> posolyte, giving a 1.88 V cell potential [150,163]. Battery cycling of the BzNSN/Croc<sup>2-</sup> asymmetric RFB gave charge/discharge plateaus about the expected 1.88 V cell potential and achieved 100 % theoretical capacity on the first charge (Figure 100). Despite this, fast capacity fade was observed such that only 40 % of the capacity remained after 10 cycles. Given that previous battery experiments with a BzNSN negolyte achieved vastly improved capacity retention (only ~20 % capacity loss

after 160 cycles) [150], the capacity loss in the BzNSN/Croc<sup>2-</sup> battery was attributed to a failure of the membrane to separate the ROM electrolytes. Whereas Duan et al. used mixed electrolytes in their experiments to decrease membrane crossover [150] (i.e. a single electrolyte containing a 1:1 mixture of both the ROM posolyte and negolyte was used in both half-cells), this methodology is not possible for the BzNSN/Croc<sup>2-</sup> battery due to the proximity of the Croc<sup>2-</sup>/Croc<sup>•3-</sup> and BzNSN/BzNSN<sup>•-</sup> redox potentials. Membrane crossover of the pink Croc<sup>2-</sup> species into the colourless BzNSN electrolyte was visually observed during the experiment and therefore the Croc<sup>2-</sup> reduction to the unstable Croc<sup>•3-</sup> species in the BzNSN half-cell is a parasitic reaction to the BzNSN reduction process. In addition to the capacity loss via electrolyte cross-contamination through the membrane, the parasitic reaction causes additional capacity loss by unbalancing the cell and decreasing the total quantity of Croc<sup>2-</sup> redox material in the battery. Thus, it was hypothesised that the BzNSN/Croc<sup>2-</sup> battery would achieve much higher capacity retention given that a highly selective membrane was applied to maintain the separation of the ROM electrolytes.

Due to the lack of high-performance membranes that combine high ionic conductivity and selectivity for NA electrolytes, an alternative ROM negolyte with a higher redox potential was targeted such that Croc<sup>2-</sup> reduction is not a parasitic reaction. Tetracyanoquinodimethane (TCNQ) is a low molecular weight ROM which undergoes two sequential one-electron reductions to a dianion via a radical anion intermediate [270]. Similar to Croc<sup>2-</sup>, TCNQ is also a dicyanomethylene derivative which is prepared via the Knoevenagel condensation of *p*-benzoquinone with malononitrile. Despite the reported stability of the TCNQ<sup>•-</sup> oxidation state [271], TCNQ has not yet been applied in NA RFBs due to undesirably high redox potentials and low solubility in MeCN (~10 mM due to its low polarity). Although TCNQ is not a suitable ROM for application in RFBs, its redox potentials are significantly more positive than the Croc<sup>2-</sup>/Croc<sup>•3-</sup> redox couple, thus allowing its use as a model compound for a mixed-electrolyte asymmetric RFB which mitigates membrane limitations. By voltammetry, potential differences of 169 mV between the TCNQ/TCNQ<sup>•-</sup> and Croc<sup>2-</sup>/Croc<sup>•-</sup> redox couples and 1.38 V between the Croc<sup>•-</sup>

/Croc and  $\text{TCNQ}^{\bullet-}/\text{TCNQ}^{2-}$  redox couples were measured, therefore allowing the two-electron  $\text{TCNQ}/\text{Croc}^{2-}$  battery to be charged without the cell potential exceeding 1.8 V. Battery cycling of the 169 mV one-electron  $\text{TCNQ}/\text{Croc}^{2-}$  cell gave charge-discharge curves around the expected cell potential corresponding to the reversible electrolysis of  $\text{TCNQ}/\text{Croc}^{2-}$  to the radical anions  $\text{TCNQ}^{\bullet-}/\text{Croc}^{\bullet-}$  (Figure 101b). Despite this, a gradual capacity loss was observed such that  $\approx 70\%$  capacity remained after 50 cycles (Figure 101c).

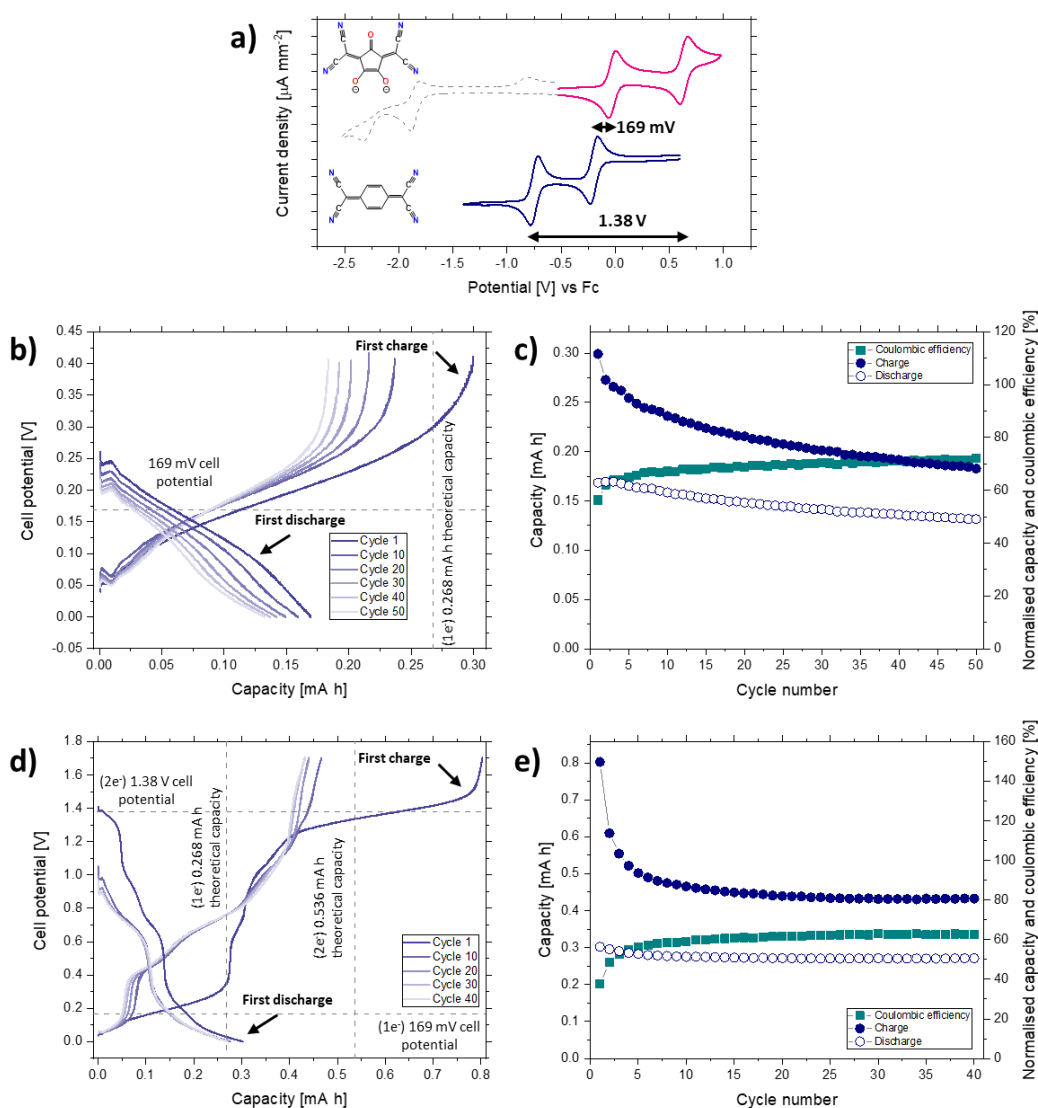


**Figure 101.** a) Cyclic voltammetry of 1 mM TCNQ and  $\text{TBA}_2\text{Croc}$  in 0.1 M  $\text{TBA PF}_6$ , MeCN, GC WE at  $50 \text{ mV s}^{-1}$ . Asymmetric battery charge-discharge curves of 1 mM  $\text{TBA}_2\text{Croc}$  vs 1 mM TCNQ mixed electrolytes in 0.1 M  $\text{TBA PF}_6$ , MeCN electrolyte at  $\pm 0.48 \text{ mA cm}^{-2}$  (Celgard porous separator) to b) the one-electron battery and d) two-electron battery. The upper and

**lower threshold potentials were 0.4 and 0 V respectively for the one-electron battery and 1.7 and 0 V respectively for the two-electron battery. The capacities and coulombic efficiencies for the one-electron and two-electron batteries are given in c) and e) respectively.**

In addition, a large hysteresis between the charge and discharge capacities was observed which was attributed to the lower threshold potential (0 V) not being sufficiently lower than the cell potential to fully discharge the cell each cycle. Regardless, the results suggest that the TCNQ<sup>•-</sup> and Croc<sup>•-</sup> radical states are reasonably stable.

Battery cycling of the two-electron cell gave charge plateaus on the first cycle which were consistent with the one-electron 169 mV electrolysis and the following 1.38 V electrolysis. On the first charge the cell significantly exceeded the theoretical two-electron capacity and performed poorly thereafter such that the cell cycled at inconsistent capacities and exhibited multiple charge/discharge plateaus, which were unrecognisable of the TCNQ/Croc<sup>2-</sup> chemistry (Figure 101d). In part, the inconsistent capacities and observed hysteresis can be attributed to the non-selectivity of the porous separator applied: due to the nature of the two-electron cycling, the timescales for individual charge or discharge steps are double that of the one-electron cycling which therefore allows more time for the membrane crossover of charged states and therefore low coulombic efficiencies due to self-discharge. In addition, it is evident from the evolution of the charge/discharge plateaus that significant chemical changes to the electrolyte occurred which is also a contribution for the observed inconsistency in the capacities. Decomposition of the TCNQ<sup>2-</sup> and/or Croc oxidation states occurred after their formation to form decomposition products which are redox active, thus giving charge/discharge plateaus at unexpected cell potentials. Due to the high complexity of the two-electron asymmetric TCNQ/Croc<sup>2-</sup> battery, it is challenging to identify the decomposition mechanism from the plethora of possible chemical and free-radical reactions.

## 7.4 Conclusions

In summary,  $\text{Croc}^{2-}$  was presented as a new redox material for applications in NA RFBs. From the onset,  $\text{Croc}^{2-}$  has many properties desirable for application including its low molecular weight, multiple oxidation states and bond-delocalised structure. By use of voltammetry, three reversible redox couples were identified which may be applied to produce a 1.82 or 2.48 V symmetric RFB design. Bulk electrolysis and battery cycling techniques revealed instability issues relating to the radical anionic states  $\text{Croc}^{\bullet-}$  and  $\text{Croc}^{\bullet 3-}$  and the neutral  $\text{Croc}$  molecule which cause rapid capacity loss. Specifically, there is evidence that a radical disproportionation mechanism of the  $\text{Croc}^{\bullet 3-}$  state prevents the use of  $\text{Croc}^{2-}$  as a negolyte and therefore as a symmetric battery electrolyte. Such a radical disproportionation mechanism is possible in many of the ROMs explored to date, however it has been overlooked in the literature as a possibility for causing capacity decay in ROM RFBs. By use of independent single-redox couple and asymmetric battery methods,  $\text{Croc}^{2-}$  was demonstrated as a promising ROM posolyte for use in future asymmetric RFBs. In addition,  $\text{Croc}^{2-}$  is the first anionic posolyte proposed to date. The application of  $\text{Croc}^{2-}$  in asymmetric ROM RFB designs is at present challenging due the lack of suitable membrane materials because the  $\text{Croc}^{2-}/\text{Croc}^{\bullet 3-}$  redox couple will act as an undesirable parasitic reaction in the negolyte if the  $\text{Croc}^{2-}$  posolyte crosses through the membrane. The reasonably high 1 M solubility of the  $\text{Croc}^{2-}$  species is promising for application, however the measurement of the charged states solubility may be lower.

The work described here highlights the difficulty in achieving symmetric ROM electrolytes for RFB application. Small organic molecules with multiple stable oxidation states which are separated by a large potential difference are rare. In addition, such an ideal ROM must fulfil a higher number of selection criteria compared to those which are used in only one half of a battery design. Research must aim to study and evaluate all oxidation states of novel ROM materials in order to assess their stability and performance because as demonstrated herein, cyclic voltammetry alone is inadequate. Methodologies such as bulk electrolysis, post-

battery cycling voltammetry and independent redox couple methods are effective experiments for the diagnosis of capacity loss mechanisms.

# Chapter 8

## Conclusions

### 8.1 Summary

To conclude, RFBs are promising energy storage technologies for grid-scale energy storage due to their decoupled power and capacity [6]. However, widespread implementation of the battery technology is at present hindered by technical and economic challenges which ultimately originate from the low energy density [110]. To surpass this limitation, the application of more electrochemically stable non-aqueous battery solvents will afford RFBs with larger cell potentials and enhancements in capacity [66]. Development of the NA RFB technology is therefore a viable pathway towards energy storage targets as in theory the high cost of the electrolyte can be offset by enhanced energy density. Herein, a set of new inorganic redox materials and a novel organic species were studied for application in novel symmetric NA RFBs whereby the same electrolyte serves as both the RFB posolyte and negolyte. In addition, a series of electrochemical cells (both glass and flowing) were developed and characterised by use of the ferrocene/ferrocenium ion redox couple as a model chemistry.

MCCs such as the Co(II) azole-pyridine complexes in Chapter 5 display good stability at relatively long timescales (>2 days) and their unique ligand structure enables structural modification to improve their properties. As such, an increase in energy density of the complexes was demonstrated without significantly increasing their molecular weight. Despite this, their large size and low polarity gave undesirably low solubility. In contrast, the metal dithiolene complexes in Chapter 6 displayed higher solubility (metal centre dependent) but their charged oxidation states were typically unstable, thus limiting application. The degradation mechanisms of these complexes were challenging to rationalise; however, it was suspected that the small dithiolene ligands are too small to protect the metal centre. In addition, the 4-coordinate  $M_{mnt}$  complexes are likely to coordinate with

other chemical species to form 5-coordinate species, thus giving a reaction site for decomposition/discharge mechanisms to occur. The application of ROMs for NA RFB energy storage was also investigated in this work. A new ROM - croconate violet, which gives three reversible redox couples, was fully characterised for application. Here, the low cost and higher solubility (1 M in MeCN) was promising for application, however similar instability of its charged oxidation states was encountered. As ROMs yield radicals in aprotic electrolytes when charged, the decomposition mechanisms are very complex, however radical disproportionation of the radical trianion was identified.

## 8.2 Retrospectives

Despite the high promise of the NA RFB concept, the technology exists only within academic research at present and NA RFBs have only been demonstrated in small single cell experiments thus far. Indeed, although a considerable number of redox materials have been screened, few have demonstrated the desired properties for application.

In terms of the cell potential, the research field has been quite successful as NA RFB designs with cell potentials in excess of 2 V have been frequently reported [99,128,129,135,143,152,272]. For example, complex **2** in Chapter 5,  $V_{mnt}$  in Chapter 6 and  $Croc^{2-}$  in Chapter 7 all give theoretical cell potentials above 2 V. Despite this, NA RFBs have yet to fully utilise the electrochemical stability region of the base electrolyte, with  $\sim 3$  V being the highest achieved [133,147]. There is therefore the need to identify new negolyte and posolyte materials which undergo redox transitions at lower/higher potentials respectively to give a NA RFB with a substantial 4 V cell potential. Such a NA RFB would therefore not require such highly concentrated electrolytes to be utilised, offsetting the electrolyte cost [110,273]. This challenge is a significant research hurdle as standard potentials are inherent to the molecular structure of redox species because of their discrete molecular orbital energies. In addition, materials exhibiting very high/low redox potentials are likely to be strong chemical oxidising/reducing agents respectively. It is therefore unlikely that the redox potentials of a redox species can be

substantially shifted by  $>1$  V without losses in chemical stability [133,134,205]. A large beneficial shift of  $\sim 500$  mV is demonstrated in Chapter 5 whereby the Co(III/II) redox couple potential is moved to a higher potential by azole substitution, however the electrochemical performance was adversely affected as in refs [133,134].

The electrochemical kinetics of novel redox materials for NA RFBs is again another success of the NA RFB research field [98]. As highlighted in this thesis and more generally in the literature, redox species in NA electrolyte demonstrate excellent electrochemical rate constants ( $>10^{-3}$  cm s $^{-1}$ ) at carbon-based electrodes as compared to simple metal ion redox couples in aqueous media ( $10^{-6}$  to  $10^{-2}$  cm s $^{-1}$ ) [22]. The rationale for this is that changes in geometry and solvation are typically minimal in MCCs and ROMs in NA electrolyte. Activation overpotentials are therefore less significant in NA RFBs as compared to their aqueous counterparts.

The main challenges for NA redox materials lies in their solubility and stability. MCCs are typically poorly soluble on account of their low charge density and large size, however they can demonstrate good long-term stability because their inert ligands tend to protect the reactive metal core from other molecules. Almost paradoxically, ROMs can demonstrate excellent solubility due to their small size and strong interactions with organic solvents, however their stability is at present inadequate because of the high reactivity of their radical states. Promising progress has been made in the literature towards both increasing MCC solubility [133,134] and ROM stability [161,181,182] via rational design, however the research field has not yet perfected a single redox material.

Beyond the specific challenges with the redox materials, more urgent challenges exist with the NA RFB technology that must be addressed. Firstly, the low conductivity of NA electrolytes remains a practical limitation because high cell ASR results in considerably more overpotential and lower voltaic efficiency, thus limiting power density [97]. Secondly, suitable membranes for NA RFBs do not presently exist due to the challenges of synthesising ionic-exchange polymers for organic solvents. Therefore, high rates of membrane crossover (fast self-discharge)

and low coulombic efficiency are commonly observed when operating NA RFBs at high concentration [69]. The development of symmetric electrolytes or the size-exclusion approach [51,116] are plausible pathways to mitigate membrane limitations, however high-performance membranes would still be required in both cases. Furthermore, as discussed in Chapter 5, it is naive to assume that the crossover of redox species in a symmetric RFB will not impact the cathode/anode reactions as effects such as electrode absorption can be problematic.

### 8.3 Future work

Research thus far has typically applied redox materials from other research disciplines without regard for the specific design criteria for NA RFBs. Therefore, research must first target more realistic redox materials, such as MCCs employing earth-abundant elements, and then engineer the molecular structure towards desirable properties. Although some ground-breaking studies have achieved this [182,189], these methodologies are still infantile as structure-function relationships remain poorly explored. It is therefore clear that a synthetic molecular engineering approach is key for progress in NA RFB research.

The stability of redox materials must become the primary design criteria for application. This is because materials with lifetimes less than ~5 years are unsuitable from a techno-economic perspective. Therefore, the research field must focus on quantifying and improving the stability of redox materials for application. Furthermore, this should be achieved by isolating redox materials in charged oxidation states (chemically or electrochemically) and then measuring their half-life in ex-situ studies, such as by long-term NMR [274] or EPR [151]. Indeed, the research field's over-reliance on voltammetry for assessing stability is inadequate because the technique does not simulate the realistic battery conditions in terms of timescale or concentration. In addition, simple 'robust' redox couples such as the Fc/FcBF<sub>4</sub> model chemistry (Chapter 4) give surprising capacity loss in battery experiments, yet the FcBF<sub>4</sub> decomposition mechanism has not been elucidated in the literature thus far. Future work should address the instability of simple species, such as FcBF<sub>4</sub>, to understand the decomposition mechanisms. This

knowledge can then guide rational design towards indefinitely stable redox species.

In reflection of the redox materials presented in this thesis, there are numerous possible studies to conduct. For example, the azole-pyridine complexes in Chapter 5 could be further developed by synthesising a larger library of ligands or by applying alternative transition metal centres such as manganese, iron or nickel. In addition, solubilising groups could be easily grafted to the azole-pyridine ligand structure to enhance the solubility of the corresponding complexes [134]. In consideration of the metal dithiolene complexes in Chapter 6, it is possible that more sophisticated derivatives could afford higher stability, solubility or more electron transfers [275] as only one ligand structure was studied in the present work. Similar possibilities exist for the croconate violet ROM in Chapter 7 as other pseudooxocarbon derivatives exist, and in addition Croc (much alike other dioxolene analogues [276]) is also a bidentate ligand [259,266].

Beyond the redox materials presented in this thesis, there are numerous alternative compounds which may be applied in RFBs. Indeed, the possibilities are near endless because the research field is still young, and the materials summarised in section 1.5 are merely the first to be considered. Future work should aim to further explore both conventional and unconventional redox materials, or develop alternative RFB designs, because the RFB technology is highly adaptable. Furthermore, the future of the RFB technology is unclear because many imaginative design ideologies are being pursued by the wider research community.



# References

- [1] C.G. Armstrong, K.E. Toghil, Cobalt(II) complexes with azole-pyridine type ligands for non-aqueous redox-flow batteries: Tunable electrochemistry via structural modification, *J. Power Sources*. 349 (2017) 121–129. doi:10.1016/j.jpowsour.2017.03.034.
- [2] C.G. Armstrong, K.E. Toghil, Stability of molecular radicals in organic non-aqueous redox flow batteries: A mini review, *Electrochem. Commun.* 91 (2018) 19–24. doi:10.1016/j.elecom.2018.04.017.
- [3] R. Hogue, C. Armstrong, K. Toghil, Dithiolene Complexes of First Row Transition Metals for Symmetric Non-Aqueous Redox Flow Batteries, *ChemSusChem*. 12 (2019) 4506–4515. doi:10.1002/cssc.201901702.
- [4] C.G. Armstrong, R.W. Hogue, K.E. Toghil, Application of the dianion croconate violet for symmetric organic non-aqueous redox flow battery electrolytes, *J. Power Sources*. 440 (2019) 227037. doi:10.1016/j.jpowsour.2019.227037.
- [5] B. Dawoud, E. Amer, D. Gross, Vanadium redox flow batteries: a technological review, *Int. J. Energy Res.* 31 (2007) 135–147. doi:10.1002/er.
- [6] A.Z. Weber, M.M. Mench, J.P. Meyers, P.N. Ross, J.T. Gostick, Q. Liu, Redox flow batteries: a review, *J. Appl. Electrochem.* 41 (2011) 1137–1164. doi:10.1007/s10800-011-0348-2.
- [7] J. Cho, S. Jeong, Y. Kim, Commercial and research battery technologies for electrical energy storage applications, *Prog. Energy Combust. Sci.* 48 (2015) 84. doi:http://dx.doi.org/10.1016/j.pecs.2015.01.002.
- [8] M.H. Chakrabarti, S. a. Hajimolana, F.S. Mjalli, M. Saleem, I. Mustafa, Redox Flow Battery for Energy Storage, *Arab. J. Sci. Eng.* 38 (2013) 723–739. doi:10.1007/s13369-012-0356-5.
- [9] N.H. Hagedorn, H.L. Thaller, Design Flexibility of Redox Flow Systems, *NASA Arch. TM-82854* (1982) 1–19.
- [10] M. Skyllas-Kazacos, D. Kasherman, D.R. Hong, M. Kazacos, Characteristics and performance of 1 kW UNSW vanadium redox battery, *J. Power Sources*. 35 (1991) 399–404. doi:10.1016/0378-7753(91)80058-6.
- [11] S. Miyake, N. Tokuda, Vanadium redox-flow battery for a variety of applications, 2001 *Power Eng. Soc. Summer Meet. Conf. Proc. (Cat. No.01CH37262)*. 1 (2001) 450–451. doi:10.1109/PESS.2001.970067.
- [12] G.L. Soloveichik, *Flow Batteries : Current Status and Trends*, *Chem. Rev.* (2014). doi:10.1021/cr500720t.
- [13] Q. Huang, Q. Wang, Next-generation, high-energy-density redox flow batteries,

Chempluschem. 80 (2015) 312–322. doi:10.1002/cplu.201402099.

- [14] X. Wei, W. Pan, W. Duan, A. Hollas, Z. Yang, B. Li, Z. Nie, J. Liu, D. Reed, W. Wang, V. Sprenkle, Materials and Systems for Organic Redox Flow Batteries: Status and Challenges, *ACS Energy Lett.* 2 (2017) 2187–2204. doi:10.1021/acseenergylett.7b00650.
- [15] A. Poullikkas, A comparative overview of large-scale battery systems for electricity storage, *Renew. Sustain. Energy Rev.* 27 (2013) 778–788. doi:10.1016/j.rser.2013.07.017.
- [16] C. Ponce de León, a. Frías-Ferrer, J. González-García, D. a. Szánto, F.C. Walsh, Redox flow cells for energy conversion, *J. Power Sources.* 160 (2006) 716–732. doi:10.1016/j.jpowsour.2006.02.095.
- [17] M.K. Ravikumar, S. Rathod, N. Jaiswal, S. Patil, A. Shukla, The renaissance in redox flow batteries, *J. Solid State Electrochem.* (2016) 1–22. doi:10.1007/s10008-016-3472-4.
- [18] T. Li, J. Xu, C. Wang, W. Wu, D. Su, G. Wang, The latest advances in the critical factors (positive electrode, electrolytes, separators) for sodium-sulfur battery, *J. Alloys Compd.* 792 (2019) 797–817. doi:10.1016/j.jallcom.2019.03.343.
- [19] K. Xu, Nonaqueous liquid electrolytes for lithium-based rechargeable batteries, *Chem. Rev.* 104 (2004) 4303–4417. doi:10.1021/cr030203g.
- [20] M.A. Rahman, X. Wang, C. Wenz, High energy density metal-air batteries: A review, *J. Electrochem. Soc.* 160 (2013) A1759–A1771. doi:10.1149/2.062310jes.
- [21] M. Stone, Redox flow batteries for energy storage, *Energy Storage Rep.* (n.d.). <http://energystoragereport.info/redox-flow-batteries-for-energy-storage/> (accessed August 1, 2016).
- [22] J. Noack, N. Roznyatovskaya, T. Herr, P. Fischer, The Chemistry of Redox-Flow Batteries, *Angew. Chemie Int. Ed.* 54 (2015) 9776–9809. doi:10.1002/anie.201410823.
- [23] M. Skyllas-Kazacos, M.H. Chakrabarti, S. a. Hajimolana, F.S. Mjalli, M. Saleem, Progress in Flow Battery Research and Development, *J. Electrochem. Soc.* 158 (2011) R55. doi:10.1149/1.3599565.
- [24] W. Kangro, H. Pieper, Zur Frage Der Speicherung Von Elektrischer Energie In Flüssigkeiten, *Electrochim. Acta.* 7 (1962) 435–448. doi:10.1080/00194501003759811.
- [25] M. Bartolozzi, Development of redox flow batteries. A historical bibliography, *J. Power Sources.* 27 (1989) 219–234. doi:10.1016/0378-7753(89)80037-0.
- [26] H.L. Thaller, Electrically Rechargeable Redox Flow Cells, *NASA Arch. NASA-TM-X-* (1974) 1–8.
- [27] J. Giner, K. Cahill, Advanced screening of electrode couples, *NASA Arch. NASA CR-15* (1980) 1–48.
- [28] N.H. Hagedorn, NASA Redox Storage System Development Project. Final Report., *NASA Arch.*

- TM-83677 (1984).
- [29] Y.K. Zeng, T.S. Zhao, L. An, X.L. Zhou, L. Wei, A comparative study of all-vanadium and iron-chromium redox flow batteries for large-scale energy storage, *J. Power Sources*. 300 (2015) 438–443. doi:10.1016/j.jpowsour.2015.09.100.
- [30] A.K. Manohar, K.M. Kim, E. Plichta, M. Hendrickson, S. Rawlings, S.R. Narayanan, A High Efficiency Iron-Chloride Redox Flow Battery for Large-Scale Energy Storage, *J. Electrochem. Soc.* 163 (2016) A5118–A5125. doi:10.1149/2.0161601jes.
- [31] M. Rychcik, M. Skyllas-Kazacos, Characteristics of a new all-vanadium redox flow battery, *J. Power Sources*. 22 (1988) 59–67. doi:10.1016/0378-7753(88)80005-3.
- [32] E. Sum, M. Rychcik, M. Skyllas-kazacos, Investigation of the V(V)/V(IV) system for use in the positive half-cell of a redox battery, *J. Power Sources*. 16 (1985) 85–95. doi:10.1016/0378-7753(85)80082-3.
- [33] E. Sum, M. Skyllas-Kazacos, A study of the V(II)/V(III) redox couple for redox flow cell applications, *J. Power Sources*. 15 (1985) 179–190. doi:10.1016/0378-7753(85)80071-9.
- [34] X. Wu, J. Liu, X. Xiang, J. Zhang, J. Hu, Y. Wu, Electrolytes for vanadium redox flow batteries, *Pure Appl. Chem.* 86 (2014) 661–669. doi:10.1515/pac-2013-1213.
- [35] M. Skyllas-Kazacos, F. Grossmith, Efficient vanadium redox flow cell, *J. Electrochem. Soc.* (1987) 2950–2953. <http://jes.ecsdl.org/content/134/12/2950.short>.
- [36] T. Mohammadi, S.C. Chieng, M. Skyllas-Kazacos, Water transport study across commercial ion exchange membranes in the vanadium redox flow battery, *J. Memb. Sci.* 133 (1997) 151–159. doi:10.1016/S0376-7388(97)00092-6.
- [37] P. Singh, B. Jonshagen, Zinc-bromine battery for energy storage, *J. Power Sources*. 35 (1991) 405–410. doi:10.1016/0378-7753(91)80059-7.
- [38] B. Schwenzer, J. Zhang, S. Kim, L. Li, J. Liu, Z. Yang, Membrane development for vanadium redox flow batteries, *ChemSusChem*. 4 (2011) 1388–1406. doi:10.1002/cssc.201100068.
- [39] X. Ke, J.M. Prahl, J.I.D. Alexander, J.S. Wainright, T.A. Zawodzinski, R.F. Savinell, Rechargeable redox flow batteries: flow fields, stacks and design considerations, *Chem. Soc. Rev.* (2018). doi:10.1039/C8CS00072G.
- [40] J.D. Milshtein, K.M. Tenny, J.L. Barton, J. Drake, R.M. Darling, F.R. Brushett, Quantifying Mass Transfer Rates in Redox Flow Batteries, *J. Electrochem. Soc.* 164 (2017) E3265–E3275. doi:10.1149/2.0201711jes.
- [41] A. Forner-Cuenca, E.E. Penn, A.M. Oliveira, F.R. Brushett, Exploring the Role of Electrode Microstructure on the Performance of Non-Aqueous Redox Flow Batteries, *J. Electrochem. Soc.* 166 (2019) A2230–A2241. doi:10.1149/2.0611910jes.
- [42] K. V. Greco, A. Forner-Cuenca, A. Mularczyk, J. Eller, F.R. Brushett, Elucidating the Nuanced Effects of Thermal Pretreatment on Carbon Paper Electrodes for Vanadium Redox Flow

Batteries, *ACS Appl. Mater. Interfaces*. 10 (2018) 44430–44442.

doi:10.1021/acsami.8b15793.

- [43] J. Noack, J. Tubke, A comparison of materials and treatment of materials for vanadium redox flow battery, *ECS Trans.* 25 (2010) 235–245. doi:10.1017/CBO9781107415324.004.
- [44] A. Parasuraman, T.M. Lim, C. Menictas, M. Skyllas-Kazacos, Review of material research and development for vanadium redox flow battery applications, *Electrochim. Acta.* 101 (2013) 27–40. doi:10.1016/j.electacta.2012.09.067.
- [45] P. Arora, Z.J. Zhang, Battery Separators, *Chem. Rev.* 104 (2004) 4419–4462.
- [46] X. Li, H. Zhang, Z. Mai, H. Zhang, I. Vankelecom, Ion exchange membranes for vanadium redox flow battery (VRB) applications, *Energy Environ. Sci.* 4 (2011) 1147. doi:10.1039/c0ee00770f.
- [47] B. Schwenzer, J. Zhang, S. Kim, L. Li, J. Liu, Z. Yang, Membrane Development for Vanadium Redox Flow Batteries, *ChemSusChem*. 4 (2011) 1388–1406.
- [48] H. Prifti, A. Parasuraman, S. Winardi, T.M. Lim, M. Skyllas-Kazacos, Membranes for Redox Flow Battery Applications, *Membranes (Basel)*. 2 (2012) 275–306. doi:10.3390/membranes2020275.
- [49] T.N.L. Doan, T.K.A. Hoang, P. Chen, Recent development of polymer membranes as separators for all-vanadium redox flow batteries, *RSC Adv.* 5 (2015) 72805–72815. doi:10.1039/C5RA05914C.
- [50] X. Wei, B. Li, W. Wang, Porous Polymeric Composite Separators for Redox Flow Batteries, *Polym. Rev.* 55 (2015) 247–272. doi:10.1080/15583724.2015.1011276.
- [51] E.C. Montoto, G. Nagarjuna, J.S. Moore, J. Rodríguez-López, Redox active polymers for non-aqueous redox flow batteries: validation of the size-exclusion approach, *J. Electrochem. Soc.* 164 (2017) A1688–A1694. doi:10.1149/2.1511707jes.
- [52] S.-H. Shin, S.-H. Yun, S.-H. Moon, A review of current developments in non-aqueous redox flow batteries: characterization of their membranes for design perspective, *RSC Adv.* 3 (2013) 9095–9116. doi:10.1039/c3ra00115f.
- [53] J.R. Varcoe, P. Atanassov, D.R. Dekel, A.M. Herring, M. a. Hickner, P. a. Kohl, A.R. Kucernak, W.E. Mustain, K. Nijmeijer, K. Scott, T. Xu, L. Zhuang, Anion-exchange membranes in electrochemical energy systems, *Energy Environ. Sci.* 7 (2014) 3135–3191. doi:10.1039/b000000x.
- [54] S.S. Ivanchev, Fluorinated proton-conduction nafion-type membranes, the past and the future, *Russ. J. Appl. Chem.* 81 (2008) 569–584. doi:10.1134/S1070427208040010.
- [55] Y. Sone, P. Ekdunge, D. Simonsson, Proton Conductivity of Nafion 117 as Measured by a Four-Electrode AC Impedance Method, *J. Electrochem. Soc.* 143 (1996) 1254–1259. doi:10.1149/1.1836625.

## References

- [56] T. Mohammadi, M. Skyllas-Kazacos, Evaluation of the chemical stability of some membranes in vanadium solution, *J. Appl. Electrochem.* 27 (1996) 153–160. doi:10.1023/A:1018495722379.
- [57] D. Chen, M. a Hickner, V5+ degradation of sulfonated Radel membranes for vanadium redox flow batteries., *Phys. Chem. Chem. Phys.* 15 (2013) 11299–305. doi:10.1039/c3cp52035h.
- [58] S. Kim, T.B. Tighe, B. Schwenzer, J. Yan, J. Zhang, J. Liu, Z. Yang, M.A. Hickner, Chemical and mechanical degradation of sulfonated poly(sulfone) membranes in vanadium redox flow batteries, *J. Appl. Electrochem.* 41 (2011) 1201–1213. doi:10.1007/s10800-011-0313-0.
- [59] B. Tian, C.W. Yan, F.H. Wang, Modification and evaluation of membranes for vanadium redox battery applications, *J. Appl. Electrochem.* 34 (2004) 1205–1210. doi:10.1007/s10800-004-1765-2.
- [60] T. Mohammadi, M. Skyllas Kazacos, Modification of anion-exchange membranes for vanadium redox flow battery applications, *J. Power Sources.* 63 (1996) 179–186. doi:10.1016/S0378-7753(96)02463-9.
- [61] P.S. Son, M. Oh, J. Ye, S. Choi, Counter anion effects in anion exchange membrane-fabricated non-aqueous vanadium redox flow battery, *Anal. Sci. Technol.* 28 (2015) 341–346.
- [62] S. Maurya, S.H. Shin, K.W. Sung, S.H. Moon, Anion exchange membrane prepared from simultaneous polymerization and quaternization of 4-vinyl pyridine for non-aqueous vanadium redox flow battery applications, *J. Power Sources.* 255 (2014) 325–334. doi:10.1016/j.jpowsour.2014.01.047.
- [63] D.H. Kim, S.J. Seo, M.J. Lee, J.S. Park, S.H. Moon, Y.S. Kang, Y.W. Choi, M.S. Kang, Pore-filled anion-exchange membranes for non-aqueous redox flow batteries with dual-metal-complex redox shuttles, *J. Memb. Sci.* 454 (2014) 44–50. doi:10.1016/j.memsci.2013.11.051.
- [64] S. Maurya, S.H. Shin, M.K. Kim, S.H. Yun, S.H. Moon, Stability of composite anion exchange membranes with various functional groups and their performance for energy conversion, *J. Memb. Sci.* 443 (2013) 28–35. doi:10.1016/j.memsci.2013.04.035.
- [65] K.-W. Sung, S.-H. Shin, S.-H. Moon, Characterization of Commercial Membranes for Non-aqueous Vanadium Redox Flow Battery, *Korean Chem. Eng. Res.* 51 (2013) 615–621. doi:10.9713/kcer.2013.51.5.615.
- [66] Y. Huang, S. Gu, Y. Yan, S.F.Y. Li, Nonaqueous redox-flow batteries: features, challenges, and prospects, *Curr. Opin. Chem. Eng.* 8 (2015) 105–113. doi:10.1016/j.coche.2015.04.001.
- [67] K. Izutsu, *Electrochemistry in Nonaqueous Solutions*, Wiley-VCH Verlag GmbH & Co. KGaA, 2009. <http://onlinelibrary.wiley.com/book/10.1002/9783527629152>.
- [68] Y. Ding, C. Zhang, L. Zhang, Y. Zhou, G. Yu, Molecular engineering of organic electroactive materials for redox flow batteries, *Chem. Soc. Rev.* 47 (2018) 69–103. doi:10.1039/c7cs00569e.

- [69] I.L. Escalante-Garcia, J.S. Wainright, L.T. Thompson, R.F. Savinell, Performance of a Non-Aqueous Vanadium Acetylacetonate Prototype Redox Flow Battery: Examination of Separators and Capacity Decay, *J. Electrochem. Soc.* 162 (2014) A363–A372. doi:10.1149/2.0471503jes.
- [70] B. Huskinson, S. Nawar, M.R. Gerhardt, M.J. Aziz, Novel Quinone-Based Couples for Flow Batteries, *ECS Trans.* 53 (2013) 101–105. doi:10.1149/05307.0101ecst.
- [71] Q. Chen, L. Eisenach, M.J. Aziz, Cycling analysis of a quinone-bromide redox flow battery, *J. Electrochem. Soc.* 163 (2016) A5057–A5063. doi:10.1149/2.0081601jes.
- [72] S.D. Pineda Flores, G.C. Martin-Noble, R.L. Phillips, J. Schrier, Bio-Inspired Electroactive Organic Molecules for Aqueous Redox Flow Batteries. 1. Thiophenoquinones, *J. Phys. Chem. C.* 119 (2015) 21800–21809. doi:10.1021/acs.jpcc.5b05346.
- [73] M.R. Gerhardt, E.S. Beh, L. Tong, R.G. Gordon, M.J. Aziz, Comparison of Capacity Retention Rates During Cycling of Quinone-Bromide Flow Batteries, *MRS Adv.* (2016) 1. doi:10.1557/adv.2016.
- [74] Y. Xu, Y. Wen, J. Cheng, Y. Yanga, Z. Xie, G. Cao, Novel organic redox flow batteries using soluble quinonoid compounds as positive materials, *WNWEC 2009 - 2009 World Non-Grid-Connected Wind Power Energy Conf.* (2009) 475–478. doi:10.1109/WNWEC.2009.5335870.
- [75] M.R. Gerhardt, L. Tong, R. Gómez-Bombarelli, Q. Chen, M.P. Marshak, C.J. Galvin, A. Aspuru-Guzik, R.G. Gordon, M.J. Aziz, Anthraquinone Derivatives in Aqueous Flow Batteries, *Adv. Energy Mater.* 7 (2017). doi:10.1002/aenm.201601488.
- [76] Q. Chen, L. Eisenach, M.J. Aziz, Cycling Analysis of a Quinone-Bromide Redox Flow Battery, *J. Electrochem. Soc.* 163 (2016) A5057–A5063. doi:10.1149/2.0081601jes.
- [77] Y. Xu, Y. Wen, J. Cheng, G. Cao, Y. Yang, Study on a single flow acid Cd–chloranil battery, *Electrochem. Commun.* 11 (2009) 1422–1424. doi:10.1016/j.elecom.2009.05.021.
- [78] T.J. Carney, S.J. Collins, J.S. Moore, F.R. Brushett, Concentration-Dependent Dimerization of Anthraquinone Disulfonic Acid and Its Impact on Charge Storage, *Chem. Mater.* 29 (2017) 4801–4810. doi:10.1021/acs.chemmater.7b00616.
- [79] B. Huskinson, M.P. Marshak, M.R. Gerhardt, M.J. Aziz, Cycling of a Quinone-Bromide Flow Battery for Large-Scale Electrochemical Energy Storage, 115 (n.d.) 2–5.
- [80] S. Er, C. Suh, M.P. Marshak, A. Aspuru-Guzik, Computational design of molecules for an all-quinone redox flow battery, *Chem. Sci.* 6 (2015) 885–893. doi:10.1039/c4sc03030c.
- [81] K. Wedege, E. Dražević, D. Konya, A. Bientien, Organic redox species in aqueous flow batteries: redox potentials, chemical stability and solubility, *Sci. Rep.* 6 (2016) 39101. doi:10.1038/srep39101.
- [82] B. Yang, L. Hooper-Burkhardt, F. Wang, G.K. Surya Prakash, S.R. Narayanan, An Inexpensive

## References

- Aqueous Flow Battery for Large-Scale Electrical Energy Storage Based on Water-Soluble Organic Redox Couples, *J. Electrochem. Soc.* 161 (2014) A1371–A1380. doi:10.1149/2.1001409jes.
- [83] B. Huskinson, M.P. Marshak, C. Suh, S. Er, M.R. Gerhardt, C.J. Galvin, X. Chen, A. Aspuru-Guzik, R.G. Gordon, M.J. Aziz, A metal-free organic–inorganic aqueous flow battery, *Nature*. 505 (2014) 195–198. doi:10.1038/nature12909.
- [84] K. Lin, Q. Chen, M.R. Gerhardt, L. Tong, S.B. Kim, L. Eisenach, A.W. Valle, D. Hardee, R.G. Gordon, M.J. Aziz, M.P. Marshak, Alkaline quinone flow battery, *Science* (80-. ). 813 (2014).
- [85] Q. Chen, M.R. Gerhardt, L. Hartle, M.J. Aziz, A Quinone-Bromide Flow Battery with 1 W/cm<sup>2</sup> Power Density, *J. Electrochem. Soc.* 163 (2015) A5010–A5013. doi:10.1149/2.0021601jes.
- [86] E.S. Beh, D. De Porcellinis, R.L. Gracia, K.T. Xia, R.G. Gordon, M.J. Aziz, A neutral pH aqueous organic–organometallic redox flow battery with extremely high capacity retention, *ACS Energy Lett.* 2 (2017) 639–644. doi:10.1021/acsendergylett.7b00019.
- [87] T. Hagemann, J. Winsberg, M. Grube, I. Nischang, T. Janoschka, N. Martin, M.D. Hager, U.S. Schubert, An aqueous all-organic redox-flow battery employing a (2,2,6,6-tetramethylpiperidin-1-yl)oxyl-containing polymer as catholyte and dimethyl viologen dichloride as anolyte, *J. Power Sources*. 378 (2018) 546–554. doi:10.1016/j.jpowsour.2017.09.007.
- [88] C. Debruler, B. Hu, J. Moss, J. Luo, T.L. Liu, A Sulfonate-Functionalized Viologen Enabling Neutral Cation Exchange, Aqueous Organic Redox Flow Batteries toward Renewable Energy Storage, *ACS Energy Lett.* 3 (2018) 663–668. doi:10.1021/acsendergylett.7b01302.
- [89] B. Hu, Y. Tang, J. Luo, G. Grove, Y. Guo, T.L. Liu, Improved radical stability of viologen anolytes in aqueous organic redox flow batteries, *Chem. Commun.* 54 (2018) 6871–6874. doi:10.1039/c8cc02336k.
- [90] T. Liu, X. Wei, Z. Nie, V. Sprenkle, W. Wang, A Total Organic Aqueous Redox Flow Battery Employing a Low Cost and Sustainable Methyl Viologen Anolyte and 4-HO-TEMPO Catholyte, *Adv. Energy Mater.* 6 (2016). doi:10.1002/aenm.201501449.
- [91] J. Luo, B. Hu, C. Debruler, T.L. Liu, A  $\pi$ -Conjugation Extended Viologen as a Two-Electron Storage Anolyte for Total Organic Aqueous Redox Flow Batteries, *Angew. Chemie - Int. Ed.* 57 (2018) 231–235. doi:10.1002/anie.201710517.
- [92] C. Chen, S. Zhang, Y. Zhu, Y. Qian, Z. Niu, J. Ye, Y. Zhao, X. Zhang, Pyridyl group design in viologens for anolyte materials in organic redox flow batteries, *RSC Adv.* 8 (2018) 18762–18770. doi:10.1039/c8ra02641f.
- [93] J.B. Gerken, Y.Q. Pang, M.B. Lauber, S.S. Stahl, Structural Effects on the pH-Dependent Redox Properties of Organic Nitroxyls: Pourbaix Diagrams for TEMPO, ABNO, and Three TEMPO Analogs, *J. Org. Chem.* 83 (2018) 7323–7330. doi:10.1021/acs.joc.7b02547.

- [94] M.H. Chakrabarti, R.A.W. Dryfe, E.P.L. Roberts, Organic electrolytes for redox flow batteries, *J. Chem. Soc. Pakistan*. 29 (2007) 294–300.  
<http://www.scopus.com/inward/record.url?eid=2-s2.0-36549008135&partnerID=40&md5=0cda50df7629f80b2ac35ba3fecc3cbb>.
- [95] Y.-W.D. Chen, Solution Redox Couples for Electrochemical Energy Storage, *J. Electrochem. Soc.* 128 (1981) 1460. doi:10.1149/1.2127663.
- [96] Y. Matsuda, K. Tanaka, M. Okada, Y. Takasu, M. Morita, T. Matsumura-Inoue, A rechargeable redox battery utilizing ruthenium complexes with non-aqueous organic electrolyte, *J. Appl. Electrochem.* 18 (1988) 909–914. doi:10.1007/BF01016050.
- [97] J.D. Milshtein, J.L. Barton, T.J. Carney, J.A. Kowalski, R.M. Darling, F.R. Brushett, Towards low resistance nonaqueous redox flow batteries, *J. Electrochem. Soc.* 164 (2017) A2487–A2499. doi:10.1149/2.0741712jes.
- [98] K. Gong, Q. Fang, S. Gu, S.F.Y. Li, Y. Yan, Nonaqueous redox-flow batteries: organic solvents, supporting electrolytes, and redox pairs, *Energy Environ. Sci.* 8 (2015) 3515–3530. doi:10.1039/C5EE02341F.
- [99] T. Ma, Z. Pan, L. Miao, C. Chen, M. Han, Z. Shang, J. Chen, Porphyrin-Based Symmetric Redox-Flow Batteries towards Cold-Climate Energy Storage, *Angew. Chemie - Int. Ed.* 57 (2018) 3158–3162. doi:10.1002/anie.201713423.
- [100] L. Su, R.M. Darling, K.G. Gallagher, W. Xie, J.L. Thelen, A.F. Badel, J.L. Barton, K.J. Cheng, N.P. Balsara, J.S. Moore, F.R. Brushett, An Investigation of the Ionic Conductivity and Species Crossover of Lithiated Nafion N117 in Nonaqueous Electrolytes, *J. Electrochem. Soc.* 163 (2016) A5253–A5262. doi:10.1149/2.03211601jes.
- [101] K. Izutsu, *Electrochemistry in Nonaqueous Solutions*, Wiley-VCH Verlag GmbH & Co. KGaA, 2002.
- [102] A. Ejigu, P.A. Greatorex-Davies, D.A. Walsh, Room temperature ionic liquid electrolytes for redox flow batteries, *Electrochem. Commun.* 54 (2015) 55–59. doi:10.1016/j.elecom.2015.01.016.
- [103] J.S. Baek, J.S. Park, S.S. Sekhon, T.H. Yang, Y.G. Shul, J.H. Choi, Preparation and characterisation of non-aqueous proton-conducting membranes with the low content of ionic liquids, *Fuel Cells*. 10 (2010) 762–769. doi:10.1002/fuce.200900176.
- [104] D. Zhang, Q. Liu, X. Shi, Y. Li, Tetrabutylammonium hexafluorophosphate and 1-ethyl-3-methyl imidazolium hexafluorophosphate ionic liquids as supporting electrolytes for non-aqueous vanadium redox flow batteries, *J. Power Sources*. 203 (2012) 201–205. doi:10.1016/j.jpowsour.2011.10.136.
- [105] K. Teramoto, T. Nishide, Shin'okumura, K. Takao, Y. Ikeda, Studies on metal complexes as active materials in redox-flow battery using ionic liquids as electrolyte: electrochemical

- properties of  $[\text{Fe}(\text{L})_x][\text{Tf}_2\text{N}]_2$  (L: Multidentate Ligands,  $x = 2$  or  $3$ ) in 1-butyl-3-methylimidazolium bis(trifluoromethylsulfonyl)imide, *Electrochem. (Tokyo, Jpn.)*. 82 (2014) 566–572. doi:10.5796/electrochemistry.82.566.
- [106] M.H. Chakrabarti, F.S. Mjalli, I.M. AlNashef, M.A. Hashim, M.A. Hussain, L. Bahadori, C.T.J. Low, Prospects of applying ionic liquids and deep eutectic solvents for renewable energy storage by means of redox flow batteries, *Renew. Sustain. Energy Rev.* 30 (2014) 254–270. doi:10.1016/j.rser.2013.10.004.
- [107] K. Takechi, Y. Kato, Y. Hase, A highly concentrated catholyte based on a solvate ionic liquid for rechargeable flow batteries, *Adv. Mater.* 27 (2015) 2501–2506. doi:10.1002/adma.201405840.
- [108] P. Singh, Application of Non-Aqueous Solvents to Batteries, *J. Power Sources*. 11 (1984) 135–142.
- [109] J.A. Kowalski, L. Su, J.D. Milshtein, F.R. Brushett, Recent advances in molecular engineering of redox active organic molecules for nonaqueous flow batteries, *Curr. Opin. Chem. Eng.* 13 (2016) 45–52. doi:10.1016/j.coche.2016.08.002.
- [110] R. Dmello, J.D. Milshtein, F.R. Brushett, K.C. Smith, Cost-driven materials selection criteria for redox flow battery electrolytes, *J. Power Sources*. 330 (2016) 261–272. doi:10.1016/j.jpowsour.2016.08.129.
- [111] M.O. Bamgbopa, N. Pour, Y. Shao-Horn, S. Almheiri, Systematic selection of solvent mixtures for non-aqueous redox flow batteries – vanadium acetylacetonate as a model system, *Electrochim. Acta*. 223 (2017) 115–123. doi:10.1016/j.electacta.2016.12.014.
- [112] T. Herr, P. Fischer, J. Tübke, K. Pinkwart, P. Elsner, Increasing the energy density of the non-aqueous vanadium redox flow battery with the acetonitrile-1,3-dioxolane-dimethyl sulfoxide solvent mixture, *J. Power Sources*. 265 (2014) 317–324. doi:10.1016/j.jpowsour.2014.04.141.
- [113] A. a. Shinkle, T.J. Pomaville, A.E.S. Sleightholme, L.T. Thompson, C.W. Monroe, Solvents and supporting electrolytes for vanadium acetylacetonate flow batteries, *J. Power Sources*. 248 (2014) 1299–1305. doi:10.1016/j.jpowsour.2013.10.034.
- [114] R.W. Hogue, K.E. Toghiani, Metal Coordination Complexes in Non-Aqueous Redox Flow Batteries, *Curr. Opin. Electrochem.* 18 (2019) 37–45. doi:10.1016/j.coelec.2019.08.006.
- [115] M. Burgess, J.S. Moore, J. Rodríguez-López, Redox active polymers as soluble nanomaterials for energy storage, *Acc. Chem. Res.* 49 (2016) 2649–2657. doi:10.1021/acs.accounts.6b00341.
- [116] S.E. Doris, A.L. Ward, A. Baskin, P.D. Frischmann, N. Gavvalapalli, E. Chénard, C.S. Sevov, D. Prendergast, J.S. Moore, B.A. Helms, Macromolecular design strategies for preventing active-material crossover in non-aqueous all-organic redox-flow batteries, *Angew. Chemie Int. Ed.*

56 (2017) 1595–1599. doi:10.1002/anie.201610582.

- [117] J. Winsberg, T. Hagemann, S. Muench, C. Friebe, B. Häupler, T. Janoschka, S. Morgenstern, M.D. Hager, U.S. Schubert, Poly(boron-dipyrromethene)—A redox-active polymer class for polymer redox-flow batteries, *Chem. Mater.* 28 (2016) 3401–3405. doi:10.1021/acs.chemmater.6b00640.
- [118] J. Kim, J.H. Kim, K. Ariga, Redox-active polymers for energy storage nanoarchitectonics, *Joule*. 1 (2017) 739–768. doi:10.1016/j.joule.2017.08.018.
- [119] L.E. Vangelder, A.M. Kosswattaarachchi, P.L. Forrestel, T.R. Cook, E.M. Matson, Polyoxovanadate-Alkoxide clusters as multi-electron charge carriers for symmetric non-Aqueous redox flow batteries, *Chem. Sci.* 9 (2018) 1692–1699. doi:10.1039/c7sc05295b.
- [120] A.A. Shinkle, A.E.S.S. Sleightholme, L.D. Griffith, L.T. Thompson, C.W. Monroe, Degradation mechanisms in the non-aqueous vanadium acetylacetonate redox flow battery, *J. Power Sources*. 206 (2012) 490–496. doi:10.1016/j.jpowsour.2010.12.096.
- [121] J.-H. Kim, K.J. Kim, M.-S. Park, N.J. Lee, U. Hwang, H. Kim, Y.-J. Kim, Development of metal-based electrodes for non-aqueous redox flow batteries, *Electrochem. Commun.* 13 (2011) 997–1000. doi:10.1016/j.elecom.2011.06.022.
- [122] S.A. Richert, P.K.S. Tsang, D.T. Sawyer, Ligand-centered redox processes for manganese, iron and cobalt,  $MnL_3$ ,  $FeL_3$ , and  $CoL_3$ , complexes (L = acetylacetonate, 8-quinolate, picolinate, 2,2'-bipyridyl, 1,10-phenanthroline) and for their tetrakis(2,6-dichlorophenyl)porphinato complexes  $[M(Por)]$ , *Inorg. Chem.* 28 (1989) 2471–2475. doi:10.1021/ic00311a044.
- [123] J. Mun, M.-J. Lee, J.-W. Park, D.-J. Oh, D.-Y. Lee, S.-G. Doo, Non-Aqueous Redox Flow Batteries with Nickel and Iron Tris(2,2'-bipyridine) Complex Electrolyte, *Electrochem. Solid-State Lett.* 15 (2012) A80. doi:10.1149/2.033206esl.
- [124] S.M. Laramie, J.D. Milshtein, T.M. Breault, F.R. Brushett, L.T. Thompson, Performance and cost characteristics of multi-electron transfer, common ion exchange non-aqueous redox flow batteries, *J. Power Sources*. 327 (2016) 681–692. doi:10.1016/j.jpowsour.2016.07.015.
- [125] M.S. Park, N.J. Lee, S.W. Lee, K.J. Kim, D.J. Oh, Y.J. Kim, High-energy redox-flow batteries with hybrid metal foam electrodes, *ACS Appl. Mater. Interfaces*. 6 (2014) 10729–10735. doi:10.1021/am5025935.
- [126] M.H. Chakrabarti, E.P.L. Roberts, C. Bae, M. Saleem, Ruthenium based redox flow battery for solar energy storage, *Energy Convers. Manag.* 52 (2011) 2501–2508. doi:10.1016/j.enconman.2011.01.012.
- [127] A.E.S. Sleightholme, A.A. Shinkle, Q. Liu, Y. Li, C.W. Monroe, L.T. Thompson, Non-aqueous manganese acetylacetonate electrolyte for redox flow batteries, *J. Power Sources*. 196 (2011) 5742–5745. doi:10.1016/j.jpowsour.2011.02.020.
- [128] Q. Liu, A.A. Shinkle, Y. Li, C.W. Monroe, L.T. Thompson, A.E.S. Sleightholme, Non-aqueous

- chromium acetylacetonate electrolyte for redox flow batteries, *Electrochem. Commun.* 12 (2010) 1634–1637. doi:10.1016/j.elecom.2010.09.013.
- [129] Q. Liu, A.E.S. Sleightholme, A.A. Shinkle, Y. Li, L.T. Thompson, Non-aqueous vanadium acetylacetonate electrolyte for redox flow batteries, *Electrochem. Commun.* 11 (2009) 2312–2315. doi:10.1016/j.elecom.2009.10.006.
- [130] M.M. Chakrabarti, N.N. Brandon, M.M. Hashim, F.F. Mjalli, I.I. AlNashef, L. Bahadori, N.S. a Manan, M. a Hussain, V. Yufit, Cyclic voltammetry of iron (III) acetylacetonate in quaternary ammonium and phosphonium based deep eutectic solvents, *Int. J. Electrochem. Sci.* 8 (2013) 9652–9676.
- [131] X. Xing, D. Zhang, Y. Li, A non-aqueous all-cobalt redox flow battery using 1,10-phenanthrolinecobalt(II) hexafluorophosphate as active species, *J. Power Sources.* 279 (2015) 205–209. doi:10.1016/j.jpowsour.2015.01.011.
- [132] X. Xing, Y. Zhao, Y. Li, A non-aqueous redox flow battery based on tris(1,10-phenanthroline) complexes of iron(II) and cobalt(II), *J. Power Sources.* 293 (2015) 778–783. doi:10.1016/j.jpowsour.2015.06.016.
- [133] J.A. Suttill, J.F. Kucharyson, I.L. Escalante-Garcia, P.J. Cabrera, B.R. James, R.F. Savinell, M.S. Sanford, L.T. Thompson, Metal acetylacetonate complexes for high energy density non-aqueous redox flow batteries, *J. Mater. Chem. A.* 3 (2015) 7929–7938. doi:10.1039/C4TA06622G.
- [134] P.J. Cabrera, X. Yang, J.A. Suttill, R.E.M. Brooner, L.T. Thompson, M.S. Sanford, Evaluation of Tris-Bipyridine Chromium Complexes for Flow Battery Applications: Impact of Bipyridine Ligand Structure on Solubility and Electrochemistry, *Inorg. Chem.* 54 (2015) 10214–10223. doi:10.1021/acs.inorgchem.5b01328.
- [135] P.J. Cabrera, X. Yang, J.A. Suttill, K.L. Hawthorne, R.E.M. Brooner, M.S. Sanford, L.T. Thompson, Complexes Containing Redox Noninnocent Ligands for Symmetric, Multielectron Transfer Nonaqueous Redox Flow Batteries, *J. Phys. Chem. C.* 119 (2015) 15882–15889. doi:10.1021/acs.jpcc.5b03582.
- [136] A.M. Kosswattaarachchi, T.R. Cook, Concentration-dependent charge-discharge characteristics of non-aqueous redox flow battery electrolyte combinations, *Electrochim. Acta.* 261 (2018) 296–306. doi:10.1016/j.electacta.2017.12.131.
- [137] J. Mun, D.-J. Oh, M.S. Park, O. Kwon, H.-T. Kim, S. Jeong, Y.G. Kim, M.-J. Lee, Highly Soluble Tris(2,2'-bipyridine) Metal Bis(trifluoromethanesulfonyl)imide Complexes for High Energy Organic Redox Flow Batteries, *J. Electrochem. Soc.* 165 (2018) A215–A219. doi:10.1149/2.0791802jes.
- [138] S. Hwang, H. seung Kim, J.H. Ryu, S.M. Oh, N-ferrocenylphthalimide; A single redox couple formed by attaching a ferrocene moiety to phthalimide for non-aqueous flow batteries, *J.*

Power Sources. 395 (2018) 60–65. doi:10.1016/j.jpowsour.2018.05.053.

- [139] D. Zhang, H. Lan, Y. Li, The application of a non-aqueous bis(acetylaceton)ethylenediamine cobalt electrolyte in redox flow battery, *J. Power Sources*. 217 (2012) 199–203. doi:10.1016/j.jpowsour.2012.06.038.
- [140] C. Yang, G. Nikiforidis, J.Y. Park, J. Choi, Y. Luo, L. Zhang, S.C. Wang, Y.T. Chan, J. Lim, Z. Hou, M.H. Baik, Y. Lee, H.R. Byon, Designing Redox-Stable Cobalt–Polypyridyl Complexes for Redox Flow Batteries: Spin-Crossover Delocalizes Excess Charge, *Adv. Energy Mater.* 8 (2018) 1–10. doi:10.1002/aenm.201702897.
- [141] E. Benazzi, V. Cristino, S. Caramori, L. Meda, R. Boaretto, C.A. Bignozzi, Electrochemical characterization of polypyridine iron(II) and cobalt(II) complexes for organic redox flow batteries, *Polyhedron*. 140 (2018) 99–108. doi:10.1016/j.poly.2017.12.001.
- [142] C.S. Sevov, S.L. Fisher, L.T. Thompson, M.S. Sanford, Mechanism-Based Development of a Low-Potential, Soluble, and Cyclable Multielectron Anolyte for Nonaqueous Redox Flow Batteries, *J. Am. Chem. Soc.* 138 (2016) 15378–15384. doi:10.1021/jacs.6b07638.
- [143] G.M. Duarte, J.D. Braun, P.K. Giesbrecht, D.E. Herbert, Redox non-innocent bis(2,6-diimine-pyridine) ligand-iron complexes as anolytes for flow battery applications, *Dalt. Trans.* 46 (2017) 16439–16445. doi:10.1039/c7dt03915h.
- [144] Y. Ding, Y. Zhao, Y. Li, J.B. Goodenough, G. Yu, A high-performance all-metallocene-based, non-aqueous redox flow battery, *Energy Environ. Sci.* 10 (2017) 491–497. doi:10.1039/C6EE02057G.
- [145] L. Cosimbescu, X. Wei, M. Vijayakumar, W. Xu, M.L. Helm, S.D. Burton, C.M. Sorensen, J. Liu, V. Sprenkle, W. Wang, Anion-Tunable Properties and Electrochemical Performance of Functionalized Ferrocene Compounds, *Sci. Rep.* 5 (2015) 14117. doi:10.1038/srep14117.
- [146] A.M. Kosswattarachchi, T.R. Cook, Mixed-Component Catholyte and Anolyte Solutions for High-Energy Density Non-Aqueous Redox Flow Batteries, *J. Electrochem. Soc.* 165 (2018) A194–A200. doi:10.1149/2.0751802jes.
- [147] T. Chu, I.A. Popov, G.A. Andrade, S. Maurya, P. Yang, E.R. Batista, B.L. Scott, R. Mukundan, B.L. Davis, Linked Picolinamide Nickel Complexes as Redox Carriers for Nonaqueous Flow Batteries, *ChemSusChem*. 12 (2019) 1304–1309. doi:10.1002/cssc.201802985.
- [148] P.J. Cappillino, H.D. Pratt, N.S. Hudak, N.C. Tomson, T.M. Anderson, M.R. Anstey, Application of Redox Non-Innocent Ligands to Non-Aqueous Flow Battery Electrolytes, *Adv. Energy Mater.* 4 (2014) 1300566. doi:10.1002/aenm.201300566.
- [149] J. Huang, B. Pan, W. Duan, X. Wei, R.S. Assary, L. Su, F.R. Brushett, L. Cheng, C. Liao, M.S. Ferrandon, W. Wang, Z. Zhang, A.K. Burrell, L.A. Curtiss, I.A. Shkrob, J.S. Moore, L. Zhang, The lightest organic radical cation for charge storage in redox flow batteries, *Sci. Rep.* 6 (2016) 32102. doi:10.1038/srep32102.

## References

- [150] W. Duan, J. Huang, J.A. Kowalski, I.A. Shkrob, M. Vijayakumar, E. Walter, B. Pan, Z. Yang, J.D. Milshtein, B. Li, C. Liao, Z. Zhang, W. Wang, J. Liu, J.S. Moore, F.R. Brushett, L. Zhang, X. Wei, "Wine-dark sea" in an organic flow battery: storing negative charge in 2,1,3-benzothiadiazole radicals leads to improved cyclability, *ACS Energy Lett.* 2 (2017) 1156–1161. doi:10.1021/acsenergylett.7b00261.
- [151] X. Wei, W. Xu, J. Huang, L. Zhang, E. Walter, C. Lawrence, M. Vijayakumar, W. a Henderson, T. Liu, L. Cosimbescu, B. Li, V. Sprenkle, W. Wang, Radical compatibility with nonaqueous electrolytes and Its impact on an all-organic redox flow battery, *Angew. Chemie Int. Ed.* 54 (2015) 8684–8687. doi:10.1002/anie.201501443.
- [152] R.A. Potash, J.R. McKone, S. Conte, H.D. Abruña, On the benefits of a symmetric redox flow battery, *J. Electrochem. Soc.* 163 (2016) A338–A344. doi:10.1149/2.0971602jes.
- [153] M. Park, D.-S. Shin, J. Ryu, M. Choi, N. Park, S.Y. Hong, J. Cho, Organic-Catholyte-Containing Flexible Rechargeable Lithium Batteries, *Adv. Mater.* (2015) n/a-n/a. doi:10.1002/adma.201502329.
- [154] X. Xing, Y. Huo, X. Wang, Y. Zhao, Y. Li, A benzophenone-based anolyte for high energy density all-organic redox flow battery, *Int. J. Hydrogen Energy.* 42 (2017) 17488–17494. doi:10.1016/j.ijhydene.2017.03.034.
- [155] S.-K. Park, J. Shim, J. Yang, K.-H. Shin, C.-S. Jin, B.S. Lee, Y.-S. Lee, J.-D. Jeon, Electrochemical properties of a non-aqueous redox battery with all-organic redox couples, *Electrochem. Commun.* 59 (2015) 68–71. doi:10.1016/j.elecom.2015.07.013.
- [156] J.D. Milshtein, A.P. Kaur, M.D. Casselman, J.A. Kowalski, S. Modekrutti, P.L. Zhang, N.H. Attanayake, C.F. Elliott, S.R. Parkin, C. Risko, F.R. Brushett, S.A. Odom, N. Harsha Attanayake, C.F. Elliott, S.R. Parkin, C. Risko, F.R. Brushett, S.A. Odom, High current density, long duration cycling of soluble organic active species for non-aqueous redox flow batteries, *Energy Environ. Sci.* 9 (2016) 3531–3543. doi:10.1039/C6EE02027E.
- [157] V. Pasala, C. Ramachandra, S. Sethuraman, K. Ramanujam, A High Voltage Organic Redox Flow Battery with Redox Couples  $O_2$  /Tetrabutylammonium Complex and Tris(4-bromophenyl)amine as Redox Active Species, *J. Electrochem. Soc.* 165 (2018) A2696–A2702. doi:10.1149/2.0661811jes.
- [158] F.R. Brushett, J.T. Vaughey, A.N. Jansen, An all-organic non-aqueous lithium-ion redox flow battery, *Adv. Energy Mater.* 2 (2012) 1390–1396. doi:10.1002/aenm.201200322.
- [159] J.D. Milshtein, J.L. Barton, R.M. Darling, F.R. Brushett, 4-Acetamido-2,2,6,6-tetramethylpiperidine-1-oxyl as a model organic redox active compound for nonaqueous flow batteries, *J. Power Sources.* 327 (2016) 151–159. doi:10.1016/j.jpowsour.2016.06.125.
- [160] K.H. Hendriks, C.S. Sevov, M.E. Cook, M.S. Sanford, Multielectron cycling of a low-potential anolyte in alkali metal electrolytes for nonaqueous redox flow batteries, *ACS Energy Lett.* 2

(2017) 2430–2435. doi:10.1021/acseenergylett.7b00559.

- [161] J. Zhang, J. Huang, L.A. Robertson, I.A. Shkrob, L. Zhang, Comparing calendar and cycle life stability of redox active organic molecules for nonaqueous redox flow batteries, *J. Power Sources*. 397 (2018) 214–222. doi:10.1016/j.jpowsour.2018.07.001.
- [162] E. V. Carino, J. Staszak-Jirkovsky, R.S. Assary, L.A. Curtiss, N.M. Markovic, F.R. Brushett, Tuning the stability of organic active materials for nonaqueous redox flow batteries via reversible, electrochemically mediated Li<sup>+</sup> coordination, *Chem. Mater.* 28 (2016) 2529–2539. doi:10.1021/acs.chemmater.5b04053.
- [163] J. HUANG, W. Duan, J. Zhang, I.A. Shkrob, R. Surendran Assary, B. Pan, L. Chen, Z. Zhang, X. Wei, L. Zhang, R.S. Assary, B. Pan, C. Liao, Z. Zhang, X. Wei, L. Zhang, Substituted thiadiazoles as energy-rich anolytes for nonaqueous redox flow cells, *J. Mater. Chem. A*. 6 (2018) 6251–6254. doi:10.1039/C8TA01059E.
- [164] A.P. Kaur, N.E. Holubowitch, S. Ergun, C.F. Elliott, S.A. Odom, A highly soluble organic catholyte for non-aqueous redox flow batteries, *Energy Technol.* 3 (2015) 476–480. doi:10.1002/ente.201500020.
- [165] J. Huang, Z. Yang, M. Vijayakumar, W. Duan, A. Hollas, B. Pan, W. Wang, X. Wei, L. Zhang, A two-electron storage nonaqueous organic redox flow battery, *Adv. Sustain. Syst.* 2 (2018) 1700131. doi:10.1002/adsu.201700131.
- [166] X. Wei, W. Xu, M. Vijayakumar, L. Cosimbescu, T. Liu, V. Sprenkle, W. Wang, TEMPO-based catholyte for high-energy density nonaqueous redox flow batteries, *Adv. Mater.* 26 (2014) 7649–7653. doi:10.1002/adma.201403746.
- [167] L. Su, M. Ferrandon, J.L. Barton, N.U. de la Rosa, J.T. Vaughey, F.R. Brushett, An investigation of 2,5-di-tert-butyl-1,4-bis(methoxyethoxy)benzene in ether-based electrolytes, *Electrochim. Acta*. 246 (2017) 251–258. doi:10.1016/j.electacta.2017.05.167.
- [168] J.A. Kowalski, M.D. Casselman, A.P. Kaur, J.D. Milshtein, C.F. Elliott, S. Modekrutti, N.H. Attanayake, N. Zhang, S.R. Parkin, C. Risko, F.R. Brushett, S.A. Odom, A stable two-electron-donating phenothiazine for application in nonaqueous redox flow batteries, *J. Mater. Chem. A*. 5 (2017) 24371–24379. doi:10.1039/C7TA05883G.
- [169] T. Hagemann, J. Winsberg, B. Häupler, T. Janoschka, J.J. Gruber, A. Wild, U.S. Schubert, A bipolar nitronyl nitroxide small molecule for an all-organic symmetric redox-flow battery, *NPG Asia Mater.* 9 (2017). doi:10.1038/am.2016.195.
- [170] J. Friedl, M.A. Lebedeva, K. Porfyrakis, U. Stimming, T.W. Chamberlain, All-Fullerene-Based Cells for Nonaqueous Redox Flow Batteries, *J. Am. Chem. Soc.* 140 (2018) 401–405. doi:10.1021/jacs.7b11041.
- [171] J. Zhang, I.A. Shkrob, R.S. Assary, S.O. Tung, B. Silcox, L.A. Curtiss, L. Thompson, L. Zhang, Toward improved catholyte materials for redox flow batteries: what controls chemical

- stability of persistent radical cations?, *J. Phys. Chem. C* 121 (2017) 23347–23358. doi:10.1021/acs.jpcc.7b08281.
- [172] C.S. Sevov, S.K. Samaroo, M.S. Sanford, Cyclopropenium salts as cyclable, high-potential catholytes in nonaqueous media, *Adv. Energy Mater.* 7 (2017) 1602027. doi:10.1002/aenm.201602027.
- [173] Z. Li, S. Li, S. Liu, K. Huang, D. Fang, F. Wang, S. Peng, Electrochemical properties of an all-organic redox flow battery using 2,2,6,6-tetramethyl-1-piperidinyloxy and N-methylphthalimide, *Electrochem. Solid-State Lett.* 14 (2011) A171. doi:10.1149/2.012112esl.
- [174] H. Kim, K.-J. Lee, Y.-K. Han, J.H. Ryu, S.M. Oh, A comparative study on the solubility and stability of p-phenylenediamine-based organic redox couples for non-aqueous flow batteries, *J. Power Sources*. 348 (2017) 264–269. doi:10.1016/j.jpowsour.2017.03.019.
- [175] X. Wei, W. Duan, J. Huang, L. Zhang, B. Li, D. Reed, W. Xu, V. Sprenkle, W. Wang, A high-current, stable nonaqueous organic redox flow battery, *ACS Energy Lett.* 1 (2016) 705–711. doi:10.1021/acsenergylett.6b00255.
- [176] J. Huang, L. Su, J.A. Kowalski, J.L. Barton, M. Ferrandon, A.K. Burrell, F.R. Brushett, L. Zhang, A subtractive approach to molecular engineering of dimethoxybenzene-based redox materials for non-aqueous flow batteries, *J. Mater. Chem. A* 3 (2015) 14971–14976. doi:10.1039/C5TA02380G.
- [177] J. Zhang, Z. Yang, I.A. Shkrob, R.S. Assary, S. on Tung, B. Silcox, W. Duan, J. Zhang, C.C. Su, B. Hu, B. Pan, C. Liao, Z. Zhang, W. Wang, L.A. Curtiss, L.T. Thompson, X. Wei, L. Zhang, Annulated dialkoxybenzenes as catholyte materials for non-aqueous redox flow batteries: achieving high chemical stability through bicyclic substitution, *Adv. Energy Mater.* 7 (2017) 1701272. doi:10.1002/aenm.201701272.
- [178] N.H. Attanayake, J.A. Kowalski, K. V. Greco, M.D. Casselman, J.D. Milshtein, S.J. Chapman, S.R. Parkin, F.R. Brushett, S.A. Odom, Tailoring Two-Electron-Donating Phenothiazines to Enable High-Concentration Redox Electrolytes for Use in Nonaqueous Redox Flow Batteries, *Chem. Mater.* 31 (2019) 4353–4363. doi:10.1021/acs.chemmater.8b04770.
- [179] W. Duan, R.S. Vemuri, J.D. Milshtein, S. Laramie, R.D. Dmello, J. Huang, L. Zhang, D. Hu, M. Vijayakumar, W. Wang, J. Liu, R.M. Darling, L. Thompson, K. Smith, J.S. Moore, F.R. Brushett, X. Wei, A symmetric organic-based nonaqueous redox flow battery and its state of charge diagnostics by FTIR, *J. Mater. Chem. A* 4 (2016) 5448–5456. doi:10.1039/C6TA01177B.
- [180] S. Ergun, C.F. Elliott, A.P. Kaur, S.R. Parkin, S.A. Odom, Overcharge performance of 3,7-disubstituted N-ethylphenothiazine derivatives in lithium-ion batteries, *Chem. Commun.* 50 (2014) 5339–5341. doi:10.1039/C3CC47503D.
- [181] J. Zhang, J. Huang, L.A. Robertson, R.S. Assary, I.A. Shkrob, L. Zhang, Elucidating Factors

Controlling Long-Term Stability of Radical Anions for Negative Charge Storage in Nonaqueous Redox Flow Batteries, *J. Phys. Chem. C.* 122 (2018) 8116–8127. doi:10.1021/acs.jpcc.8b01434.

- [182] C.S. Sevov, D.P. Hickey, M.E. Cook, S.G. Robinson, S. Barnett, S.D. Minter, M.S. Sigman, M.S. Sanford, Physical organic approach to persistent, cyclable, low-potential electrolytes for flow battery applications, *J. Am. Chem. Soc.* 139 (2017) 2924–2927. doi:10.1021/jacs.7b00147.
- [183] L. Meda, F. Oldani, G. Tozzola, S. Caramori, E. Benazzi, V. Cristino, C.A. Bignozzi, Searching for new redox-complexes in organic flow batteries, *Solid State Ionics.* 317 (2018) 142–148. doi:10.1016/j.ssi.2018.01.017.
- [184] P. Leung, D. Aili, Q. Xu, A. Rodchanarowan, A.A. Shah, Rechargeable organic-air redox flow batteries, *Sustain. Energy Fuels.* 2 (2018) 2252–2259. doi:10.1039/c8se00205c.
- [185] X. Wang, X. Xing, Y. Huo, Y. Zhao, Y. Li, H. Chen, Study of tetraethylammonium bis(trifluoromethylsulfonyl)imide as a supporting electrolyte for an all-organic redox flow battery using Benzophenone and 1,4-di-tert-butyl-2,5-dimethoxybenzene as active species, *Int. J. Electrochem. Sci.* 13 (2018) 6676–6683. doi:10.20964/2018.07.56.
- [186] H. Kim, S. Hwang, Y. Kim, J.H. Ryu, S.M. Oh, K.J. Kim, Bi-functional effects of lengthening aliphatic chain of phthalimide-based negative redox couple and its non-aqueous flow battery performance at stack cell, *APL Mater.* 6 (2018) 047901. doi:10.1063/1.5010210.
- [187] W. Wang, W. Xu, L. Cosimbescu, D. Choi, L. Li, Z. Yang, Anthraquinone with tailored structure for a nonaqueous metal–organic redox flow battery, *Chem. Commun.* 48 (2012) 6669. doi:10.1039/c2cc32466k.
- [188] J. Huang, L. Cheng, R.S. Assary, P. Wang, Z. Xue, A.K. Burrell, L.A. Curtiss, L. Zhang, Liquid catholyte molecules for nonaqueous redox flow batteries, *Adv. Energy Mater.* 5 (2015) 1401782. doi:10.1002/aenm.201401782.
- [189] C.S. Sevov, R.E.M. Brooner, E. Chénard, R.S. Assary, J.S. Moore, J. Rodríguez-López, M.S. Sanford, Evolutionary design of low molecular weight organic anolyte materials for applications in nonaqueous redox flow batteries, *J. Am. Chem. Soc.* 137 (2015) 14465–14472. doi:10.1021/jacs.5b09572.
- [190] G. Kwon, K. Lee, M.H. Lee, G. Kwon, K. Lee, M.H. Lee, B. Lee, S. Lee, S. Jung, Bio-inspired Molecular Redesign of a Multi-redox Catholyte for High-Energy Non-aqueous Organic Redox Flow Batteries Bio-inspired Molecular Redesign of a Multi-redox Catholyte for High-Energy Non-aqueous Organic Redox Flow Batteries, *Chem.* (n.d.) 1–15. doi:10.1016/j.chempr.2019.07.006.
- [191] B. Ok, W. Na, T. Kwon, Y. Kwon, S. Cho, S. Man, A.S. Lee, J. Hong, C. Min, Understanding the enhanced electrochemical performance of TEMPO derivatives in non-aqueous lithium ion

- redox flow batteries, *J. Ind. Eng. Chem.* (2019) 6–11. doi:10.1016/j.jiec.2019.08.027.
- [192] N.L. Bauld, Radicals, ion radicals, and triplets, Wiley-VCH, Inc., 1997.
- [193] A.J. Bard, L.R. Faulkner, *Electrochemical Methods Fundamentals and Applications* 2nd Ed, John Wiley & Sons, Inc., 2001.
- [194] R.G. Compton, C.E. Banks, *Understanding Voltammetry* 2nd Ed, Imperial College Press, 2014.
- [195] H.H. Girault, *Analytical and physical electrochemistry*, EPFL press, 2004.
- [196] G. Gritzner, J. Kuta, Recommendations on reporting electrode potentials in nonaqueous solvents, *Pure Appl. Chem.* 56 (1984) 461–466.
- [197] R.R. Gagne, C.A. Koval, G.C. Lisensky, Ferrocene as an Internal Standard for Electrochemical Measurements, *Inorg. Chem.* 19 (1980) 2854–2855. doi:10.1021/ic50211a080.
- [198] K.H. Hendriks, S.G. Robinson, M.N. Braten, C.S. Sevov, B.A. Helms, M.S. Sigman, S.D. Minter, M.S. Sanford, High-Performance Oligomeric Catholytes for Effective Macromolecular Separation in Nonaqueous Redox Flow Batteries, *ACS Cent. Sci.* (2018) acscentsci.7b00544. doi:10.1021/acscentsci.7b00544.
- [199] S. Wang, J. Wang, Y. Gao, Development and use of an open-source, user-friendly package to simulate voltammetry experiments, *J. Chem. Educ.* 94 (2017) 1567–1570. doi:10.1021/acs.jchemed.6b00986.
- [200] F.J. Vidal-Iglesias, J. Solla-Gullón, V. Montiel, A. Aldaz, Errors in the use of the Koutecky-Levich plots, *Electrochem. Commun.* 15 (2012) 42–45. doi:10.1016/j.elecom.2011.11.017.
- [201] S. Treimer, A. Tang, D.C. Johnson, A consideration of the application of Koutecký-Levich plots in the diagnoses of charge-transfer mechanisms at rotated disk electrodes, *Electroanalysis*. 14 (2002) 165–171. doi:10.1002/1521-4109(200202)14:3<165::AID-ELAN165>3.0.CO;2-6.
- [202] K. Likit-Anurak, K. Uthaichana, K. Punyawudho, Y. Khunatorn, The Performance and Efficiency of Organic Electrolyte Redox Flow Battery Prototype, *Energy Procedia*. 118 (2017) 54–62. doi:10.1016/j.egypro.2017.07.012.
- [203] M. Skyllas-Kazacos, C. Menictas, T. Lim, *Redox flow batteries for medium-to large-scale energy storage*, Woodhead Publishing Limited, 2013. doi:10.1533/9780857097378.3.398.
- [204] D. Aaron, Z. Tang, A.B. Papandrew, T.A. Zawodzinski, Polarization curve analysis of all-vanadium redox flow batteries, *J. Appl. Electrochem.* 41 (2011) 1175–1182. doi:10.1007/s10800-011-0335-7.
- [205] B. Hwang, M.-S.S. Park, K. Kim, Ferrocene and cobaltocene derivatives for non-aqueous redox flow batteries, *ChemSusChem*. 8 (2015) 310–314. doi:10.1002/cssc.201403021.
- [206] X.L. Zhou, T.S. Zhao, L. An, Y.K. Zeng, L. Wei, Critical transport issues for improving the performance of aqueous redox flow batteries, *J. Power Sources*. 339 (2017) 1–12.

doi:10.1016/j.jpowsour.2016.11.040.

- [207] M. Park, J. Ryu, W. Wang, J. Cho, Material design and engineering of next-generation flow-battery technologies, *Nat. Rev. Mater.* 2 (2016) 16080. doi:10.1038/natrevmats.2016.80.
- [208] M.O. Bamgbopa, Y. Shao-Horn, S. Almheiri, The potential of non-aqueous redox flow batteries as fast-charging capable energy storage solutions: demonstration with an iron–chromium acetylacetonate chemistry, *J. Mater. Chem. A* 5 (2017) 13457–13468. doi:10.1039/C7TA02022H.
- [209] S. Hwang, H. seung Kim, J.H. Ryu, S.M. Oh, Ni(II)-chelated thio-crown complex as a single redox couple for non-aqueous flow batteries, *Electrochem. Commun.* 85 (2017) 36–39. doi:10.1016/j.elecom.2017.10.015.
- [210] M.J. Baran, M.N. Braten, E.C. Montoto, Z.T. Gossage, L. Ma, E.C. Chénard, J.S. Moore, J. Rodríguez-López, B.A. Helms, Designing Redox-Active Oligomers for Crossover-Free, Nonaqueous Redox-Flow Batteries with High Volumetric Energy Density, *Chem. Mater.* 30 (2018) 3861–3866. doi:10.1021/acs.chemmater.8b01318.
- [211] J.D. Saraidaridis, B.M. Bartlett, C.W. Monroe, Spectroelectrochemistry of Vanadium Acetylacetonate and Chromium Acetylacetonate for Symmetric Nonaqueous Flow Batteries, *J. Electrochem. Soc.* 163 (2016) A1239–A1246. doi:10.1149/2.0441607jes.
- [212] T. Herr, J. Noack, P. Fischer, J. Tübke, 1,3-Dioxolane, tetrahydrofuran, acetylacetone and dimethyl sulfoxide as solvents for non-aqueous vanadium acetylacetonate redox-flow-batteries, *Electrochim. Acta.* 113 (2013) 127–133. doi:10.1016/j.electacta.2013.09.055.
- [213] A.A. Shinkle, A.E.S. Sleightholme, L.T. Thompson, C.W. Monroe, Electrode kinetics in non-aqueous vanadium acetylacetonate redox flow batteries, *J. Appl. Electrochem.* 41 (2011) 1191–1199. doi:10.1007/s10800-011-0314-z.
- [214] X. Wei, L. Cosimbescu, W. Xu, J.Z. Hu, M. Vijayakumar, J. Feng, M.Y. Hu, X. Deng, J. Xiao, J. Liu, V. Sprenkle, W. Wang, Towards High-Performance Nonaqueous Redox Flow Electrolyte Via Ionic Modification of Active Species, *Adv. Energy Mater.* 5 (2015) n/a-n/a. doi:10.1002/aenm.201400678.
- [215] D. Astruc, Why is Ferrocene so Exceptional?, *Eur. J. Inorg. Chem.* 2017 (2017) 6–29. doi:10.1002/ejic.201600983.
- [216] N.G. Connelly, W.E. Geiger, Chemical redox agents for organometallic chemistry, *Chem. Rev.* 96 (1996) 877–910. doi:10.1021/cr940053x.
- [217] M. Malischewski, M. Adelhardt, J. Sutter, K. Meyer, K. Seppelt, Isolation and structural and electronic characterization of salts of the decamethylferrocene dication, *Science* (80-. ). 353 (2016) 678–682. doi:10.1126/science.aaf6362.
- [218] F. Yang, D. Wang, Y. Zhao, K.L. Tsui, S.J. Bae, A study of the relationship between coulombic efficiency and capacity degradation of commercial lithium-ion batteries, *Energy*. 145 (2018)

- 486–495. doi:10.1016/j.energy.2017.12.144.
- [219] A. Singh, D.R. Chowdhury, A. Paul, A kinetic study of ferrocenium cation decomposition utilizing an integrated electrochemical methodology composed of cyclic voltammetry and amperometry, *Analyst*. 139 (2014) 5747–5754. doi:10.1039/c4an01325e.
- [220] J.P. Hurvois, C. Moinet, Reactivity of ferrocenium cations with molecular oxygen in polar organic solvents: Decomposition, redox reactions and stabilization, *J. Organomet. Chem.* 690 (2005) 1829–1839. doi:10.1016/j.jorganchem.2005.02.009.
- [221] G. Zotti, G. Schiavon, S. Zecchin, D. Favretto, Dioxygen-decomposition of ferrocenium molecules in acetonitrile: The nature of the electrode-fouling films during ferrocene electrochemistry, *J. Electroanal. Chem.* 456 (1998) 217–221. doi:10.1016/S0022-0728(98)00279-4.
- [222] D.L. Jameson, K. a Goldsby, 2,6-Bis(N-Pyrazolyl)Pyridines - the Convenient Synthesis of a Family of Planar Tridentate N<sub>3</sub> Ligands That Are Terpyridine Analogs, *J. Org. Chem.* 55 (1990) 4992–4994. doi:10.1021/jo00304a007.
- [223] N.M. Shavaleev, F. Kessler, M. Grätzel, M.K. Nazeeruddin, Redox properties of cobalt(II) complexes with azole-pyridines, *Inorganica Chim. Acta.* 407 (2013) 261–268. doi:10.1016/j.ica.2013.07.057.
- [224] E. Mosconi, J.H. Yum, F. Kessler, C.J.G. Garcia, C. Zuccaccia, A. Cinti, M.K. Nazeeruddin, M. Grätzel, F. De Angelis, Cobalt Electrolyte/Dye Interactions in Dye-Sensitized Solar Cells: A Combined Computational and Experimental Study, *J Am Chem Soc.* 134 (2012) 19438–19453. doi:10.1021/ja3079016.
- [225] A.J. Downard, G.E. Honey, P.J. Steel, Synthesis , Spectroscopy , and Electrochemistry of Ruthenium ( II ) Complexes of, *Inorg. Chem.* 30 (1991) 3733–3737.
- [226] M.A.M. Garcia, A. Gelling, D.R. Noble, K.G. Orrell, A.G. Osborne, V. Sik, Fluxional Rhenium(I) Tricarbonyl Halide Complexes of Substituted Pyrazolpyridine Ligands. Nuclear Magnetic Resonance Studies of 1,4 Metallotropic Shifts, *Polyhedron.* 15 (1996) 371–379.
- [227] N.M. Shavaleev, R. Scopelliti, M. Grätzel, M.K. Nazeeruddin, Steric hindrance at metal centre quenches green phosphorescence of cationic iridium(III) complexes with 1-(2-pyridyl)-pyrazoles, *Inorganica Chim. Acta.* 404 (2013) 210–214. doi:10.1016/j.ica.2013.03.002.
- [228] T. Ayers, S. Scott, J. Goins, N. Caylor, D. Hathcock, S.J. Slattery, D.L. Jameson, Redox and spin state control of Co (II) and Fe (II) N-heterocyclic complexes, *Inorganica Chim. Acta.* 307 (2000) 7–12. doi:10.1016/S0020-1693(00)00179-1.
- [229] S. Hayami, Y. Komatsu, T. Shimizu, H. Kamihata, Y.H. Lee, Spin-crossover in cobalt(II) compounds containing terpyridine and its derivatives, *Coord. Chem. Rev.* 255 (2011) 1981–1990. doi:10.1016/j.ccr.2011.05.016.
- [230] S. Kremer, W. Henke, D. Reinen, High-spin-low-spin equilibriums of cobalt(2+) in the

terpyridine complexes  $\text{Co}(\text{terpy})_2\text{X}_2\cdot n\text{H}_2\text{O}$ , *Inorg. Chem.* 21 (1982) 3013–3022.  
doi:10.1021/ic00138a019.

- [231] J.A. McCleverty, Metal 1,2-Dithiolene and Related Complexes, *Prog. Inorganic Chem.* 10 (1968) 49–221.
- [232] R. Eisenberg, H.B. Gray, Noninnocence in metal complexes: A dithiolene dawn, *Inorg. Chem.* 50 (2011) 9741–9751. doi:10.1021/ic2011748.
- [233] R. Sarangi, S.D.B. George, D.J. Rudd, R.K. Szilagy, X. Ribas, C. Rovira, M. Almeida, K.O. Hodgson, B. Hedman, E.I. Solomon, Sulfur K-edge X-ray absorption spectroscopy as a probe of ligand-metal bond covalency: Metal vs ligand oxidation in copper and nickel dithiolene complexes, *J. Am. Chem. Soc.* 129 (2007) 2316–2326. doi:10.1021/ja0665949.
- [234] S. Sproules, T. Weyhermüller, S. Debeer, K. Wieghardt, Six-membered electron transfer series  $[\text{V}(\text{dithiolene})(3)](z)$  ( $z = 1+, 0, 1-, 2-, 3-, 4-$ ). An X-ray absorption spectroscopic and density functional theoretical study., *Inorg. Chem.* 49 (2010) 5241–61.  
doi:10.1021/ic100344f.
- [235] A. Hoepping, R. Mengel, R. Mayer, An alternative synthesis of sodium cyanodithioformate and the disodium salt of cis-1,2-dicyanoethylene-1,2-dithiol, *J. Fur Prakt. Chemie - Chem. - Zeitung.* 340 (1998) 269–270. doi:10.1002/prac.19983400311.
- [236] M. Glodde, S. Liu, P.R. Varanasi, Fluorine-free photoacid generators for 193 nm lithography based on non-sulfonate organic superacids, *J. Photopolym. Sci. Technol.* 23 (2010) 173–184. doi:10.2494/photopolymer.23.173.
- [237] A. Davison, N. Edelstein, R.H. Holm, A.H. Maki, Synthetic and Electron Spin Resonance Studies of Six-Coordinate Complexes Related by Electron-Transfer Reactions, *J. Am. Chem. Soc.* 86 (1964) 2799–2805. doi:10.1021/ja01068a010.
- [238] J.F. Weiher, L.R. Melby, R.E. Benson, 1,2-Dicyanoethylene-1,2-dithiolate Chelates, *J. Am. Chem. Soc.* 86 (1964) 4329–4333. doi:10.1021/ja01074a019.
- [239] A. Davison, R.H. Holm, R.E. Benson, W. Mahler, Metal Complexes Derived from cis-1,2-dicyano-1,2-ethylenedithiolate and Bis(Trifluoromethyl)-1,2-dithiete, *Inorg. Synth.* 10 (1967) 8–26.
- [240] G. Bähr, G. Schleitzer, Contributions to the chemistry of carbon disulphide and selenium carbon, I. Message: Salts of cyanodithioic acid, *Chem. Ber.* 88 (1955) 1771–1777.
- [241] G. Schleitzer, G. Bähr, Contributions to the chemistry of carbon disulphide and selenium carbon, II. The condensing spontaneous desulphurization of salts and esters of cyan-dithioic acid. Free cyan-dithioformic acid, *Chem. Ber.* 90 (1957) 438–443.
- [242] T.E. Mines, W.E. Geiger, Electrochemical Generation and Spectral Characterization of the Bis(maleonitriledithiolato)nickel Trianion, *Inorg. Chem.* 12 (1973) 1189–1191. doi:10.1021/ic50123a043.

## References

- [243] A. Vlček, A.A. Vlček, Bis(maleonitriledithiolato)Cobalt Redox Series, *Inorganica Chim. Acta.* 64 (1982) 213–214. doi:10.1016/S0020-1693(00)90351-7.
- [244] A. Vlček, A.A. Vlček, Metal-localized protonation of  $Mmnt_3-2$  ( $M = Rh, Co$ ) complexes, *Inorganica Chim. Acta.* 41 (1980) 123–131. doi:10.1016/S0020-1693(00)88441-8.
- [245] L.D. Field, N.G. Jones, P. Turner, Reduction of a coordinated acetonitrile ligand: Synthesis of an ethylimido complex of tungsten, *Organometallics.* 17 (1998) 2394–2398. doi:10.1021/om970829v.
- [246] N.F. Yan, G.R. Li, X.P. Gao, Electroactive Organic Compounds as Anode-Active Materials for Solar Rechargeable Redox Flow Battery in Dual-Phase Electrolytes, *J. Electrochem. Soc.* 161 (2014) A736–A741. doi:10.1149/2.065405jes.
- [247] A.J. Fatiadi, H.S. Isbell, W.F. Sager, Cyclic Polyhydroxy Ketones. 1. Oxidation Products of Hexahydroxybenzene (Benzenehexol), *J. Res. Natl. Bur. Stand. Phys. Chem.* 67A (1963) 153–162. doi:10.6028/jres.067A.015.
- [248] B. Zhao, M.H. Back, The photochemistry of the rhodizonate dianion in aqueous solution, *Can. J. Chem.* 69 (1991) 528–532. doi:10.1139/v91-079.
- [249] G. Speier, E. Speier, B. Noll, C.G. Pierpont, Reduction and Aerobic Oxidation of Hexaketocyclohexane ( $C_6O_6$ ) by Reaction with Metallic Copper, *Inorg. Chem.* 36 (1997) 1520–1521. doi:10.1021/ic970077x.
- [250] N.E.W.A. Of, New Applications of malononitrile, (n.d.).
- [251] G. Seitz, P. Imming, Oxocarbons and Pseudooxocarbons, *Chem. Rev.* 92 (1992) 1227–1260. doi:10.1021/cr00014a004.
- [252] E. Speier, B. Noll, C.G. Pierpont, Reduction and Aerobic Oxidation of Hexaketocyclohexane ( $C_6O_6$ ) by Reaction with Metallic Copper Ga University of Veszpre, 1669 (1997) 1520–1521. doi:10.1021/ic970077x.
- [253] R. West, Chemistry of the oxocarbons, *Isr. J. Chem.* 20 (1980) 300–307.
- [254] D. Braga, L. Maini, F. Grepioni, Croconic acid and alkali metal croconate salts: Some new insights into an old story, *Chem. - A Eur. J.* 8 (2002) 1804–1812. doi:10.1002/1521-3765(20020415)8:8<1804::AID-CHEM1804>3.0.CO;2-C.
- [255] F. Serratos, Acetylene Diethers: A Logical Entry to Oxocarbons, *Acc. Chem. Res.* 16 (1983) 170–176. doi:10.1021/ar00089a004.
- [256] D. Sazou, G. Kokkinidis, Electrochemical oxidation of squaric and croconic acids on Pt and Pt surfaces modified by underpotential heavy metal monolayers in acid solutions, *Can. J. Chem.* 65 (2006) 397–403. doi:10.1139/v87-067.
- [257] P. Fabre, P. Castan, D. Deguenon, N. Paillous, A photo-oxidation of croconic acid into oxalic acid, 1304 (1995) 1298–1304.

- [258] R. Carbó, R. Albalat, J. Claret, J.M. Orts, A. Rodes, Electrochemical behaviour of oxocarbons on single crystal platinum electrodes Part IV. Rhodizonic acid in 0.5 M sulphuric acid medium, *J. Electroanal. Chem.* 424 (1997) 185–196. doi:10.1016/S0022-0728(96)04916-9.
- [259] B. Soula, A. Galibert, B. Donnadieu, P. Fabre, Complexation of croconate violet with copper(II). Crystal structures, spectroscopic characterizations and redox studies, *Inorganica Chim. Acta.* 324 (2001) 90–98.
- [260] L.M. Doane, A.J. Fatiadi, Electrochemical oxidation of croconate salts; Evidence of the chemical equivalence of the carbonyl oxygen atom and the dicyanomethylene group, *Angew. Chem. Int. Ed. Engl.* 21 (1982) 635–636.
- [261] L.M. Doane, A.J. Fatiadi, Electrochemical oxidation of several oxocarbon salts in N,N-dimethylformamide, *J. Electroanal. Chem.* 135 (1982) 193–209.
- [262] A.J. Fatiadi, Synthesis of 1,3-(dicyanomethylene)croconate salts. New bond-delocalized dianion, “croconate violet,” *J. Am. Chem. Soc.* 100 (1978) 2586–2587.
- [263] W.M. Teles, R.D.A. Farani, D.S. Maia, N.L. Speziali, M.I. Yoshida, L.F.C. De Oliveira, F.C. Machado, Crystal structure, thermal analysis and spectroscopic properties of Tetrabutylammonium 3,5-bis(dicyanomethylene)-cyclopentane-1,2,4-trionate: An intriguing pseudo-oxocarbon and its zinc(II) complex, *J. Mol. Struct.* 783 (2006) 52–60. doi:10.1016/j.molstruc.2005.08.020.
- [264] A.J. Fatiadi, Pseudooxocarbons. Synthesis of 1,2,3-tris(dicyanomethylene)croconate salts. A new bond-delocalized dianion, croconate blue, *J. Org. Chem.* 45 (1980) 1338–1339.
- [265] P.L. Fabre, F. Dumestre, B. Soula, A.M. Galibert, Spectroelectrochemical behaviour in dimethylformamide of pseudo-oxocarbons dianions derived from the croconate dianion, *Electrochim. Acta.* 45 (2000) 2697–2705. doi:10.1016/S0013-4686(00)00324-8.
- [266] F. Dumestre, B. Soula, A.-M. Galibert, P.-L. Fabre, G. Bernardinelli, B. Donnadieu, P. Castan, Synthesis and Characterization of cobalt(II) complexes of croconate and dicyanomethylene-substituted derivatives, *J. Chem. Soc., Dalt. Trans.* (1998) 4131–4137. doi:10.1081/MA-120016047.
- [267] F. Freeman, The chemistry of malononitrile, *Chem. Rev.* 69 (1969) 591–624. doi:10.1021/cr60261a001.
- [268] G. Cahiez, M. Alami, R.J.K. Taylor, M. Reid, J.S. Foot, L. Fader, V. Sikervar, Manganese Dioxide, in: *Encycl. Reagents Org. Synth.*, 2017: pp. 1–16.
- [269] K.M. Abraham, Influence of Nonaqueous Solvents on the Electrochemistry of Oxygen in the Rechargeable Lithium – Air Battery Lithium - Air Battery, (2016) 9178–9186. doi:10.1021/jp102019y.
- [270] T.H. Le, A. Nafady, X. Qu, L.L. Martin, A.M. Bond, Detailed electrochemical analysis of the redox chemistry of tetrafluorotetracyanoquinodimethane TCNQF<sub>4</sub>, the radical anion

## References

- [TCNQF<sub>4</sub>]<sup>2-</sup>, and the dianion [TCNQF<sub>4</sub>]<sup>2-</sup> in the presence of trifluoroacetic acid, *Anal. Chem.* 83 (2011) 6731–6737. doi:10.1021/ac201373d.
- [271] T.H. Le, A. Nafady, X. Qu, A.M. Bond, L.L. Martin, Redox and acid-base chemistry of 7,7,8,8-tetracyanoquinodimethane, 7,7,8,8-tetracyanoquinodimethane radical anion, 7,7,8,8-tetracyanoquinodimethane dianion, and dihydro-7,7,8,8-tetracyanoquinodimethane in acetonitrile, *Anal. Chem.* 84 (2012) 2343–2350. doi:10.1021/ac2030514.
- [272] S.H. Oh, C.-W. Lee, D.H. Chun, J.-D. Jeon, J. Shim, K.H. Shin, J.H. Yang, A metal-free and all-organic redox flow battery with polythiophene as the electroactive species, *J. Mater. Chem. A* 2 (2014) 19994–19998. doi:10.1039/C4TA04730C.
- [273] R.M. Darling, K.G. Gallagher, J.A. Kowalski, S. Ha, F.R. Brushett, Pathways to low-cost electrochemical energy storage: a comparison of aqueous and nonaqueous flow batteries, *Energy Environ. Sci.* 7 (2014) 3459–3477. doi:10.1039/C4EE02158D.
- [274] K. Lin, R. Gómez-Bombarelli, E.S. Beh, L. Tong, Q. Chen, A. Valle, A. Aspuru-Guzik, M.J. Aziz, R.G. Gordon, A redox-flow battery with an alloxazine-based organic electrolyte, *Nat. Energy* 1 (2016) 16102. doi:10.1038/nenergy.2016.102.
- [275] P. Banerjee, S. Sproules, T. Weyhermüller, S. Debeer George, K. Wieghardt, Electronic structure of the [tris(dithiolene)chromium](z) (z = 0, 1-, 2-, 3-) electron transfer series and their manganese(IV) analogues. An X-ray absorption spectroscopic and density functional theoretical study., *Inorg. Chem.* 48 (2009) 5829–47. doi:10.1021/ic900154v.
- [276] P. Zanello, M. Corsini, Homoleptic, mononuclear transition metal complexes of 1,2-dioxolenes: Updating their electrochemical-to-structural (X-ray) properties, *Coord. Chem. Rev.* 250 (2006) 2000–2022. doi:10.1016/j.ccr.2005.12.017.



## Appendix A: Physical properties of solvents

**Table 11. Physical properties of solvents for electrochemical devices (standard conditions).**

Values reproduced from [19,67,68,98,100,101].

Solvent	Density [g cm <sup>-3</sup> ]	Freezing point [°C]	Boiling point [°C]	Viscosity [mPa s]	Relative permittivity	Dipole moment [D]	E <sub>red</sub> [V] vs SHE	E <sub>ox</sub> [V] vs SHE	LD <sub>50</sub> [g <sub>oral</sub> kg <sub>rat</sub> <sup>-1</sup> ]
Water (H <sub>2</sub> O)	1.00	0.0	100.0	0.890	78.390	1.77	0.00	1.23	
<b>Alcohols</b>									
Methanol (MeOH)	0.79	-97.7	64.5	0.551	32.700	1.71	-0.76	1.54	16.89
Ethanol (EtOH)	0.78	-114.5	78.3	1.083	24.600	1.74			10.47
1-Propanol	0.80	-126.2	97.2	1.943	20.500	1.71			8.04
2-Propanol (iPrOH)	0.78	-88.0	82.2	2.044	19.900	1.66			5.05
<b>Ethers</b>									
Dimethoxymethane	0.86	-105.0	41.0	0.330	2.700	2.41			6.42
Anisole	0.99	-37.5	153.8	0.895	4.330	1.25			3.70
Tetrahydrofuran (THF)	0.89	-108.4	66.0	0.460	7.580	1.75	-3.00	2.70	2.45
2-Methyltetrahydrofuran	0.86	-137.0	80.0	0.470	6.200	1.60			> 0.3
1,4-Dioxane	1.03	11.8	101.3	1.087	2.210	0.45			4.20
1,3-Dioxolane (DOL)	1.06	-95.0	78.0	0.590	7.100	1.25			5.20
4-methyl-1,3-dioxolane	0.99	-125.0	85.0	0.600	6.800	1.43			
1,2-Dimethoxyethane (DME)	0.86	-69.0	84.5	0.455	7.200	1.71	-3.50	2.10	5.37
Diglyme	0.94	-64.0	159.8	0.989		1.97			5.40
<b>Ketones</b>									
Acetone	0.78	-94.7	56.1	0.303	20.600	2.70			5.80
Acetylacetone	0.98	-23.2	138.3	0.694	25.700	2.78			0.57
<b>Nitriles</b>									
Acetonitrile (MeCN)	0.79	-43.8	81.6	0.341	35.900	3.53	-2.60	3.50	6.69
Methoxyacetonitrile (MAN)	0.96	-35.0	120.0	0.700	36.000		-2.50	3.20	0.98
Propionitrile	0.77	-92.8	97.4	0.389	28.900	3.50			0.04
Butyronitrile	0.79	-111.9	117.6	0.515	24.800	3.50			
Isobutyronitrile	0.77	-71.5	103.8	0.456	20.400	3.61			0.05
Benzonitrile	1.00	-12.7	191.1	1.237	25.200	4.01			1.00

Novel Non-Aqueous Symmetric Redox Materials for Redox Flow Battery Energy Storage

3-Methoxypropionitrile	0.93	-57.0	165.0	1.100	36.000		-2.50	3.30	4.39
<b>Amines</b>									
Ethylenediamine	0.89	11.3	116.9	1.540	12.900	1.90			1.2
Pyridine	0.98	-41.6	115.3	0.884	12.900	2.37			1.5
<b>Amides</b>									
Formamide	1.13	2.5	210.5	3.300	111.000	3.37			5.33
N-Methylacetamide	0.96	30.5	206.0	3.650	191.300	4.27			3.95
N,N-Dimethylformamide (DMF)	0.94	-60.4	153.0	0.802	36.700	3.24	-2.80	1.80	2.80
N,N-Dimethylacetamide (DMA)	0.94	-20.0	166.1	0.927	37.800	3.79			5.68
N-Methyl-2-pyrrolidinone (NMP)	1.03	-24.4	202.0	1.670	32.200	4.09			3.91
3-Methoxypropionitrile (MPN)	0.94	-57.0	165.0	1.100	36.000		-2.5	3.30	4.39
<b>Carbonates</b>									
Propylene carbonate (PC)	1.20	-54.5	241.7	2.530	64.920	4.94	-2.80	3.80	5.00
Ethylene carbonate (EC)	1.32	36.4	248.2	1.900	89.800	4.90			> 5.00
$\gamma$ -butyrolactone ( $\gamma$ -BL)	1.13	-43.4	204.0	1.730	39.100	4.12	-2.80	5.40	1.54
$\gamma$ -valerolactone ( $\gamma$ -VL)	1.05	-31.0	208.0	2.000	34.000	4.29	-2.80	5.40	8.80
Dimethyl carbonate (DMC)	1.07	4.6	91.0	0.590	3.107	0.76			> 5.00
Diethyl carbonate (DEC)	0.97	74.3	126.0	0.750	2.805	0.96			> 4.88
Ethyl methyl carbonate (EMC)	0.97	-53.0	110.0	0.650	2.958	0.89			
1,2-Butylene carbonate (BC)	1.14	-53.0	240.0	3.200	53.000		-2.80	4.40	
<b>Others</b>									
Hexane	0.65	-95.3	68.7	0.294	1.880	0.085			25.00
Benzene	0.88	5.5	80.1	0.603	2.270	0.00			> 5.96
Toluene	0.86	-95.0	110.6	0.553	2.380	0.31			5.58
Nitromethane (NM)	1.13	-28.6	101.2	0.614	36.700	3.17	-1.00	2.90	0.94
Nitroethane (NE)	1.05	-90.0	115.0	0.680	28.000		-1.10	3.20	1.1
Nitrobenzene (NB)	1.20	5.8	210.8	1.620	34.800	4.00			0.59
1,2-Dichloroethane (DCE)	1.26	-35.7	83.5	0.730	10.370	1.86	-2.10	2.00	0.77
Dichloromethane (DCM)	1.32	-95.0	40.0	0.390	8.930				2.00
Dimethyl sulfoxide (DMSO)	1.10	18.5	189.0	1.990	46.500	4.06	-2.70	1.70	28.3
Ethyl acetate	0.90	-83.6	77.1	0.426	6.020	1.82			5.62
Trimethyl phosphate (TMP)	1.07	-46.0	197.0	2.200	21.000		-2.70	3.70	0.84
4-Methyl-2-pentanone	0.80	-84.0	117.0	0.550	13.100				2.08

## Appendix B: EDX analysis

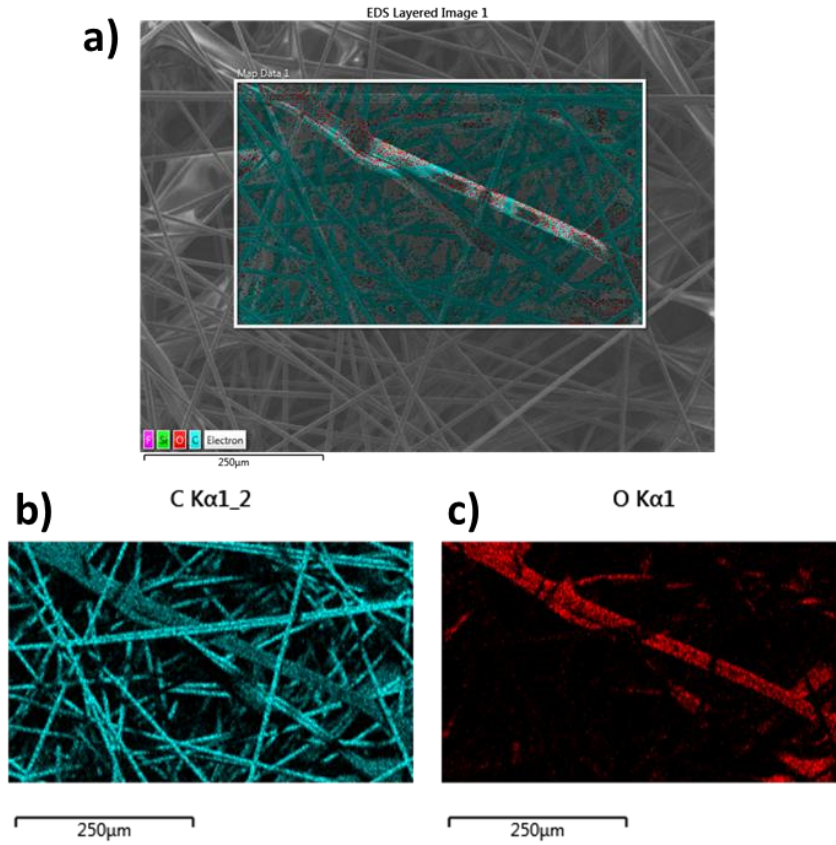


**Figure 102. EDX analysis of the carbon paper electrode material (20301A, Technical Fibre Products Ltd.) in Figure 28. a) EDX analysis region containing fibres and binder, b) false-colour map of carbon, c) false-colour map of oxygen. 250 μm scale.**

## Appendix C: UV-vis Solubility Calibrations

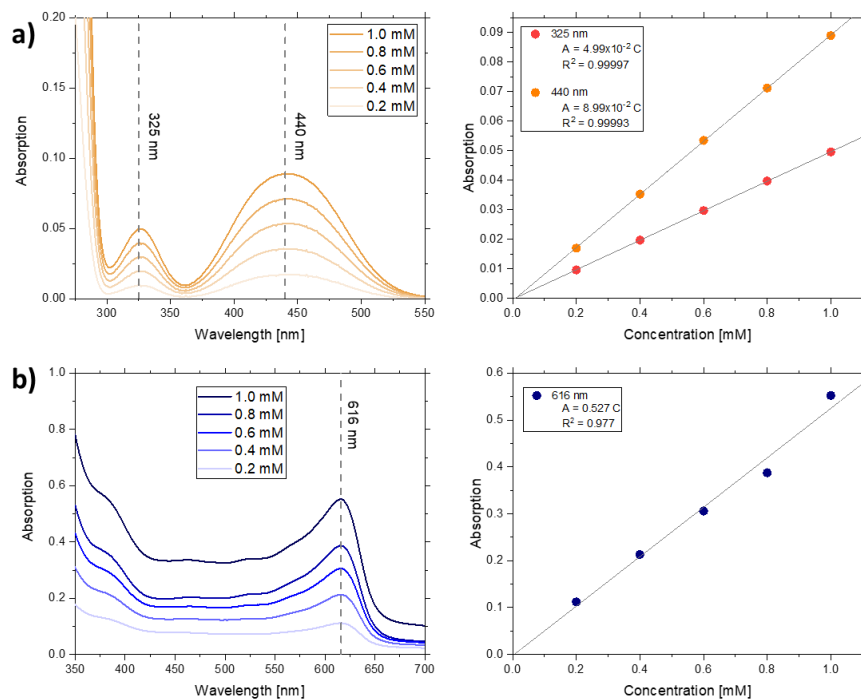
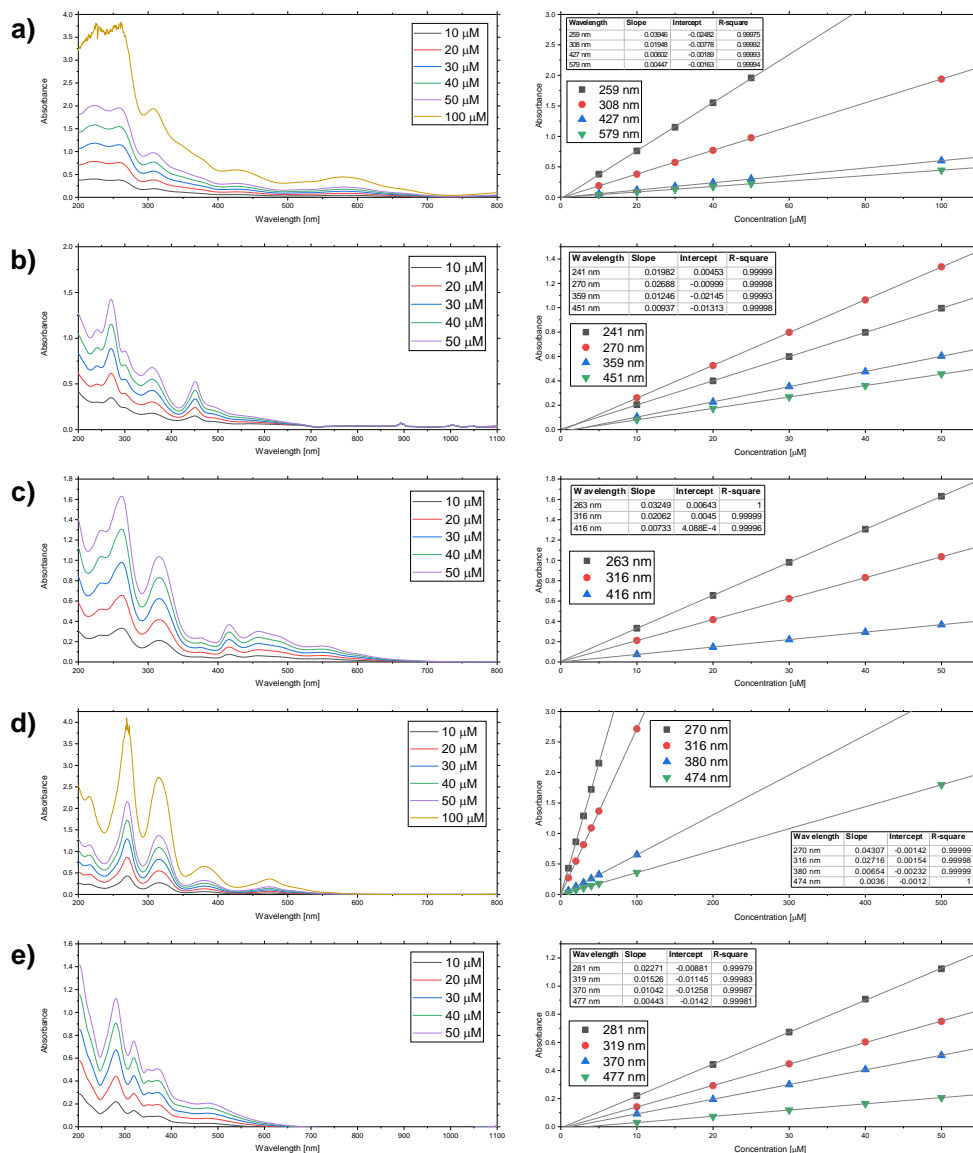
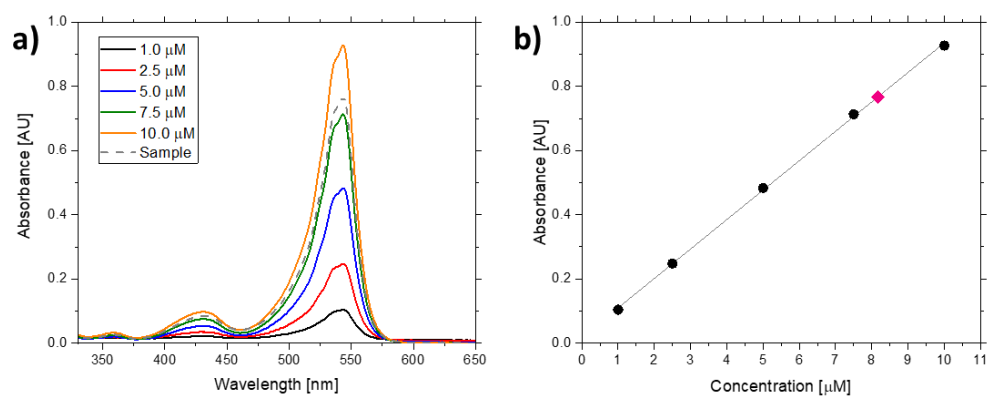


Figure 103. UV-vis calibrations and Beer-Lambert plots for a) Fc and b) FcBF<sub>4</sub>.



**Figure 104. UV-vis spectra as a function of  $M_{mnt}$  concentration and Beer-Lambert calibrations. a)  $V_{mnt}$ , b)  $Fe_{mnt}$ , c)  $Co_{mnt}$ , d)  $Ni_{mnt}$ , e)  $Cu_{mnt}$**



**Figure 105. a) UV-vis absorption spectra as a function TBA<sub>2</sub>Croc concentration and b) Beer-Lambert calibration plot. The unknown concentration sample is shown on the spectra in grey and in the calibration in pink.**